UNIVERSITY OF CALIFORNIA

Santa Barbara

# Synthesis and Hierarchical Structure of Functional Organic Materials

A dissertation submitted in partial satisfaction of the

requirements for the degree Doctor of Philosophy

in Materials

by

Brenden McDearmon

Committee in charge:

Professor Craig Hawker, Chair

Professor Michael Chabinyc

Professor Stephen Wilson

Professor Javier Read de Alaniz

September 2017

The dissertation of Brenden McDearmon is approved.

_____

Stephen Wilson

_____

Javier Read de Alaniz

_____

Michael Chabinyc

_____

Craig Hawker, Committee Chair

August 2017

ACKNOWLEDGEMENTS

I would like to thank: Eunhee Lim for her help with the GIWAXS and OFET data in the pentacyclic project as well as her help analyzing the GIWAXS data in the cyclic BDT project; Kathryn O'Hara for her help collecting the GIWAXS data for both the pentacyclic project and cyclic BDT project; Hidenori Nakayama for his help making and characterizing the solar cell devices in the pentacyclic project; Yingdong Luo for his help with some of the early small molecule work in the pentacyclic project; In-Hwan Lee for his help synthesizing some of the BDT starting material as well as some of the comonomers in the cyclic BDT project; Isaac Robledo for his help synthesizing some of the cyclic BDT material; Naveen R. Venkatesan for his help collecting some of the GIWAXS data for the cyclic BDT project; and Caitlin Sample and Neil Dolinski for their help with the mechanical testing and surface contact angle measurements in the bottlebrush network project. I would also like to thank Michael Chabinyc for all of his help and advice teaching me and helping me with the organic electronic projects, and I would like to thank Craig Hawker for his help throughout my PhD. Additionally, I would like to thank both Will Gutekunst and Yingdong Luo for all of their help training me in organic chemistry and answering many of my in lab questions. I would also like to thank the rest of the Hawker group members who have been so helpful throughout the years answering questions and discussing ideas. Thank you.

VITA OF Brenden McDearmon

September 2017

EDUCATION

Bachelor of Science in Biomedical Engineering, Washington University in St. Louis, May 2012
Doctor of Philosophy in Materials, University of California, Santa Barbara, September 2017 (expected)

PROFESSIONAL EMPLOYMENT

2017: Teaching Assistant, Department of Materials, University of California, Santa Barbara

PUBLICATIONS

McDearmon, B., Lim, E., O'Hara, K., Nakayama, H., Luo, Y., Chabinyc, M. L. and Hawker, C. J. (2017), Synthesis of a versatile pentacyclic building block for organic electronics. J. Polym. Sci. Part A: Polym. Chem., 55: 2618–2628.

"Effect of Side-Chain Topology on Conjugated Polymer Aggregation" in progress

"Concise and Versatile Synthesis of Well-Defined Functional Photocrosslinkable Bottlebrush Networks." in progress

FIELDS OF STUDY

Major Field: Polymer Chemistry and Engineering supervised by Professor Craig Hawker

ABSTRACT

Synthesis and Hierarchical Structure of Functional Organic Materials

by

Brenden McDearmon

The design and synthesis of new organic materials is necessary to meet society's needs. A central tenant of material science is that function follows form. With this in mind: 1) a one-step procedure to a new versatile pentacyclic benzodibenzofuranquinone building block for organic electronic applications is developed; 2) the effect of side-chain topology on conjugated polymer interchain interactions, morphology, and optical properties are studied by comparing a novel macrocyclic benzodithiophene unit to its more traditional linear acyclic analogue; and 3) a short and modular synthetic route to functional and well-defined photocrosslinked bottlebrush networks is developed. All of three of these projects highlight how molecular architecture and design can be used to engineer macroscopic material properties and tailor function from form. In particular, conjugated polymers and organic electronics are an interesting class of materials wherein the electronic properties of the materials are dictated by several hierarchical orders of structure. The primary level of structure is the (co)monomer structure which dictates energetics of the polymer backbone. The aggregation, self-assembly, and interaction of these conjugated polymer chains then form higher-order structures which determine the overall material properties and device performance. Project 1 addresses this primary level of structure by developing simple inexpensive and versatile new building blocks for organic electronic materials. Project 2 studies how higher-order structure and properties

of organic electronic materials are impacted by primary molecular structure. This is done by comparing materials based on a macrocyclic benzodithiophene unit which disrupts conjugated polymer aggregation and interchain interactions to materials based on its acyclic linear analogue which does not. Project 3 examines this structure-property mantra through the lens of a different class of materials—soft compliant elastomeric bottlebrush networks. In bottlebrush networks, the macromolecular architecture of the bottlebrush polymers results in their soft and compliant mechanical properties. A concise and modular strategy for synthesizing well-defined and functional photocrosslinkable bottlebrush networks is demonstrated. With versatility in the monomer, macromonomer, bottlebrush polymer, and crosslinked bottlebrush network, these hierarchical levels of structure can be tailored and the resulting macroscopic mechanical and chemical properties can be tuned. This strategy makes these materials more accessible and enables further use of these bottlebrush materials for various applications in fields such as biomaterials.

TABLE OF CONTENTS

# I. Introduction

A central tenant of material sciences is that structure begets function. In the field of biomacromolecules and proteins, this tenant is further codified by the primary, secondary, tertiary, and quaternary structure nomenclature describing the monomer sequence, local secondary structure of the backbone, global structural fold of the protein, and inter-protein interactions. This nomenclature describes the hierarchical assembly of these macromolecules and underscores the importance of molecular architecture on the resulting macromolecular structure, interactions, and material properties. Likewise, the field of synthetic organic materials can be viewed through this lens—monomer design and monomer sequence being the primary level of structure; polymer architecture and backbone connectivity being like the secondary and tertiary levels of structure; and, finally, physical association, self-assembly, and aggregation of these molecules and macromolecules into macroscopic materials being the quaternary level of structure. Through molecular and macromolecular design, these hierarchical levels of structure can be used to improve functionality, probe and test our understanding of the underlying physics, and engineer new materials. By designing novel monomer structures, characterizing their hierarchical assembly, and providing simple and versatile synthetic platforms, this dissertation seeks to establish new building blocks for material science, probe the evolution of structure to function, and provide a simple useful framework for others to build off this work. Work in this dissertation can be split into two classes of materials: 1) organic electronic materials wherein the bulk electrical and optical properties are the material properties of interest, and 2) elastic and compliant bottlebrush

networks wherein the bulk mechanical and chemical properties are the material properties of interest. In each of these two classes of materials, the material properties of interest are dictated by the hierarchical levels of structure from which they are built.

Organic electronics are a class of materials which combine the mechanical properties and processability of polymers and small molecules with the electrical and optical properties of semiconductors. Typical polymers such as polystyrene in plastic knives and forks, polyethylene in plastic grocery bags, and polyvinyl chloride (PVC) in pipes are electrically insulating. When a reasonable voltage is applied across such a material, no current results. The insulating property of these materials is a result of the electrons in these materials being tightly held in covalent bonds resulting in a low dielectric constant, large band gap, and insulating character. Organic electronic materials are capable of shrinking this band gap to give rise to semiconducting properties by delocalizing electrons in $sp^2$ π-conjugated frameworks. As the π-conjugated framework gets larger and larger the energy of the band gap decreases until an effective conjugation length is reached. This is similar to the decrease in spacing between energy levels for a quantum mechanical particle in a box with increasing length of the box[1]. This for example is why polystyrene with its π electrons in isolated benzene rings is insulating whereas poly(p-phenylene vinylene) which has the benzene units electrically coupled through $sp^2$ hybridized bonds has a lower band gap making it semiconducting (Figure 1).

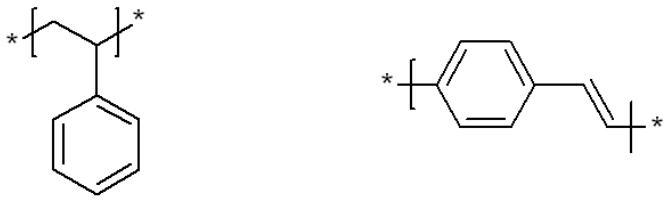

Polystyrene Poly(p-phenylene vinylene)

**Figure 1: Comparison of insulating polystyrene and semiconducting poly(p-phenylene vinylene).**

With a sufficiently narrow band gap, organic electronic materials possess new material properties and available applications relative to non-semiconducting plastics. Such properties and applications include optical band gaps in the visible range enabling the creation of organic photovoltaic devices and organic light emitting diodes. Organic electronic materials offer several advantages over more traditional inorganic semiconducting materials. Organic electronic materials can be synthesized from more abundant elements such as carbon, nitrogen, sulfur, and hydrogen utilizing the tools of organic chemistry to create a variety of materials with finely tuned electrical and mechanical properties, and such materials can be solution processed thereby improving the economic scalability of large area devices. Conjugated polymers can be roughly separated into two parts—1) the aromatic backbone which delocalizes charge and, to first order approximation, establishes the electronic properties of the material and 2) the side-chains which promote solubility and processability of the material[3,4,5,6]. However, as noted the backbone only dictates the electronic properties of the material to a first order approximation, and the aggregation and interaction of these conjugated polymers in the solid state are critical to understanding and developing high performance materials. Typically, alkyl side-chains are used to promote solubility of the conjugated backbone

and enable solution processability. This leads to materials which can roughly be viewed as semiconducting molecular wires embedded in a matrix of grease. Obviously, the way in which these semiconducting wires overlap and the amount of this 'grease' is critical to a conjugated material's ability to transport charge over a macroscopic length scale. However, without side-chains (i.e. without this 'grease'), most conjugated polymers would be insoluble and non-processable. Chapter III of this dissertation deals with the development of novel pentacyclic benzodibenzofuran building blocks for organic electronics while chapter IV studies the aggregation and self-assembly of conjugated polymers using a novel cyclic benzodithiophene to disrupt π-stacking effecting both the thermodynamic and geometrical constraints of the self-assembly and aggregation process.

Bottlebrush polymers are another class of materials with hierarchical structure which controls their unique properties. Bottlebrush polymers are polymers wherein the repeat units are themselves also polymers (Figure 2).

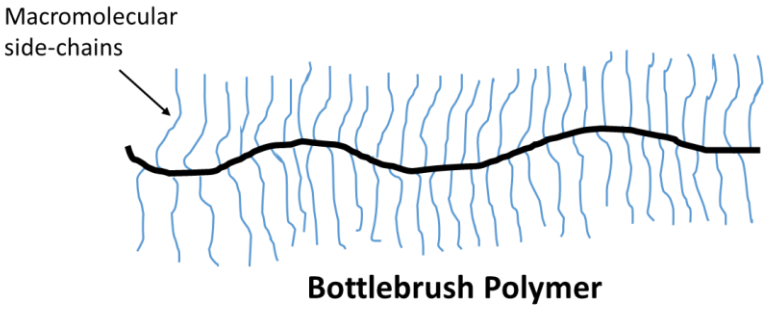


**Figure 2: Schematic depiction of a bottlebrush polymer.**

There are multiple length scales relevant to properties of a bottlebrush material: 1) A backbone length scale dictated by the chemical repeat unit, size of the macromolecular side-chain, and linear repeat density of the macromolecular side chains along the

backbone; 2) A side-chain length scale dictated by the chemical identity of the macromolecular side-chains as well as the repeat density of the side-chains along the backbone; and 3) macroscopic length scales wherein the bulk properties are dictated by these backbone and side-chain length scales as well as any higher order aggregation and structuring. For example, for long side-chains that have a high linear density along the backbone, steric repulsion between the side-chains force the side-chains and backbone to extend and stiffen which dramatically effects these material's properties relative to their corresponding non-bottlebrush analogues[7]. In particular, bottlebrush networks are materials made up of sparsely crosslinked bottlebrushes. Owing to the large size of bottlebrushes, the distance between crosslinking sites can be very large. Using low $T_g$ macromolecular side-chains in these bottlebrush networks to fill in the volume between these crosslinking sites in much the same way solvent is used to fill in the volume between sparsely crosslinked polymer gels can result in super-soft and compliant materials with moduli comparable to nature biomaterials[8]. Bottlebrush materials therefore offer another example of how controlling the hierarchical structure from molecule, to polymer, polymer architecture, and higher order macromolecular assembly can be used to control material properties. Chapter V of this dissertation provides a simple and versatile approach to well-define and functional bottlebrush networks with soft and compliant material properties.

## II. Case Studies in Conjugated Polymer Design

Organic electronics offer the promise of low cost, light weight, solution processed, plastic electronics. With a wide range of applications including light emitting devices, light harvesting devices, and transistors an array of materials have been developed over the last several decades. Fundamental to the development and understanding of high performance materials in these device applications has been the development of our understanding of how molecular structure impacts morphology leading to the macroscopic material properties which enable these high-performance devices. This structure-morphology-performance paradigm is ubiquitous within the field of organic electronics and serves to explain material properties such as field effect mobilities, power conversion efficiencies, and fluorescent intensity. This structure-morphology-performance paradigm is well-studied by probing the effect of a minor structural variation such as the difference in side-chain architecture or heteroatom substitution on morphology and the resulting material performance. Such studies help to develop design rules which guide the future development of high performance materials.

### *PBDTTPD and Linear vs Branched Side-Chains*

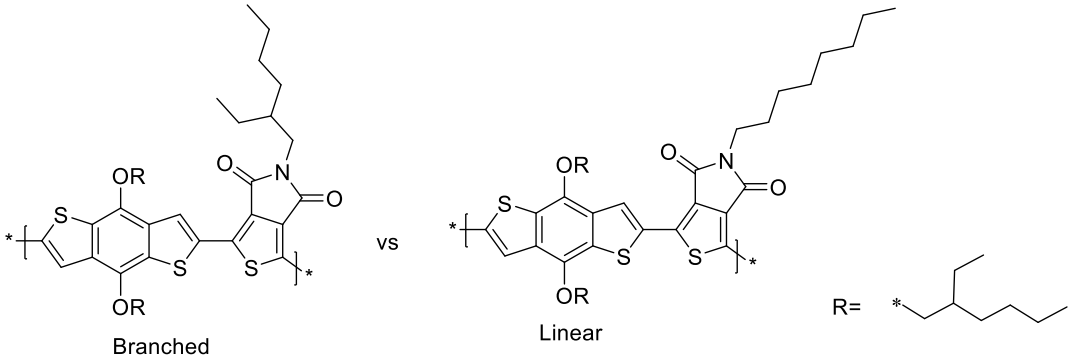


Originally synthesized in the Leclerc[10], Jen[11], and Fréchet[12] groups, the PBDTTPD family

of polymers have become a well-studied high-performance material in bulk heterojunction solar cells. The benzodithiophene (BDT) unit or the thieno[3,4-c]pyrrole-4,6-dione (TPD) unit can be synthesized with different solubilizing groups which has enabled a diverse library of PBDTTPD derivatives to be generated and characterized[13,14,15,16]. Such experiments have led to a better understanding of the structure-morphology-performance relationship in bulk heterojunction devices and has led to the development of new design principles guiding future material development. In particular, the PBDTTPD derivatives wherein the BDT unit has two ethylhexyl groups and the TPD unit has either the branched ethylhexyl group or linear octyl group has proven to be an interesting case study. Differing only in the connectivity of this side-chain, these structural isomers demonstrate how side-chain architecture impacts device performance.

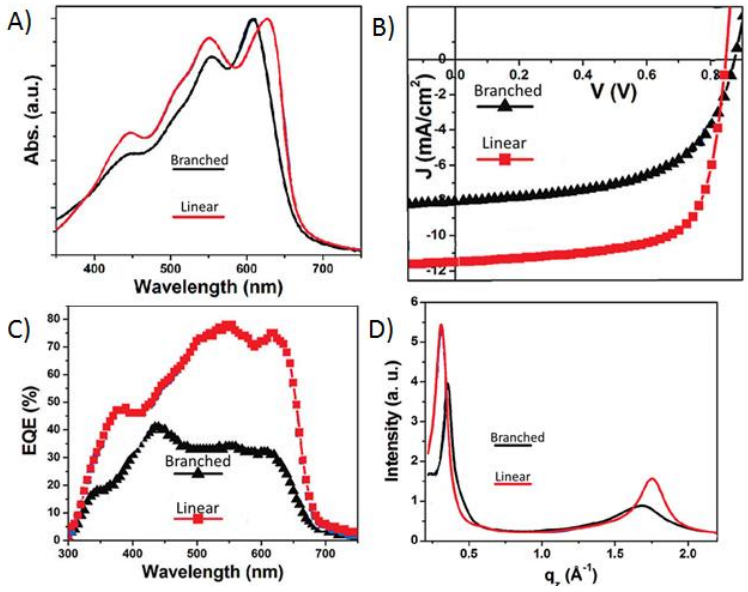


**Figure 3: A) Thin film absorption measurements; B) Solar cell current density-voltage plots; C) External quantum efficiency plots; and D) Grazing incidence X-**

**ray scattering plots. Adapted with permission from Piliego et al.[12] JACS 132, no. 22 (2010): 7595-7597. Copyright 2010 American Chemical Society.**

GIXS and absorption measurements on neat films of the branched and linear derivatives indicate that the linear derivative adopts a more planar backbone configuration as evidenced by its more red-shifted absorption spectrum with shorter and less disordered π-stacking as evidenced by the more narrow π-π peak in the GIXS at higher q (Figure 3A and D). When blended with $PC_{61}BM$, the linear derivative was seen to outperform the branched derivative with PCE >6% relative to the <4% seen in the branched derivative. This increased efficiency is due to the significantly enhanced short circuit current and fill factor of the linear derivative as seen in the J-V curve as well as the enhanced EQE for the devices made with the linear derivative (Figure 3B and C).

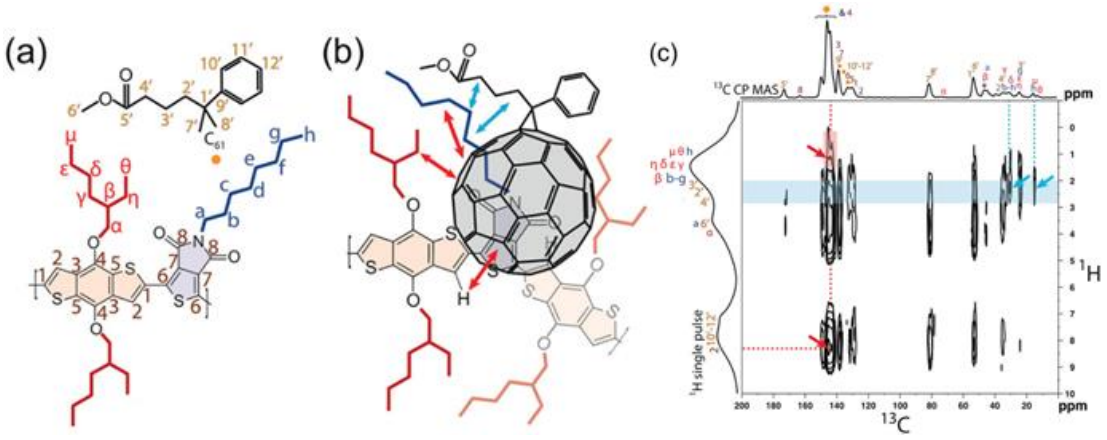


**Figure 4: a) Component structures with NMR signals labeled; b) Hypothesized molecular docking arrangement; c) solid-state 2D $^{13}C\{^{1}H\}$ dipolar-mediated heteronuclear correlation NMR spectroscopy the red arrows indicate $^{1}H$ polymer resonances correlated with C60 $^{13}C$ resonances while the blue arrows indicate the Phenyl-butyric acid methyl ester $^{1}H$ resonances which correlate with $^{13}C$ resonances**

**on the linear side-chain of the TPD derivative. These interactions are depicted by the arrows in b. Reprinted and adapted with permission from Graham et al.[17] JACS 136, no. 27 (2014): 9608-9618. Copyright 2014 American Chemical Society**

The Amassian, Beaujuge, and McGehee groups have since proposed that the enhanced solar cell performance of the linear derivative is due to a more favorable polymer-fullerene interaction[17]. Using a series of experiments diluting either the branched derivative or linear derivative with fullerene to minimize polymer-polymer interactions and thereby only measure the differences in polymer-fullerene interactions, PCE, JSC, and sub-band gap EQE measurements all showed the linear derivative to outperform the branched derivative. The sub-band gap EQE measurements indicate that the linear derivative adopts a more favorable and less energetically disordered charge transfer state with $PC_{61}BM$ than the branched derivative. This the authors argued was due to a favorable molecular docking interaction between the less sterically crowded linear TPD repeat unit as opposed to the more sterically crowded branched derivative. This hypothesis was supported with solid-state 2D $^{13}C\{^{1}H\}$ dipolar-mediated heteronuclear correlation NMR spectroscopy which showed a stronger correlation between NMR resonances on the linear TPD group with those on the fullerene than those between a different PBDTTPD derivative that had linear C14 groups on the BDT unit and the branched ethylhexyl groups on the TPD unit (Figure 4).

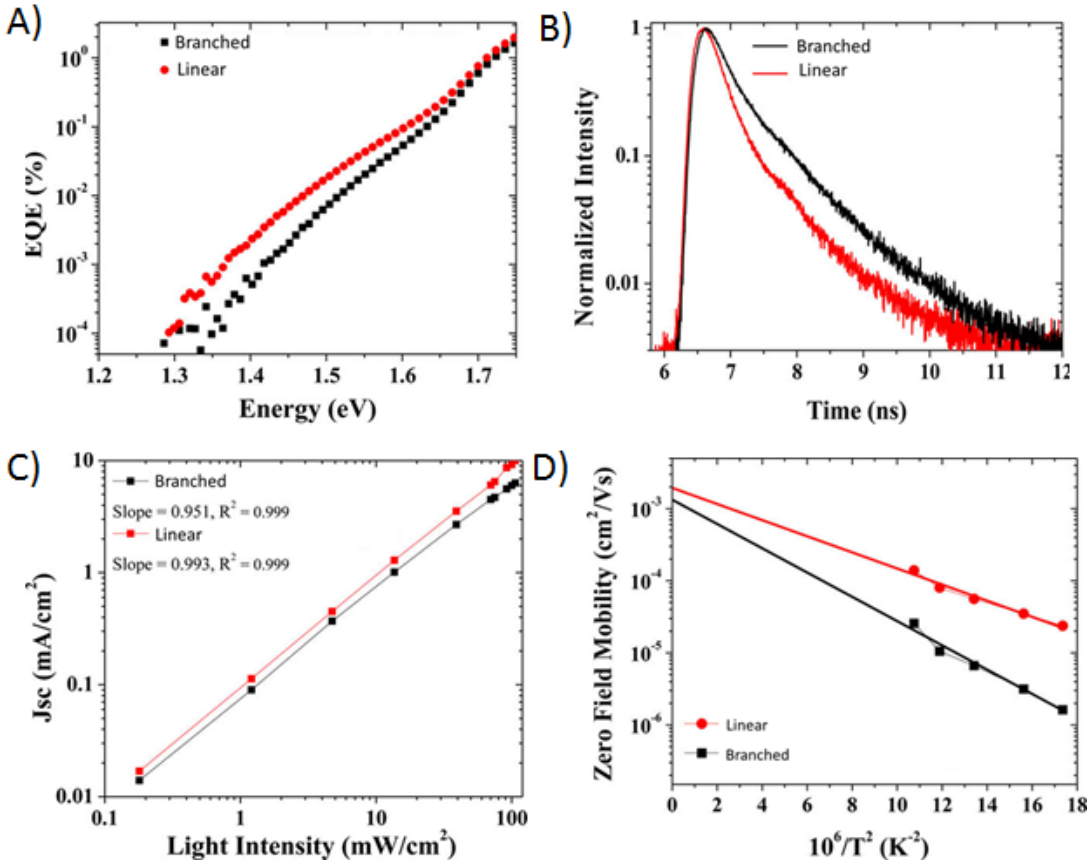


**Figure 5: A) Sub-bandgap external quantum efficiency; B) transient photoluminescent decay; C) short circuit current with increasing light intensity; and D) zero field mobility as a function of temperature. Reprinted with permission from Constantinou et al. [18] ACS applied materials & interfaces 7, no. 48 (2015): 26999-27005. Copyright 2015 American Chemical Society.**

These results were further corroborated by the So group[18]. Higher sub-bandgap EQE and faster transient photoluminescent decays for blends of the linear derivative with $PC_{61}BM$ indicate better charge generation (Figure 5A and B). Measuring the short circuit current with increasing irradiation intensity showed that blends of the linear derivative with $PC_{61}BM$ underwent less bimolecular recombination (Figure 5C). The greater

dependence of the zero-field hole mobility on temperature for the branched derivative indicates more energetic disorder in these devices (Figure 5D). These results are consistent with GIXS measurements showing that blends of $PC_{61}BM$ and the linear derivative are more ordered with a more pronounced π-stacking peak than the branched derivative. The structure of blends of $PC_{61}BM$ with the linear derivative have been more extensively characterized[19,20,21]. Such characterization has shown the linear PBDTTPD derivative to adopt a morphology consisting of three phases 1) small regions of aggregated polymer surrounded by 2) amorphous regions of intermixed polymer with fullerene within a network of 3) $PC_{61}BM$ rich regions that percolate through the BHJ.

These results show that the linear PBDTTPD derivative has a more favorable interaction with $PC_{61}BM$ than the branched analogue. This more favorable interaction promotes more efficient charge carrier generation. This is coupled with a more ordered morphology and better π-stacking which promotes improved charge carrier transport and extraction. Based on such results, it has been suggested that less sterically encumbered acceptor groups promote enhanced polymer-fullerene interactions thereby promoting charge-transfer and improved photovoltaic performance[17].

***PCPDTBT and Si vs C bridging atoms***

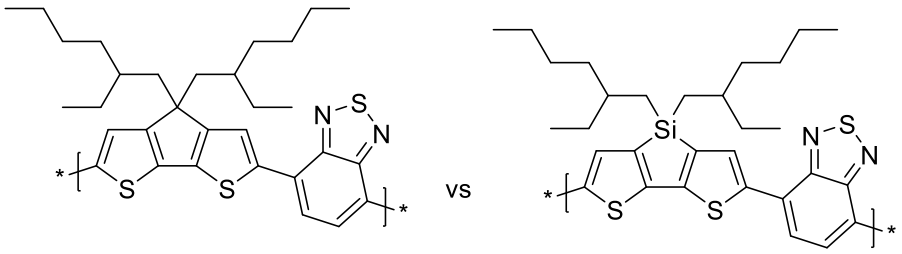

The carbon bridged PCPDTBT derivative was first reported by Brabec and co-workers[22,23] with the silicon bridged derivative being developed later by the Yang group[24]. Silicon, being one row lower on the periodic table than carbon, is a larger and more electropositive atom. This makes the bridgehead bond lengths of the silole ring longer than that of the cyclopentadiene ring causing a different backbone geometry. The σ* orbitals of the exocyclic Si-C bonds are also of sufficient energy level to participate in bonding interactions with the π* orbital of the aromatic core[25]. This atomic bridgehead substitution does not however appear to alter the HOMO-LUMO levels in this C/Si-PCPDTBT system[22,37,38]. This single atom substitution however result in pronounced morphological and performance differences between the C and Si derivatives.

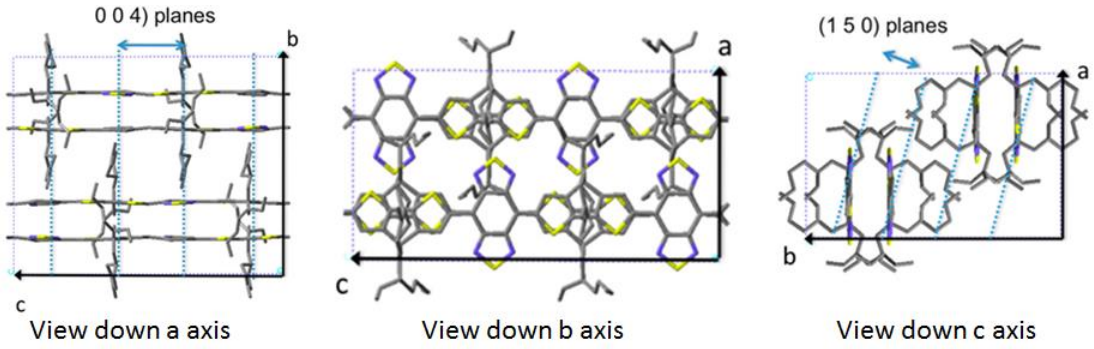


**Figure 6: Dimer structure of carbon derivative from electron diffraction of highly crystalline solvent vapor annealed films. Reprinted and adapted with permission from Fischer et al.[34] Macromolecules 48, no. 12 (2015): 3974-3982. Copyright 2015 American Chemical Society.**

The C derivative is known to adopt different morphologies based on the processing conditions. A more amorphous film is formed when spun cast from chloroform or chlorobenzene with the degree ordering and crystallinity increasing with

the use of additional additives such as 1,8-diiodooctane (DIO) and 1,8-octanedithiol (ODT)[26,27,28,29,30,31,32]. Thermal and solvent vapor annealing produce a highly crystalline and more thermodynamically stable dimer morphology (Figure 6)[32,33,34]. Films processed using high boiling point solvent additives are seen to have the most red-shifted absorption spectrum (lowest optical band gap) as well as the highest hole mobility. Solvent vapor or thermally annealed films with the dimer morphology are blue-shifted and exhibiting the lowest hole mobility[27,32,35]. The Si derivative on the other hand has been observed to form an interesting cross-hatched structure when spun cast from hot chlorobenzene (Figure 7A)[32,36]. As evidence suggests that these cross-hatched structures develop in solution, and the Si derivative aggregates much more strongly than the C derivative (Figure 7B and C), no corresponding amorphous morphology has been observed[32]. Additionally, high temperature annealing does not seem to generate the dimer structure thermodynamically favored by the C derivative[32,39]. The Si derivative is observed to have about an order of magnitude higher field effect hole mobility than the C derivative[32,37,38,39]. This may be due to the cross-hatched structure's network of interchain π-stacking promoting a more 3-dimensional charge transport pathway capable of spanning the macroscopic distances of a FET devices better than more 2-dimnesional lamellar crystallites or even the more 1-dimensional dimer crystallites seen in the C derivative.

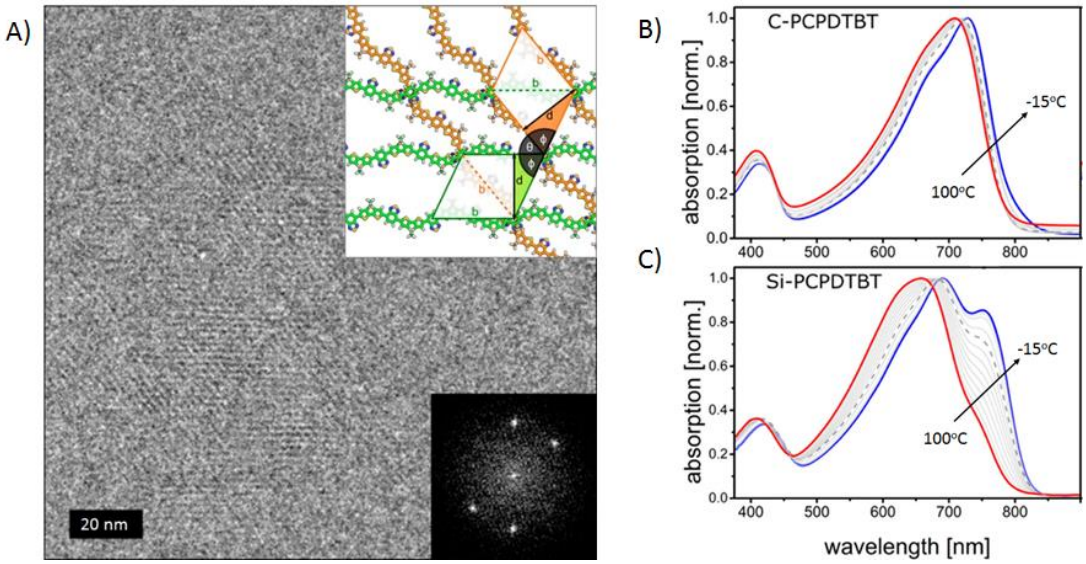


**Figure 7: A) High-Resolution TEM image of Si derivative showing cross-hatched morphology with top right inset showing a schematic of the cross-hatched backbones and the bottom right inset showing the Fourier Transform of the TEM image demonstrating preferential crossing angles at ~52° [36]; Variable temperature absorption spectroscopy of B) the C derivative and C) the Si derivative showing the Si derivative to be much more aggregated[32]. A) is adapted with permission from Takacs et al. [36] Nano letters 14, no. 6 (2014): 3096-3101. Copyright 2014 American Chemical Society. B) and C) are adapted with permission from Schulz et al.[32] Macromolecules 50, no. 4 (2017): 1402-1414. Copyright 2017 American Chemical Society.**

Both the Si and C derivatives have been extensively characterized in bulk heterojunction solar cells with PCE up to 5.6% and 5.5% respectively being reported[26,38]. The cross-hatched structure adopted by the Si derivative is seen to persist when blended with $PC_{61}BM$ and observed in HRTEM images of BHJ thin films[36]. This morphological structure and the tighter and less disordered π-π distances for the Si derivative relative to

the C derivative observed in the GIWAXS of BHJ blends may account for the larger hole and electron mobilities reported for $PC_{71}BM$ blends of the Si derivative relative to the C derivative[37,38,39,41]. Annealing has been shown to increase crystallinity and electron and hole mobility in BHJ with the Si derivative[38]. The edge-on π-stacked morphology adopted by the C derivative when spun cast from chlorobenzene with additives such as DIO is also observed in BHJ blends[28,29,40]. Spin casting blend of the C derivative with fullerene without solvent additives like DIO has been shown to result in a more amorphous structure and decreased device performance[26,27,28,29,30,40]. Additionally, thermal annealing, which may promote dimer formation, has been shown to decrease BHJ performance for the C derivative relative to films processed with DIO or ODT[26,27].

These studies show how a simple atom substitution of Si for C results in structural changes at the molecular level changing the backbone geometry. This molecular scale difference is then seen to increase aggregation in the Si derivative and promote a novel cross-hatched structure. The differences in aggregation, crystallinity, and morphology for the C and Si derivatives are then seen to impact BHJ performance.

### *PBDTTT-Th and F vs H substitution*

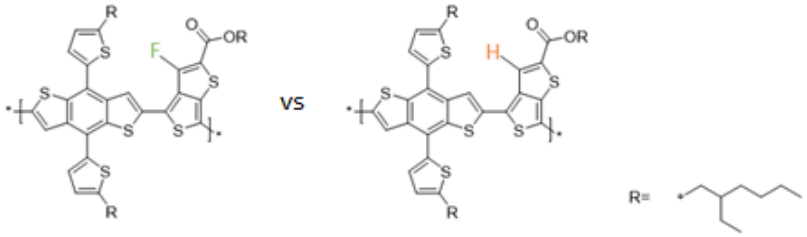


Fluorine Hydrogen

Fluorine is the most electronegative atom on the periodic table. As such, substitution of a hydrogen atom with fluorine in a monomer unit has been shown to lower

both the HOMO and LUMO levels as well as changes the polarity and dipole moment. The fluorine substituted PBDTTT-Th (PTB7-Th) was one of the first conjugated polymers to achieve a >10% PCE in single junction solar cells[42,43,44,45,46].

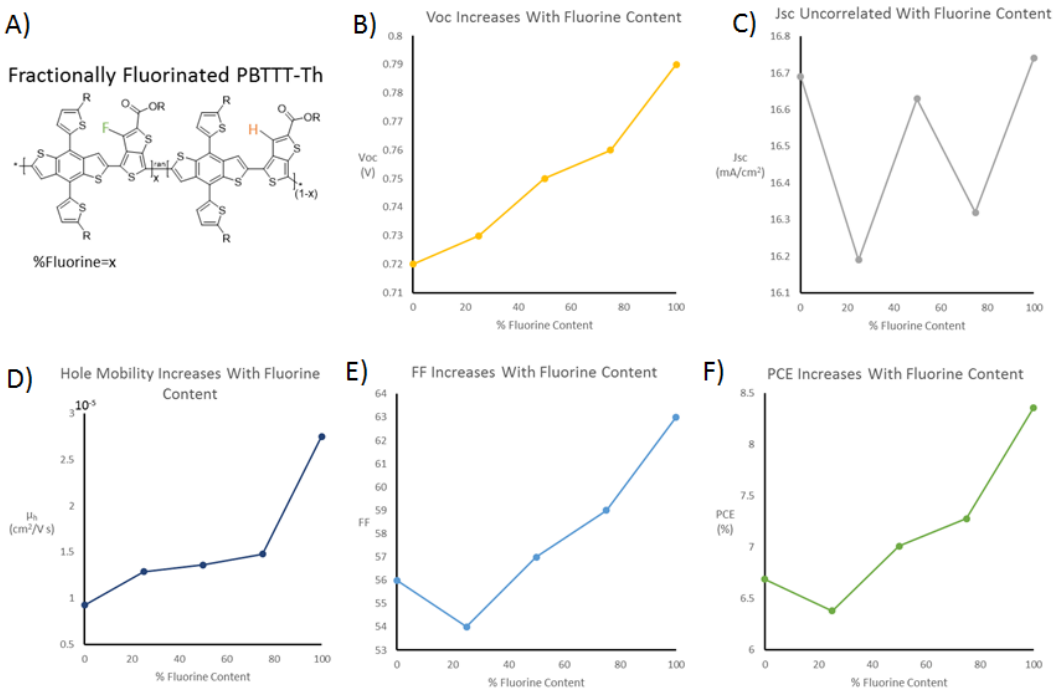


**Figure 8: A) Structure of fractionally fluorinated PBTTT-Th; B) open circuit voltage increases with % fluorination; C) short circuit current uncorrelated with % fluorination; D) hole mobility of BHJ increases with % fluorination; E) fill factor increases with % fluorination; and F) power conversion efficiency increases with % fluorination. Data adapted from Peng et al.[47].**

In a recent study, the effect of fluorine substitution on the performance and morphology of PBDTTT-Th was studied using fractionally fluorinated PBDTTT-Th derivatives[47]. The fractionally fluorinated PBDTTT-Th derivatives where synthesized by polymerizing different ratios of fluorine substituted and hydrogen substituted

thienothiophene monomers with the thienobenzodithiophene comonomer to yield a series of PBTTT-Th derivatives with fractional fluorine content ranging from 0% (100% hydrogen derivative) to 100% (0% hydrogen derivative) (Figure 8A). Both the HOMO and LUMO energies were lowered with increasing fluorine content as indicated by the increased ionization potential with increasing fluorine content from 5.22 eV for the H derivative to 5.28 eV for the F derivative as well as the slight increase in the electron affinity from 3.65 eV for the H derivative to 3.67 eV for the F derivative. This larger ionization energy is reflected in solar cell performance as an increase in open circuit voltage ($V_{oc}$) with increasing fluorine content for BHJ blends with $PC_{71}BM$ (Figure 8B). The short circuit current ($J_{sc}$) for these BHJ devices did not seem to correlate with fluorine content while the hole mobility of these devices, and hence also the fill factor (FF) were seen to increase with increasing fluorine content (Figure 8C, D and E). With roughly constant Jsc, increasing Voc, and increasing FF, the overall power conversion efficiency (PCE) was seen to increase with increasing fluorine content (Figure 8F). While the increasing Voc is readily explain by the propensity for the more electronegative fluorine to decrease the HOMO and LUMO energy levels, the increased mobility and FF are less apparent. Seeking to understand the impact of the fluorine substitution on the underlying morphology and explain this increase in mobility and FF, the authors conducted a series of grazing incidence X-ray diffraction (GIXD), transmission electron microscopy (TEM), and resonant soft X-ray scattering (RSoXS) experiments. The GIXD showed that the alkyl and π- π spacings remain relatively unchanged with varied fluorine content for the BHJ blends and the TEM experiments did not show any significant trend with fluorine content with the BHJ blends being mostly uniform with features on the order of 10 nm.

The RSoXS on the other hand showed a distinct trend with increasing fluorine content. The scattering intensity times q2 (I*q2) was observed to shift to higher q with increasing fluorine content indicates a decrease in crystallite size with increasing fluorine content. Integrating these (I*q2) peaks with along q gives the total scattering intensity which is a relative measure of the phase purity and intermixing of the polymer with the fullerene[47,48,49]. This total scattering intensity was observed to decrease with increasing fluorine content which suggest that the polymer and fullerene domains are less pure and indicating a greater extent of intermixing.

This morphological characterization suggests that the increase in mobility with fluorine content is likely do to a more interconnected network of polymer and fullerene domains enabling better charge transport through the BHJ device which accounts for the increasing FF with increasing fluorine content. Therefore, the increasing PCE with increasing fluorine content can be ascribed to the improved Voc due to the energy lowering character of fluorine as well as the increased FF due to the improved morphology resulting from the differing solubility of the fluorine derivatives relative to the hydrogen derivatives due to the increased polarity and dipole moment of the fluorene substituted derivatives.

## III. A New Pentacyclic Benzodibenzofuran Building Blocks For Organic Electronic Applications

Designing new conjugated building blocks for organic electronic materials is an important endeavor expanding the scope of accessible materials and furthering the understanding of structure-property relationships within the field. Much of the early studies of conjugated polymers focused on simple and easily accessible materials such as polyacetylene, polyaniline, poly(p-phenylenevinylene) and its various substituted derivatives, and poly(3-alkylthiophene)s (Figure 9) [50,51].

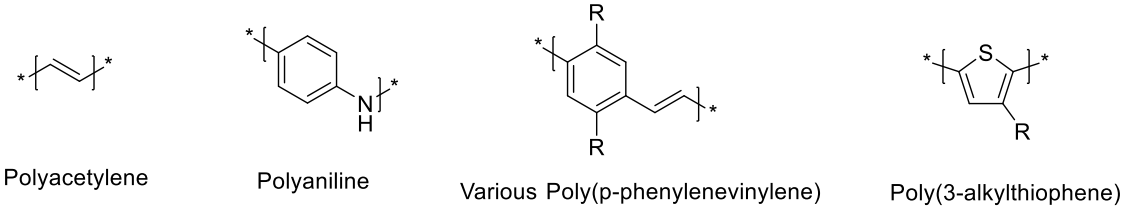


**Figure 9: Structures of various simple conjugated polymers.**

Yet as the field has grown and matured, much more complicated materials have been developed to further improve the performance of these materials in various applications (Figure 10)[52,53]

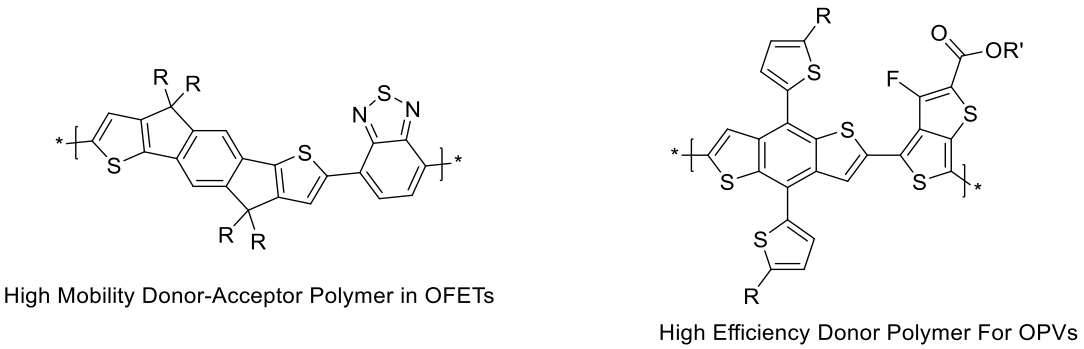


**Figure 10: Structures of representative high performance conjugated polymers.**

While such materials are great for pushing the limits of device performance, advancing our knowledge of the underlying physics, and improving our understanding of structure-property relations, they are also much more complex and synthetically challenging. Such synthetic complexity limits their accessibility and ultimately the practicality of this technology. What is needed are new building blocks which draw upon the knowledge gained from these more complicated high performing materials in their design, yet are synthetically much simpler and easily accessible. Some design principles characteristic of high performance materials are[52,53,54,55,56]:

1) large polycyclic aromatic units which serve to increase the conjugation length and rigidify the polymer backbone thereby reducing energetic disorder

2) a planar backbone which decreases torsional defects and further enhances the effective conjugation length

3) Well delocalized molecular orbitals with appropriate energy levels

A versatile and readily accessible polycyclic aromatic building block designed to satisfy criteria (1) could then be paired with appropriate co-monomers to satisfy the other two criteria. Therefore, a simple and concise route to a versatile polycyclic building block is desired.

Looking to a pair of studies from the 1950's and 60's a series of pentacyclic benzodibenzofuranquinones were prepared in a single step from the reaction of phenols with chloranil (Figure 11)[57,58].

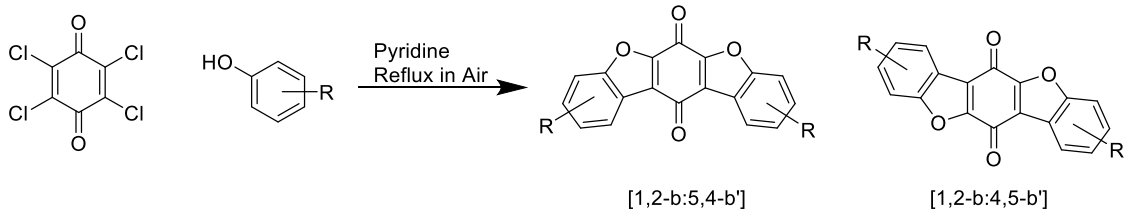


**Figure 11: Schematic of previously synthesized benzodibenzofuranquinones R=Methoxy.**

This single step access to the pentacyclic benzodibenzofuranquinone core was reasoned to be a good starting point in the synthesis of a novel polycyclic building block for organic electronic materials.

It was discovered that the reaction of the inexpensive and readily available feedstocks chloranil and 3-bromophenol in refluxing pyridine in air afforded predominately the [1,2-b:5,4-b'] substituted isomer depicted in 51% yield. The work up consisted only of allowing the reaction to cool back to room temperature, adding water, collecting the solid via filtration, washing with water and methanol until the filtrate ran clear, and then removing residual solvents in a vacuum oven to afford the product (M1) as a red crystalline powder (Figure 12).

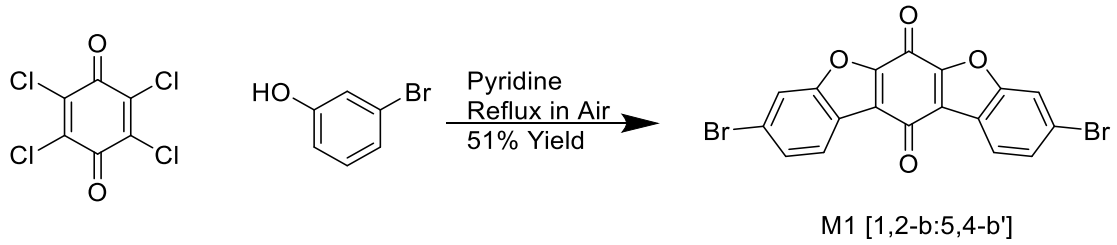


**Figure 12: Synthesis of benzodibenzofuranquinone M1.**

The structural assignment was determined via a combination of $^{1}H$ NMR, $^{13}C$ NMR, single crystal X-ray diffraction, and high-resolution mass spectrometry. $^{1}H$ NMR

confirmed the presence of 3 aromatic protons with the expected singlet, doublet, doublet splitting pattern which would be expected for this isomer formed via the c-c ring closure reaction occurring para to the bromine (Figure 13, Figure 14).

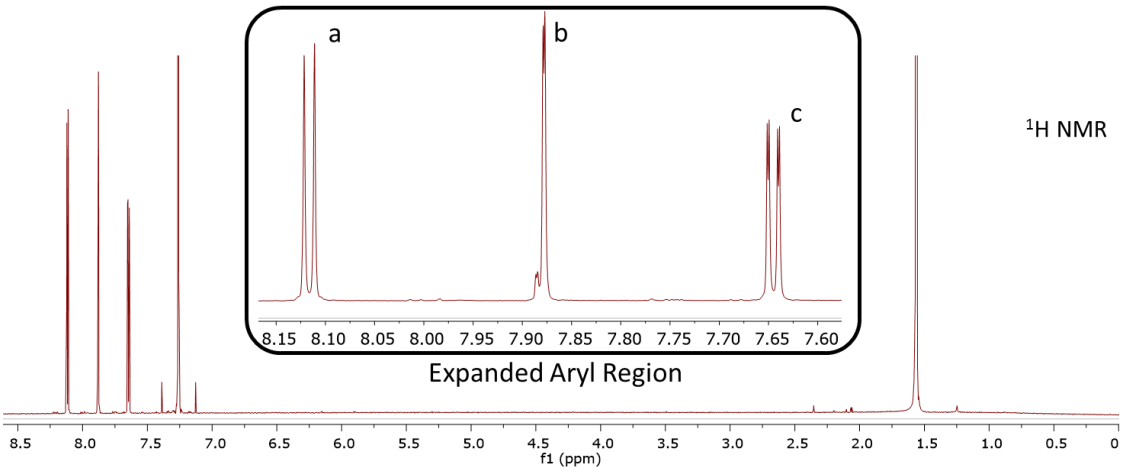


**Figure 13: $^{1}$H NMR spectrum of M1.**

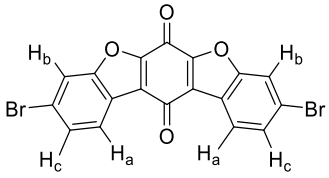


**Figure 14: Assignment of protons based on $^{1}$H NMR spectrum of M1.**

$^{13}$C NMR confirmed the presence of 10 different carbon resonances with two distinct carbonyl peaks at δ 178.4 and 166.7 respectively which is consistent with the [1,2-b:5,4-b'] isomer assignment (Figure 15).

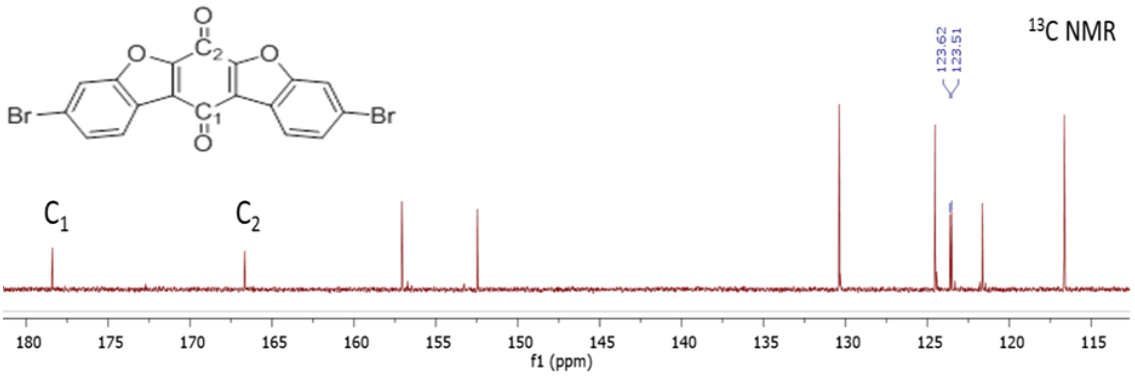


**Figure 15: $^{13}$C NMR spectrum of M1 with two distinct carbonyl peaks indicated.**

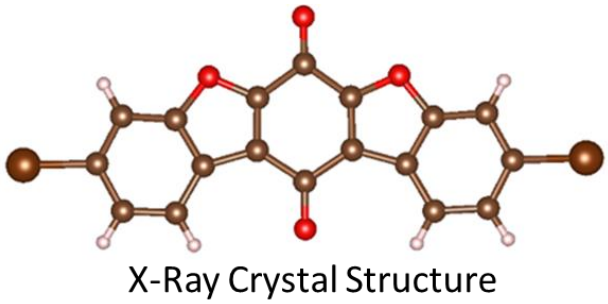


**Figure 16: Single crystal X-ray structure of M1.**

These NMR assignments were further confirmed via single crystal X-ray diffraction (**Figure 16**).

Close inspection of the $^{1}$H and $^{13}$C NMR spectra reveals a minor impurity peak at δ7.89 in the $^{1}$H NMR spectrum and a series of small resonances in the $^{13}$C NMR spectrum. This impurity is likely to be the [1,2-b:5,4-b'] substituted isomer (Figure 17).

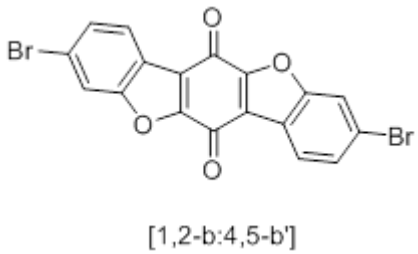


**Figure 17: Likely structure of minor isomer.**

Integration of the $^{1}$H NMR resonance at δ7.89 relative to that corresponding to the major isomer indicated a selectivity of >9:1 in favor of the [1,2-b:5,4-b'] isomer. This result is consistent with the previous literature for the condensation and ring closure reaction of chloranil with various phenols which found the [1,2-b:5,4-b'] isomer to be major isomer with a small amount of the [1,2-b:4,5-b'] isomer being formed as well. The selectivity of this reaction is remarkable considering that if both the condensation reactions of the phenol -OH with the chlorine on chloranil and the c-c bond forming ring closure reactions occurred randomly, a total of six different isomers would result (Figure 18).

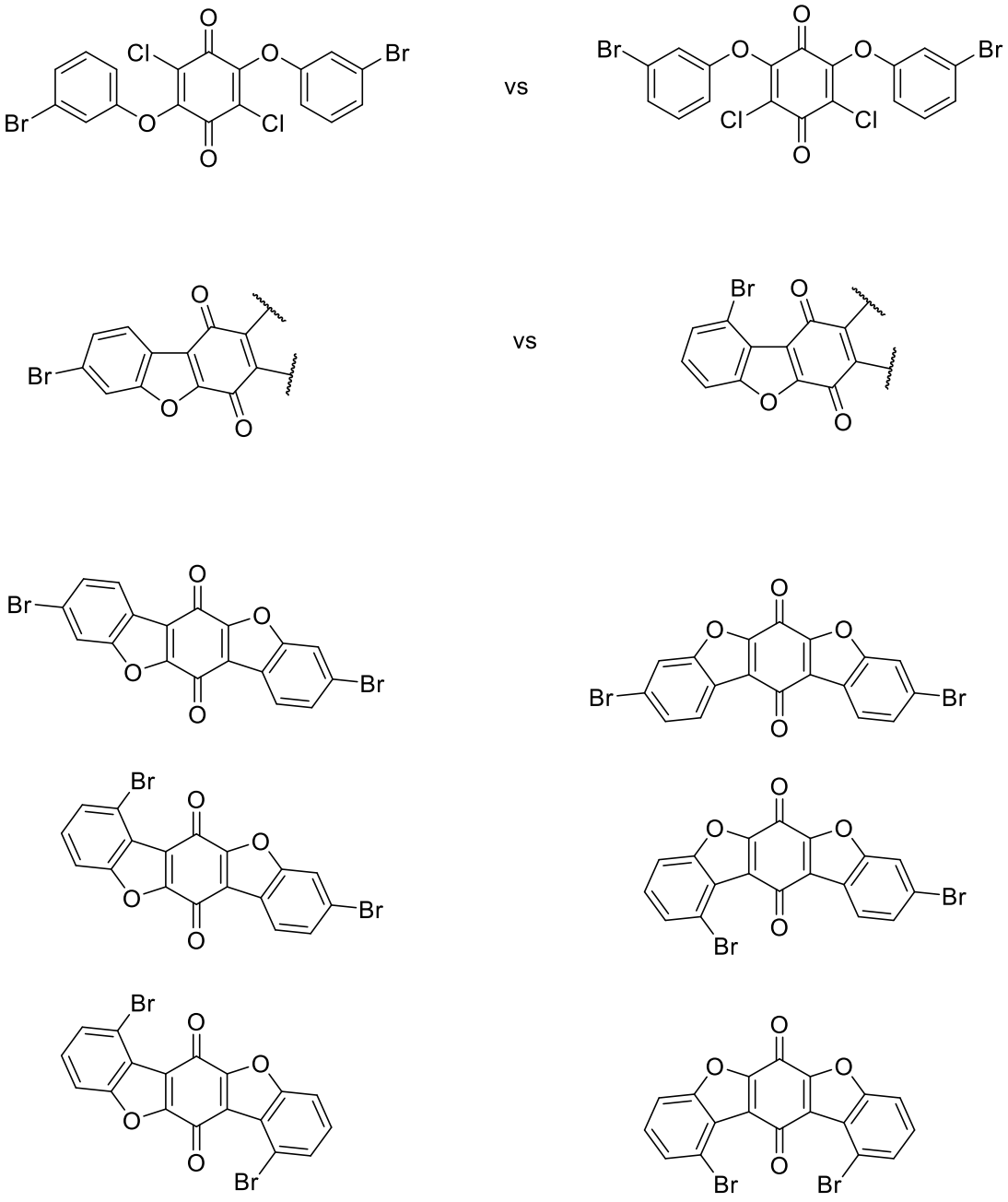


**Figure 18: All possible isomers including those not observed.**

This di-bromo substituted benzodibenzofuranquinone, having been formed by the simple reaction of the readily available and inexpensive starting materials chloranil and 3-bromophenol and purified without chromatography via a simple and scalable

precipitation, filtration, and washing procedure, was then used as the entry point to a diverse series of organic electronic materials with wide ranging properties and potential applications.

Quinones are versatile materials. They are redox active compounds capable of accepting two electrons and two protons to transition into the more electron rich hydroquinone form (Figure 19)[59].

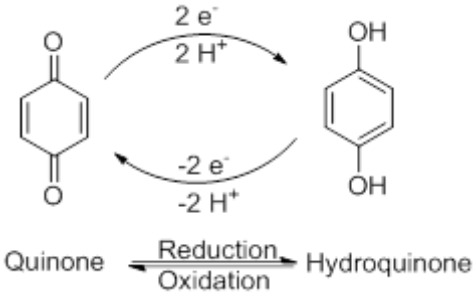


**Figure 19: Quinone/hydroquinone redox cycle.**

Likewise, when the reduction potential of the benzodibenzofuranquinone (BDBFQ) M1 was measured in anhydrous acetonitrile with 0.1M $Bu_4NPF_6$ two reduction peaks were observed as indicated by arrows in the Figure 20.

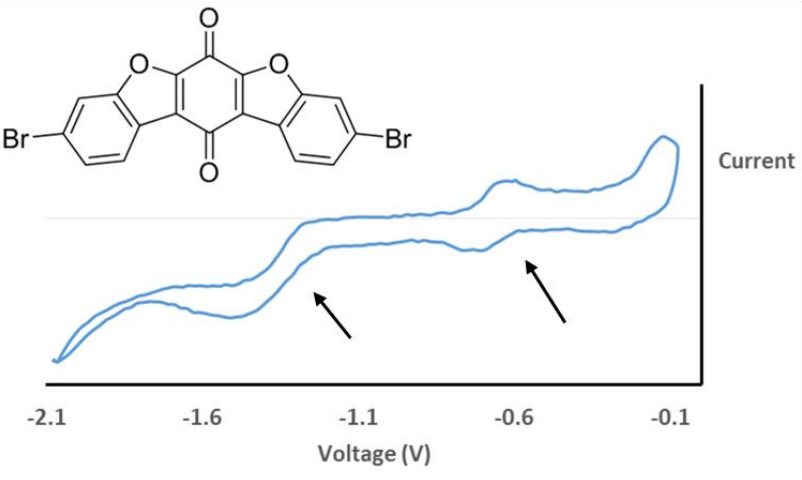


**Figure 20: Cyclic voltammetry measurement for M1 in acetonitrile with $Bu_4NPF_6$.**

Taking advantage of this redox character, two separate classes of materials were developed using the benzodibenzofuranquinone M1 building block. First, a series of conjugated polymers using a reductively alkylated benzodibenzofuran (BDBF) form M2 were developed, and second a paramethoxybenzyl (PMB) protected form M* was developed to permit further chemical modification followed by later deprotect back to the quinone form. The conversion of M1 to these reductively alkylated forms M2 and M* were achieved via reduction of the M1 quinone with $Na_2S_2O_4$ in aqueous NaOH followed by treatment with either 1-bromoheptane to form M2 or 4-methoxybenzyl chloride to form the PMB protected quinone M* (Figure 21).

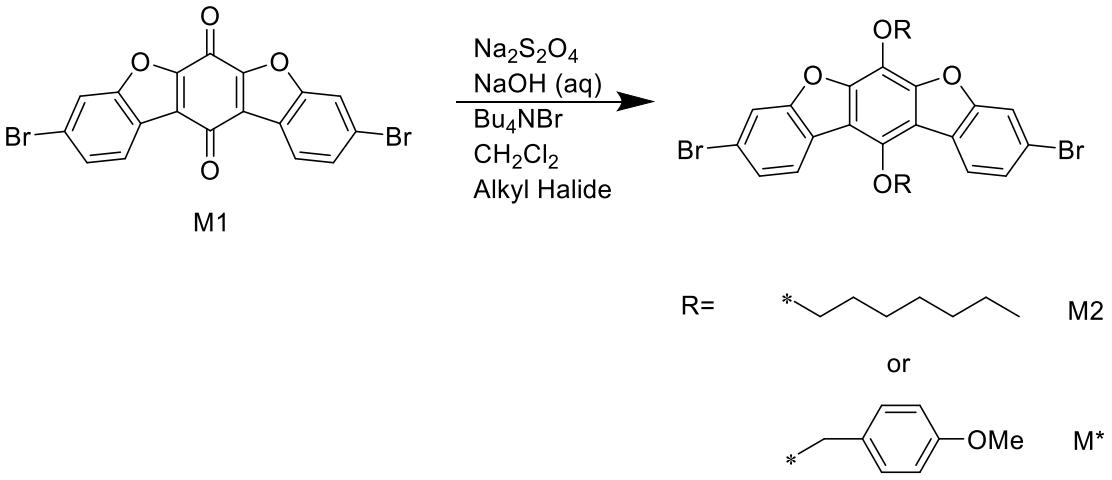


**Figure 21: Reductive alkylation of M1 to heptyl substituted M2 or PMB protected M*.**

This reductive alkylation improves the solubility of these materials and enables further purification and subsequent chemical modification. $^{1}H$ and $^{13}C$ NMR and high-resolution mass spec confirmed the successful synthesis and purification of these materials (Figure 22, Figure 23).

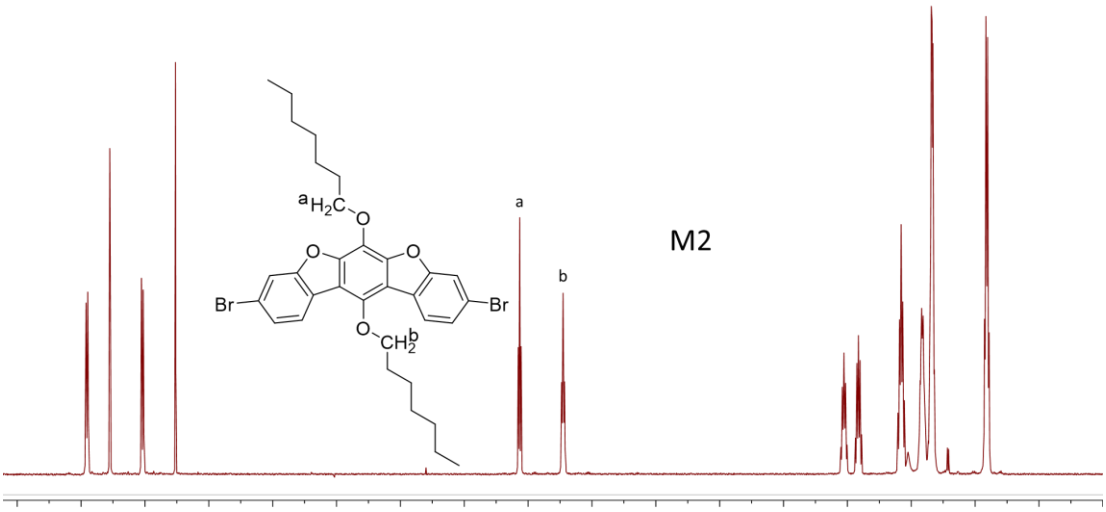


**Figure 22: $^{1}$H NMR spectrum of M2 with two distinct ether protons indicated.**

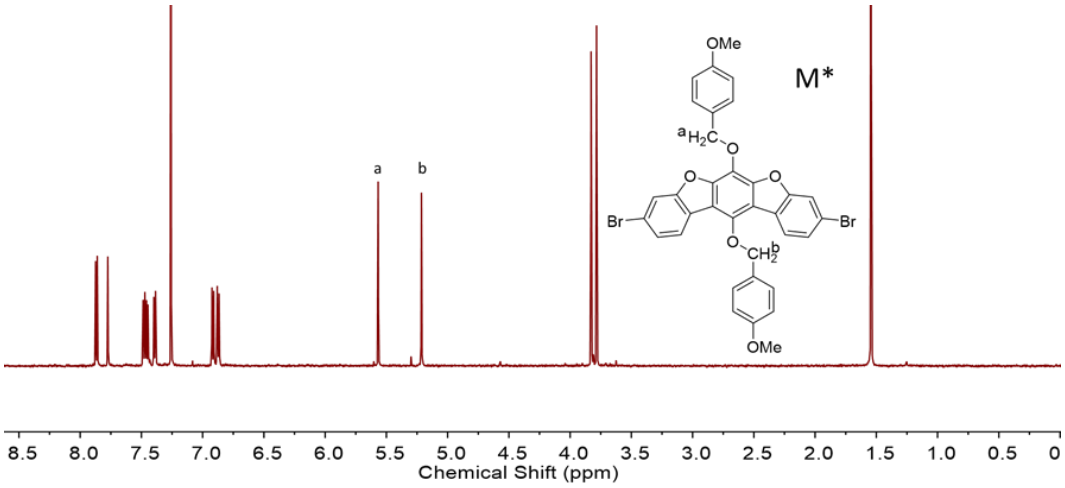


**Figure 23: $^{1}$H NMR spectrum of M* with two distinct benzyl protons indicated.**

The reductively alkylated M2 monomer was then used in the synthesis of a series of conjugated polymers. First, M2 was utilized in a Stille coupling polymerization reaction with 4,7-bis(4-hexyl-5-(trimethylstannyl)thiophen-2-yl)benzo[c][1,2,5]thiadiazole to form the P1 donor-acceptor polymer depicted. Briefly, the monomers were mixed added to a dry Schlenk flask in a 1 to 1 molar ratio followed by the appropriate amount of dry toluene. The solution was then degassed via three freeze-pump-thaw cycles before being

frozen in liquid nitrogen to allow the addition of the $Pd_2(dba)_3$ and tri(o-tolyl)phosphine catalyst components against a flow of argon. The gas in the head space of the flask was replaced with argon and the mixture warmed to room temperature before being placed in an oil bath which had been heated to 105°C. The reaction proceeded at this temperature for 24 hours before being cooled to room temperature and diluted with chlorobenzene. The polymer solution was precipitated in methanol and collected via filtration. This material was then washed in a Soxhlet with acetone and hexanes before being extracted with chloroform. Removal of solvents with a rotary evaporator afforded the P1 polymer product in 40% yield (Figure 24).

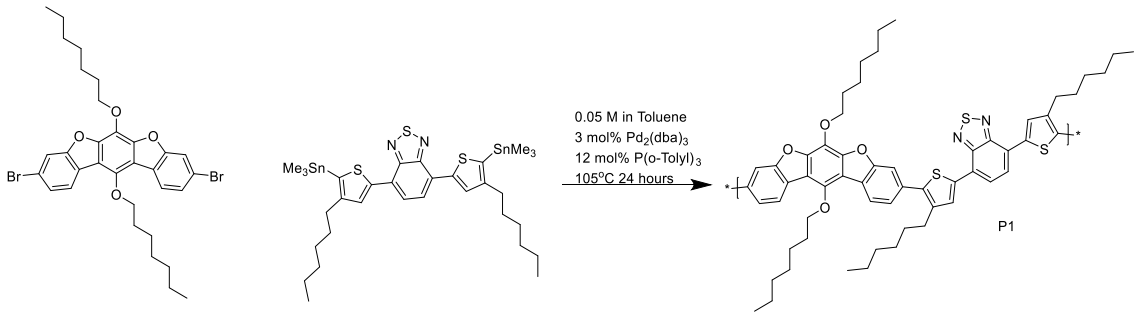


**Figure 24: Synthesis of P1.**

Gel permeation chromatography (GPC) revealed a moderate molecular weight of 14 kDa relative to polystyrene standards with a relatively low dispersity of 1.4 for a step growth polymerization (Figure 25).

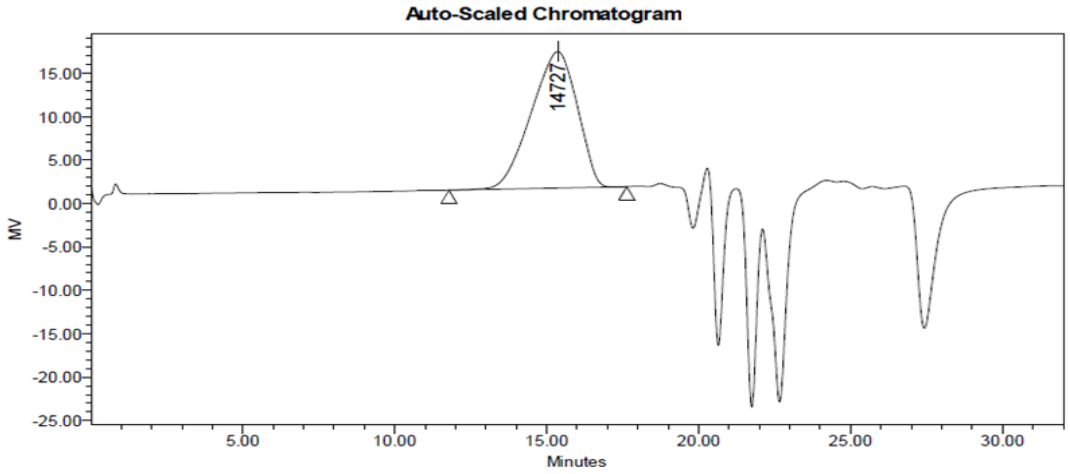


GPC Results

| | Dist Name | Mn | Mw | MP | Mz | Mz+1 | Mv | Polydispersity | MW Marker 1 | MW Marker 2 |
|---|---|---|---|---|---|---|---|---|---|---|
| 1 | | 14401 | 20129 | 14727 | 29129 | 42654 | | 1.397739 | | |

**Figure 25: GPC (chloroform) of P1 shown Mn 14 kDa and *Đ* 1.4.**

$^{1}$H NMR confirmed the chemical identity of P1 with appearance of the expected resonances (Figure 26).

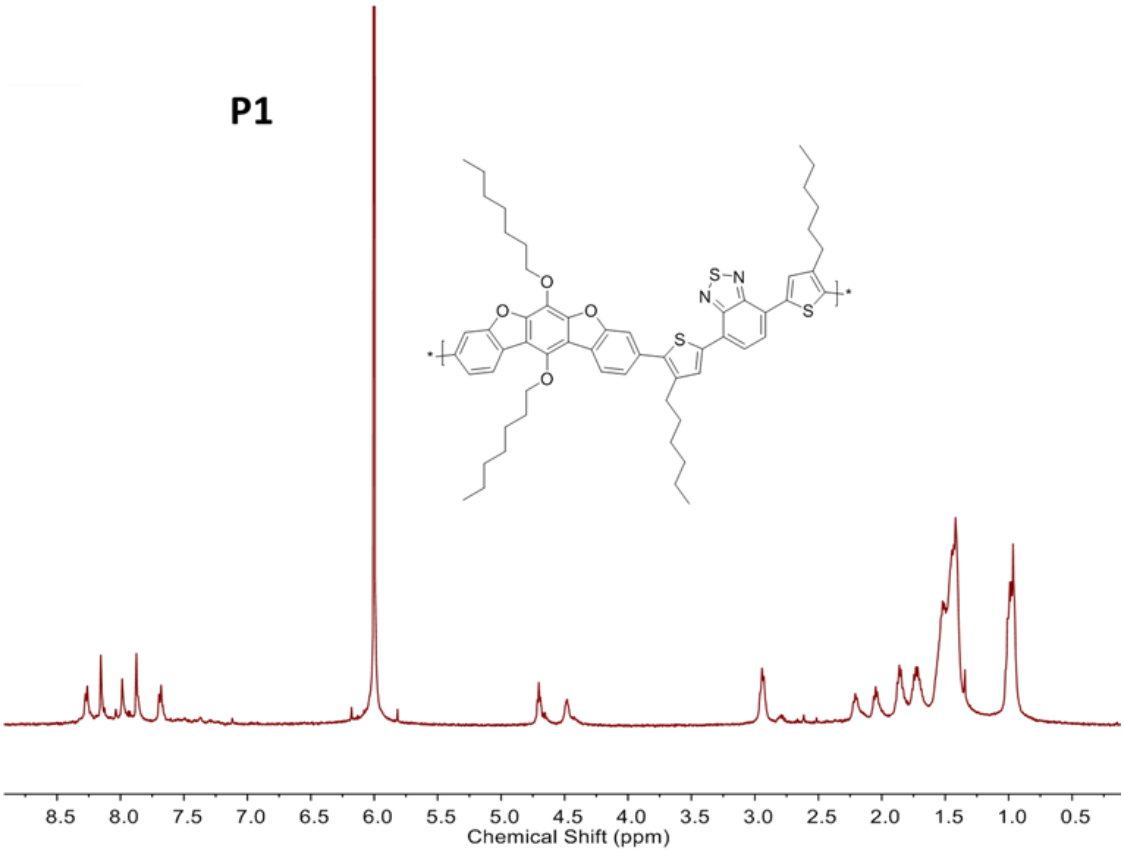


**Figure 26: $^{1}$H NMR spectrum of P1 showing expected resonances.**

Next, to increase the versatility of the pentacyclic monomer, the bromine groups of M2 were converted to pinacolborane groups via lithium/halogen exchange and subsequent quenching with 2-isopropoxy-4,4,5,5-tetramethyl-1,3,2-dioxaborolane to yield M3 (Figure 27).

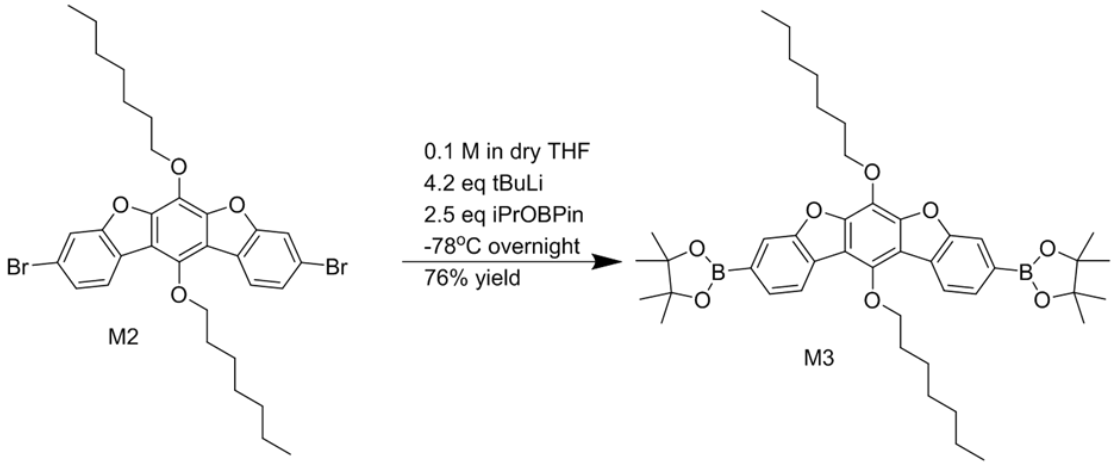


**Figure 27: Synthesis of M3.**

$^{1}H$ and $^{13}C$ NMR as well as high-resolution mass spectroscopy confirmed the identity and purity of this compound after work up and being twice recrystallized from hexanes (Figure 28, Figure 29).

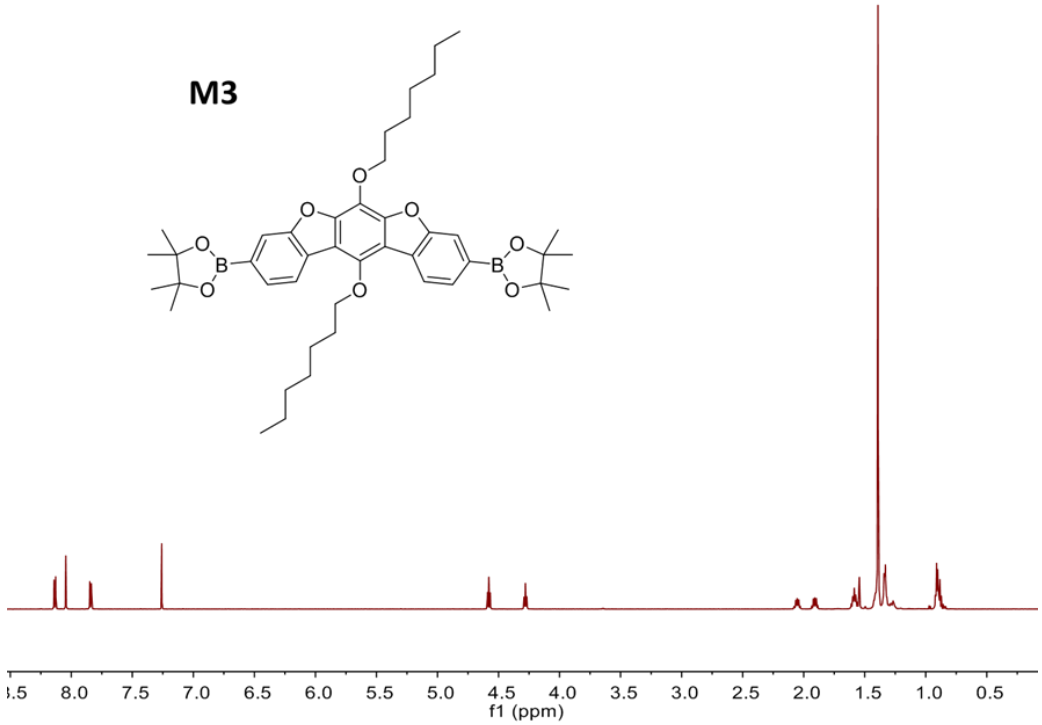


**Figure 28: $^{1}H$ NMR of M3 showing expected resonances and confirming high purity.**

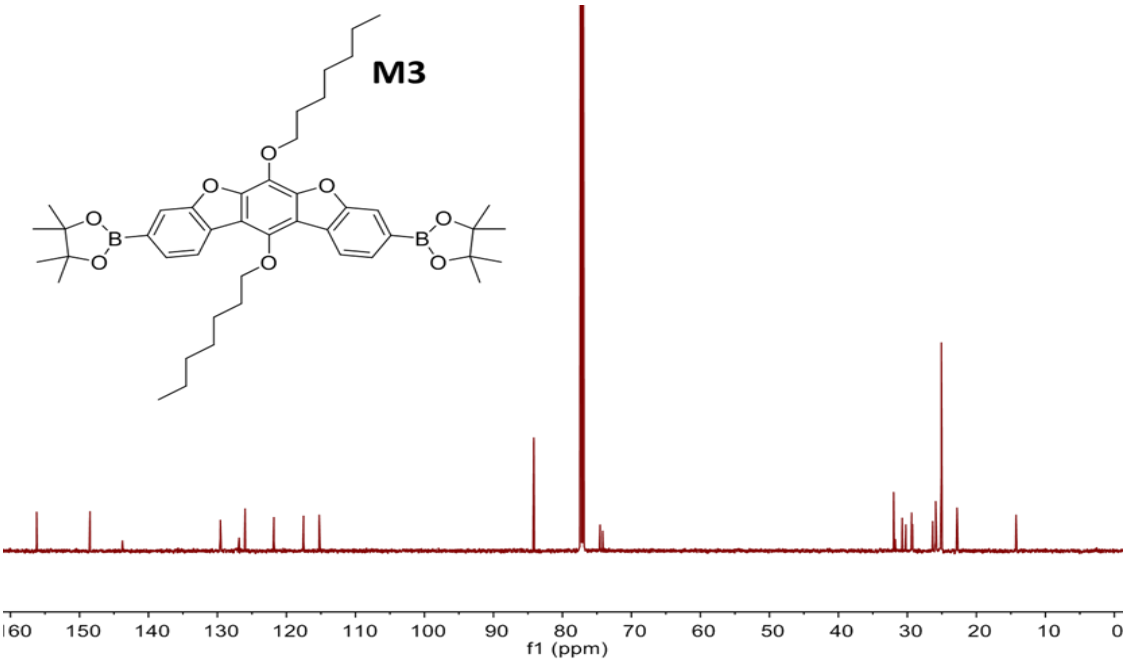


**Figure 29: $^{13}$C NMR of M3 further confirming structure.**

This M3 monomer was then used in a Suzuki coupling polymerization with 3,6-bis(5-bromothiophen-2-yl)-2,5-bis(2-hexyldecyl)-2,5-dihydropyrrolo[3,4-c]pyrrole-1,4-dione to form the polymer P2 depicted (Figure 30).

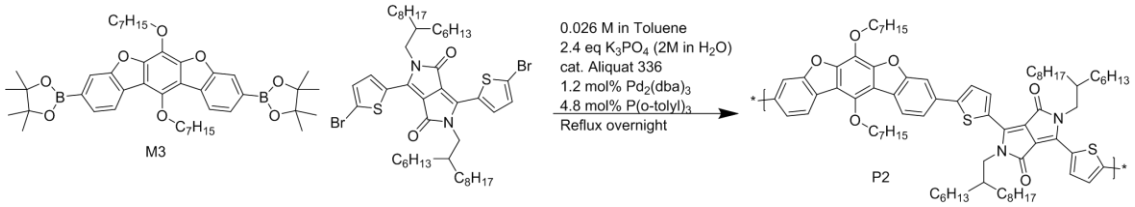


**Figure 30: Synthesis of P2 via Suzuki polymerization.**

The polymerization reaction was run as follows: The monomers were added to a Schlenk flask in a 1 to 1 molar ratio followed by toluene and 2.4 equivalents of $K_3PO_4$ as a 2M solution in water. Two drops of Aliquat 336 were added and the mixture was degassed via 3 freeze-pump-thaw cycles. The mixture was frozen in liquid nitrogen to allow the addition of 1.2 mol% $Pd_2(dba)_3$ and 4.8 mol% of P(o-tolyl)$_3$ against a flow of argon. The

gas in the headspace of the flask was replaced with argon and the mixture was heated to reflux overnight. The reaction was then cooled to room temperature and diluted with chlorobenzene. The polymer solution was precipitated in methanol and the precipitate was collected via filtration. This material was then washed in a Soxhlet apparatus with acetone followed by hexanes. A lower molecular weight fraction was eluted with dichloromethane (37% yield Mn 68 kDa PDI 3.3) followed by eluting with chloroform to give a higher molecular weight fraction (40% yield Mn 73 kDa PDI 3.2). Despite being soluble in dichloromethane and chloroform, this polymer was found to aggregate significantly in these solvents necessitating the use of high temperature GPC at 150°C in 1,2,4-trichlorobenzene (Figure 31).

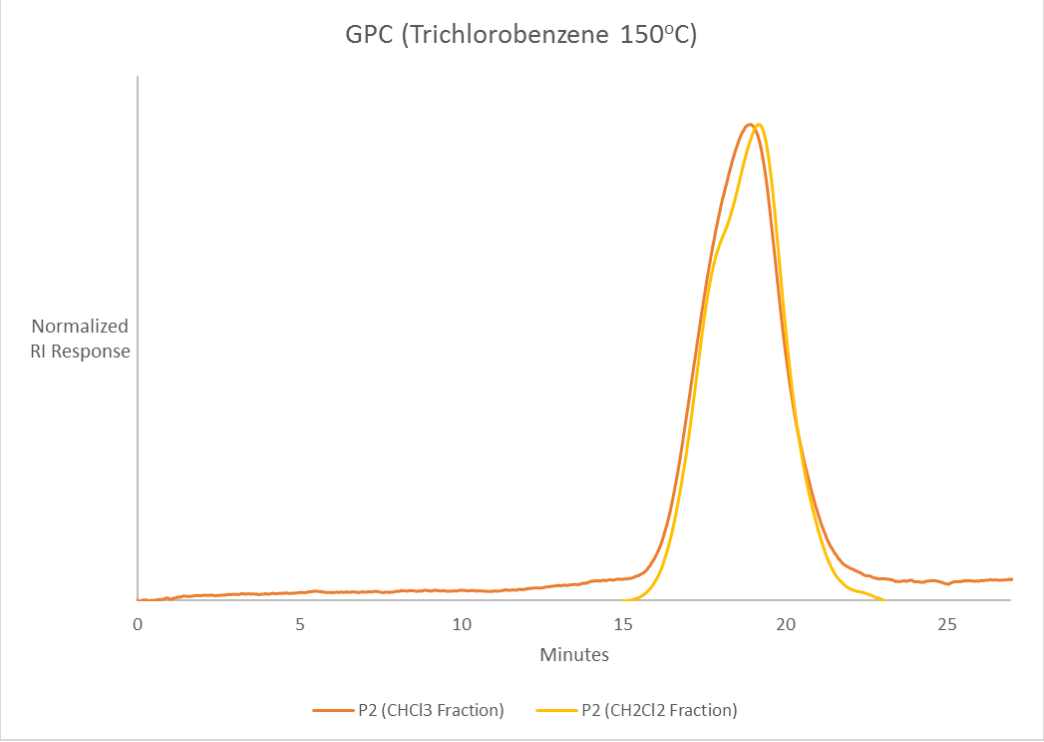


**Figure 31: GPC (1,2,4-trichlorobenzene 150°C) traces of P2 fractions.**

$^{1}$H NMR at 120$^{o}$C in deuterated 1,1,2,2-tetrachloroethane (TCE-d2) demonstrated this propensity for aggregation even at elevated temperatures as can be observed by the lack of clearly observable aromatic peaks due to this aggregation (Figure 32).

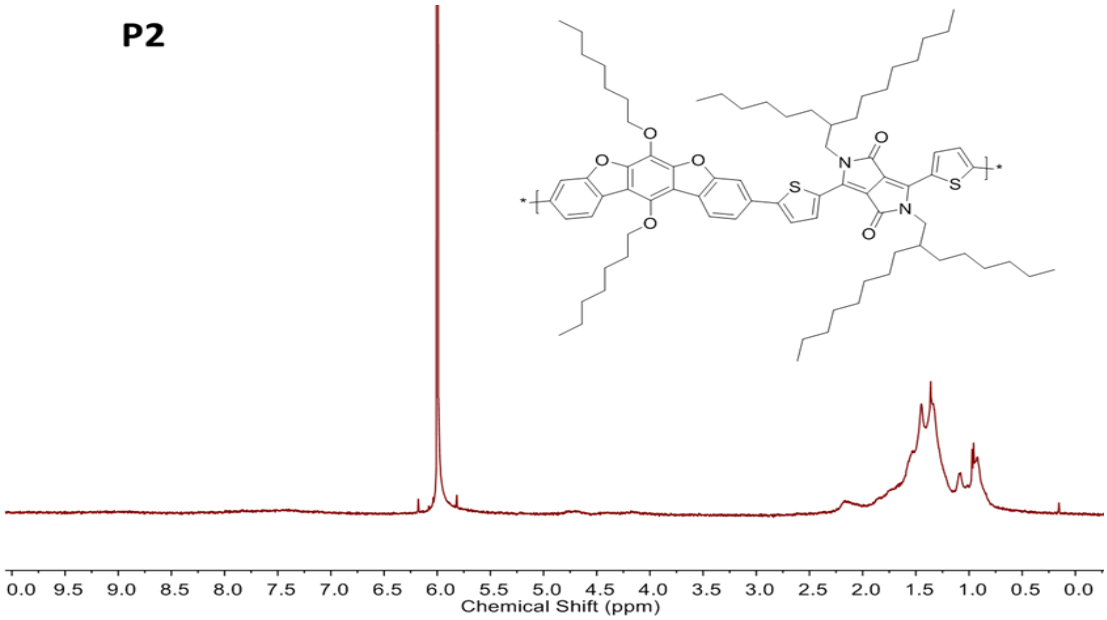


**Figure 32: $^{1}$H NMR spectrum of P2 (120$^{o}$C TCE-d2). Aggregation is evidenced by the lack of sharp visible aromatic peaks.**

To better understand the properties of the reductively alkylated benzodibenzofuran unit, the homopolymer P3 was synthesized via Suzuki coupling polymerization of M2 with M3 using the same reaction procedure described for the synthesis of P2 (Figure 33).

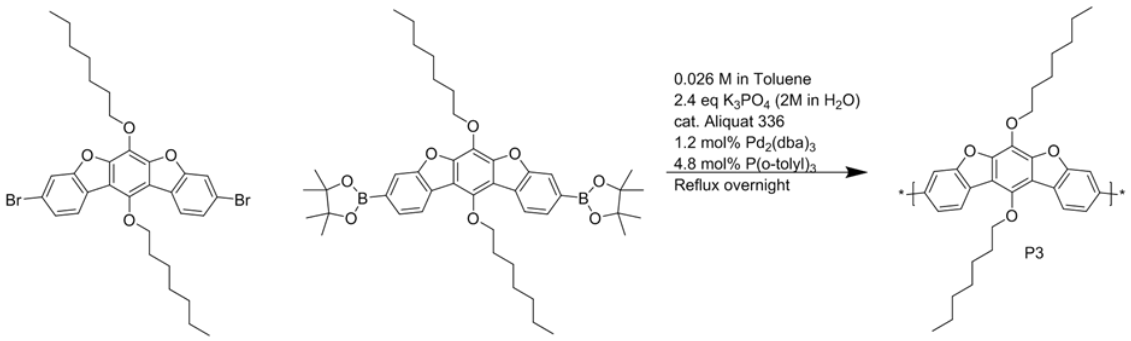


**Figure 33: Synthesis of homopolymer P3.**

After Soxhleting with acetone, hexanes, chloroform, and chlorobenzene, the product was extracted via boiling 1,1,2,2-tetrachloroethane to afford P3 in 70% yield. GPC (150$^{o}$C in 1,2,4-trichlorobenzene) recorded a Mn of 15 kDa with a dispersity of 1.5 (Figure 34).

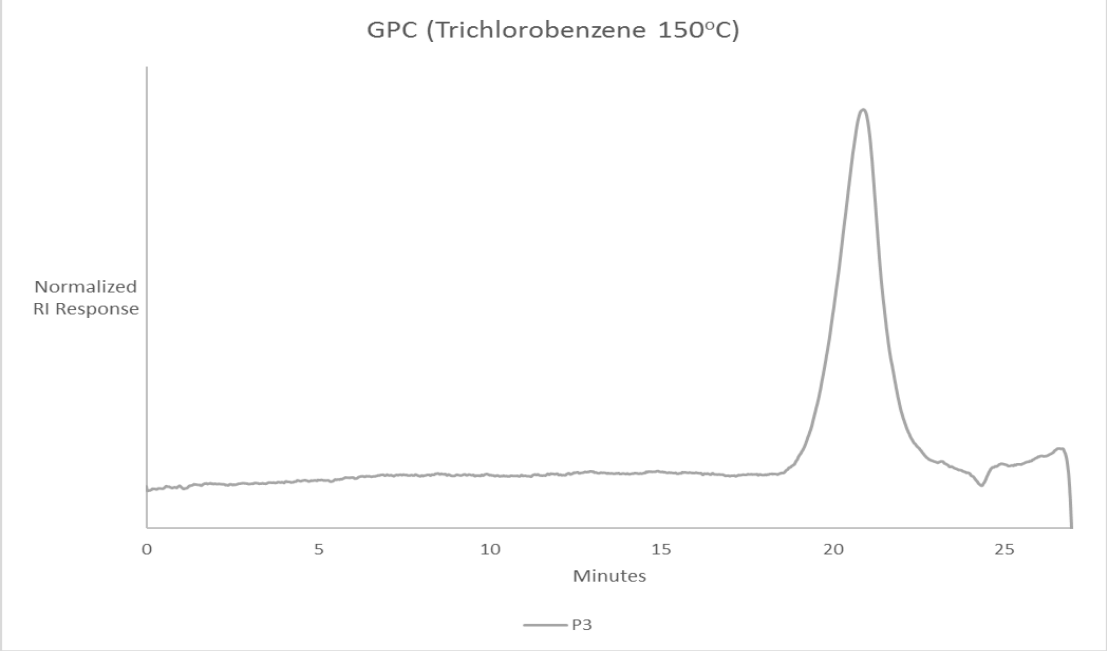


**Figure 34: GPC (1,2,4-trichlorobenzene 150$^{o}$C) trace for P3 with Mn 15 kDa and dispersity of 1.5.**

$^{1}$H NMR (TCE-d2 120$^{o}$C) confirmed the chemical identity of the material (Figure 35).

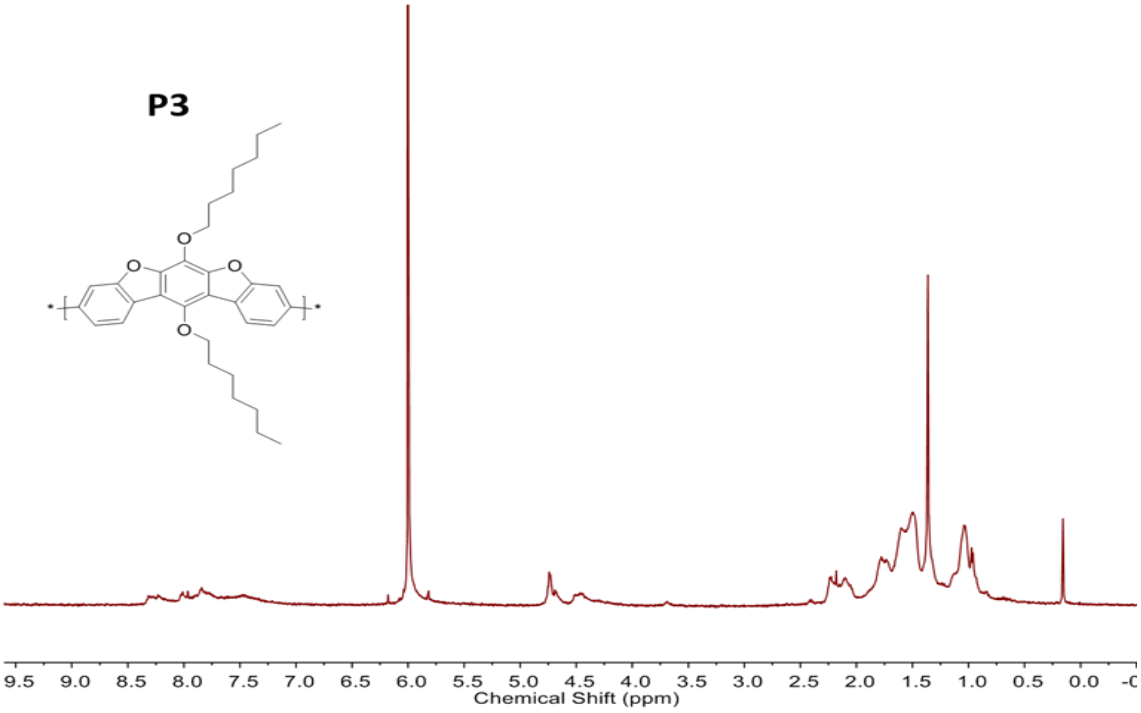


**Figure 35: $^{1}$H NMR (TCE-d2 120$^{o}$C) of P3.**

The synthesis of P1, P2, and P3 demonstrate the versatility of the reductively alkylated benzodibenzofuran core and establishes a series of interesting conjugated polymers consisting of the two donor-acceptor polymers P1 and P2 as well as the homopolymer P3 (Figure 36).

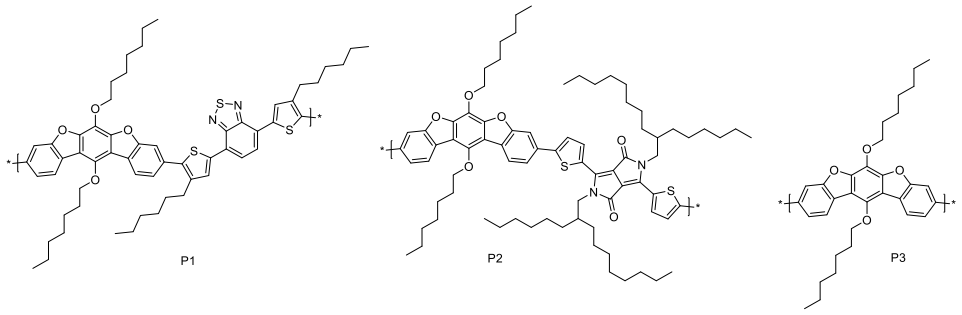


**Figure 36: Structures of synthesized conjugated polymers P1, P2, and P3.**

UV-Vis absorption spectroscopy of these three polymers as thin films show that the donor-acceptor polymers P1 and P2 have narrower optical band gaps of 1.9 eV and 1.4 eV relative

to the wider band gap homopolymer P3 with an optical band gap of 3 eV (Figure 37).

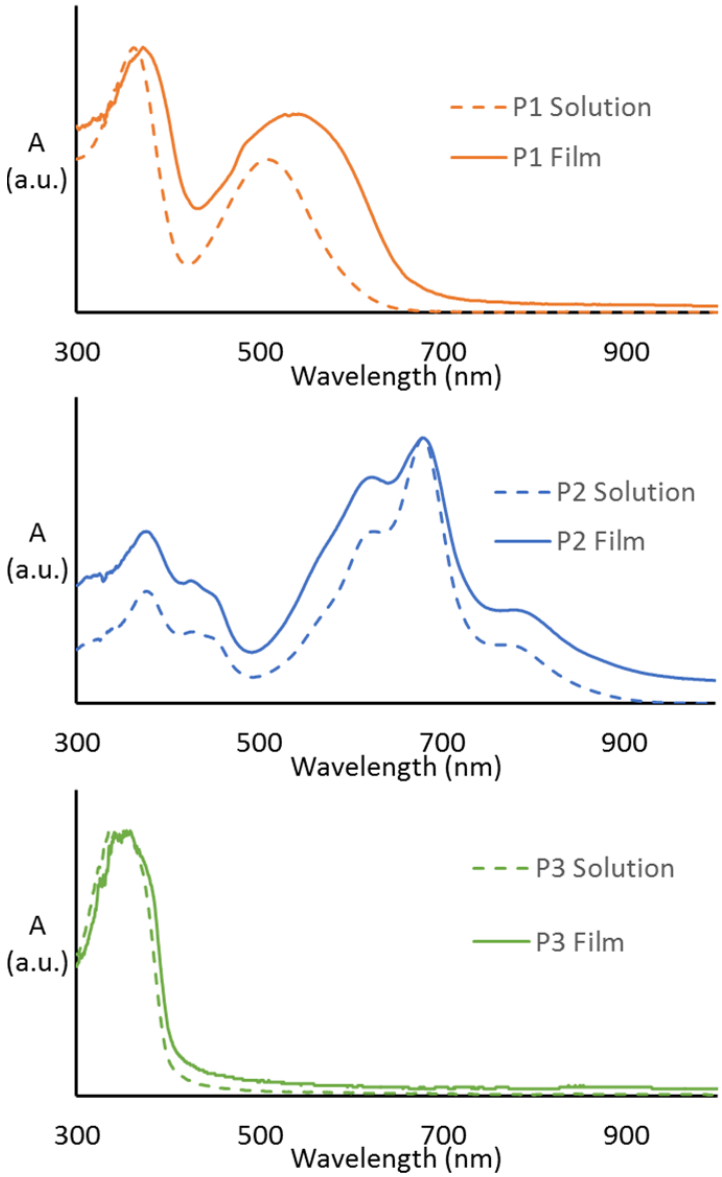


**Figure 37: Solution and thin film absorption spectrum for P1, P2, and P3.**

The similarity of the solution spectrum in chlorobenzene and solid-state spectrum for P2 both having the vibronic peak at about 800 nm further highlights the propensity for this material to aggregate in solution. Density functional theory (DFT) and time dependent density functional theory (TD-DFT) calculations using Gaussian09 and the B3LYP 6-31Gd basis set further elucidate the electronic structure of these materials. Optimized geometries for P1, P2, and P3 show a flat and undulated backbone for P1 and P2 whereas P3 has a much larger torsional angle along the backbone owing to the phenyl-phenyl interaction causing a dihedra angle of 44°. P2 is seen to have a multi-donor structure where the lowest energy intramolecular donor to acceptor transition occurs between the thiophene units and the dipyrrolopyrroledione DPP unit and a second higher energy transition occurs between the benzodibenzofuran unit and the DPP unit. This is because the benzodibenzofuran unit has a deeper HOMO level relative to the thiophene units owing to the known energy stabilizing character of oxygen in heteroaromatics relative to their sulfur heteroaromatic analogues[60]. The TD-DFT calculations, molecular orbitals, and optical transitions are outlined in Figure 38.

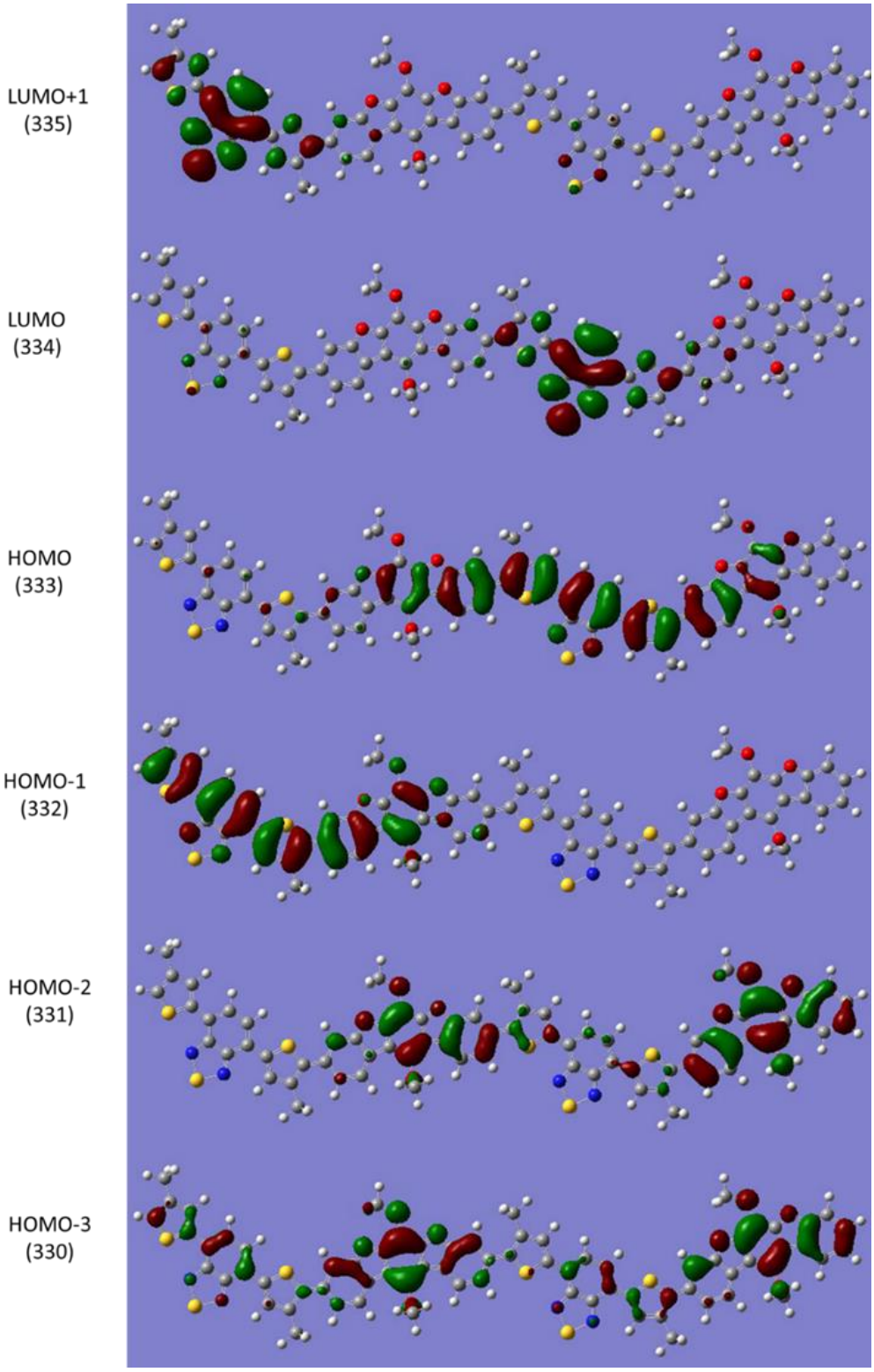


**Figure 38: TD-DFT calculations for P1 molecular orbitals.**

The calculated optical transitions show that the lowest energy transition occurs between the HOMO and LUMO levels where the HOMO level is delocalized over the backbone and the LUMO is localized predominately on the BTD unit. A second higher energy transition occurs between the HOMO-2 and HOMO-3 levels locate predominately on the benzodibenzofuran unit to the LUMO and LUMO+1 levels located predominately on the BTD unit. This second transition is characteristic of a multi-chromophore (multi-donor) effect due to the energy stabilizing character of the BDBF unit relative to the sulfur heteroaromatic thiophene units.

TD-DFT calculations for P3 show well delocalized HOMO and LUMO levels with a large torsional angle of 44$^{o}$ between each monomer unit (Figure 39).

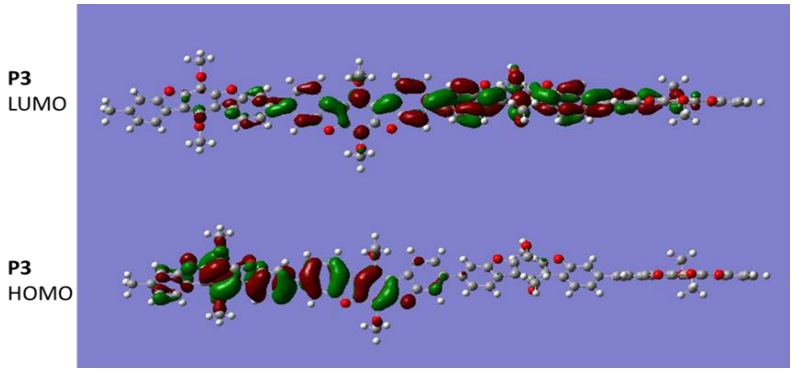


**Figure 39: TD-DFT calculations for P3.**

Similar analysis of P2 (Figure 40) shows more localized HOMO and LUMO levels situated predominately on the thiophene and DPP units. The lowest energy transitions occur within these thiophene and DPP units. A second higher energy transition is seen to arise between the lower energy orbitals localized on the BDBF unit and the DPP unit giving rise to the higher energy peak in the absorption spectrum at around 600 nm. This second transition is also characteristic of a multi-donor system.

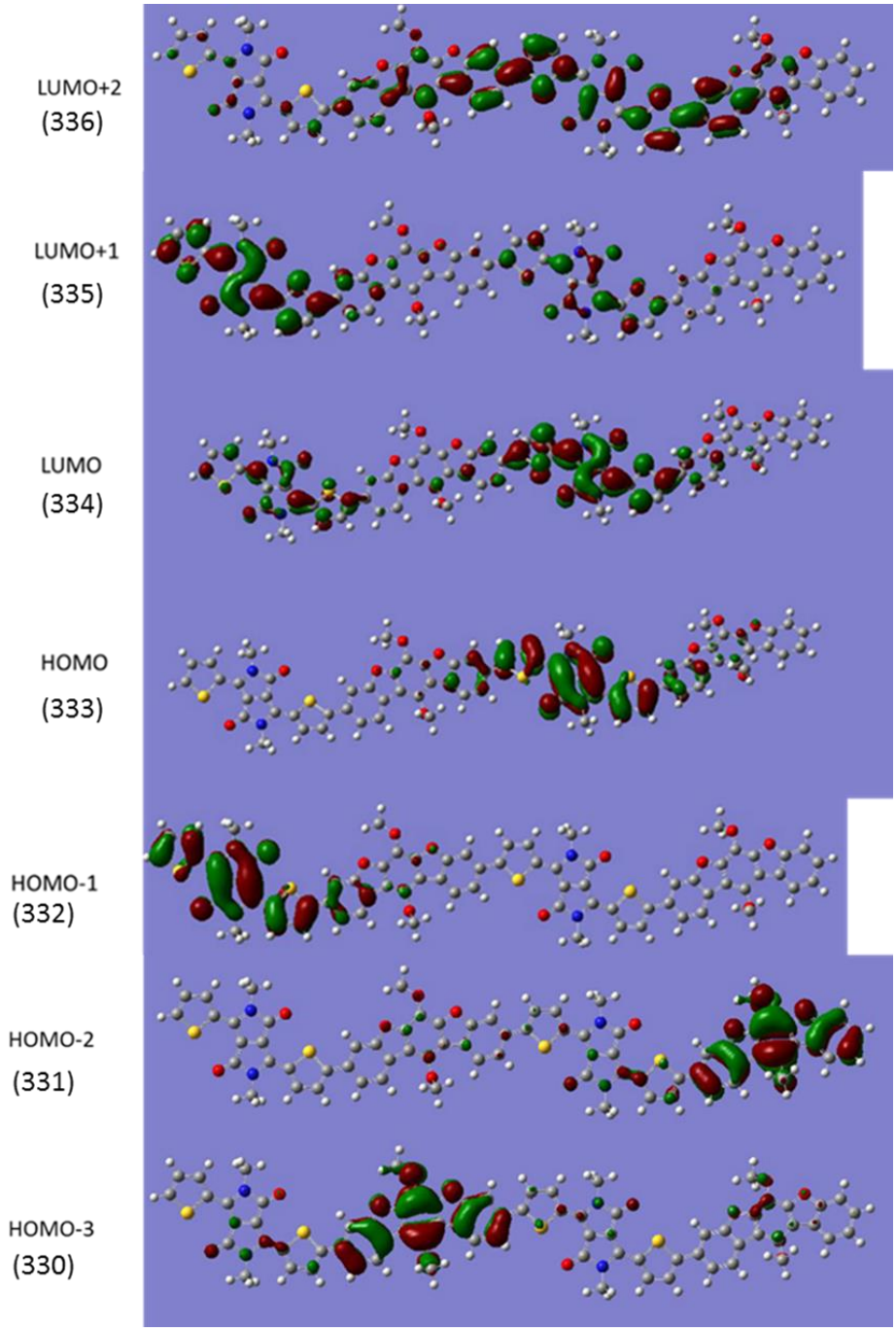


**Figure 40: TD-DFT Calculations for P2.**

Cyclic voltammetry measurements for the three polymers as thin films drop-cast on the electrode and placed in a 0.1M solution of tetrabutylammonium hexafluorophosphate in anhydrous acetonitrile are shown below and reported relative to a ferrocene/ferrocenium

standard. All three polymers are seen to exhibit a large oxidation wave at 0.6, 0.5, and 0.7 V for P1, P2, and P3 respectively. The ionization energies were then calculated from the onset oxidization energy as IE = −(4.8 + $E_{onset}$) eV to give -5.4, -5.3, and -5.5 eV respectively. These large ionization energies corresponding to deep HOMO levels further illustrate the energy stabilizing character of the BDBF unit (Figure 41).

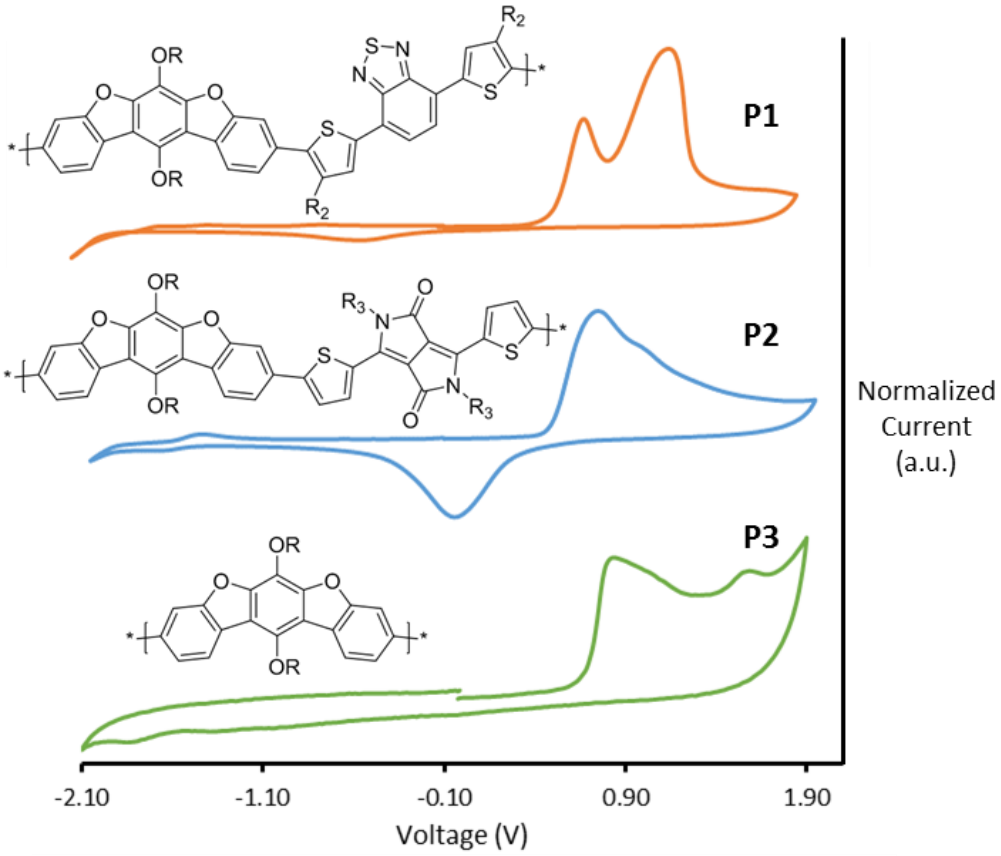


**Figure 41: Cyclic voltammetry measurements for P1, P2, and P3 in acetonitrile with $Bu_4NPF_6$.**

P2 also features a very small reduction wave at -1.5 V which corresponds with an electron affinity (EA) of -3.4 eV. The EA of P1 and P3 were estimated from their respective optical gaps to give -3.5 eV and -2.4 eV respectively. Figure 36 depicts these energy levels.

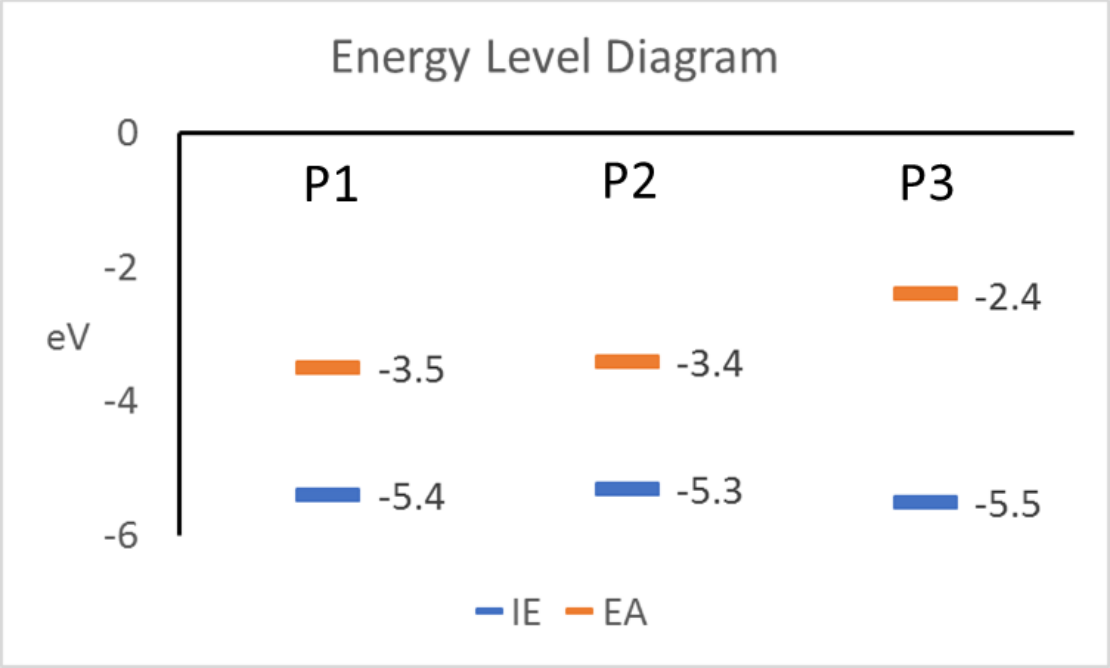


**Figure 42: Ionization (IE) and electron affinity (EA) values for P1, P2, and P3.**

As expected, the donor-acceptor polymers P1 and P2 have the narrowest band gap whereas the homopolymer P3 has a wider band gap. Furthermore, the IE of these polymers are all very low at below -5.3 eV indicative of the energy stabilizing character of the BDBF unit.

The solid-state morphology for these three polymers was then studied using grazing incidence wide angle X-ray scattering (GIWAXS). P1 and P2 were spun-cast from chloroform solutions at a concentration of 10 mg/ml and annealed at 150ºC for 10 minutes whereas P3 was drop-cast from a 1:1 mixture of 1,1,2,2-tetrachloroethane and chlorobenzene and measured as cast. All three showed reflections indicative of a semicrystalline morphology (Figure 43).

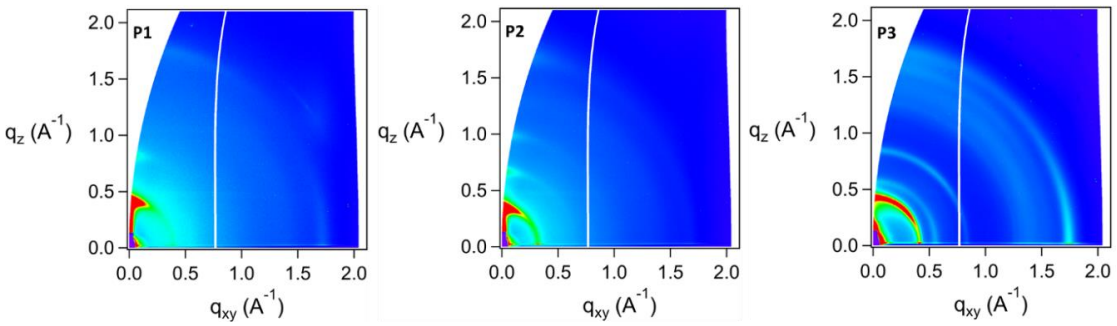


**Figure 43: GIWAXS patterns for P1, P2, and P3.**

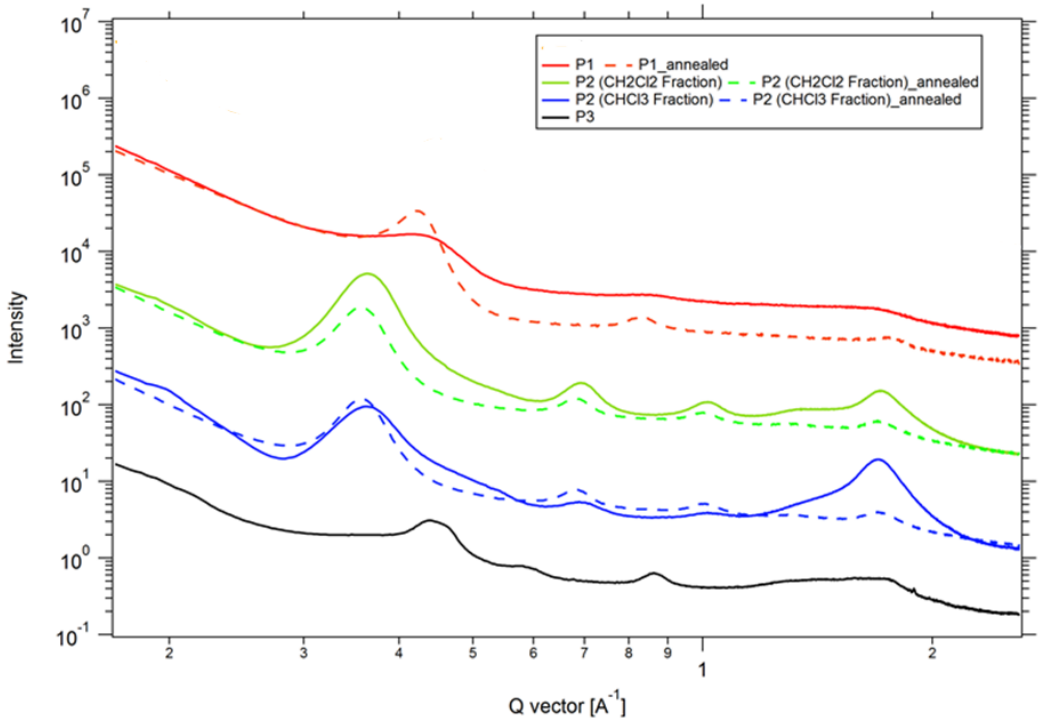


**Figure 44: Vertical line cuts from GIWAXS experiments.**

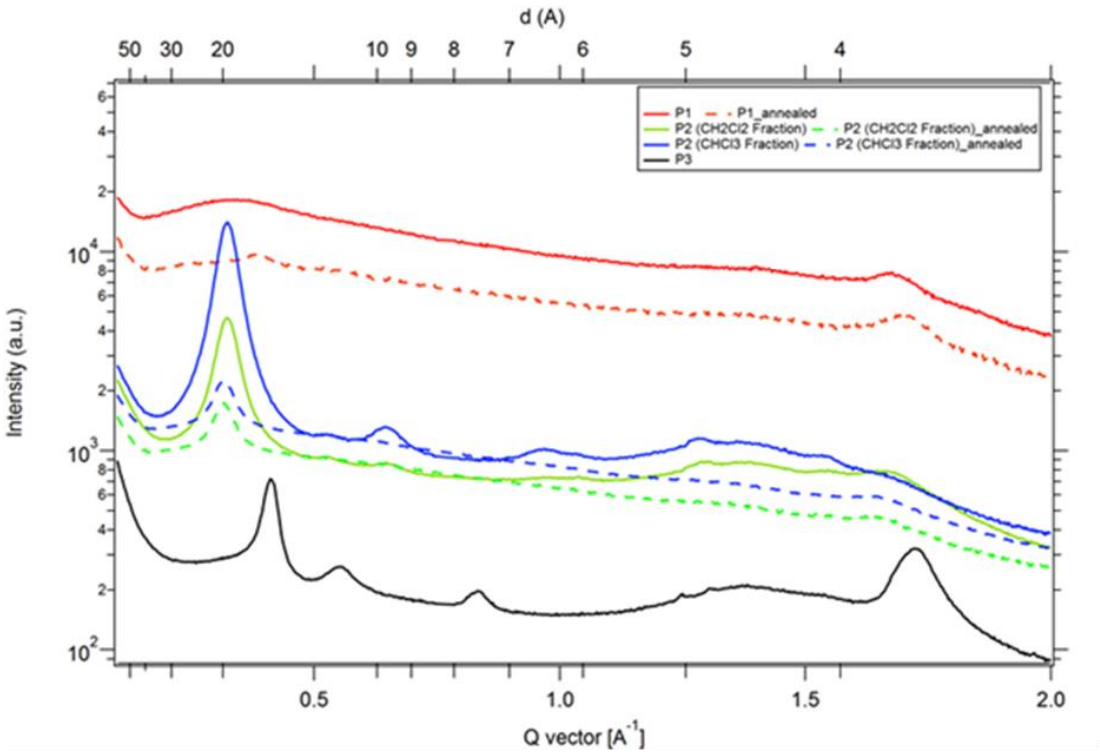


**Figure 45: Horizontal line cuts from GIWAXS experiments.**

P1 and P2 have a diffuse lamellar structure as indicated by the progression of alkyl stacking peaks in the vertical line cut with d= 14.8 and 17.6 Å. P2 appears to be more textured than P1 which is predominately edge-on as indicated by the alkyl stacking peaks occurring predominately in the out of plane direction and the π-π stacking peak occurring predominately in the in-plane direction. P3 has a more isotropic scattering pattern as expected for a drop-cast film. The alkyl d-spacing for P3 is 14.2 Å. The d-spacing for the π-π stacking occurs at 3.70, 3.76, and 3.63 Å for P1, P2, and P3 respectively. The d-spacings are seen to increase with increasing size of the side-chains of the co-monomers with P3 having the smallest d-spacings and P2 having the largest d-spacings (Figure 44, Figure 45).

P2 was chosen as an interesting candidate for further study in a field effect transistor as well as in preliminary OPV devices. This is because DPP based polymers such as P2 have been known to exhibit good charge mobility in OFETs[61,62], and the broad absorption profile of P2 which trails off at longer wavelengths around 900 nm appears good for solar cell applications. The field effect mobility of P2 was characterized in a bottom-gated top-contact field effect transistor. A heavily doped silicon wafer with a 100 nm thermal oxide layer was modified with a 100 nm layer of CYTOP, an amorphous fluoropolymer, as added dielectric. Then P2 was spun-cast from a 10 mg/ml solution in chloroform at 1000 rpm for 45 seconds followed by 3000 rpm for 30 seconds and the resulting film was annealed at 150$^{o}$C in nitrogen for 1 hour. Top gold contacts were thermally evaporated under vacuum on to the film to achieve the OFET device geometry illustrated in Figure 46.

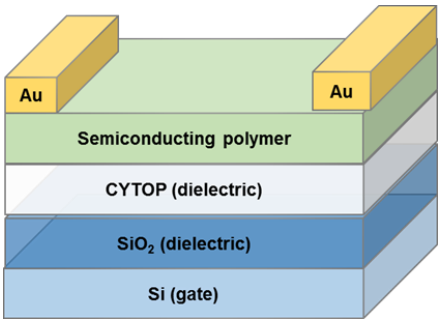


**Figure 46: Device geometry for OFET measurements.**

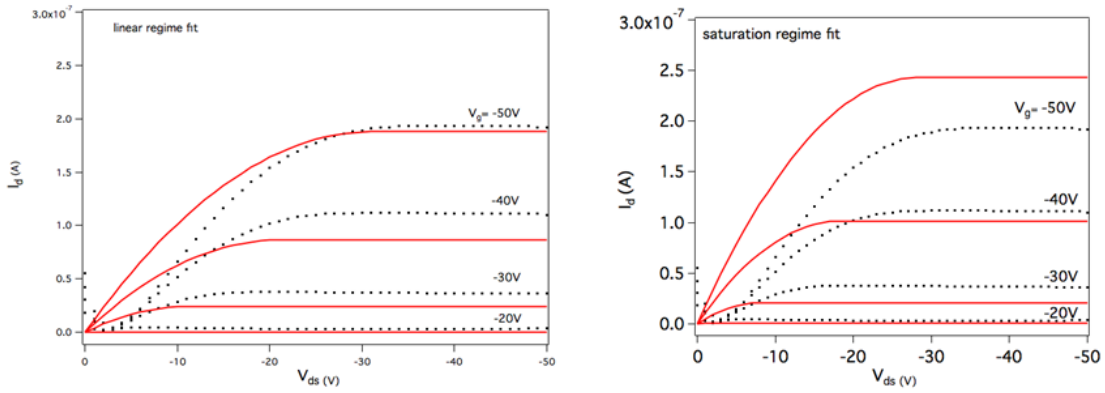


**Figure 47: Linear (left) and saturation (right) regime OFET measurements with calculated fits in red.**

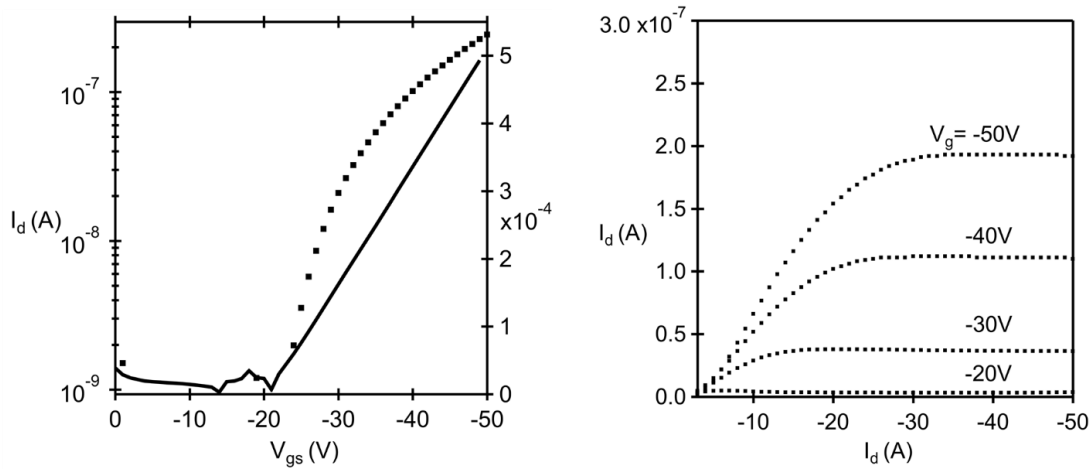


**Figure 48: transfer (left) and output (right) OFET plots. The solid line indicates is $I_d^{1/2}$ for $V_d$=-20 V.**

The dotted lines of the transfer plot indicate $I_d$ for $V_d$=-40 V and the solid line is $I_d^{1/2}$ for $V_d$=-20 V (Figure 48). The hole mobility for the material was calculated from the slope of the $I_d^{1/2}$ curve to give 0.003 $cm^2/(V\ s)$ and the threshold voltage was found to be -21.7 V. No n-type conductivity was observed. OFET mobility measurements are highly dependent on device architecture and material processing conditions[2,63,64]. These

preliminary results offer a proof of concept illustration that this material can conduct charge and operate in an OFET device.

Next, the effectiveness of P2 in solar cell devices was explored. First morphological structure of blends of P2 and $PC_{71}BM$ were studied via GIWAXS for samples spun-cast from either chlorobenzene with 1% 1,8-diiodooctane or chloroform with and without annealing. The diffuse scattering patterns indicate good intermixing of the blend (Figure 49).

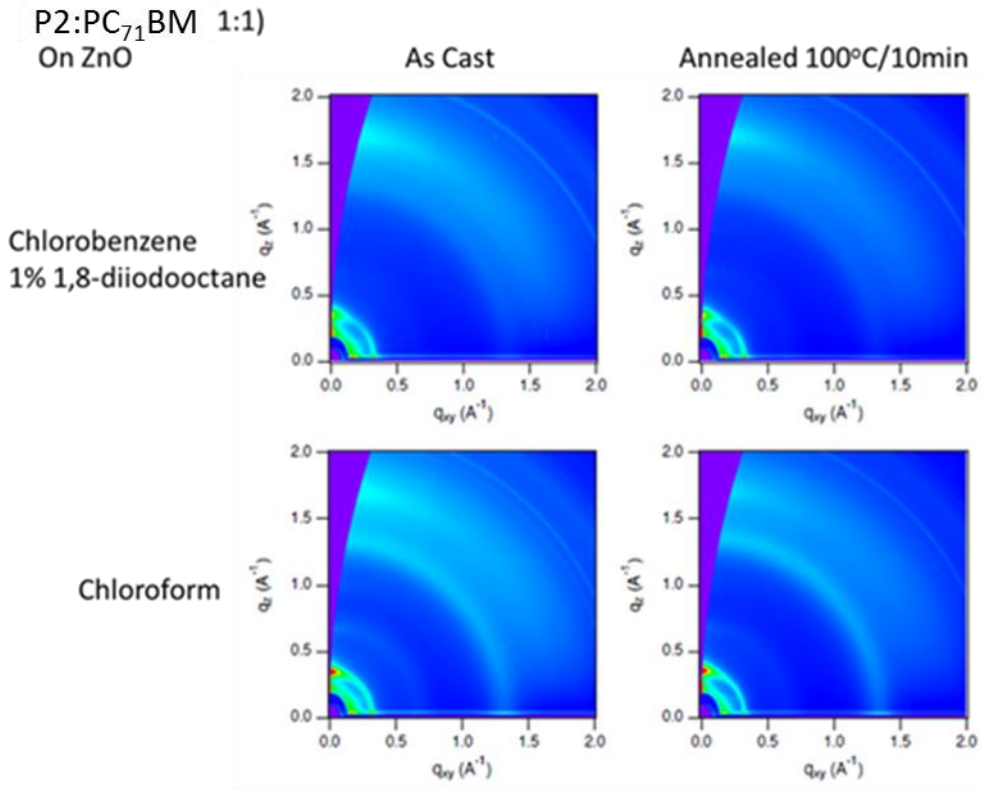


**Figure 49: GIWAXS patterns for 1:1 wt% blends of P2 and PC71BMeither as cast (left column) or annealed for 10 minutes at 100oC (right column). The solutions were either chlorobenzene with 1% 1,8-diiodooctane (top row) or chloroform (bottom row).**

Devices were fabricated on glass/ITO/ZnO(sol-gel) substrates by spin-casting various weight ratios of P2 and $PC_{71}BM$ as 10 mg/ml solutions in chlorobenzene with 1% 1,8-diiodooctane. Next, a 4 nm $MoO_3$ layer and an 80 nm silver layer were thermally evaporated on top. Current density-Voltage measurements were then performed both in the dark and under 1 Sun AM1.5 illumination. The device details and characteristics are outlined in Figure 50.

| Voc (V) | Jsc ($mA/cm^2$) | FF | PCE (%) | P2:$PC_{71}BM$ weight ratio | Spin Coat (rpm) | Anneal ($^oC$/min) |
|---|---|---|---|---|---|---|
| 0.71 | 4.91 | 0.5 | 1.73 | 1:1 | 800 | no |
| 0.75 | 4.17 | 0.48 | 1.5 | 1:1 | 800 | 100/30 |
| 0.68 | 3.84 | 0.42 | 1.08 | 1:1 | 1200 | no |
| 0.62 | 3.79 | 0.35 | 0.82 | 1:1 | 1200 | 100/30 |
| 0.73 | 5.83 | 0.58 | 2.48 | 1:2 | 800 | no |
| 0.75 | 5.11 | 0.55 | 2.11 | 1:2 | 800 | 100/30 |
| 0.73 | 5.5 | 0.6 | 2.39 | 1:2 | 1200 | no |
| 0.76 | 4.92 | 0.54 | 2 | 1:2 | 1200 | 100/30 |

**Figure 50: Table of device fabrication parameters and corresponding device performance measurements.**

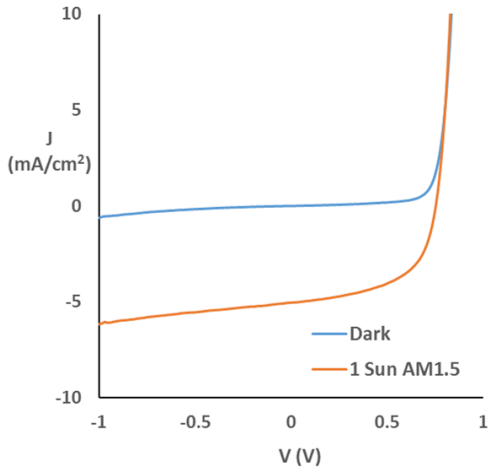


**Figure 51: Current density-voltage plot for the device indicated in the figure 44 with Voc= 0.75 V, Jsc= 5.11 mA/cm2, FF= 0.55, and PCE=2.11%.**

The J-V curve for a representative device is shown in Figure 51. A small dark current at the -1 V bias indicates a small amount of leakage current. To further understand this device's performance, incident photon to current efficiency (IPCE) measurements were taken Figure 52A. These measurements revealed a low IPCE ratio at the longer wavelengths of 700 to 900 nm even though the polymer P2 absorbs these wavelengths of light. Furthermore, the absolute absorption coefficient for an 80 nm thick film of P2 was measured and compared relative to PBDTT-FTTE, a known high performance donor material in OPVs[53] (Figure 52B and C).

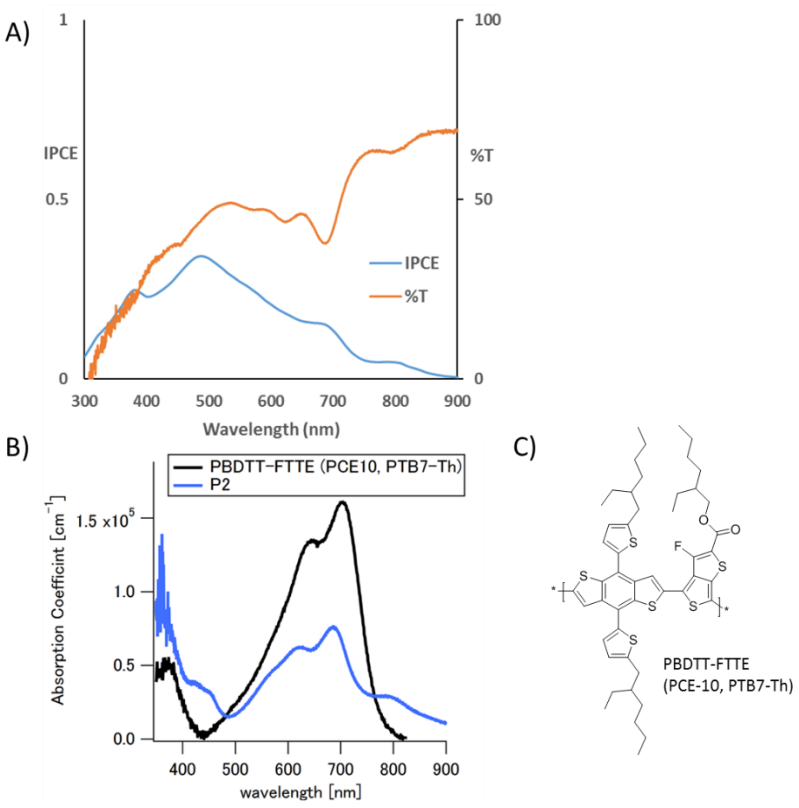


**Figure 52: A) Incident photon to current efficiency and transmittance measurements for P2:PC$_{71}$BM 1:1 wt% blend. B) Comparison of absolute absorption coefficient of P2 and high performance OPV material PBDTT-FTTE. C) Structure of PBDTT-FTTE.**

It was found that the absolute absorption coefficient was about a factor of 2 lower than the PBDTT-FTTE standard. The relatively low short circuit current of less than 6 mA/cm$^2$ for all of these devices as well as the low IPCE and low absolute coefficient of absorption which result in the overall low power conversion efficiencies of less than 2.5% are all characteristic of DPP based materials[65]. These proof of concept device measurements do however demonstrate utility of the BDBF unit in solar cell devices and offer a starting point for future materials and device optimization using this novel building block.

Returning to the M1 unit, as a further demonstration of the versatility of this compound, incorporation of the redox active quinone form into a series of materials was desired. Unfortunately, direct incorporation of the M1 unit into materials via either Stille or Suzuki coupling polymerization was unsuccessful. Such reactions only produced a brown colored mixture which did not precipitate well in methanol. It is possible that this reaction did not work because the redox cycle of the quinone M1 interferes with the redox catalytic cycle of the Pd catalyst as it is known that quinone compounds are capable of interacting with the catalytic cycle of Pd[66]. In order to circumvent this challenge, a protection/deprotection strategy was adopted. The quinone form was protected with para-methoxybenzyl (PMB) groups in the reductively alkylated form M* (Figure 53).

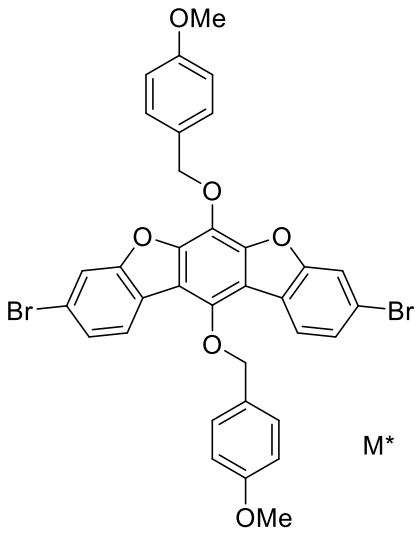


**Figure 53: Structure of paramethoxybenzyl (PMB) protected M*.**

This M* compound then proved successful in Suzuki coupling reactions. First, M* was reacted with 2,2'-(9,9-dioctyl-9H-fluorene-2,7-diyl)bis(1,3,2-dioxaborinane) using standard Suzuki polymerization conditions (Figure 54). After Soxhlet washing with

acetone and hexanes, the polymer fraction was extracted with chloroform to give P4* in 96% yield with a Mn of 18 kDa and PDI of 3.0 (Figure 55).

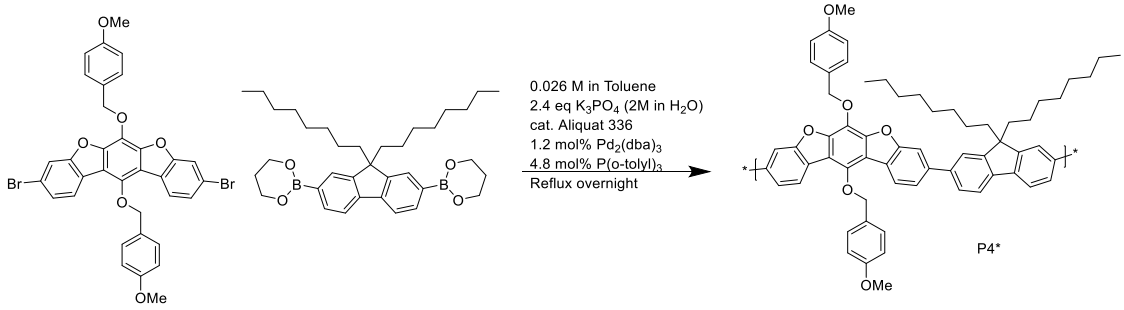


**Figure 54: Synthesis of PMB protected P4*.**

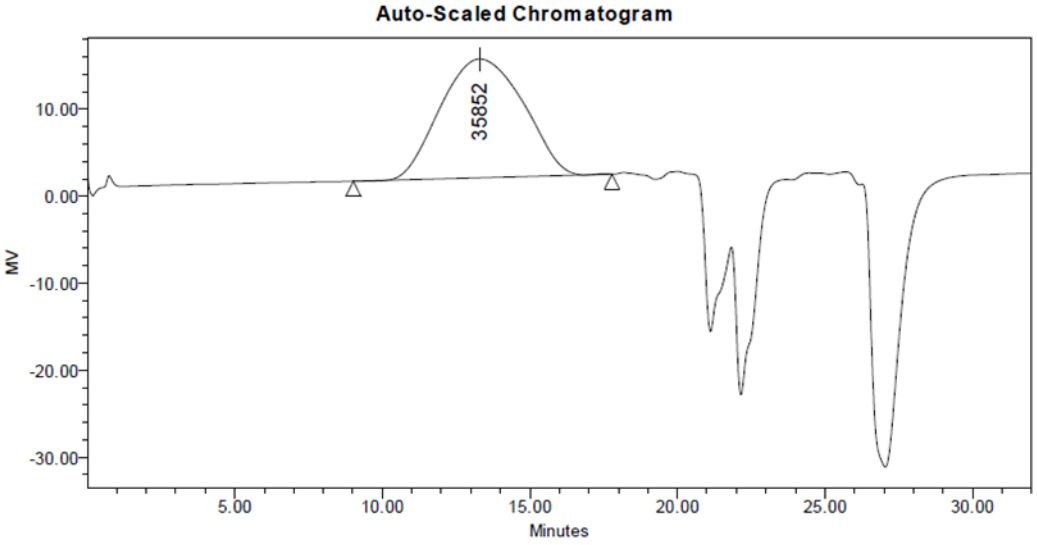


GPC Results

| | Dist Name | Mn | Mw | MP | Mz | Mz+1 | Mv | Polydispersity | MW Marker 1 | MW Marker 2 |
|---|---|---|---|---|---|---|---|---|---|---|
| 1 | | 18331 | 54542 | 35852 | 123985 | 202107 | | 2.975365 | | |

**Figure 55: GPC (chloroform) trace of P4* with Mn 18 kDa and dispersity of 2.98.**

Deprotection of P4* to P4 also proved successful. When P4* was refluxed in anisole:trifluoroacetic acid (3:1) in air, the PMB were removed and the intermediate hydroquinone was oxidized down to the quinone form. The TFA elicits the removal of

the PMB group and anisole is used as the solvent to trap the resulting alkylating agent[67]. Oxygen in the air then oxidizes the resulting hydroquinone form down to the quinone (Figure 56).

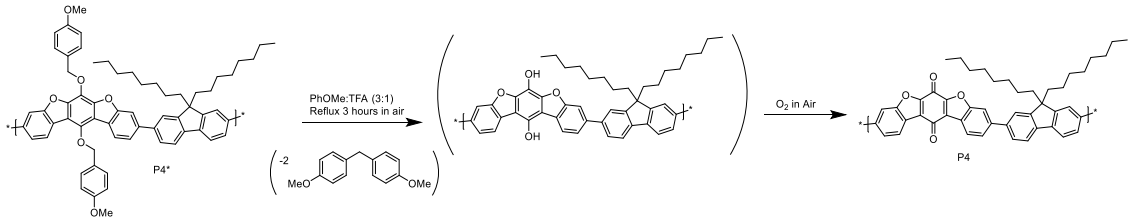


**Figure 56: Deprotection conditions for converting P4* to the quinone form P4.**

The reaction was worked up by precipitating the polymer in methanol followed by Soxhlet washing with acetone and finally eluting with chloroform. The resulting polymer had a bluish-purple color as compared to the white-gray starting material. GPC analysis (150$^{o}$C 1,2,4-trichlorobenzene) gave a Mn of 38 kDa with a PDI of 2.1 (Figure 57). This Mn is larger than the 18 kDa starting material. This is likely due to a combination of loss of lower molecular weight material during the precipitation and Soxhlet washing as reflected by the narrower PDI of 2.1 vs the 3.0 starting material, as well as an increase in aggregation due to the loss of the PMB solubilizing groups. The deprotected P4 polymer was run on a high temperature trichlorobenzene GPC in order to help minimize the effect of this expected increase in aggregation on the observed molecular weight.

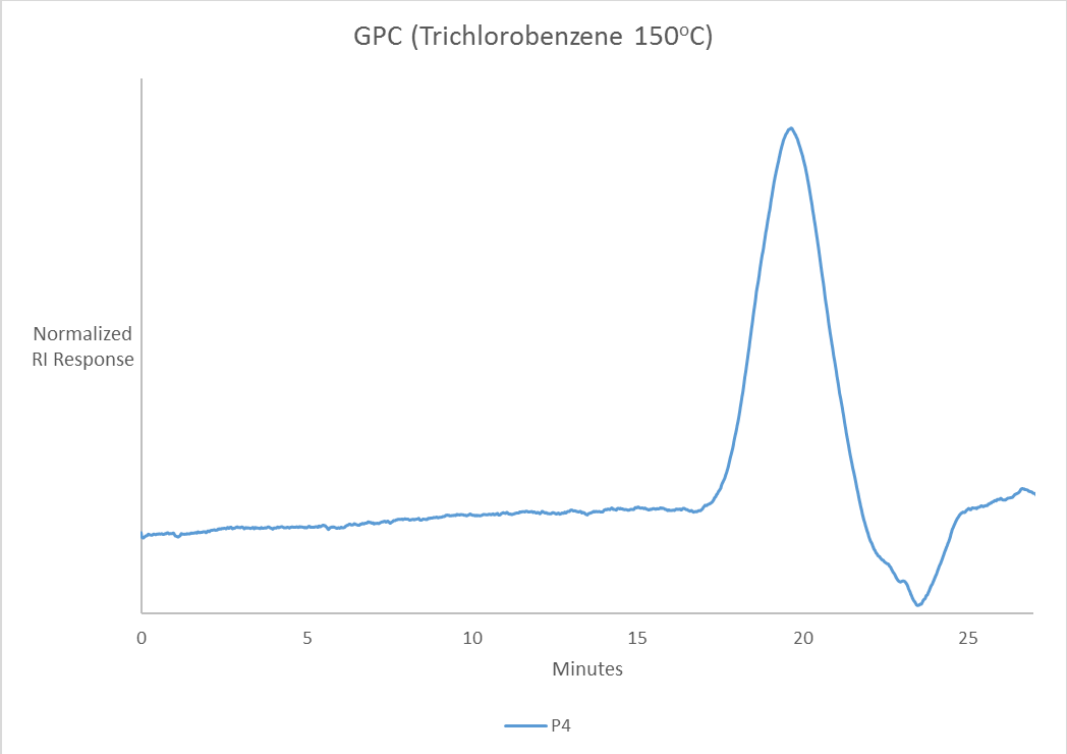


**Figure 57: GPC (1,2,4-trichlorobenzene 150°C) trace for deprotected P4 with Mn 38 kDa and dispersity of 2.1.**

Successful deprotection of PMB protected P4* to its quinone for P4 was characterized by $^{1}$H NMR spectroscopy (Figure 58, Figure 59) and Fourier transform infrared (FTIR) spectroscopy (Figure 60).

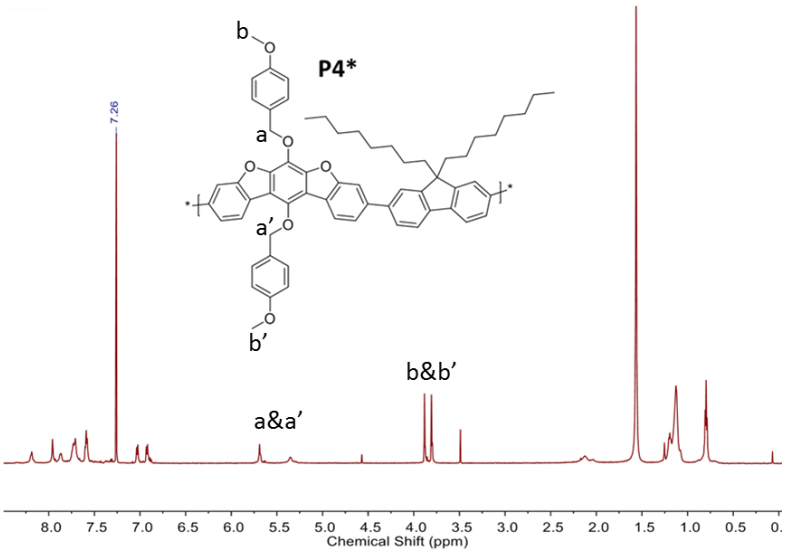


**Figure 58: $^{1}$H NMR (Chloroform-d) spectrum for P4* showing characteristic PMB peaks.**

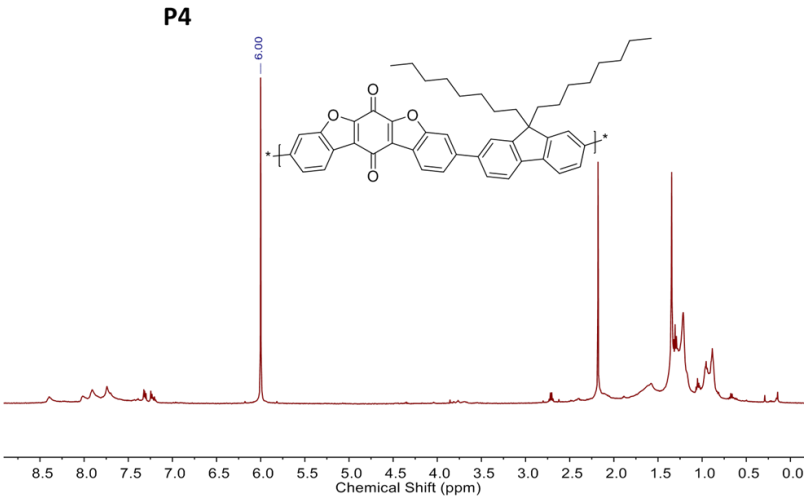


**Figure 59: 1H NMR (TCE-d2 120ºC) spectrum for P4 showing lack of characteristic PMB peaks.**

FTIR spectroscopy confirmed the appearance of a distinct carbonyl stretch at around 1670 $cm^{-1}$ indicated by the arrow in the chart below.

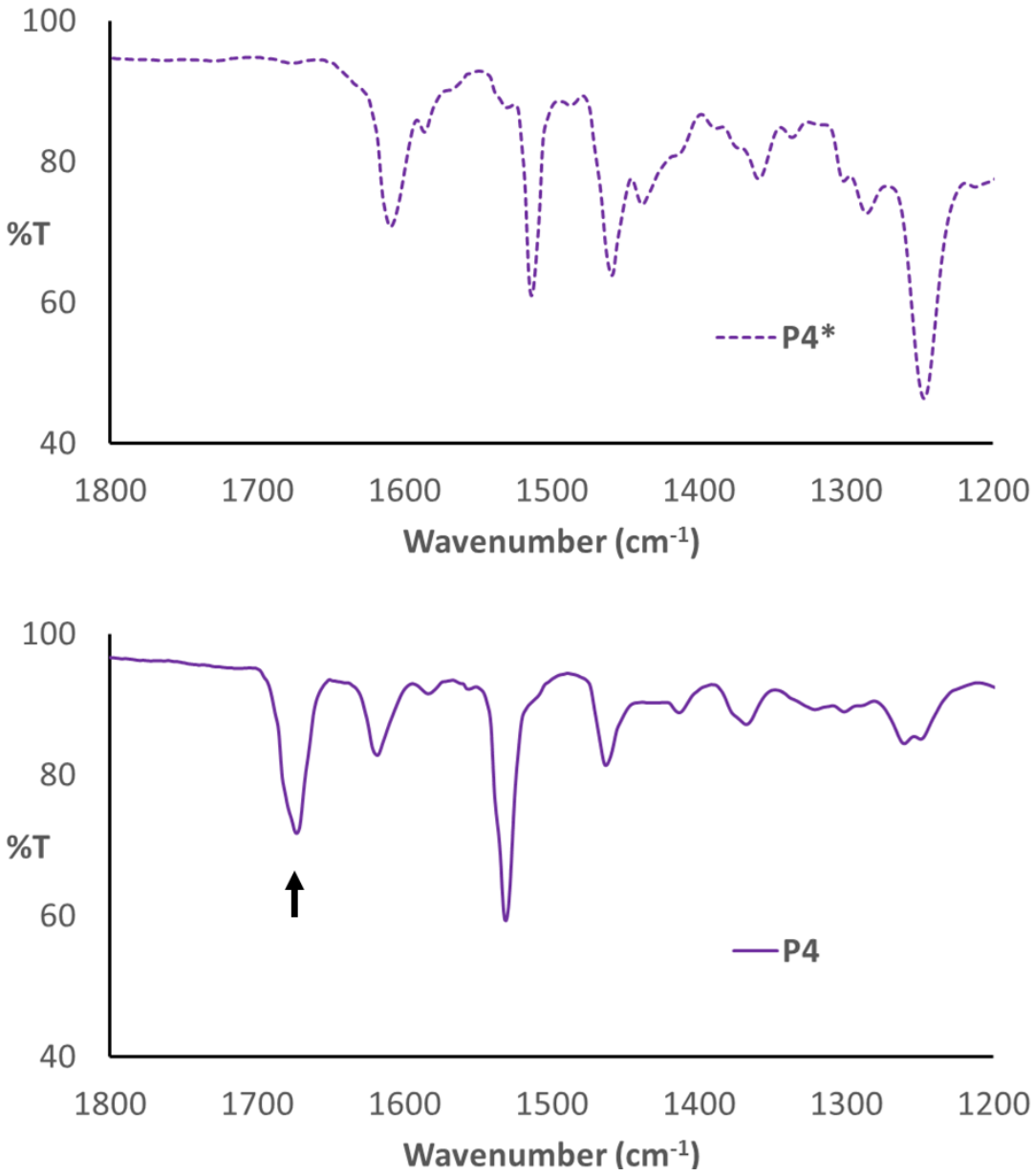


**Figure 60: FTIR spectra for P4* and P4 showing emergence of carbonyl stretch in P4 as indicated by the arrow.**

Upon deprotection, chlorobenzene solutions of the polymer became purple in color (Figure 61).

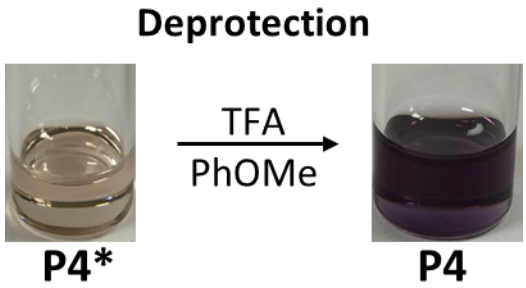


**Figure 61: Visual change corresponding with deprotection. P4* solution in chlorobenzene on the left and P4 solution in chlorobenzene on the right.**

This is reflected in a corresponding change in the UV-Vis absorption spectrum (Figure 62).

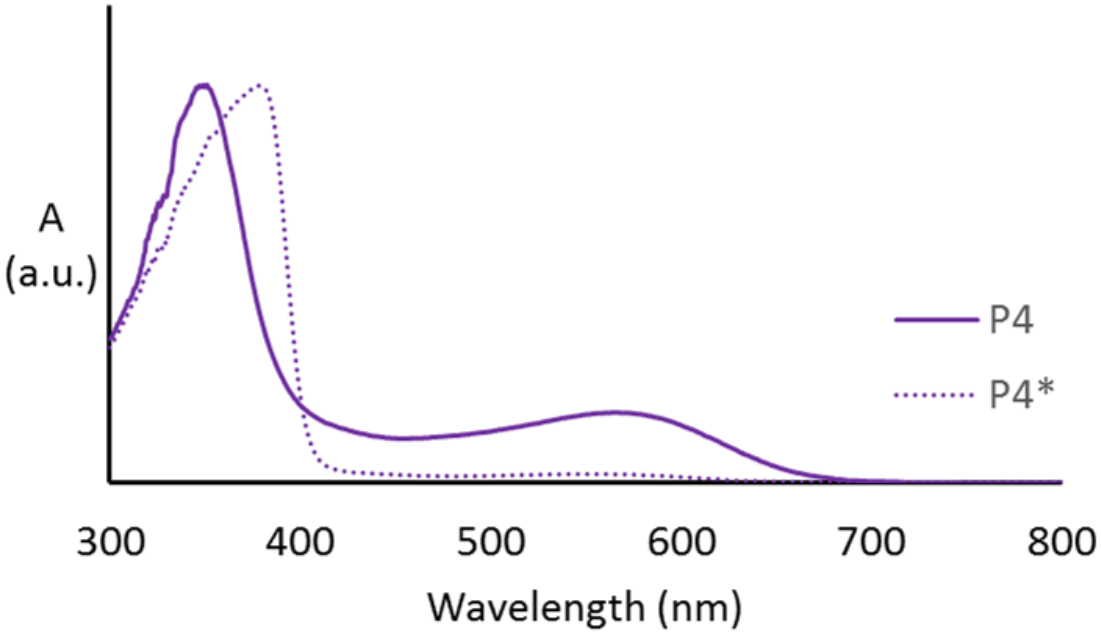


**Figure 62: Normalized absorption spectra for PMB protected P4* and deprotected P4.**

It is interesting to note that in addition to the appearance of a secondary maximum at 587 nm, the π- π* transition shifts to shorter wavelengths from 378 nm in P4* to 351 nm in P4. This is likely due to the appearance of a node in the HOMO level at the quinone unit which limits the effective conjugation length along the backbone relative to the fully conjugated reductively alkylated P4* form. This suggestion is supported with DFT calculations of the quinone material showing the presence of this node (Figure 63). These DFT calculations also show that the LUMO level is located predominately on the quinone unit and suggests that the secondary maximum is due to an intramolecular donor-acceptor transition occurring between the electron rich fluorene unit and the electron accepting quinone unit.

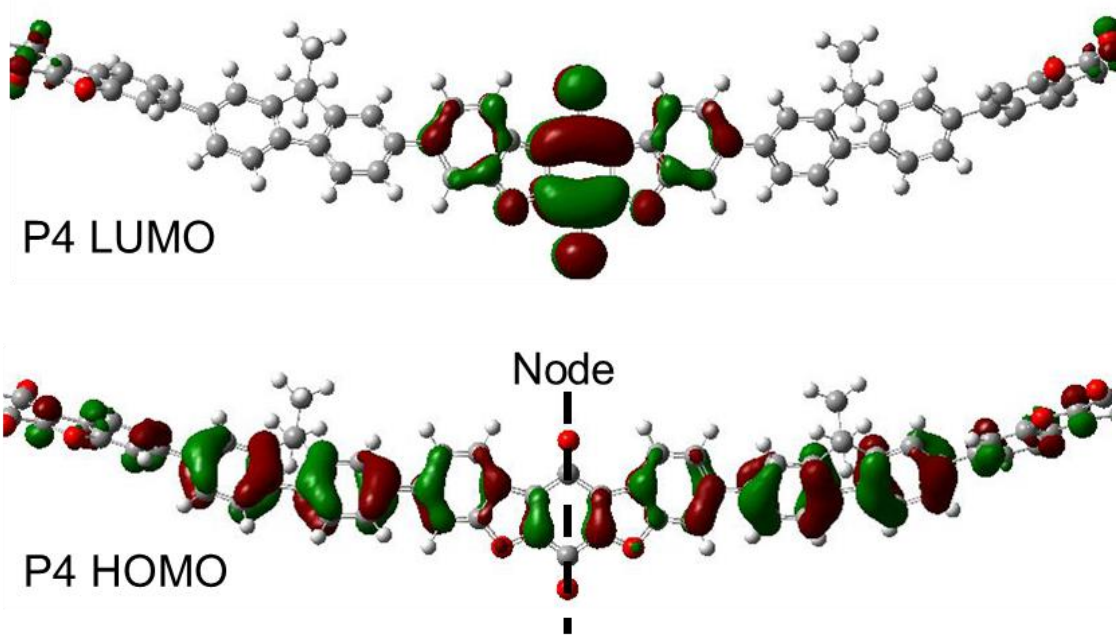


**Figure 63: Calculated HOMO and LUMO for P4 sowing a node in the HOMO at the quinone.**

Furthermore, the redox active nature of the quinone unit within the polymer backbone was verified via cyclic voltammetry. P4 was deposited as a thin film on the electrode and placed into a solution of 0.1M tetrabutylammonium hexafluorophosphate for cycling. The results are reported relative to a ferrocene/ferrocenium standard and show the presence of two reduction peaks at about -0.8 and -1.4 V respectively (Figure 64).

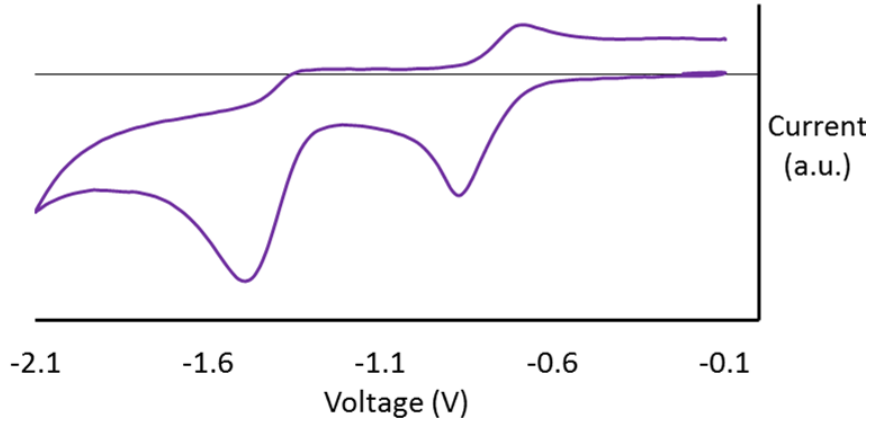


**Figure 64: Cyclic voltammetry measurements or P4 showing to reduction waves.**

Thin films of P4 spun-cast from a 10 mg/ml solution in chloroform and annealed for 10 minutes at 150$^{o}$C were analyzed via GIWAXS (Figure 65).

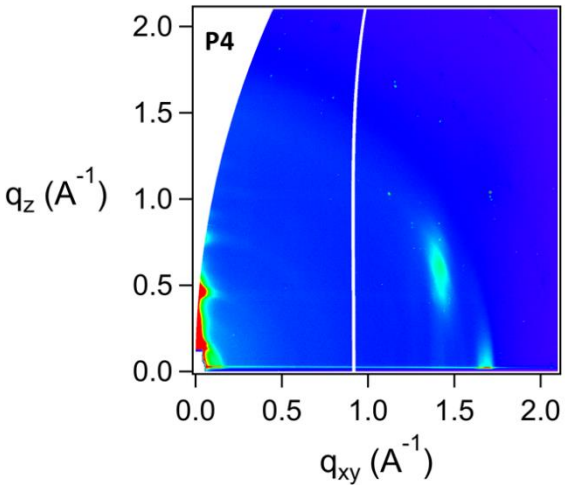


**Figure 65: GIWAXS pattern for P4.**

P4 showed a similar layered structure to the previous polymers, and, unlike many poly(fluorene) polymers, does not exhibit a hexagonally packed structure[68].

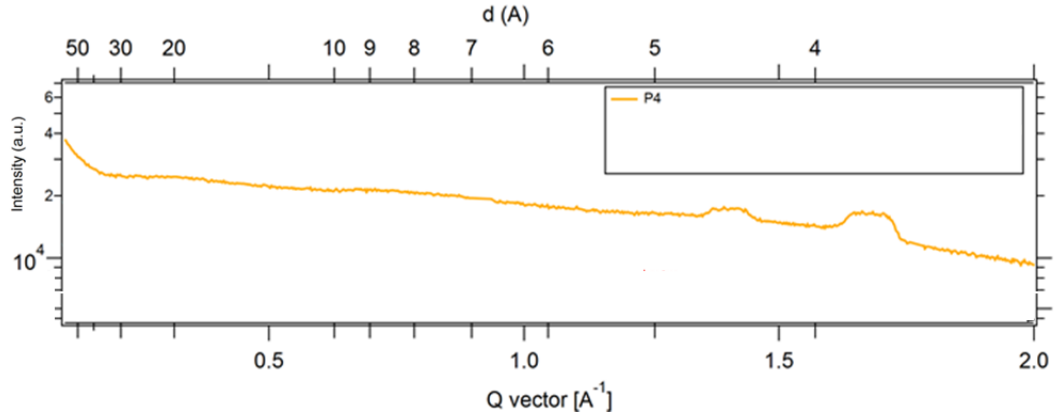


**Figure 66: Horizontal line cut of the GIWAXS pattern for P4.**

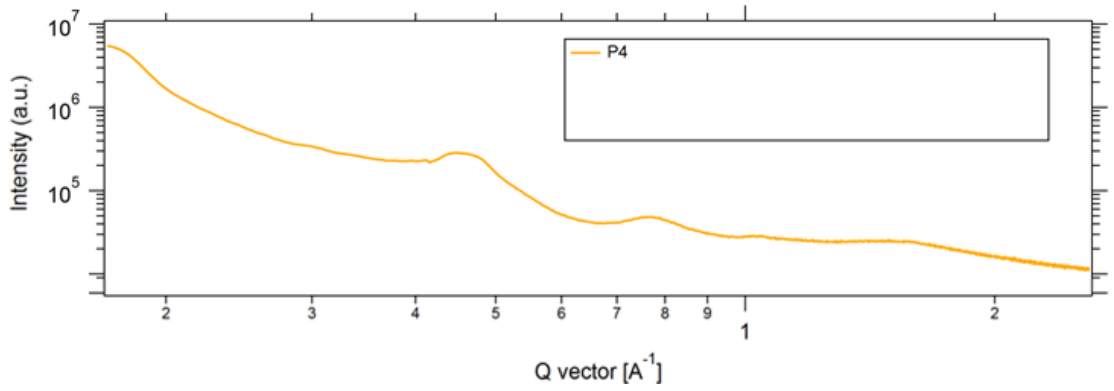


**Figure 67: Vertical line cut of the GIWAXS pattern for P4.**

The π-stacking distance is 3.73 Å and the lamellar d-spacing is 13.6 Å (Figure 60 and 61).

To further support and characterize this protection/deprotection strategy, a small molecule analogue was developed by reacting M* with the monofunctional (9,9-dipentyl-9H-fluoren-2-yl)boronic acid to give O4* (Figure 68).

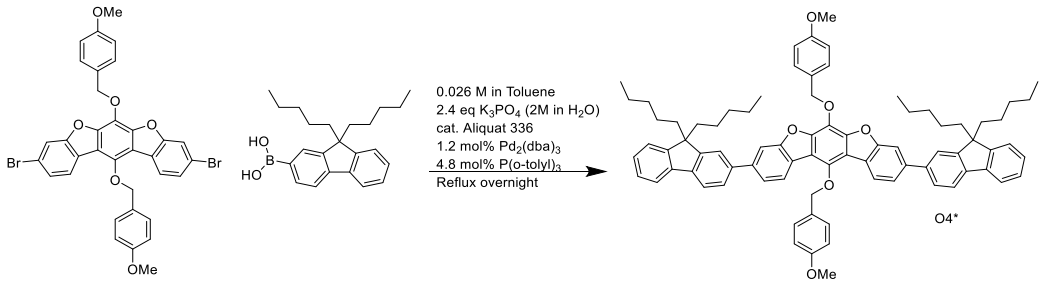


**Figure 68: Synthesis of PMB protected discrete small molecule O4*.**

This was then deprotected under the same conditions to give compound O4 (Figure 69).

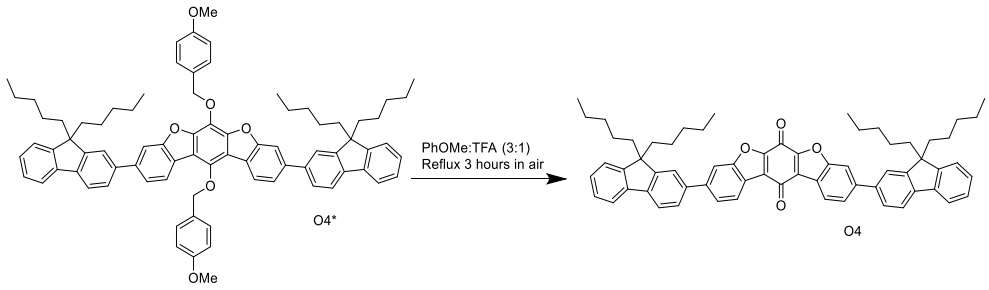


**Figure 69: Deprotection of O4* to the quinone form O4.**

$^{1}$H NMR, $^{13}$C NMR, and high-resolution mass spectroscopy confirmed the identity of compound O4 and the loss of the PMB groups. Comparison of the $^{1}$H NMR before and after deprotection are shown in Figure 70 and Figure 71 showing the loss of the PMB resonances with deprotection.

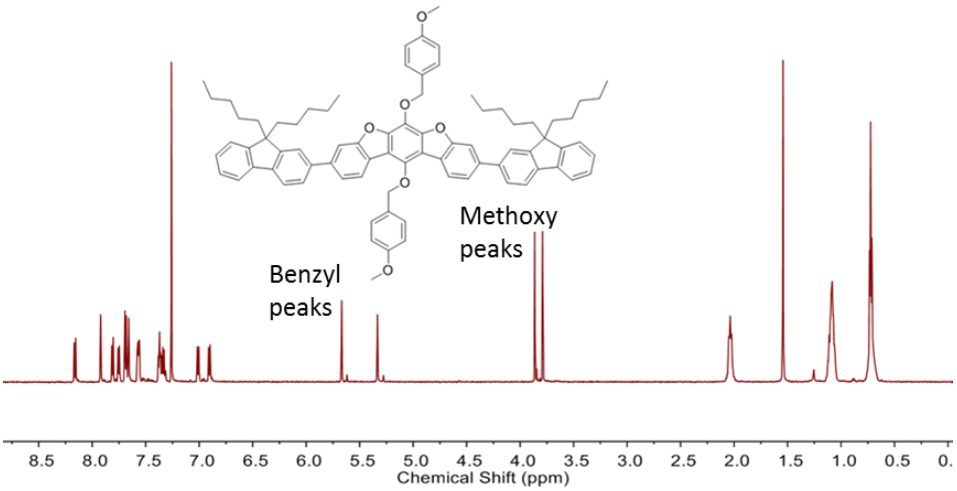


**Figure 70: $^{1}$H NMR spectrum of PMB protected O4* with distinct PMB benzyl and methoxy peaks as indicated.**

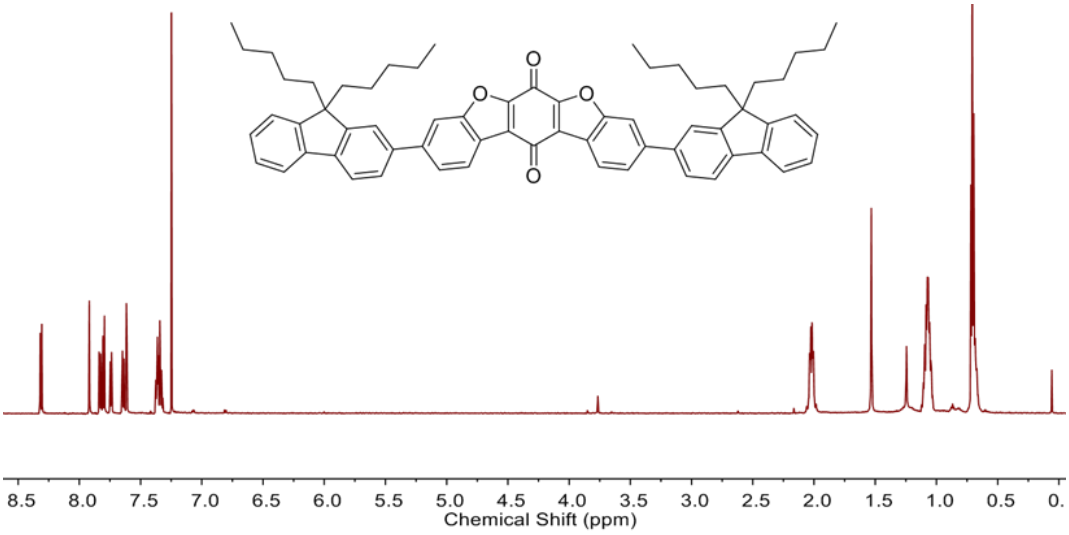


**Figure 71: $^{1}$H NMR spectrum of deprotected O4 showing lack of characteristic PMB groups.**

FTIR confirmed the appearance of a new carbonyl stretch corresponding to the quinone form upon deprotection as indicated by the arrow in Figure 72.

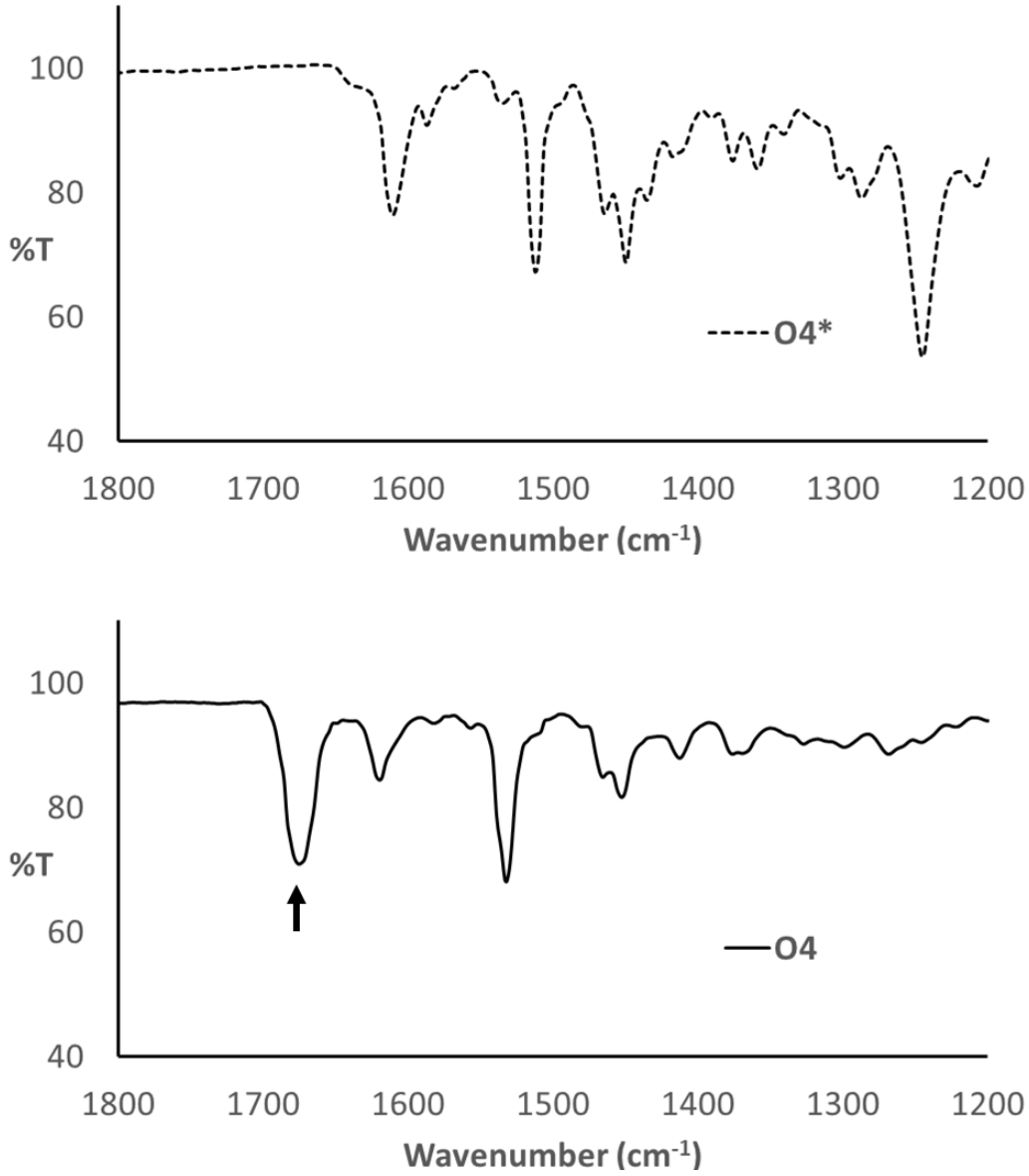


**Figure 72: FTIR spectra of PMB protected O4* and deprotected O4 showing characteristic carbonyl stretch indicated by the arrow.**

A solution of compound O4 in chlorobenzene appears purple whereas solutions of O4* in chlorobenzene are colorless. This is consistent with what was seen with P4 and is consistent with the emergence of the quinone unit (Figure 73).

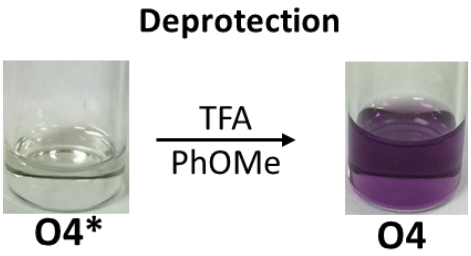


**Figure 73: Visual change corresponding with deprotection. O4* solution in chlorobenzene on the left and O4 solution in chlorobenzene on the right.**

This color change was further characterized via UV-Vis spectroscopy (Figure 73Figure 74).

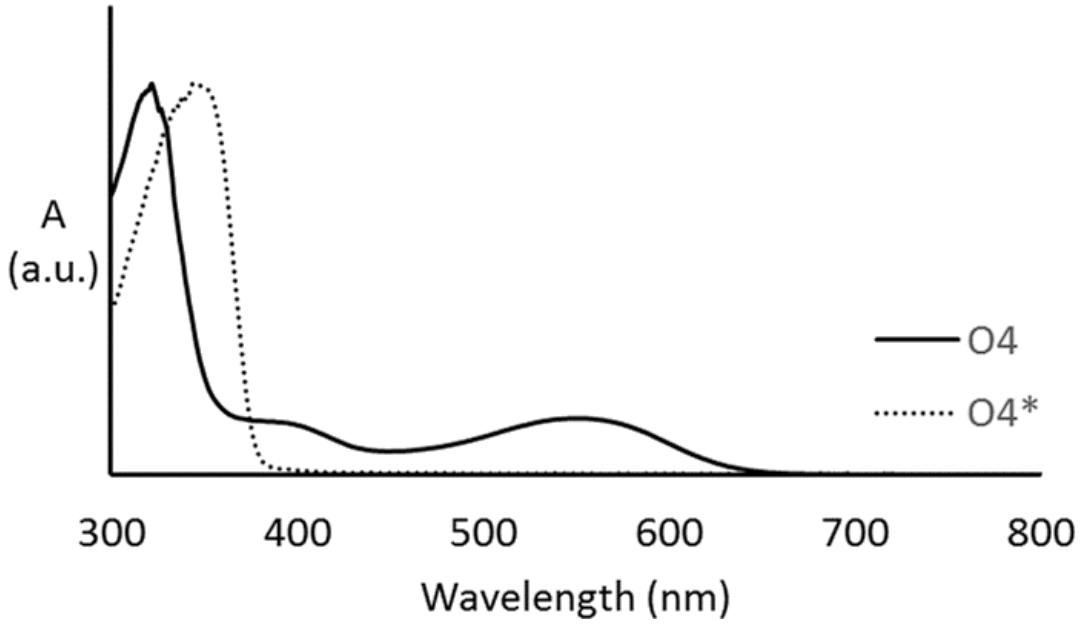


**Figure 74: Normalized absorption spectra of PMB protected O4* and deprotected O4 in chlorobenzene.**

Once again, the emergence of a secondary maximum at 552 nm was observed as well as a shift of the π- π* transition peak maximum from 345 nm in O4* to 322 nm in the deprotected O4. This is consistent with what was seen previously with P4* and P4 and further supports the idea that a node in the HOMO level is decreasing the effective conjugation length along the backbone resulting in the π- π* transition peak maximum shifting to lower wavelengths as well as the secondary maximum resulting from an intramolecular transition from the fluorene units to the quinone unit. The redox activity of the quinone unit was measure via cyclic voltammetry (CV) and is reported relative to a ferrocene/ferrocenium standard (Figure 75). The CV measurements confirmed the presence two reduction potentials at -0.8 V and -1.4 V.

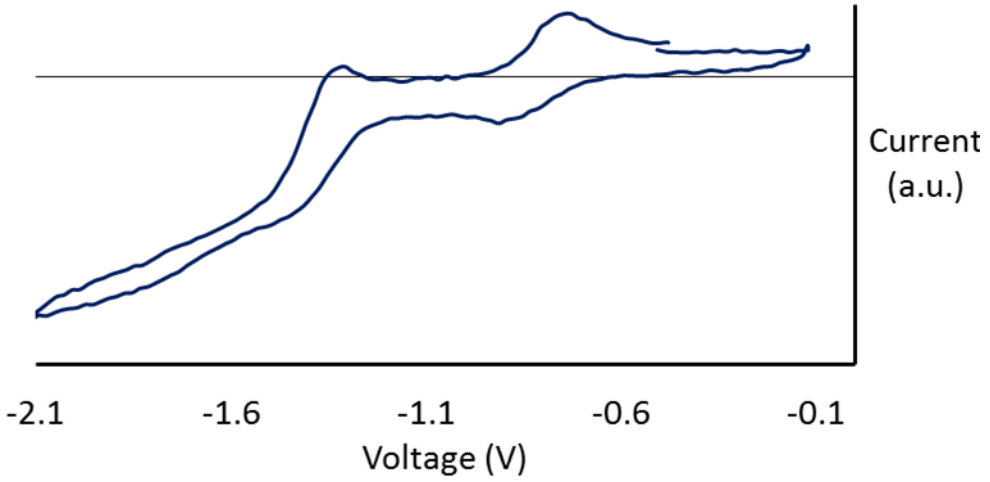


**Figure 75: Cyclic voltammetry measurements of deprotected O4 showing to reduction waves.**

Together these materials demonstrate the versatility of the M1 core. P1, P2, P3, P4*, P4, O4*, and O4 show that with a few simple chemical transformations the M1 core and its reductively alkylated BDBF analogue can be incorporated into a diverse range of materials including lower band-gap donor-acceptor polymers for transistor or OPV

applications, the wide band-gap conjugated polymer P3, and even redox active quinone materials using a novel protection/deprotection strategy. Such redox active materials could eventually find use in energy storage applications or n-type transistors[69,70,71].

## IV. Effect of Side-Chain Cyclization on Aggregation of Conjugated Polymers

Most conjugated polymers have stiff aromatic backbones that interact with each other through enthalpically favorable π-stacking interactions. Long linear or branched aliphatic side-chains are typically used to increase the entropy of mixing for these polymers in solution to enable solution processing[72]. These large floppy side-chains are able to access numerous conformations when dissolved in solution relative to them being confined in an aggregate. This difference in accessible microstates drives the entropy difference between the aggregated state and the solvated state ($\Delta S_{AS}$). With a sufficient amount of side-chain on the conjugated polymer backbone, this entropic term ($\Delta S_{AS}$) can overcome the inherent enthalpic drive for these conjugated polymers to form aggregates from solution ($\Delta H_{AS}$) and a soluble conjugated polymer will result (i.e. for a given temperature and solvent, the energetics associated with the transition from the aggregated state to the solvated state $\Delta G_{AS} = \Delta H_{AS} - T\Delta S_{AS}$ will be negative and spontaneous). Typically, this result is achieved by using an appropriately large linear or branched side-chain for a given polymer backbone to increase the $\Delta S_{AS}$ term. However, an under explored alternative approach would be to design the side-chains so as to periodically disrupt the π-stacking and thereby decrease the enthalpic term $\Delta H_{AS.}$ One way to achieve

this would be to use macrocyclic monomer units which block part of the π-face thereby reducing the backbones' ability to π-stack. Using a macrocyclic side-chain unit rather than a linear side-chain unit would have the additional effect of decreasing the entropy change $\Delta S_{AS}$ because a macrocyclic side-chain would inherently have fewer degrees of freedom than a linear side-chain of equal size due to the added topological constraint of being a loop. The decrease in $\Delta H_{AS}$ and $\Delta S_{AS}$ have opposing effects on $\Delta G_{AS}$ and the resulting degree of aggregation Figure 76 schematically depicts the hypothesized effect of linear verses cyclic side-chains.

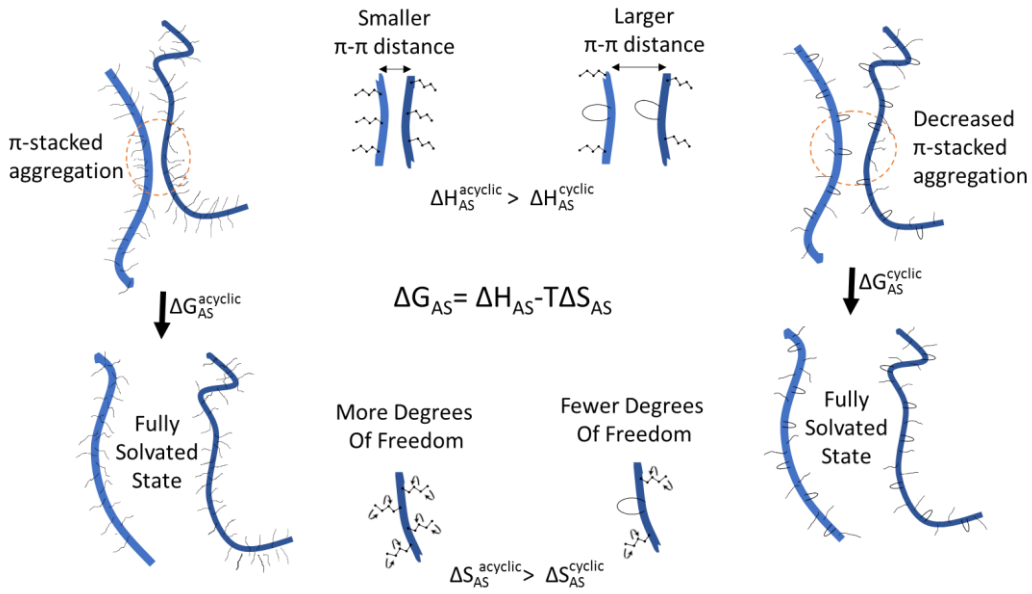


**Figure 76: Hypothesized effect of side-chain topology on conjugated polymer aggregation.**

Furthermore, the topological constraint of the macrocyclic loops will persist in the solid-state which is expected to give rise to geometrical constraints on the packing of the polymer backbones which should effect the overall morphology and material properties.

It is unclear *a priori* what morphologies will be favored by polymers containing cyclic repeat units. Some potential examples are illustrated in Figure 77.

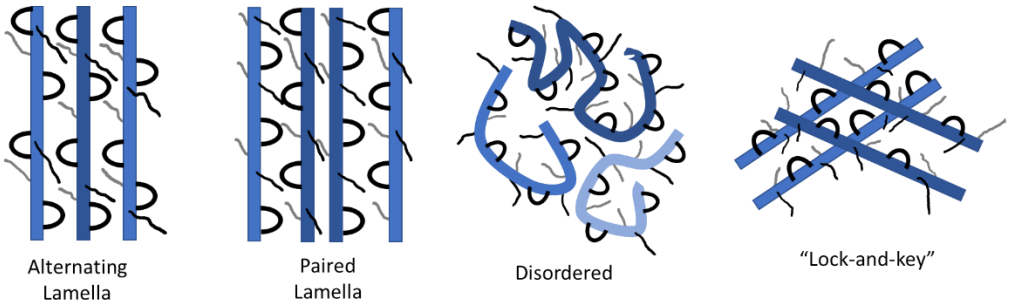


**Figure 77: Illustrations of select possible morphologies adopted by macrocyclic containing conjugated polymers.**

The first step in making and characterizing these macrocyclic containing materials was to synthesize a macrocyclic monomer unit. It was decided that benzodithiophene (BDT), as a common building block in organic electronic materials, would serve as the aromatic core[73]. It was also decided that a 10 carbon aliphatic loop connecting the two phenol oxygens would be used as this size loop had been previously reported for a hydroquinone compound[74,75,76].

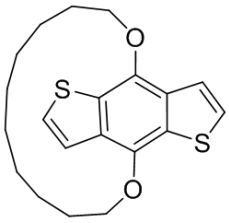


**Figure 78: Cyclic benzodithiophene (BDT) target compound.**

The first synthetic approach tried relied on a ring closing metathesis reaction as the key step (Figure 79).

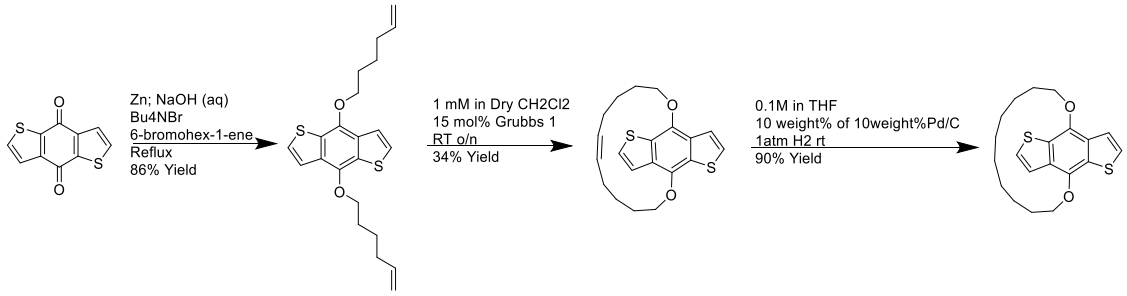


**Figure 79: Synthesis of cyclic BDT by ring closing metathesis route.**

$^{1}$H NMR and single crystal X-ray diffraction confirmed the ring closed structure (Figure 80, Figure 81).

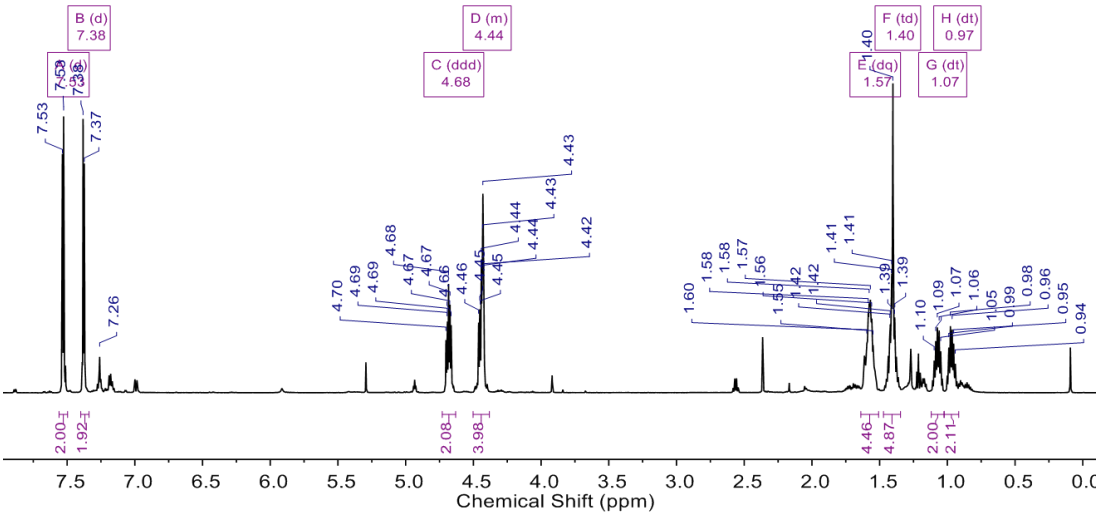


**Figure 80: $^{1}$H NMR spectrum of ring closed product**

Three views of X-ray crystal structure of cyclic olefin:

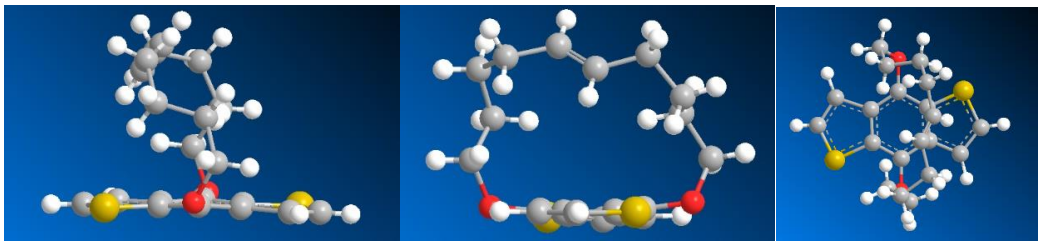

**Figure 81: Different views of the single crystal X-ray structure of the ring closed product.**

Interestingly, the olefin peak appears at δ4.68 ppm as opposed to the more typical δ5 to δ6 ppm range. This may be due to strain and/or proximity to the aromatic ring current of the BDT core. Overall, this procedure afforded the desired macrocycle in a 26% yield over 3 steps with the key step necessitating very high dilution conditions of 1 mM which decreases the scalability and practicality of the synthesis. Various tricks to try to improve this key step including the use of a conformational control element or a pseudo-phase separation strategy proved unsuccessful in improving this synthesis[76,77]. A Glaser couple route was then attempted to see if this would be a better synthetic strategy (Figure 82).

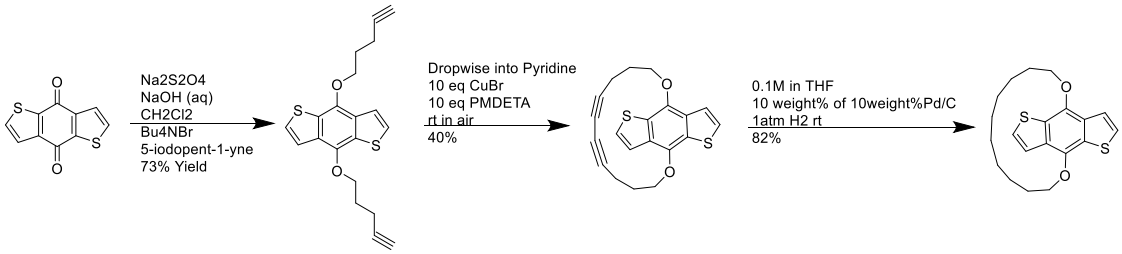


**Figure 82: Glaser coupling route to cyclic BDT.**

A couple interesting observations were made during this synthesis. First, the standard reductive alkylation conditions with Zn and NaOH (aq) did not work with the terminal alkyne. This may be due to some metal coordination to the terminal alkyne. For this reason, $Na_2S_2O_4$ in NaOH(aq) was successfully used as the reductant instead. The Glaser

coupling worked; however, the bisalkyne appeared rather strained in the X-ray crystal structure likely limiting the yield (Figure 83).

Three views of X-ray crystal structure of cyclic bisalkyne:

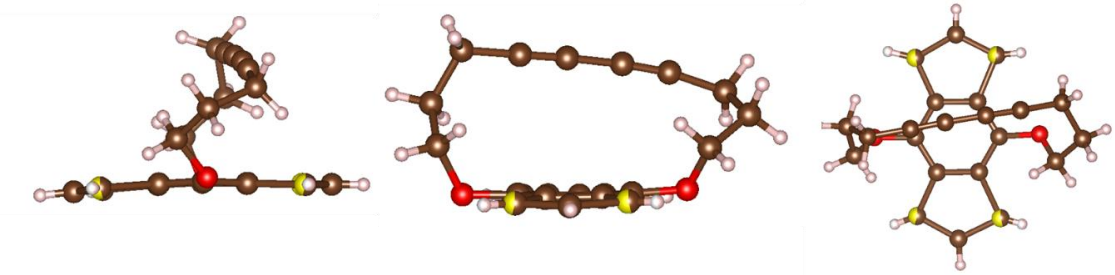

**Figure 83: Select views of the single crystal X-ray structure of the ring closed bisalkyne BDT.**

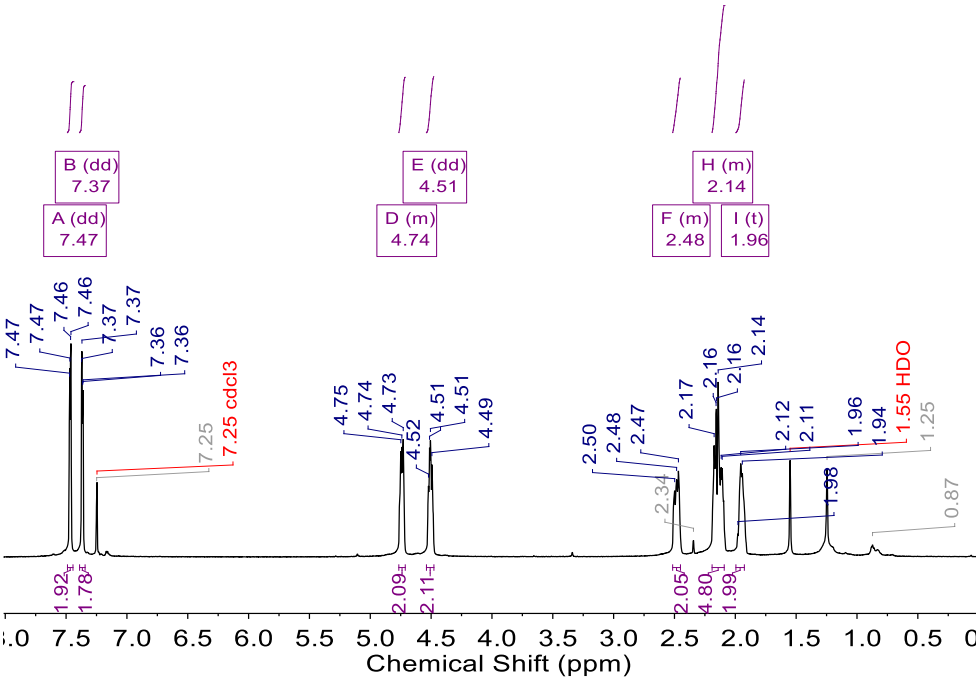


**Figure 84: $^{1}$H NMR spectrum of the ring closed bisalkyne BDT.**

Furthermore, hydrogenation of the bisalkyne with Pd/C resulted in about 15% of the acyclic derivative suggesting either a C-C activation reaction of the bisalkyne possibly

due to ring strain or an oxidative cleavage of the bisalkyne followed by generation of the acyclic derivative during the hydrogenation reaction (Figure 85)[78,79].

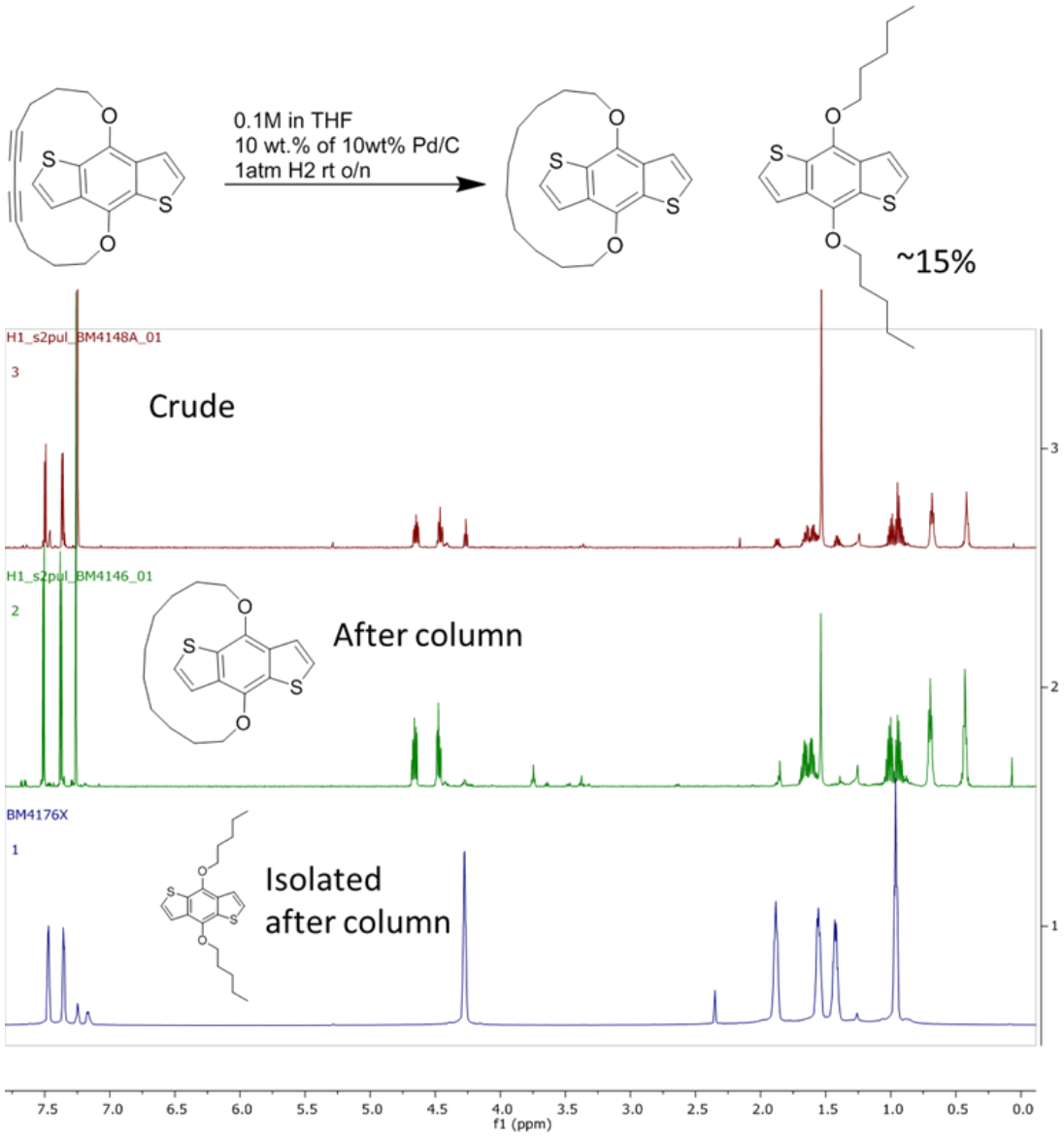


**Figure 85: Hydrogenation reaction of cyclic bisalkyne BDT showing unexpected C-bond cleavage.**

Attempts to utilize some recently developed high concentration Glaser macrocyclization conditions proved unsuccessful[80]. For these reasons, the Glaser coupling approach was

abandoned. Finally, a biphasic and bimolecular approach to the synthesis of the macrocycle was explored. The idea being to separate the BDT core as the dianionic nucleophile in one phase and have it react with the electrophilic 10 carbon bridge in another phase to form the macrocycle directly at a higher concentration than would be possible without the phase separation strategy (Figure 86).

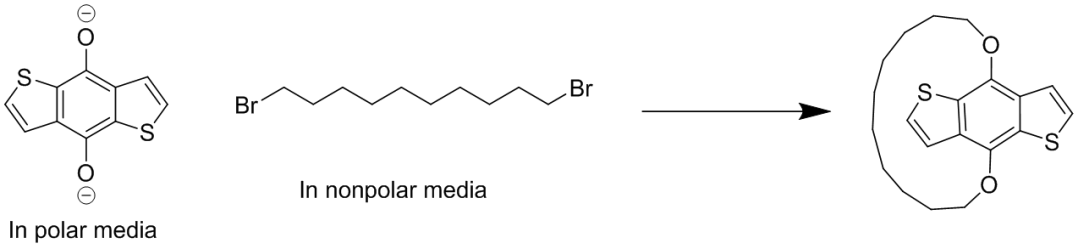


**Figure 86: Overview of macrocyclization with phase separation strategy.**

Using ethylene glycol as the polar phase and xylenes as the nonpolar phase, this route proved successful (Figure 87). The structure was verified via single crystal X-ray diffraction and NMR spectroscopy (Figure 88, Figure 89).

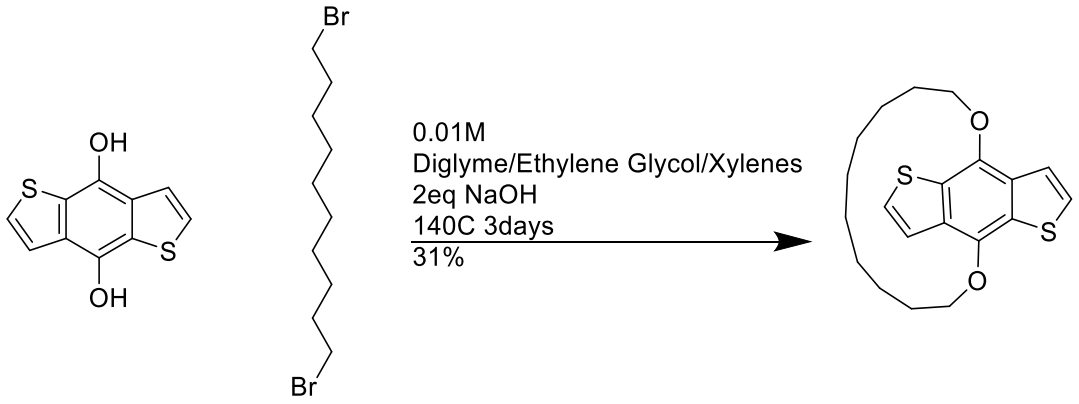


**Figure 87: Synthesis of cyclic BDT by macrophase separation strategy.**

Considering that there is only 1 step and that the concentration is 10 times higher than the 1 mM concentration used for either the ring closing metathesis approach or the Glaser coupling approach, the 31% yield was acceptable and enabled the gram scale production

of the desired cyclic BDT unit. It is interesting however to note that the selectivity of the reaction for the cyclic derivative versus acyclic oligomers was approximately 60% and the resulting 31% yield is due to the reaction not proceeding to completion. This is likely due to the fact that ethylene glycol is known to degrade into acidic byproducts at elevated temperatures even in the absence of oxygen[81]. This acid quenching of the reaction was confirmed via addition of a small amount of NaOH after completion of the reaction. This NaOH brought back the red color associated with the deprotonated dianion of BDT. This suggests that future optimization of this reaction could be achieved by using a different solvent system. One possible improvements would be the use of a DMF/Water/Hexanes system and possibly using Zn NaBr as a nonnucleophilic reductant to generate the dianion directly from the quinone form.

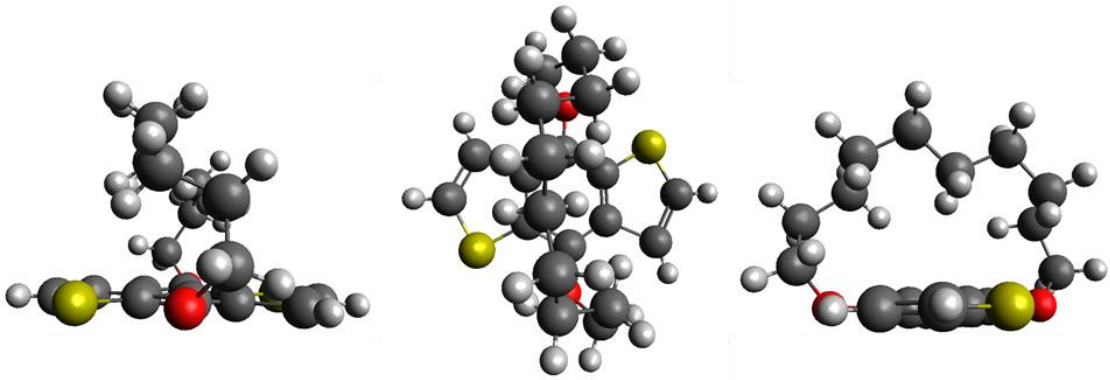

**Figure 88: Select views of the single crystal X-ray structure of the cyclic BDT synthesized via the phase separation strategy.**

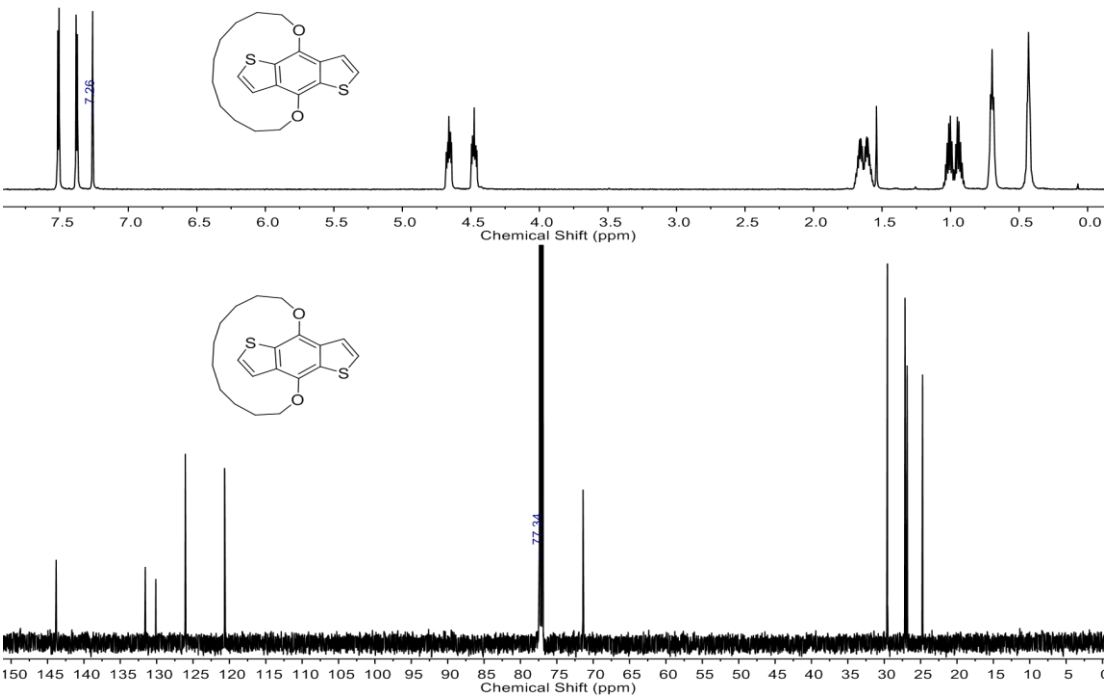


**Figure 89: $^{1}$H and $^{13}$C NMR spectra of the cyclic BDT synthesized via the phase separation strategy.**

The $^{1}$H NMR is interesting. In particular, the bridge head protons are split due to their restricted position and different chemical environment. Additionally, the methylene resonances at δ0.7 and δ0.43 ppm are unusually upfield and may result from these proton's orientation relative to the BDT core and its aromatic ring current. The acyclic BDT derivative can then be made similarly to a known procedure (Figure 90).

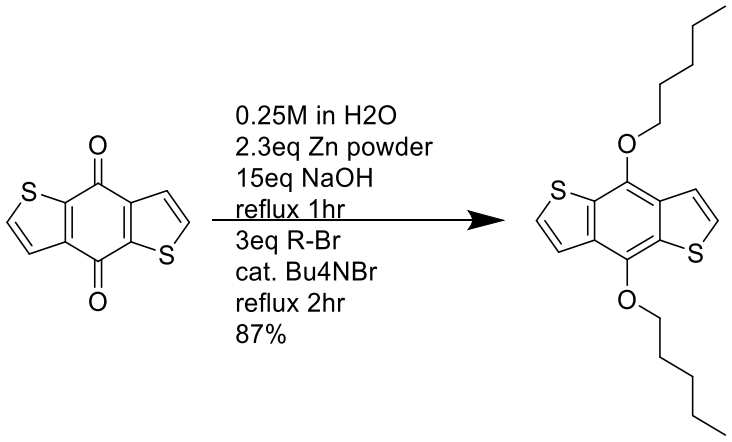


**Figure 90: Synthesis of acyclic BDT analogue.**

It is important to point out that the acyclic derivative is almost an exact isomer of the cyclic compound differing only by the connectivity of the side-chain and the difference of the two hydrogen atoms that this connectivity entails. Two views of the single crystal X-ray diffraction results illustrate the difference between the cyclic and acyclic derivatives (Figure 91)

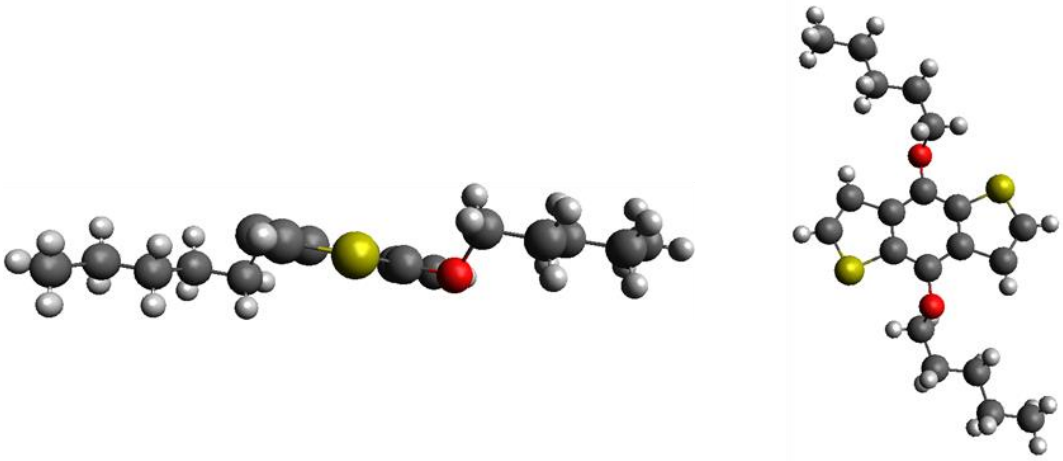

**Figure 91: Select views of the single crystal X-ray structure of the acyclic BDT.**

Additionally, the $^{1}$H NMR for the acyclic derivative does not show either the unusual splitting seen in the cyclic derivative or the unusual upfield resonances (Figure 92).

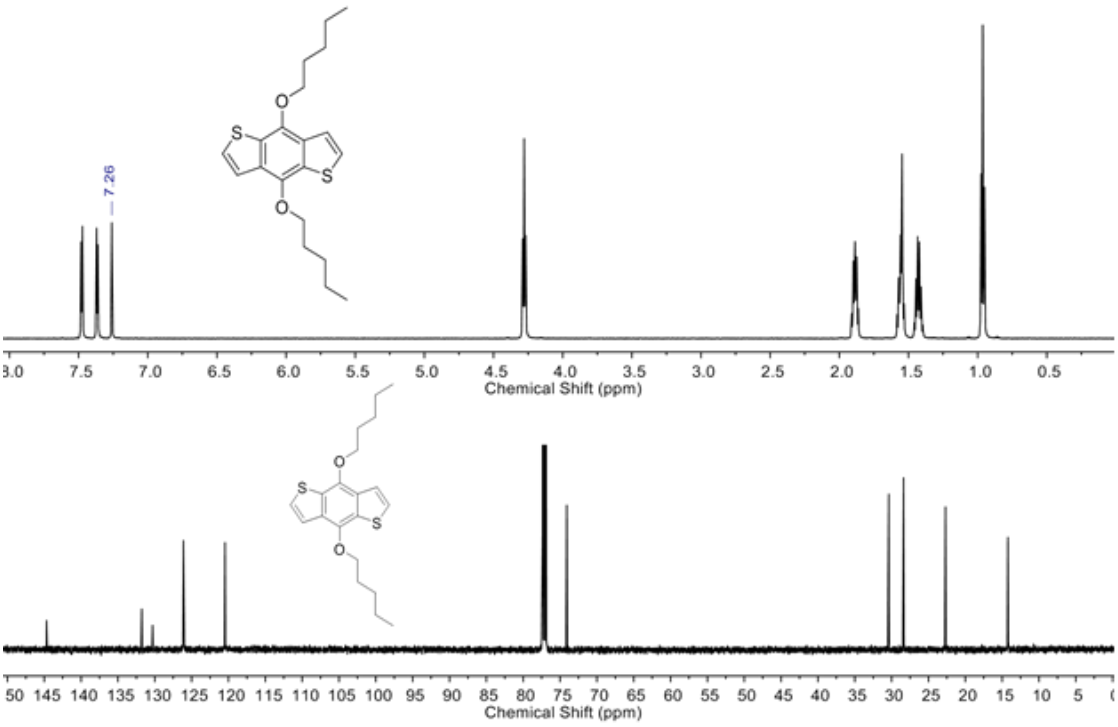


**Figure 92: $^{1}$H and $^{13}$C NMR spectra of the acyclic BDT.**

The crystal structures of the cyclic and acyclic derivatives show that the macrocyclic loop blocks one of the two π-faces in the cyclic derivative whereas both of the π-faces of the acyclic derivative remain open. The effect of this macrocyclic loop on the packing structure of these materials in the solid state can be seen from the single crystal X-ray diffraction data (Figure 93 to Figure 99). The cyclic derivative has a triclinic unit cell with several molecules in it and an overall density of 1.496 g/cm$^3$. The acyclic derivative has a monoclinic unit cell with the molecules adopting a herring bone type packing structure and an overall density of 1.269 g/cm$^3$.

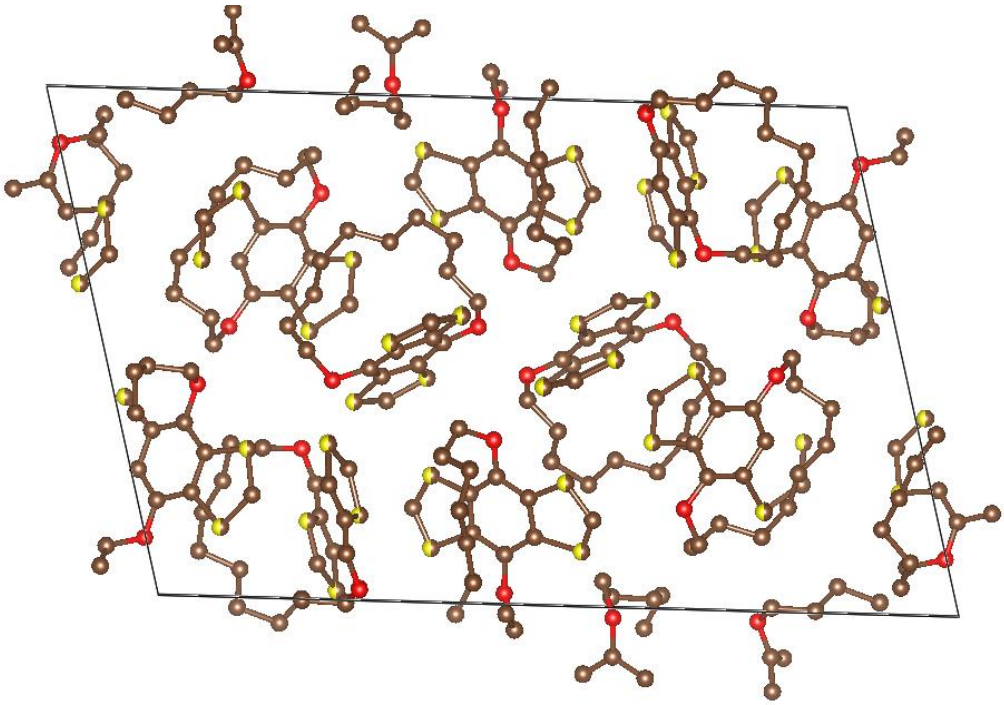

**Figure 93: View down the a axis of cyclic derivative's crystal structure.**

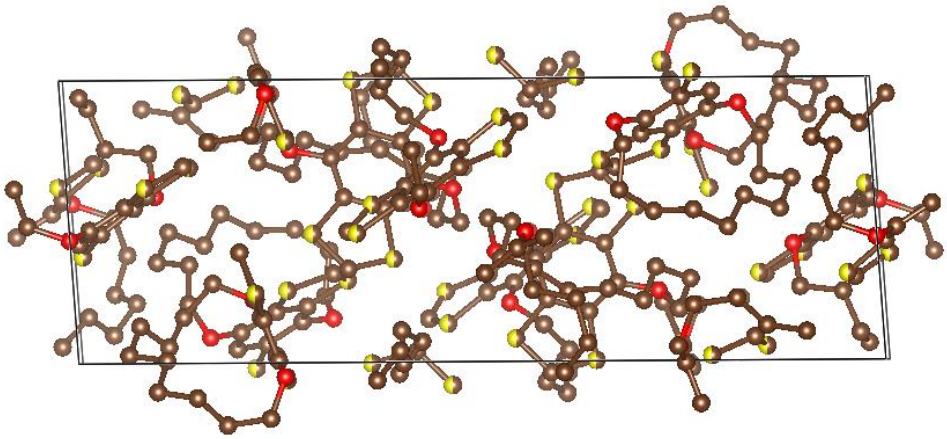

**Figure 94: View down the b axis of cyclic derivative's crystal structure.**

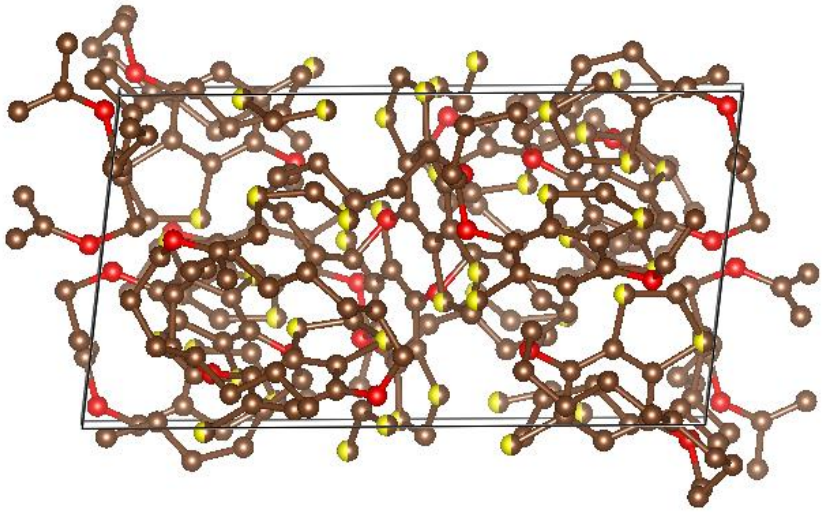

**Figure 95: View down the c axis of cyclic derivative's crystal structure.**

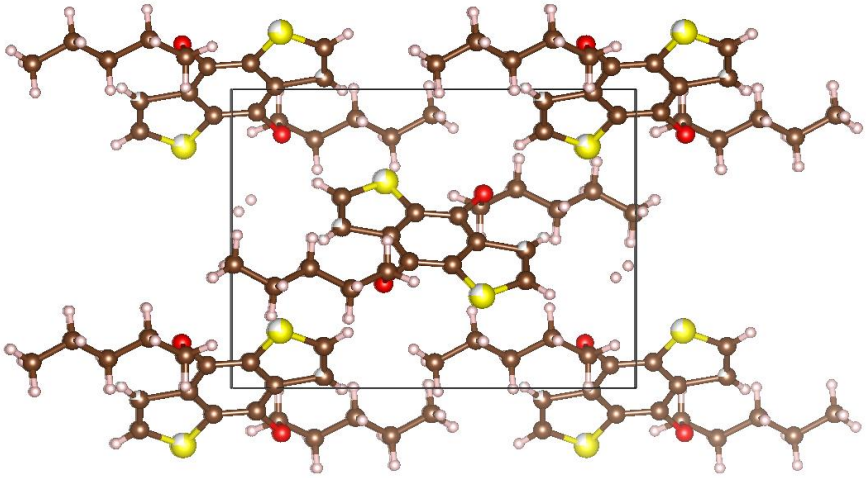

.

**Figure 96: View down the a axis of acyclic derivative's crystal structure.**

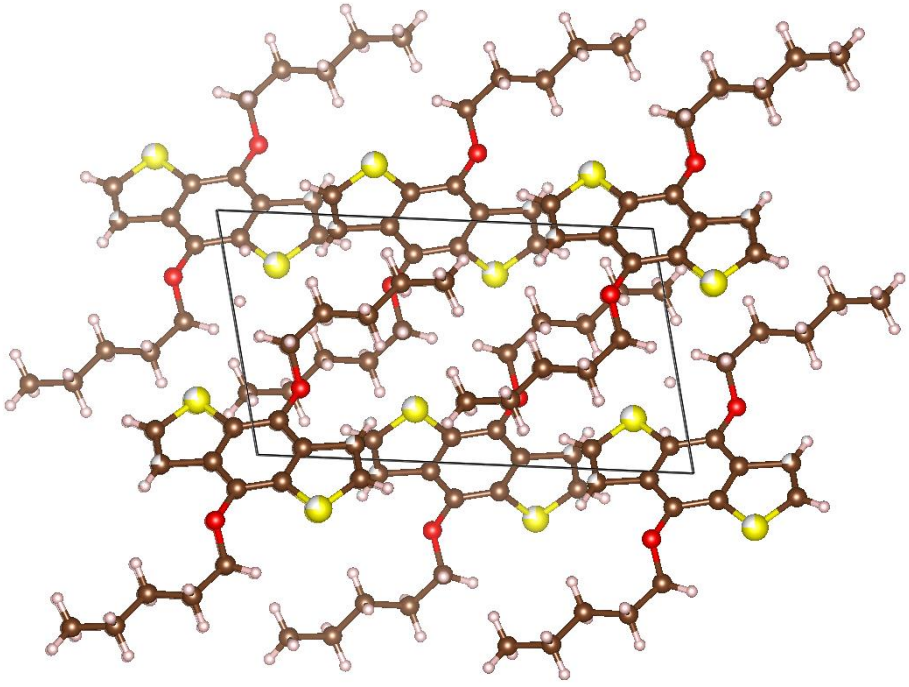

**Figure 97: View down the b axis of acyclic derivative's crystal structure.**

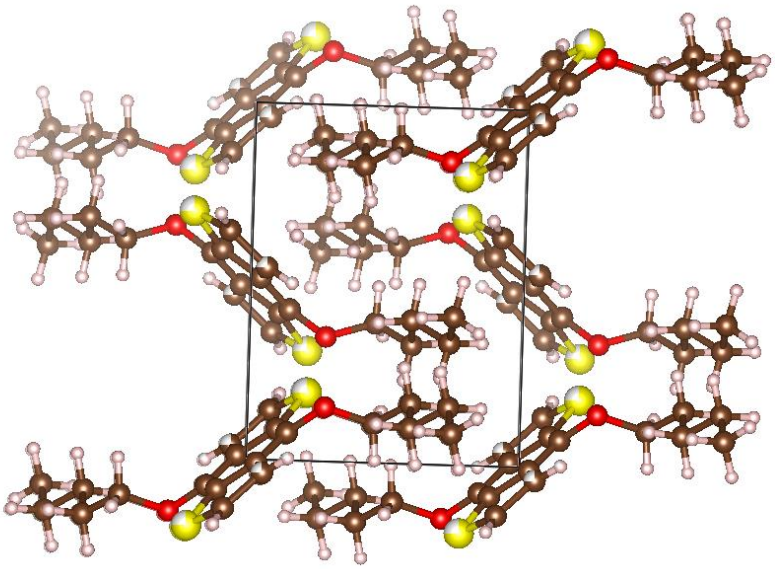

**Figure 98: View down the c axis of acyclic derivative's crystal structure.**

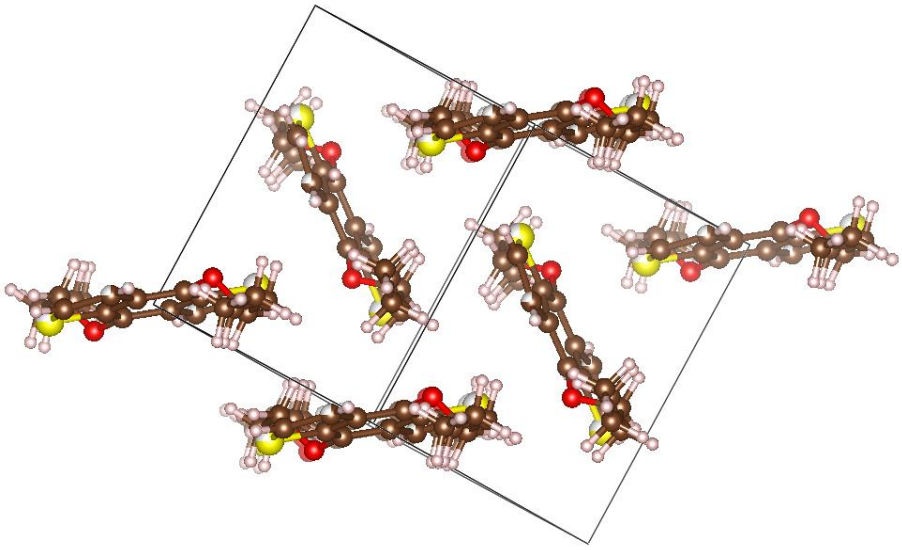

**Figure 99: Off axis view of acyclic derivative showing the herring bone packing structure.**

The thermodynamic properties of these materials were then examined via differential scanning calorimetry (Figure 100, Figure 101). The heating and cooling was conducted

at 1°C/min. The second cycle is shown. Each cycle was substantially the same to within 2°C and 1 J/g.

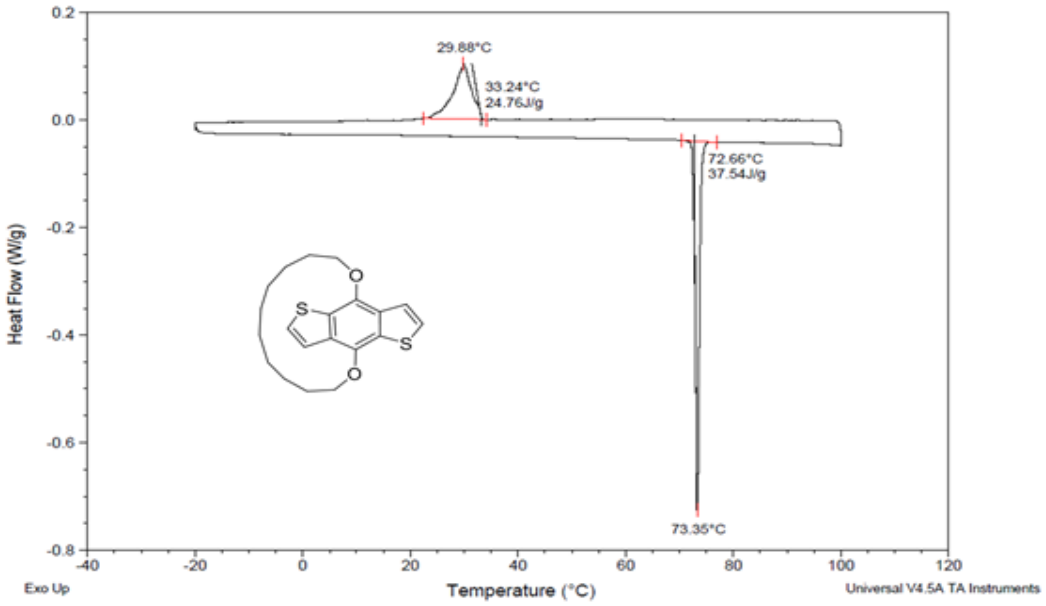


**Figure 100: DSC trace for the cyclic BDT.**

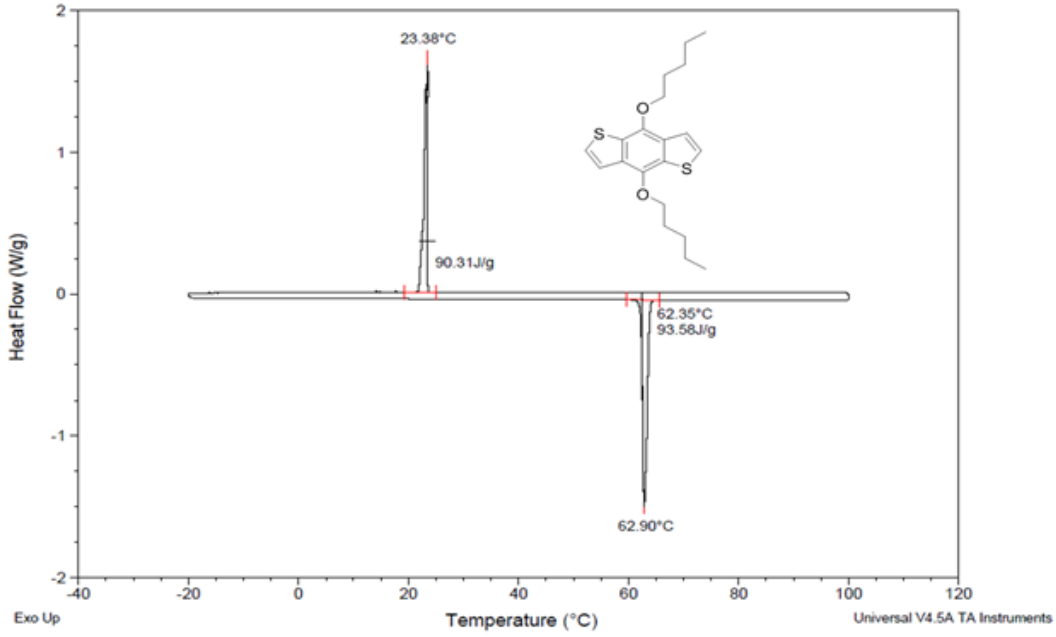


**Figure 101: DSC trace for the acyclic BDT.**

The cyclic derivative shows a melting point at 73ºC with a melting enthalpy of 37.54 J/g or 13.5 kJ/mol. The entropy of melting can be calculated from $0=\Delta G_m= \Delta H_m-T\Delta S_m$ to give 39.7 J/(mol K). The acyclic derivative is seen to have a melting transition at 63ºC with a melting enthalpy of 33.9 kJ/mol and a melting entropy of 102 J/(mol K). It is interesting to point out that while the cyclic derivative has a higher density (cyclic: 1.496 g/cm$^3$ vs acyclic: 1.269 g/cm$^3$), the acyclic derivative has a higher melting enthalpy. This demonstrates the importance of the π-π interactions because if one were to assume a simple spherically symmetric potential for each of the molecules, the denser derivative would have the larger enthalpy of melting in contrast to what is seen here experimentally. Furthermore, the entropy of melting for the acyclic derivative is seen to be higher than that of the cyclic derivative [acyclic: 102 J/(mol K) vs cyclic: 39.7 J/ (mol K)]. This is in agreement with the hypothesis outline above wherein the linear side-chains of the acyclic derivative should have a larger change in the number of accessible degrees of freedom upon melting as compared to the more constrained cyclic derivative. This is the first piece of support of the thermodynamic model for the effect of side-chain topology discussed at the beginning of this chapter. In order to further understand how this macrocycle effects both the structure and thermodynamics of organic electronic materials at the molecular level, a second series of cyclic and acyclic derivatives was prepared. The cyclic or acyclic BDT core was modified via the addition of two 3-hexyythiophene units according to the synthetic scheme shown in Figure 102.

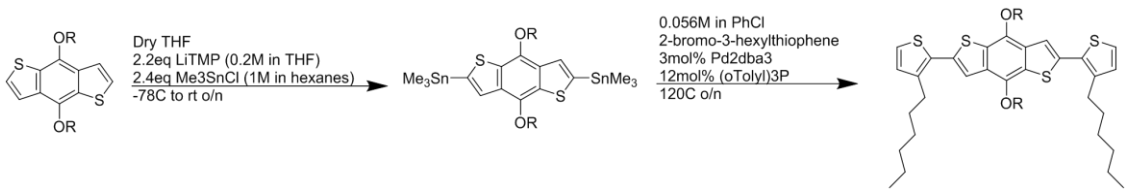


**Figure 102: Synthesis of cyclic and acyclic TBDTT derivatives.**

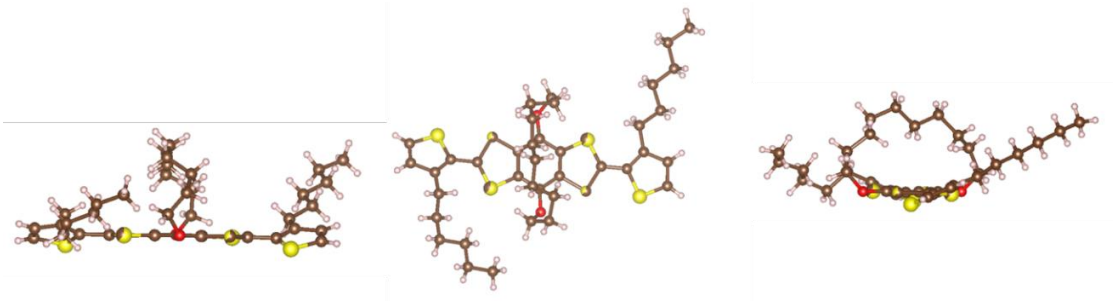

**Figure 103: Three molecular views of the cyclic derivative from the X-ray crystal structure.**

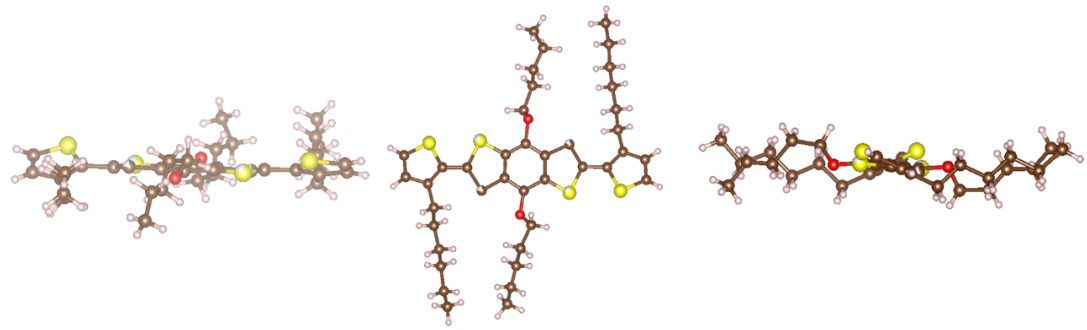

**Figure 104: Three molecular views of the acyclic derivative from the X-ray crystal structure.**

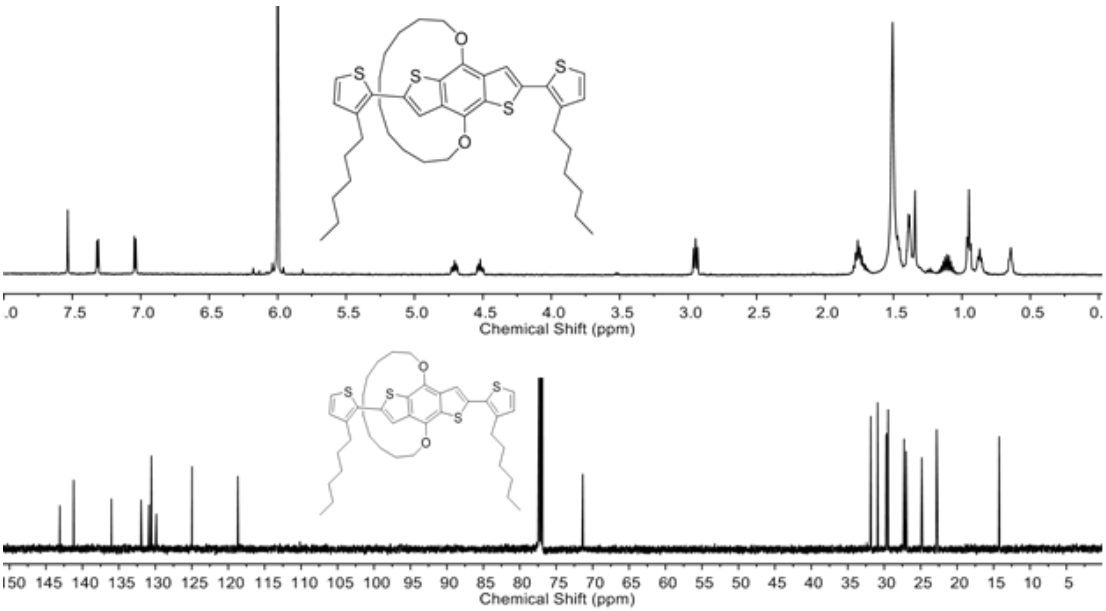


**Figure 105: $^{1}$H and $^{13}$C NMR spectra for the cyclic derivative.**

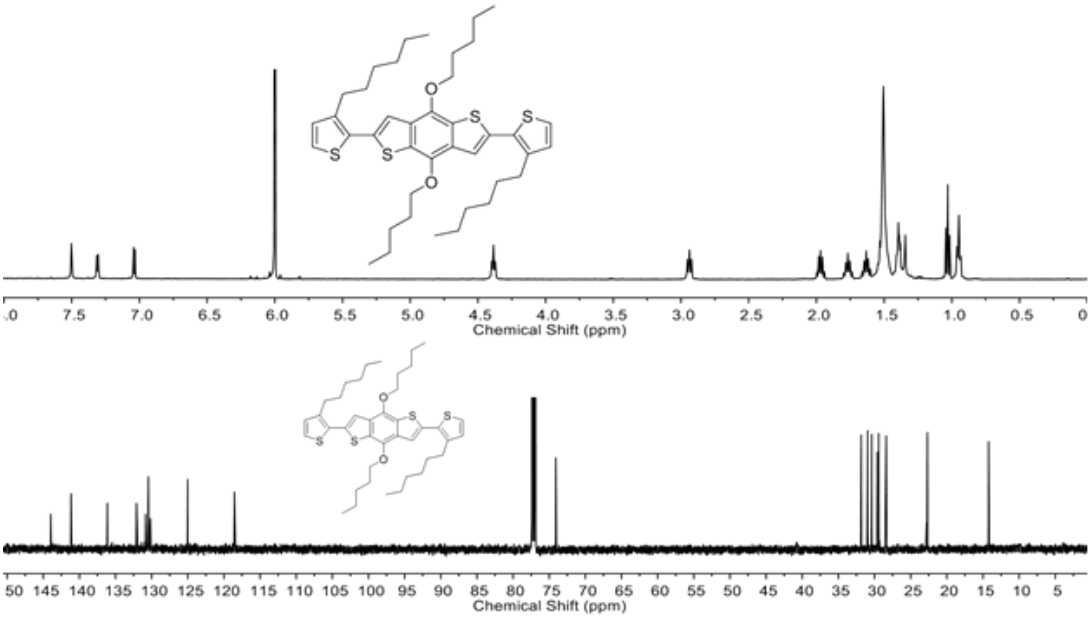


**Figure 106: $^{1}$H and $^{13}$C NMR spectra for the acyclic derivative.**

Once again, it can be seen from the crystal structures that the macrocyclic loop blocks one side of the π-face whereas that of the acyclic derivative is open on both sides (Figure 103, Figure 104). Additionally, the $^{1}$H NMR for the cyclic derivative again shows the

extra splitting for protons in the ring as well as the upfield methylene resonances (Figure 105, Figure 106). The difference in packing structure can then be seen in the unit cells of these respective materials (Figure 107 through Figure 113).

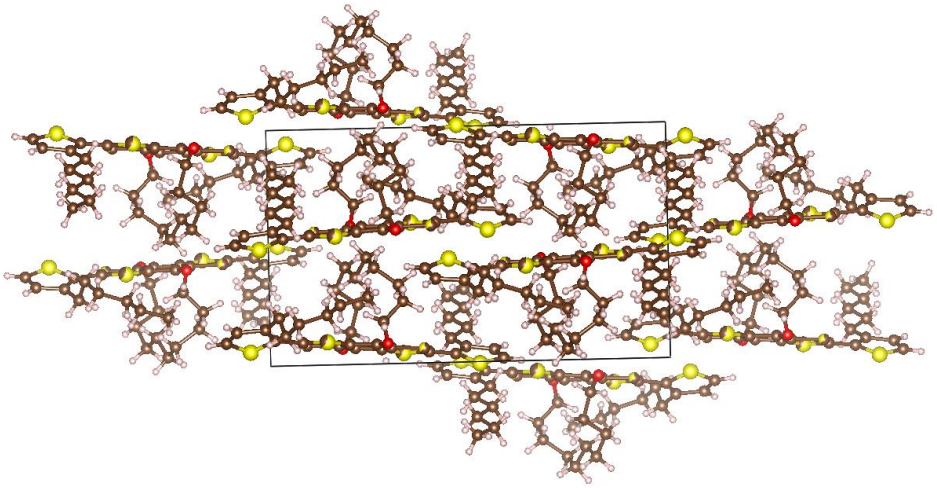

**Figure 107: View down the a axis for the cyclic derivative.**

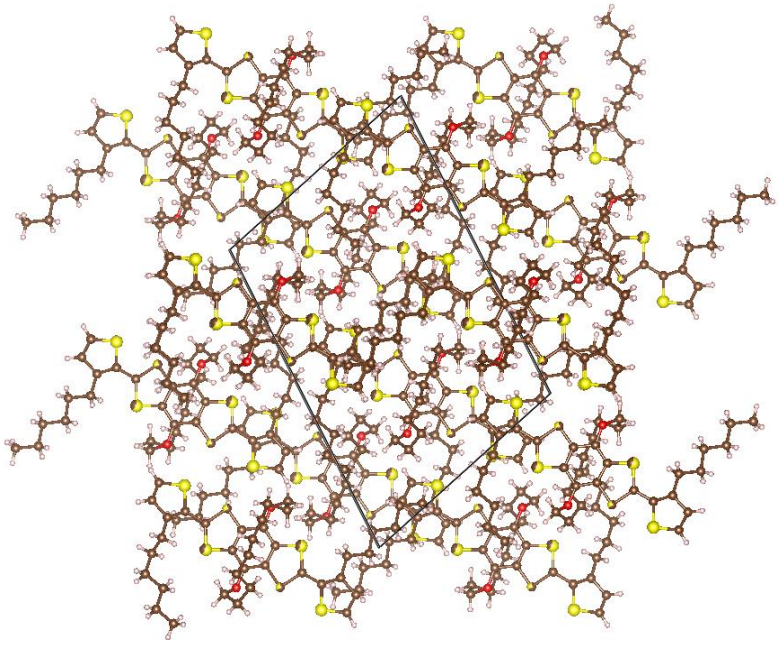

**Figure 108: View down the b axis for the cyclic derivative.**

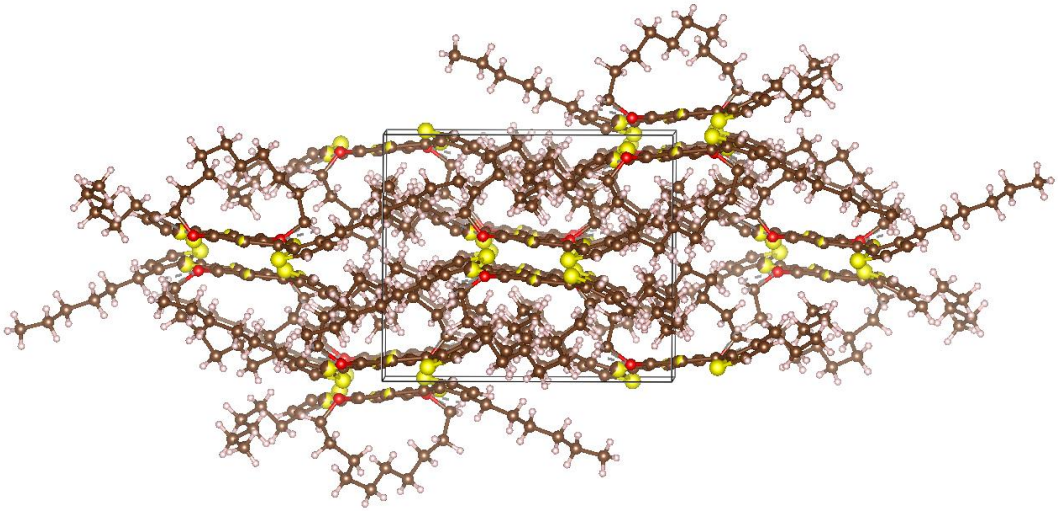

**Figure 109: View down the c axis for the cyclic derivative.**

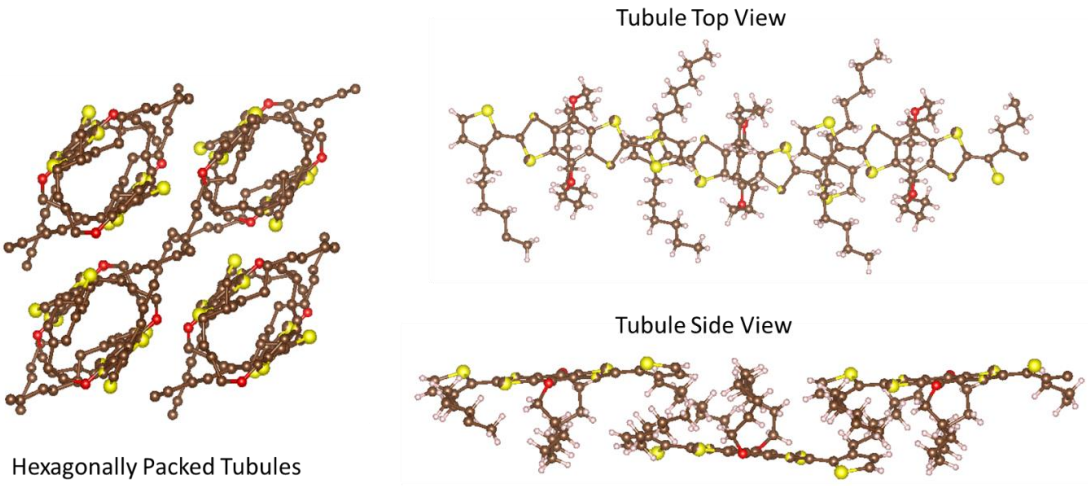


**Figure 110: Off axis view showing a hexagonal packing of tubules where the long axis of each tubule is made up of the long axis of each molecule with the loop alternating up and down as shown, and two isolated views of a three molecules in a tubule.**

The acyclic derivative was seen to pack in a different morphology. The view down the a axis shows that the acyclic molecules pack in more of a layered structure where each layered sheet has the molecules rotated relative to the sheet above (Figure 111).

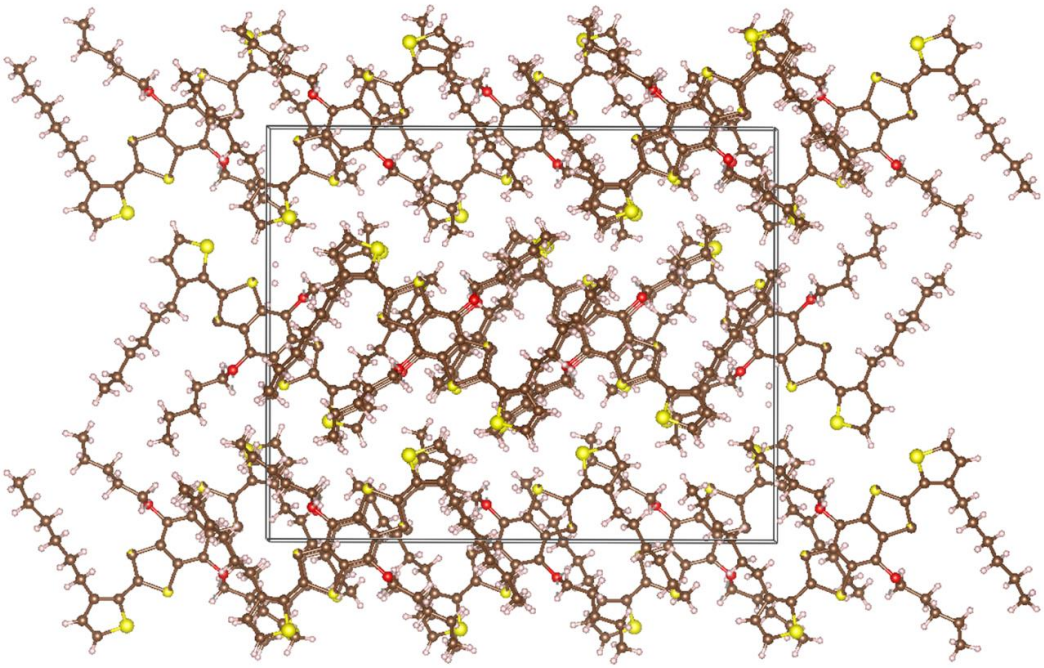

**Figure 111: View down the a axis for the acyclic derivative.**

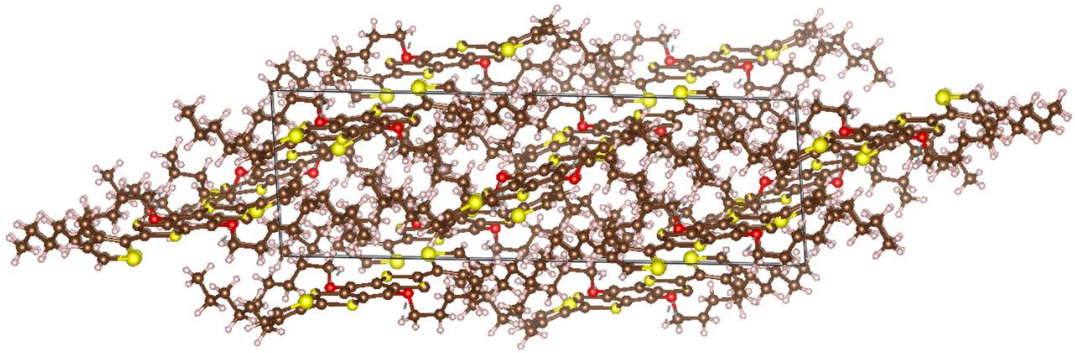

**Figure 112: View down the b axis for the acyclic derivative.**

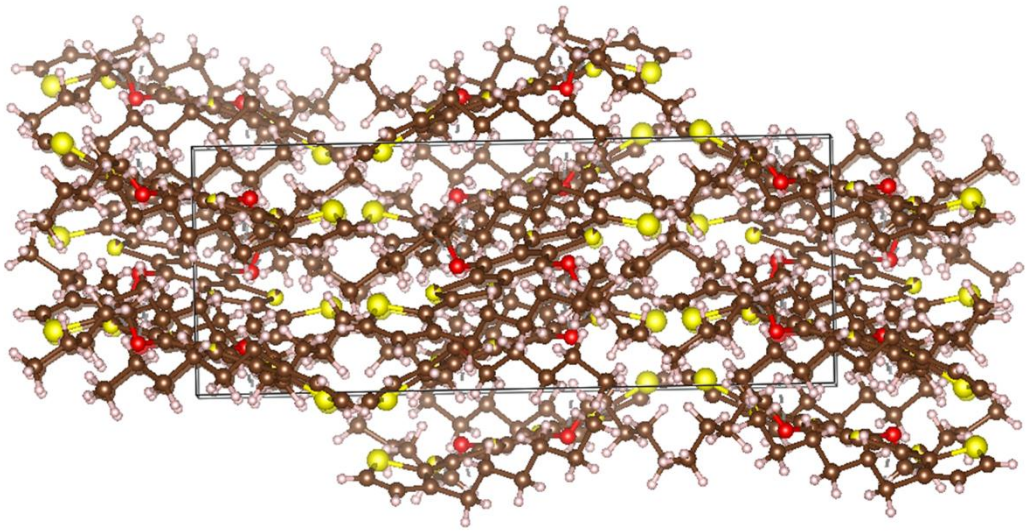

**Figure 113: View down the c axis for the acyclic derivative.**

The density of the acyclic molecule's crystal structure is much more dense than that of the cyclic derivative (acyclic: 2.513 g/cm$^3$ cyclic: 1.219 g/cm$^3$). Once again, the enthalpy and entropy of melting was higher for the acyclic derivative [acyclic: $\Delta H_m$=46.6 kJ/mol and $\Delta S_m$=146 $J/(mol{\cdot}K)$; cyclic $\Delta H_m$=31.8 kJ/mol and $\Delta S_m$=90.1 $J/(mol{\cdot}K)$]. These findings conform with what was hypothesized wherein the macrocyclic loop decreases the π-stacking thereby reducing the enthalpic drive to crystallization and the reduced degrees of freedom due to the topological constrain of the macrocycle results in a decreased entropic change on melting.

In order to understand how the cyclic unit affects the properties of conjugated polymers, the cyclic or acyclic unit was incorporated as a comonomer in a series of conjugated polymers (Figure 114).

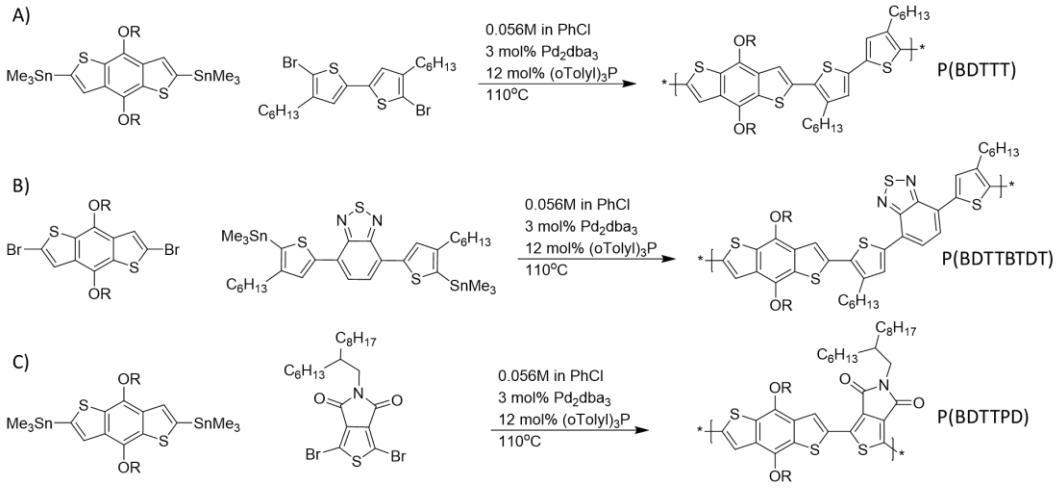


**Figure 114: Synthesis of cyclic or acyclic BDT containing conjugated polymers.**

The P(BDTTT) polymers have the exact repeat unit as the small molecule TBDTT derivatives studied above, and the P(BDTTBTDT) polymers have this TBDTT unit along with the benzothiadiazole unit. The P(BDTTPD) polymers have just the cyclic or acyclic BDT unit as a copolymer with the thienopyrroledione (TPD) unit. P(BDTTPD) polymers are a class of well-known OPV materials which have been known to display interesting morphologies including lamellar structures and even a two-dimensional cross-hatched structure (citations). These polymers were synthesized via a Stille coupling procedure wherein the aryl dibromide and aryl distannane were added to a dry Schlecnk flask in a 1:1 molar ratio followed by the appropriate amount of dry chlorobenzene. The mixture was degassed via three freeze-pump-thaw cycles and the $Pd_2dba_3$ and tri(o-tolyl)phosphine were added against a flow of argon. The mixture was then heated to 110$^o$C for 2 days. Afterwards, the reaction was allowed to cool to room temperature before being diluted with dichlorobenzene and precipitated in methanol. The precipitate was collected via filtration and the crude material was washed in a Soxhlet with acetone followed by hexanes. Additional washing and elution steps were specific to each polymer.

Different Soxhlet fractions were collected so as to obtain different molecular weight fractions for some of the materials. Testing these different molecular weight fractions helped to control for any observations which made be dependent on molecular weight. The two different chloroform fractions of the acyclic P(BDTTPD) were the result of two

Molecular Weight and Dispersity for Different Polymer Fractions

| Polymer | BDT | $M_n$ | $Đ$ | *Fraction* |
|---|---|---|---|---|
| **P(BDTTT)** | Acyclic | 49 | 2.0 | PhCl |
| **P(BDTTT)** | Cyclic | 31 | 2.2 | PhCl |
| **P(BDTTBTDT)** | Acyclic | 14 | 2.3 | PhCl |
| **P(BDTTBTDT)** | Acyclic | 25 | 2.3 | oDCB |
| **P(BDTTBTDT)** | Cyclic | 25 | 2.1 | PhCl |
| **P(BDTTPD)** | Acyclic | 7.0 | 3.0 | $CHCl_3$ |
| **P(BDTTPD)** | Acyclic | 7.1 | 2.7 | $CHCl_3$ |
| **P(BDTTPD)** | Cyclic | 3.1 | 1.4 | $CH_2Cl_2$ |
| **P(BDTTPD)** | Cyclic | 7.8 | 1.6 | $CHCl_3$ |
| **P(BDTTPD)** | Cyclic | 18 | 2.0 | PhCl |

Molecular weights were measured via gel permeation chromatography (150 °C in 1,2,4-trichlorobenzene) and reported relative to polystyrene standards in kDa.

**Figure 115: Table of Soxhlet fractions and corresponding molecular weights.**

different reactions. In addition to the GPC measurements, the successful polymerization of these materials was confirmed via $^1$H NMR (Figure 117, Figure 118, Figure 119). The upfield methylene peaks of the cyclic unit can be seen in all of the cyclic polymer derivatives. Additionally, the splitting of the bridge-head protons can be seen in the cyclic P(BDTTT) and P(BDTTBTDT) derivatives but not in the P(BDTPD). This is probably due to aggregation of the much more polar P(BDTTPD) material which, even at 120$^o$C in TCE-d2, showed a significant amount of broadening of the aromatic protons which is characteristic of aggregation for these types of materials.

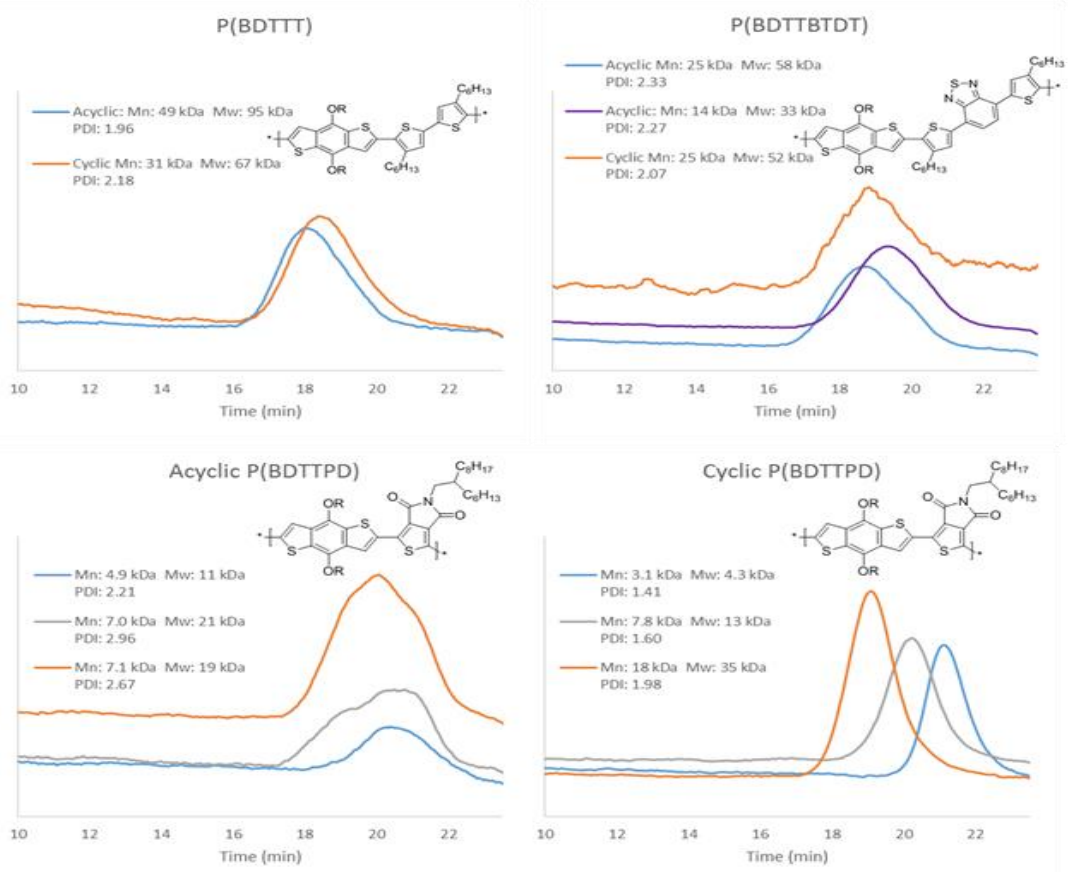


**Figure 116: GPC traces (1,2,4-trichlorobenzene 150ºC).**

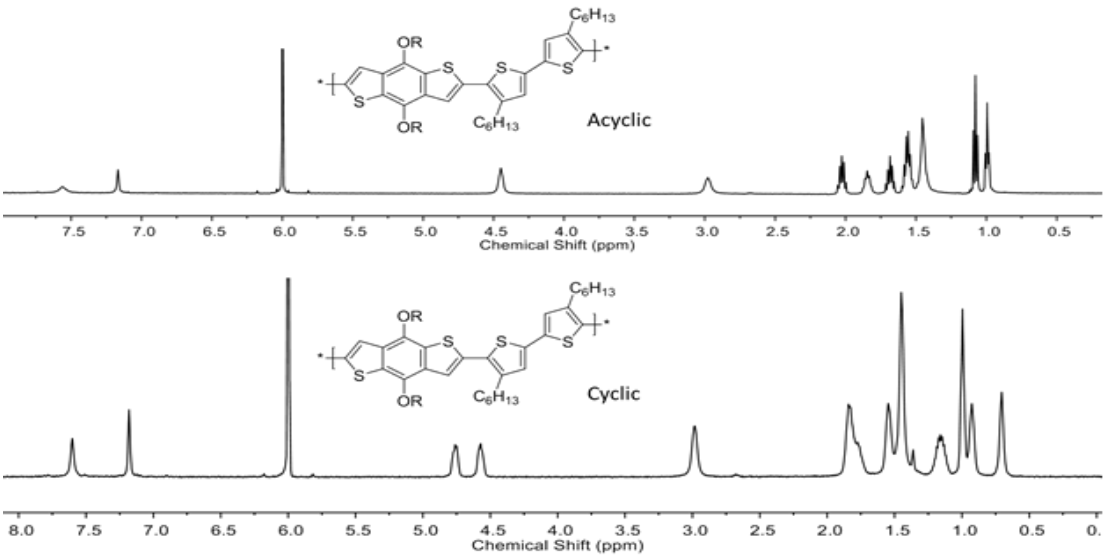


**Figure 117: $^{1}$H NMR spectra (TCE-d2 120ºC) of cyclic and acyclic P(BDTTT).**

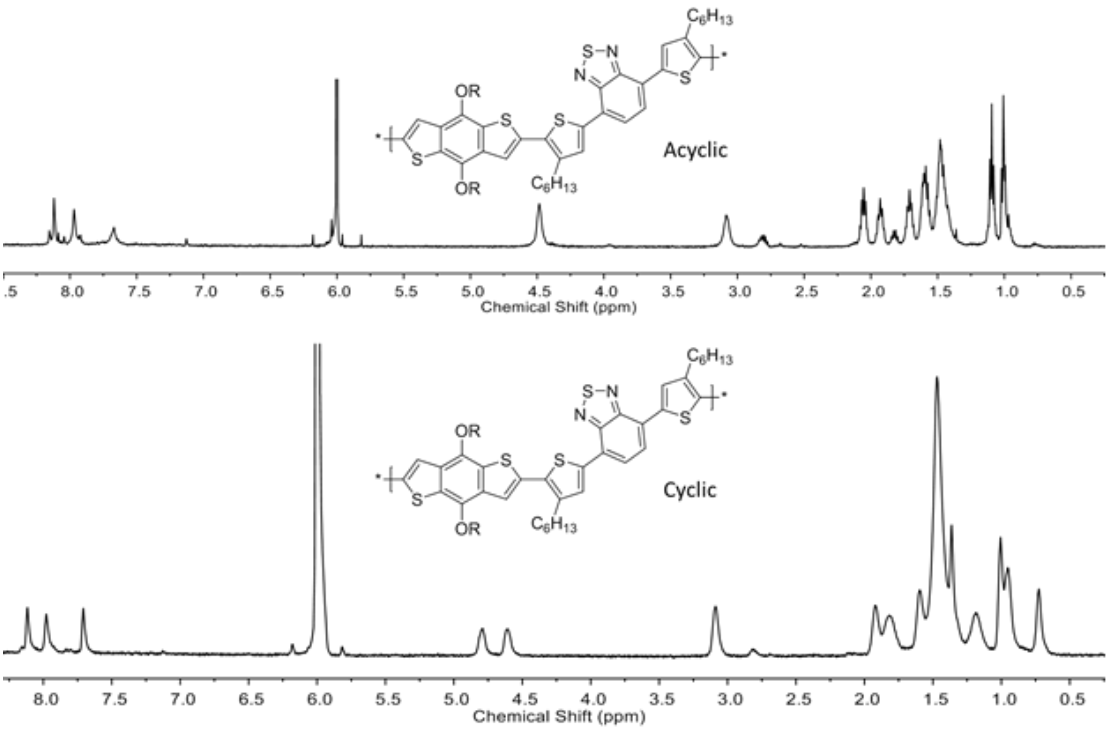


**Figure 118: $^{1}$H NMR spectra (TCE-d2 120ºC) of cyclic and acyclic P(BDTTBTDT).**

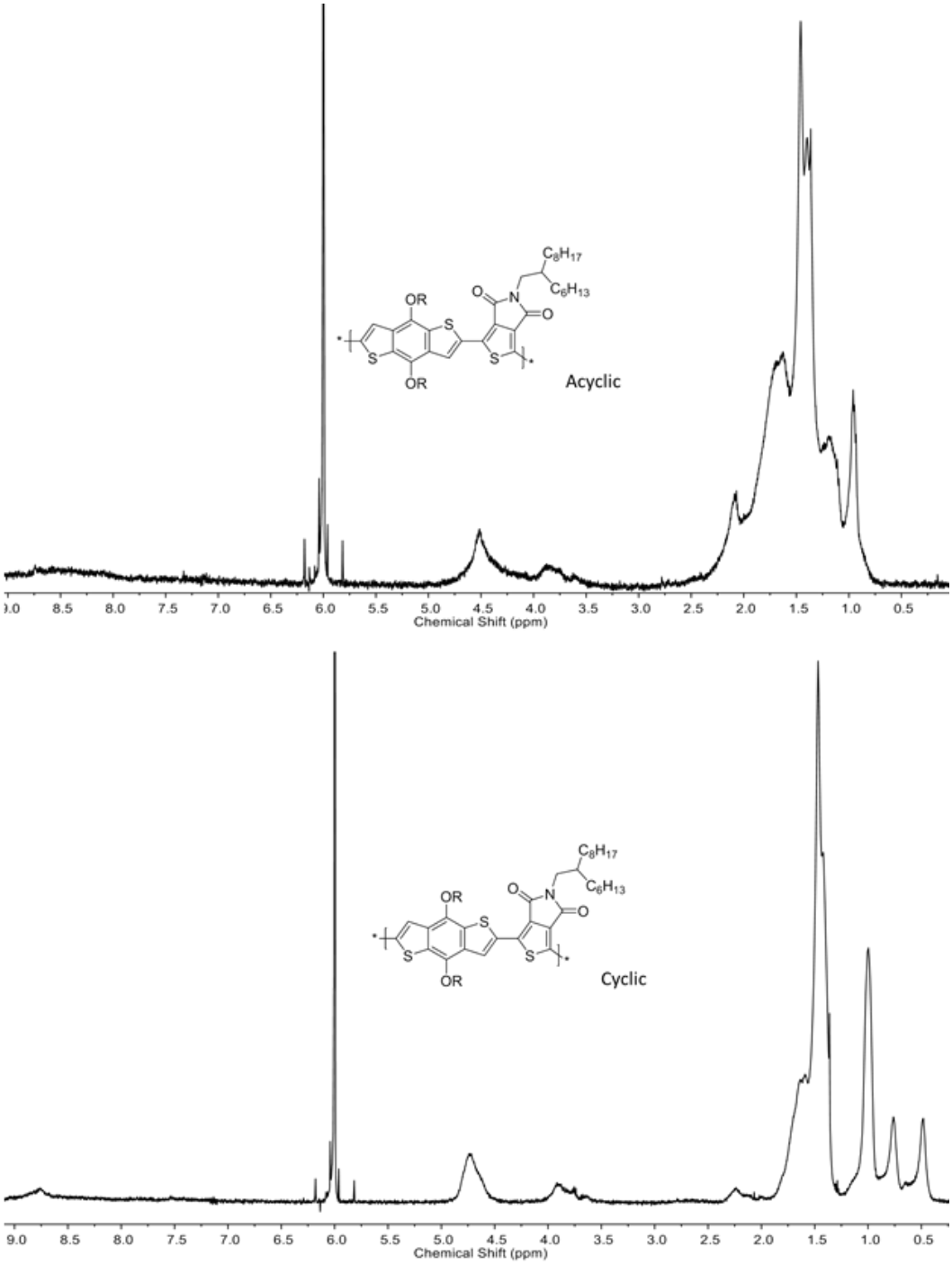


**Figure 119: $^{1}$H NMR spectra (TCE-d2 120$^{o}$C) of cyclic and acyclic P(BDTTPD).**

The aggregation of these materials in solution was then studied via variable temperature UV-Vis absorption spectroscopy.

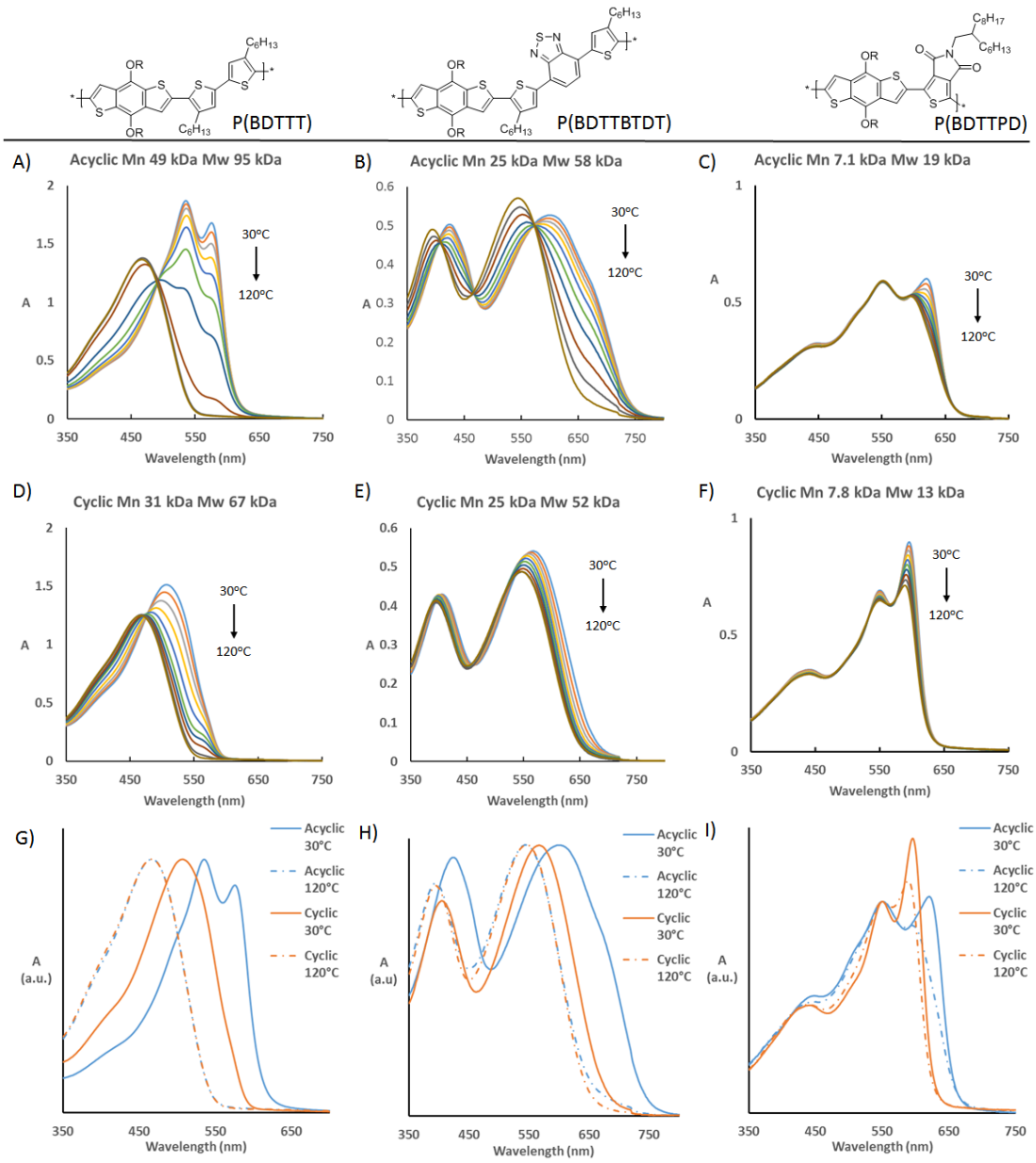


**Figure 120: Variable temperature UV-Vis absorption spectroscopy. A) Acyclic P(BDTTT); B) acyclic P(BDTTBTDT); C) acyclic P(BDTTPD); D) cyclic P(BDTTT); E) cyclic P(BDTTBTDT); F) cyclic P(BDTTPD); G) Normalized overlay of cyclic and acyclic P(BDTTT) at 30°C and 120°C; H) Normalized overlay of cyclic and acyclic P(BDTTBTDTT) at 30°C and 120°C; I) Normalized overlay of cyclic and acyclic P(BDTTPD) at 30°C and 120°C.**

The acyclic P(BDTTT) (Figure 120A) derivative shows aggregation at lower temperatures which decreases with increasing temperature. This is evidenced by the isosbestic point at 491 nm and the vibronic peaks at 535 nm and 576 nm as well as the red-shifted absorption with an onset of 663 nm at 30$^{o}$C. The cyclic P(BDTTT) derivative (Figure 120D) shows significantly reduced aggregation as evidenced by the lack of the vibronic peaks 535 nm and 576nm as well as the less red-shift absorption onset of 586 nm. There does appear to be some aggregation in this cyclic P(BDTTT) sample however as evidenced by the isosbestic point at 475 nm and the small shoulder in the variable temperature absorption profile around 562 nm. The normalized overlay of the absorption profiles for the cyclic and acyclic P(BDTTT) compounds shows that by heating to 120$^{o}$C in chlorobenzene, the aggregation is lost and the two absorption profiles converge to the same curve as expected (Figure 120G). This demonstrates that the differences in optical properties between the cyclic and acyclic P(BDTTT) derivatives are due purely to aggregation effects. The acyclic P(BDTTBTDT) sample (Figure 120B) also showed a significant amount to aggregation with isosbestic points at 573 nm, 467 nm, and 407 nm; a vibronic peak as evidenced by the shoulder at 668 nm, and a red-shifted absorption profile with an onset of 747 nm. The cyclic P(BDTTBTDT) did not show any evidence of aggregation and had a much less red-shifted absorption of 674 nm. The absorption curves of these two compounds converge at the higher temperatures with only a slight residual shoulder in the acyclic derivatives profile at 120$^{o}$C. This convergences once again demonstrates that these differences in optical properties are due to aggregation effects which go away with increased temperature, and the small residual in the acyclic derivatives 120$^{o}$C trace shows that a small amount of aggregation is still present even at

this elevated temperature. Both the cyclic and acyclic P(BDTTPD) derivatives show aggregation that was not lost upon heating. This is likely due to the much more polar thieno[3,4-c]pyrrole-4,6-dione (TPD) co-monomer. The two derivatives do appear to have different solution structures with the acyclic derivative having a more red-shift absorption onset of 659 nm relative to the cyclic derivatives absorption on set of 629 nm. Furthermore, the absorption profiles of the cyclic and acyclic derivatives no not overlay at the highest temperature measured which further suggests that the two derivatives are both still aggregated even at 120°C in chlorobenzene.

Additional characterization of the P(BDTTPD) derivatives in solution were performed using diffusion ordered nuclear magnetic spectroscopy (DOSY NMR). Using three different molecular weights of the cyclic and acyclic P(BDTTPD) derivatives in deuterated chlorobenzene at a concentration of 0.5 mg/ml, the following DOSY spectra were obtained (Figure 121):

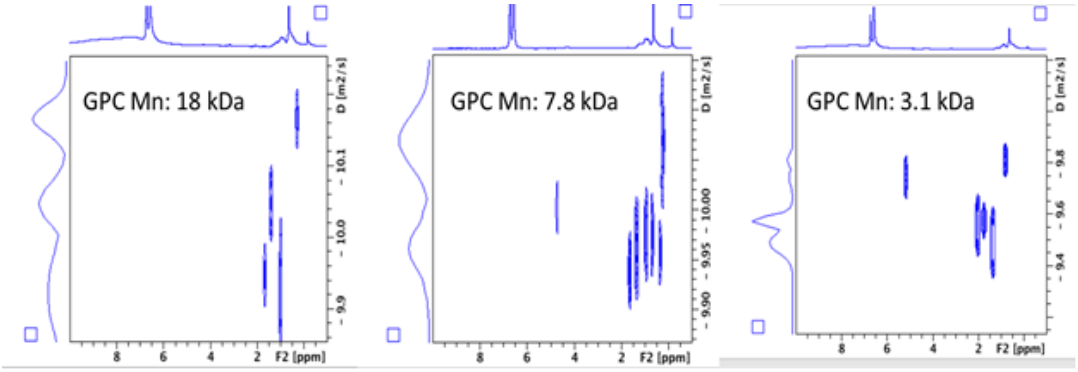


**Figure 121: DOSY NMR plots showing the diffusion coefficient for each proton signal for the three different cyclic P(BDTTPD) molecular weight samples.**

Looking at the large alkyl peak at δ1.46 for each, the diffusion coefficient was plotted against the GPC measured Mn (polystyrene equivalents) and it was found that this diffusion coefficient scales as $D_{0.5} \backsim (M_n)^{-0.58}$ (Figure 122).

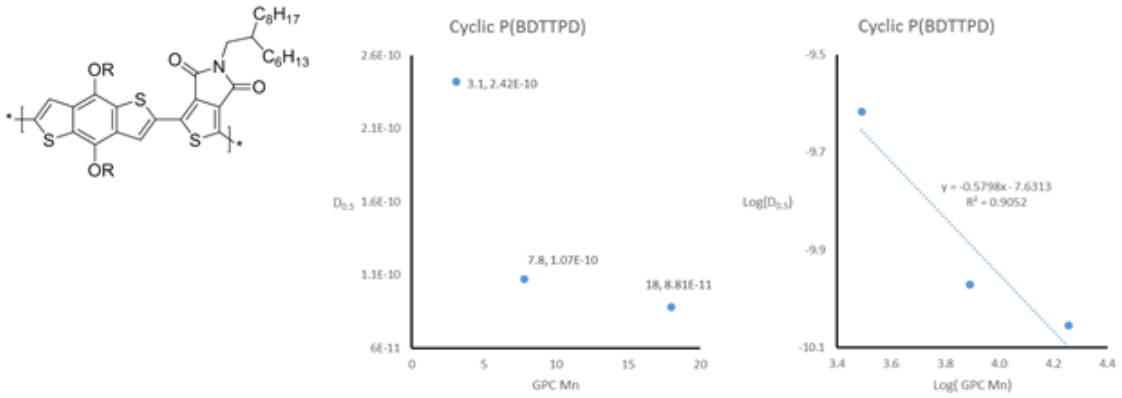


**Figure 122: Plot of diffusion coefficient of cyclic P(BDTTPD) samples as a function of polystyrene equivalent GPC molecular weight as linear-linear plot and a log-log plot with linear fit.**

The same experiments were performed on the acyclic derivatives; however, these measurements gave unclear results as seen in Figure 123.

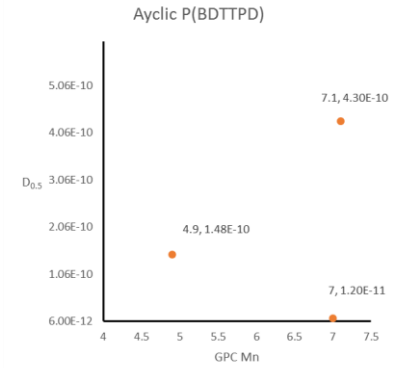


**Figure 123: Plot of diffusion coefficient of cyclic P(BDTTPD) samples as a function of polystyrene equivalent GPC molecular weight as a linear-linear plot.**

This may be due to the larger dispersity's seen in these materials relative to their cyclic analogs or possibly due to the formation of large suspended aggregates which were visible to the naked eye.

Variable concentration fluorescence measurements were then performed so as to further characterize the aggregation of these polymers in solution (Figure 124). The concentration of each polymer was adjusted until the peak absorption value for each polymer was 0.1, 0.3, and 0.6 (a. u.) in either chlorobenzene for the P(BDTTT) and P(BDTTPD) series or orthodichlorobenzene for the P(BDTTBTDT) series before being excited at 475 nm for the P(BDTTT) or 472 nm for the P(BDTTBTDT) and P(BDTTPD) series. All other measurement parameters were kept constant within each polymer series to enable comparison between the cycle and acyclic derivatives within each polymer series.

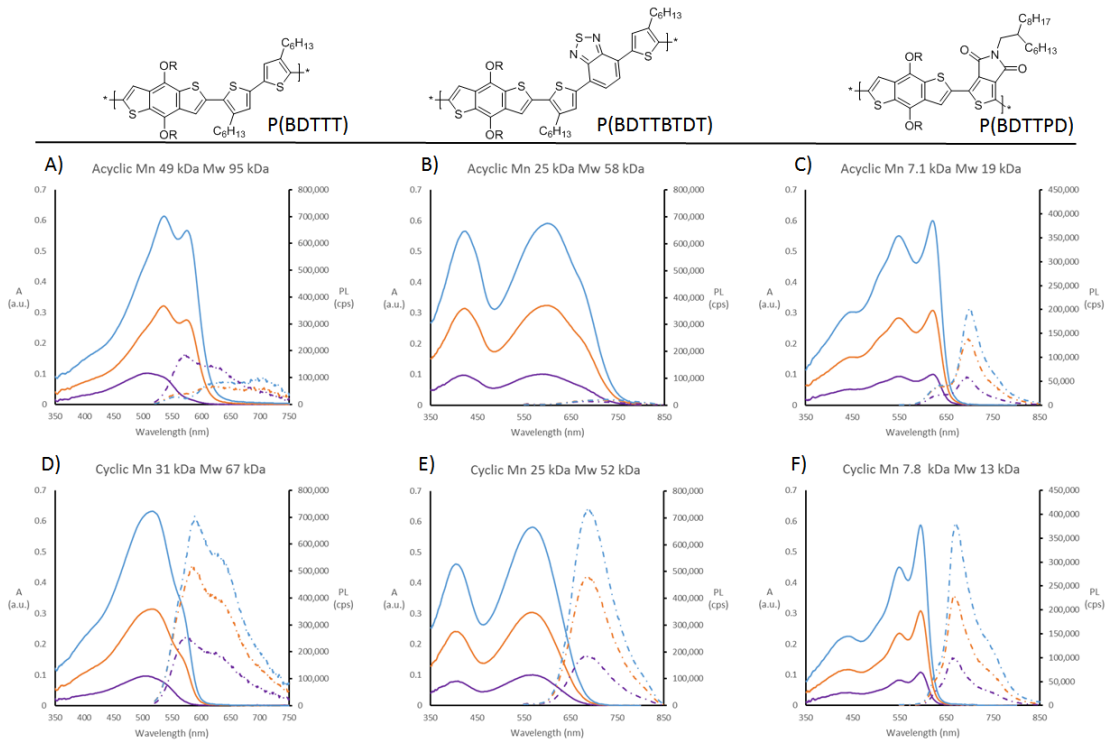


**Figure 124: Variable concentration absorption and fluorescence spectra for A) acyclic P(BDTTT); B) acyclic P(BDTTBTDT); C) acyclic P(BDTTPD); D) cyclic P(BDTTT); E) cyclic P(BDTTBTDT); and F) cyclic P(BDTTPD).**

In all of the cyclic derivatives, the photoluminescence was seen to be higher than their corresponding acyclic derivatives. All of the cyclic derivatives showed increased photoluminescent intensity with increased concentration. The acyclic P(BDTTBTDT) and P(BDTTPD) derivatives also showed an increase in photoluminescence intensity with concentration whereas the acyclic P(BDTTT) derivative showed a distinct red-shifting and quenching of the photoluminescence with increased concentration.

The difference in behavior of concentrated solutions of these polymers at 20 mg/ml in either chlorobenzene for the P(BDTTT) and P(BDTTPD) series or orthodichlorobenzene for the P(BDTTBTDT) series was then studied. It was found that

both the cyclic and acyclic P(BDTTT) polymers gelled within minutes. The acyclic P(BDTTBTDT) also gelled within minutes whereas the cyclic derivative took several days at room temperature before gelling. The acyclic P(BDTTPD) polymer gelled within hours whereas the cyclic derivative was not observed to gel over the course of the couple weeks observed. For each of these experiments, the polymer solution was heated in a vial until the polymer solution was fully dissolved and the vial was left at room temperature to cool. Gelation was determined via tipping the vial. If the contents of the vial flowed while tipped, the solutions was determined not to have gelled (Figure 125).

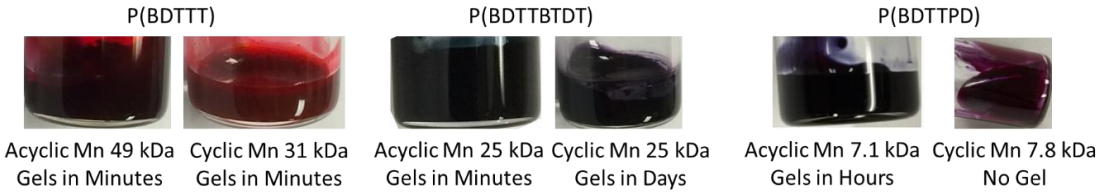


**Figure 125: Pictures of 20 mg/ml polymer mixtures with chlorobenzene for P(BDTTT) and P(BDTTPD) or orthodichlorobenzene for P(BDTTBTDT) derivatives.**

The difference in time for gelation highlights how the macrocyclic loop effects the kinetics of aggregation in addition to the differences in the structural and thermodynamic properties examined previously. The enhanced stability of the cyclic polymer solutions is a desirable feature for solution processed devices[82].

Looking now at the differences in structure and aggregation in the solid state, drop-cast films of each polymer were made from a 10 mg/ml solution of the polymer in chlorobenzene for the P(BDTTT) and P(BDTTPD) series or orthodichlorobenzene for the P(BDTTBTDT) series (Figure 126). These films were then annealed at 230$^{o}$C for 1

hour, and the fluorescence was measured in an integrating sphere exciting with the same wavelength used for the solution experiments while keeping all other measurement parameters constant within each polymer series. It was found that the cyclic derivatives had enhanced photoluminescence for each polymer series. The P(BDTTT) and P(BDTTBTDT) series additionally showed a red-shifting of the photoluminescence spectrum for the acyclic derivatives with the cyclic derivatives showing only a slight shoulder in these red-shifted regions.

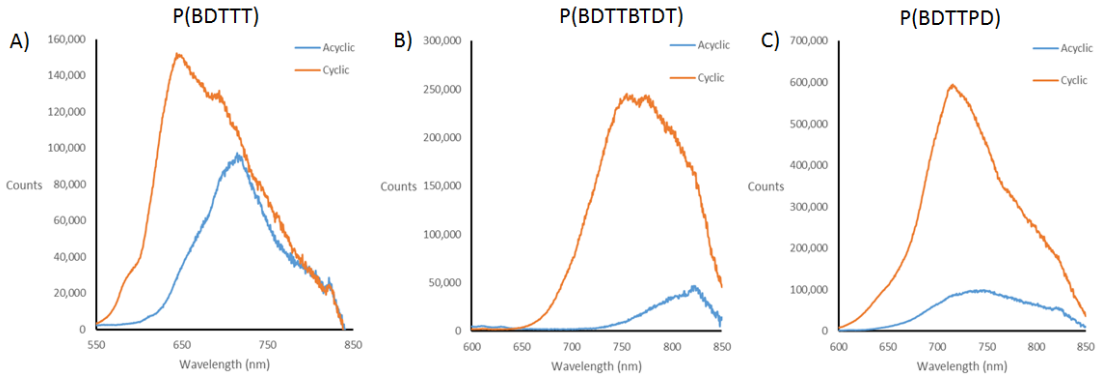


**Figure 126: Fluorescence measurements for drop cast films.**

Normalized UV-Vis absorption spectroscopy measurements performed on films spun cast at 2000 rpm for 30 seconds from 20 mg/ml polymer solutions (chlorobenzene for P(BDTTT) and P(BDTTBTDT) and orthodichlorobenzene for P(BDTTPD)) on to a glass substrate followed by an overnight annealing step at 230$^{o}$C are shown in Figure 127.

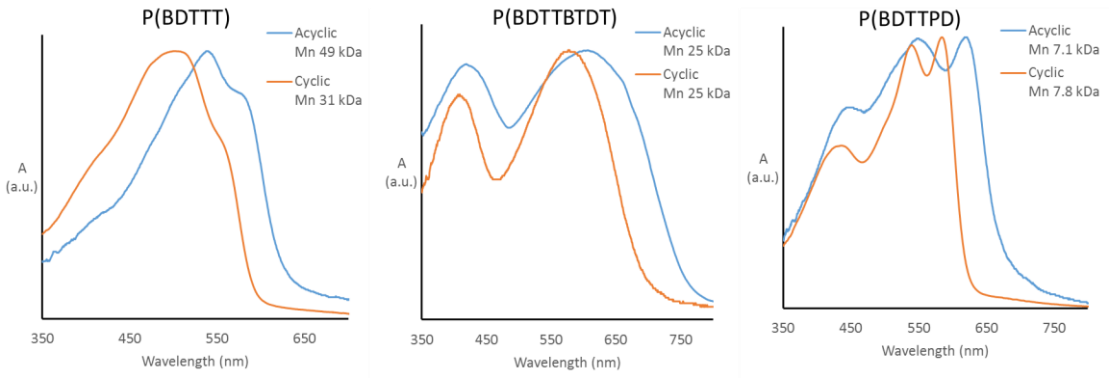


**Figure 127: Normalized absorption spectra for spun cast films.**

The acyclic derivatives all showed a more red-shifted spectrum. The acyclic P(BDTTT) derivative has an onset of absorption at 639 nm with a main peak at 542 nm and a vibronic peak at 581 nm. The cyclic P(BDTTT) has an onset of absorption of 604 nm with a main peak at 506 nm and a vibronic shoulder at 555 nm. The acyclic P(BDTTBTDT) derivative has an onset of absorption at 758 nm, and the cyclic derivative has an onset of 709 nm. The acyclic P(BDTTPD) derivative has an onset of 672 nm whereas the cyclic derivative has an onset of 620 nm. The enhanced photoluminescence of the cyclic derivatives is characteristic of a less aggregated polymer film with more J aggregate character while the more red-shifted absorption spectra and decreased photoluminescence of the acyclic derivatives are characteristic of a film with more H aggregate character[83].

Films prepared in the same manner as those used in the absorption spectroscopy studies, except for using silica substrates with a native oxide, were then used for grazing incidence wide angle X-ray scattering (GIWAXS) experiments (Figure 128).

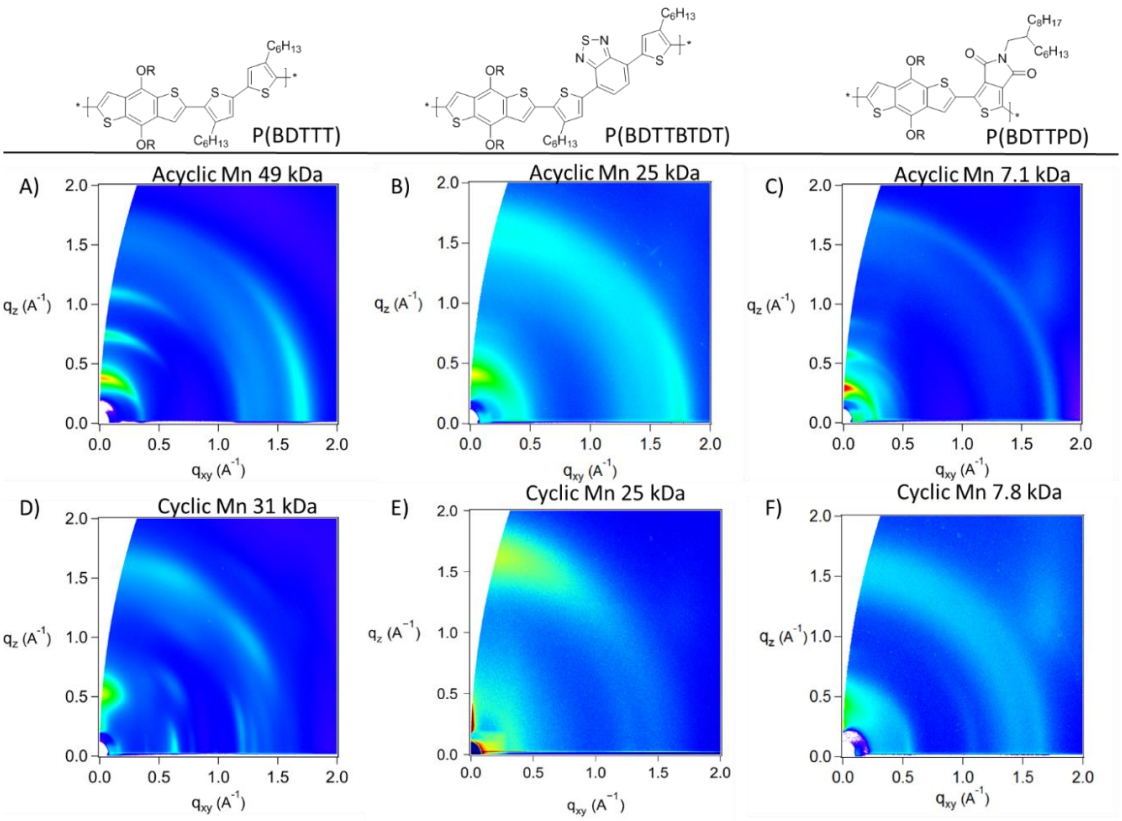


**Figure 128: GIWAXS patterns for spun cast films of A) acyclic P(BDTTT); B) acyclic P(BDTTBTDT); C) acyclic P(BDTTPD); D) cyclic P(BDTTT); E) cyclic P(BDTTBTDT); and F) cyclic P(BDTTPD).**

The acyclic P(BDTTT) has an edge-on lamellar structure with an in-plane peak at 3.84Å and out of plane alkyl spacing of 16.5Å. The alkyl spacing distance of the cyclic P(BDTTT) derivative is shorter at 11.9Å. The cyclic P(BDTTT) derivative has many high index reflections which suggests a well ordered 3-dimensional structure. The cyclic architecture therefore impacts the solid-state morphology for this series changing the layered lamellar structure of the acyclic derivative into a more 3-dimensional structure. This 3-dimensional structure may be a result of some sort of 'lock-and-key' effect arising from commensurate spacing of side-chains as a result of the cyclic architecture. The

acyclic P(BDTTBTDT) sample has in-plane alkyl stacking peak at 15.3Å with a textured but more edge-on morphology than the corresponding cyclic derivative. The π-stacking distance is 3.85Å in each. It is interesting to note the effect on texture due to the cyclic topology. Edge-on structures are typically more suited for OFET applications whereas face-on structures are typically better in OPVs[84]. It is also noteworthy that the cyclic derivative does not seem to impact the π-stacking distance for this polymer series. Acyclic P(BDTTPD) has a lamellar structure with a 21.2Å alkyl spacing while the cyclic derivative has a diffuse glassy scattering pattern with a slightly larger alkyl spacing of 25.2Å. Degree of crystallinity is an important parameter in organic electronic applications with higher crystallinity being desirable in certain applications such as OFETs and more amorphous structures being desirable in certain other applications such as OPVs[85].

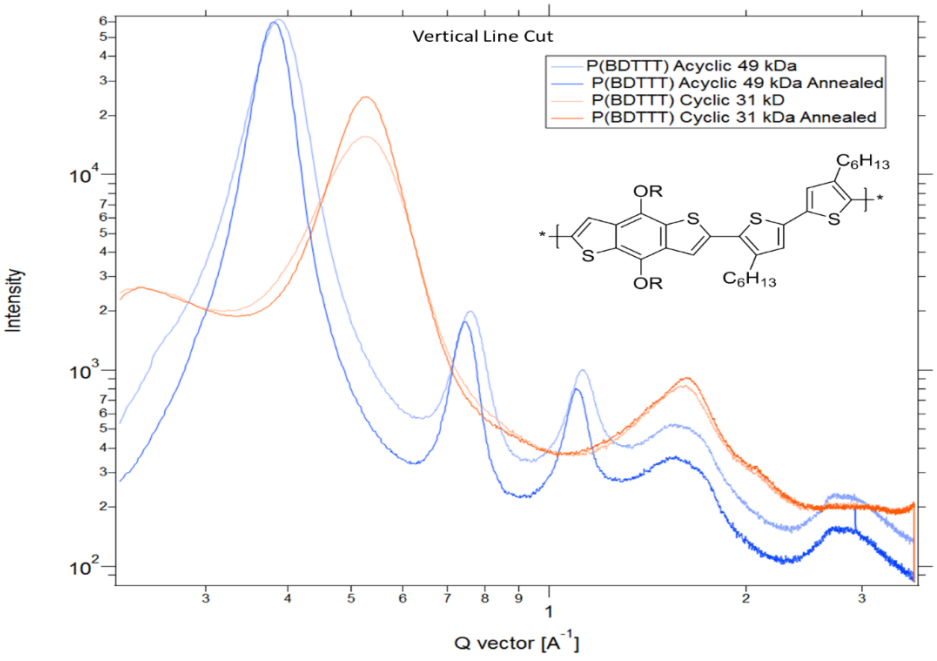


**Figure 129: Vertical line cuts for P(BDTTT) derivatives.**

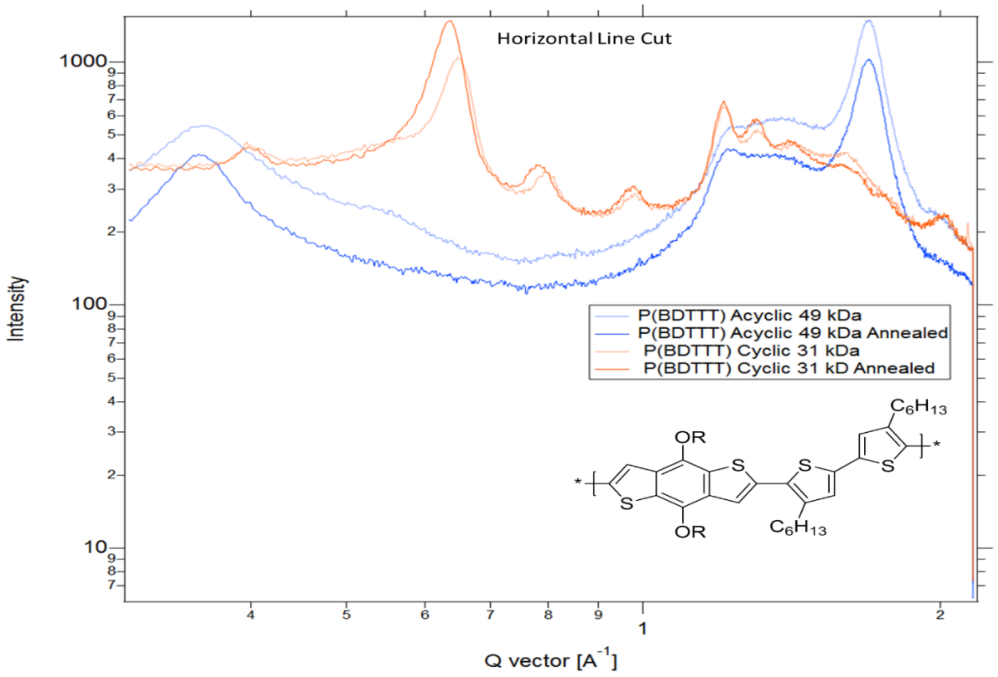


**Figure 130: Horizontal line cuts for P(BDTTT) derivatives.**

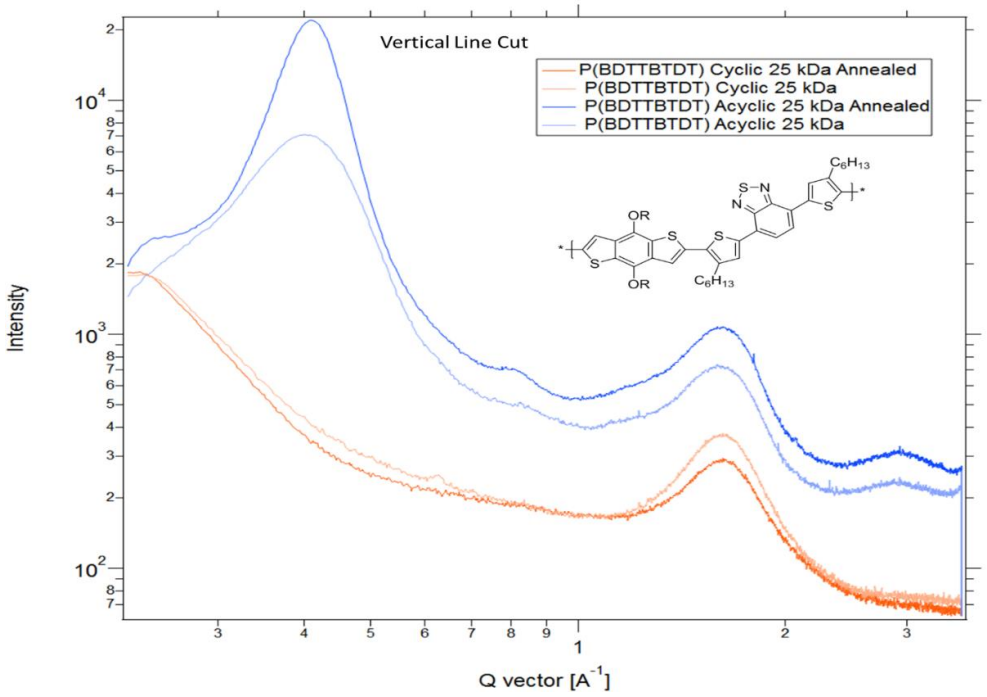


**Figure 131: Vertical line cuts for P(BDTTBTDT) derivatives.**

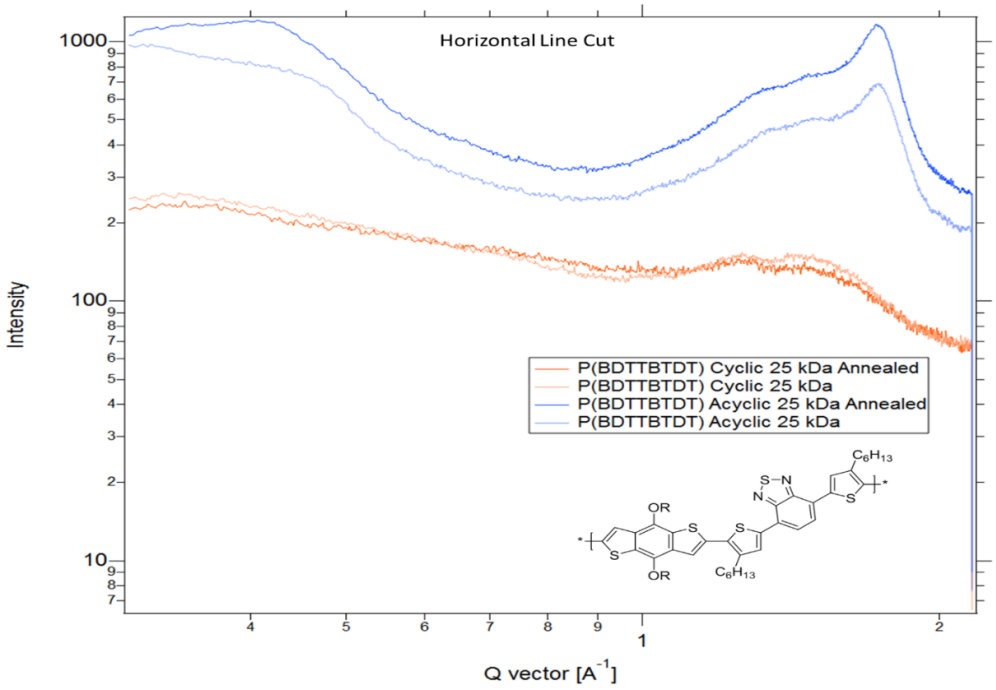


**Figure 132: Horizontal line cuts for P(BDTTBTDT) derivatives.**

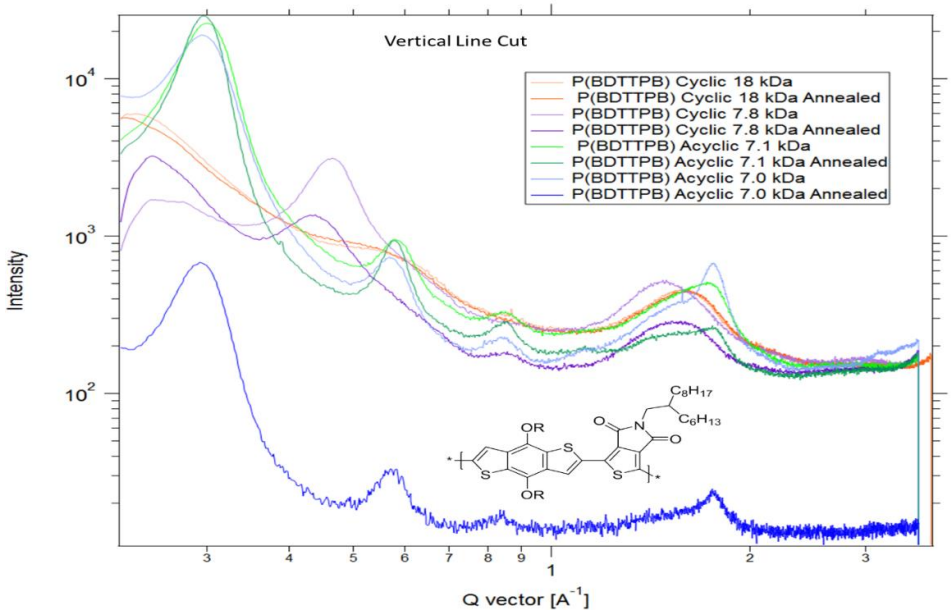


**Figure 133: Vertical line cuts for all P(BDTTPD) derivatives.**

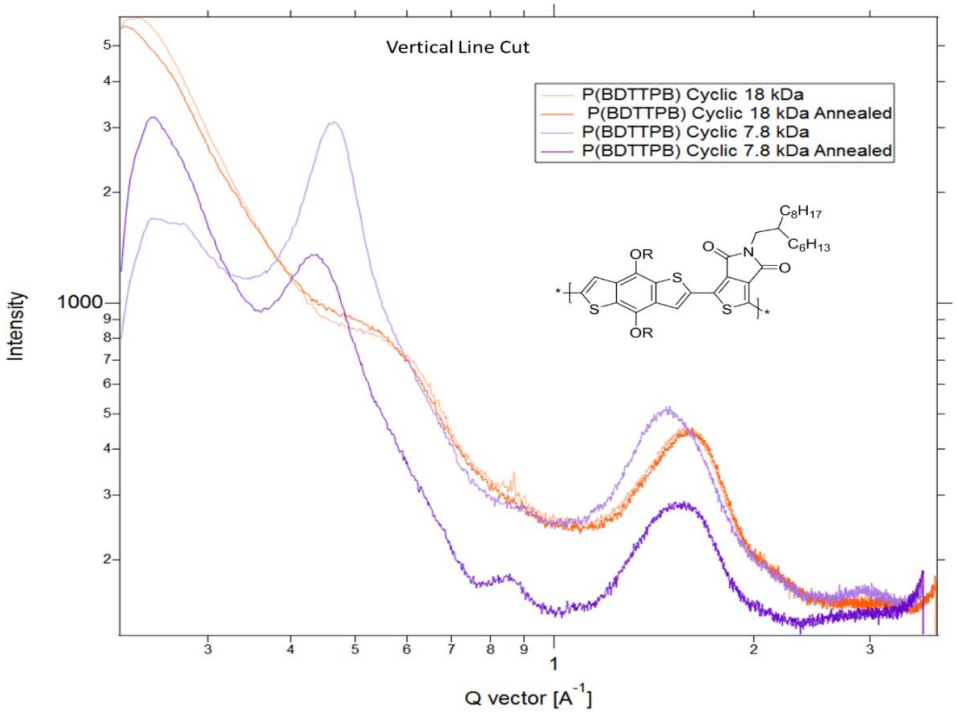


**Figure 134: Vertical line cuts for cyclic P(BDTTPD) derivatives.**

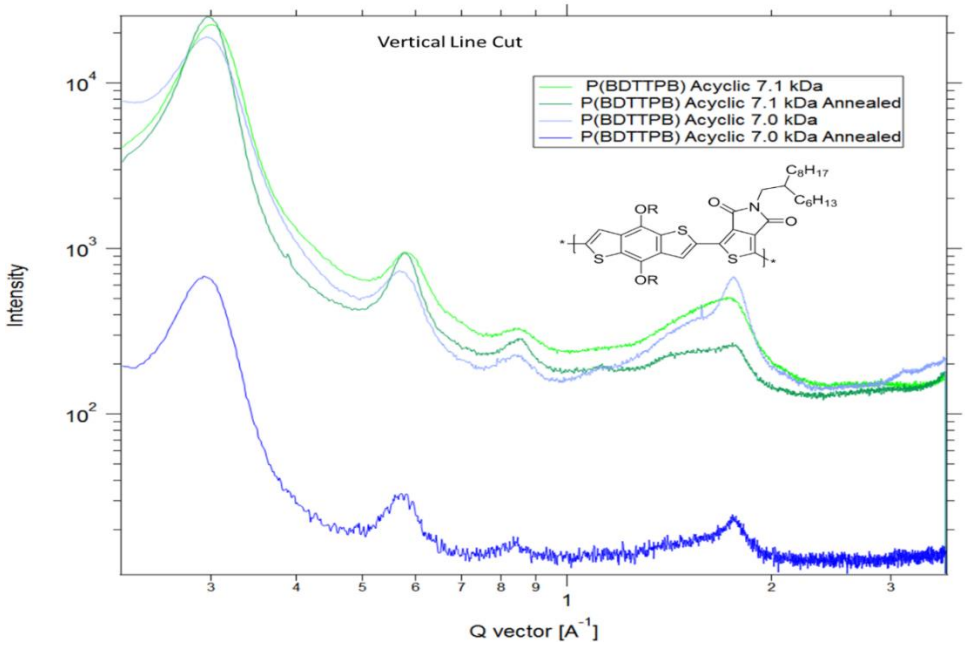


**Figure 135: Vertical line cuts for acyclic P(BDTTPD) derivatives.**

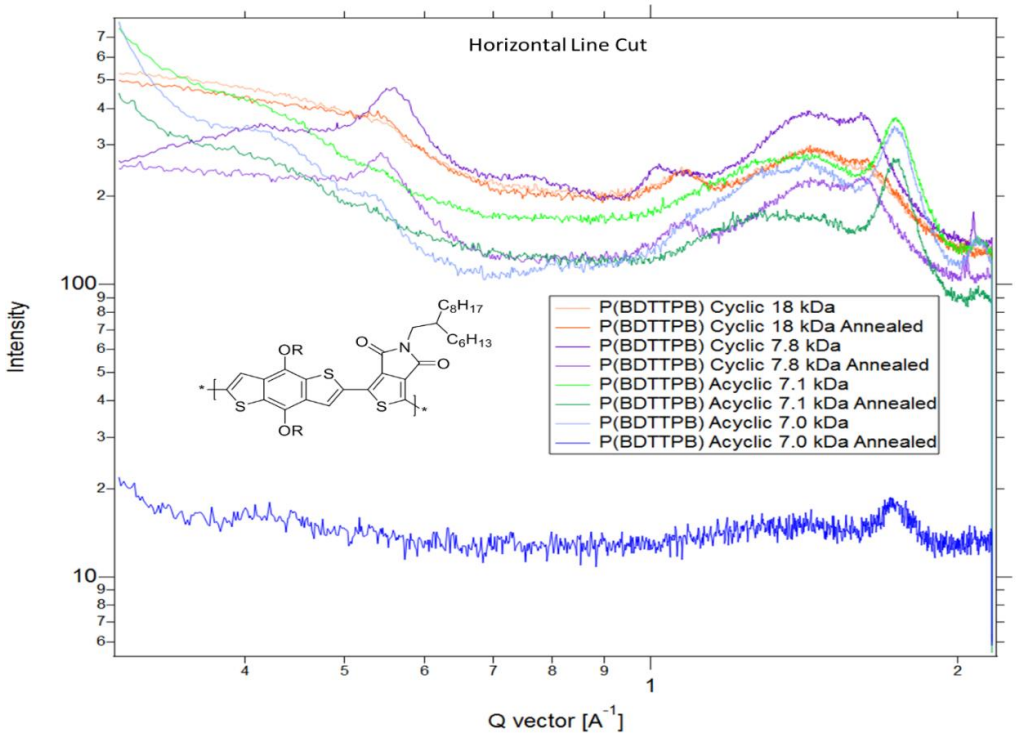


**Figure 136: Horizontal line cuts for all P(BDTTPD) derivatives.**

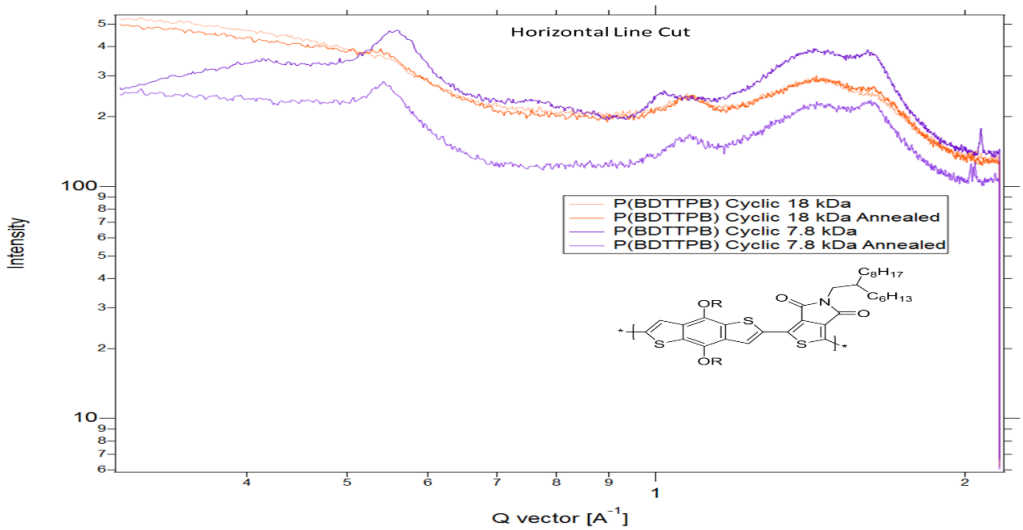


**Figure 137: Horizontal line cuts for cyclic P(BDTTPD) derivatives.**

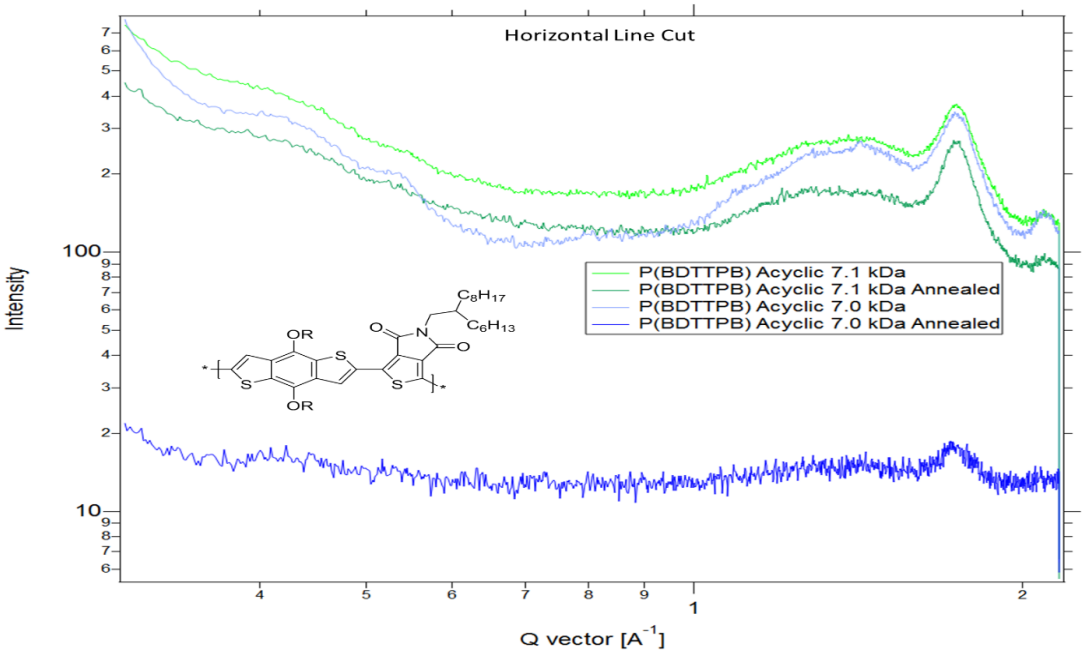


**Figure 138: Horizontal line cuts for acyclic P(BDTTPD) derivatives.**

In conclusion, the macrocyclic loop was demonstrated to have a profound effect on the thermodynamic driving forces for assembly as seen by the lowering of both the entropy and enthalpy of melting for the cyclic BDT and TBDTT relative to their acyclic analogues. Kinetics for gelation and aggregation were impacted by the cyclic unit as evidenced by the difference in gelation and time required for the development of gelation for the P(BDTTPD) and P(BDTTBTDT) series respectively. The geometric requirements of the macrocyclic loop was also seen to influence the solid-state packing structure for the small molecules as well as the conjugated polymers. This is apparent in the different packing structures seen in the single crystal X-ray analysis of the small molecules as well as in the GIWAXS diffraction studies of the conjugated polymers which consistently showed differences in texturing, morphology, and crystallinity between the cyclic and acyclic polymers. Furthermore, the macrocycle was seen to suppress aggregation and

enhance fluorescence in solution and the solid-state. All told, the macrocyclic geometry was found to dramatically impact solution and slid-state structure as well as the optoelectronic properties which critically depend on such structure.

## V. A Simple Approach to Functional and Well-Defined Photo-Crosslinkable Bottlebrush Networks

In the search for elastic and compliant materials with moduli comparable to biological materials, bottlebrush networks stand out from the crowd[7,8,9]. Unlike polymer gels which achieve low moduli and large elasticity via being swollen in a good solvent, bottlebrush networks need not be swollen to achieve their desired mechanical properties[8,9]. This is because the arms of the bottlebrushes take up the role of the solvent in a traditional gel to fill in the space between crosslinks and 'swell' the gel. This affords material which has the same desirable mechanical properties of a traditional polymer gel, but does not have the downside of requiring a solvent which could otherwise diffuse or evaporate out. Previous approaches to photo-crosslinkable bottlebrushes typically require multiple synthetic steps as seen in the 6 step synthesis of the coumarin functionalized photo-crosslinkable bottlebrush depicted in Figure 139[86]:

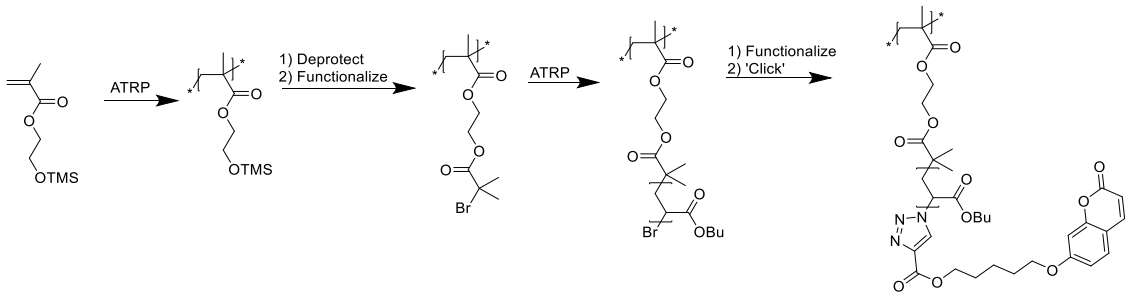


**Figure 139: representative literature route to photo-crosslinkable bottlebrushes[86].**

In order to improve access to these desirable material, a concise and versatile approach is required. To this end, a 3 step synthesis of photo-crosslinkable bottlebrush materials was proposed (Figure 140).

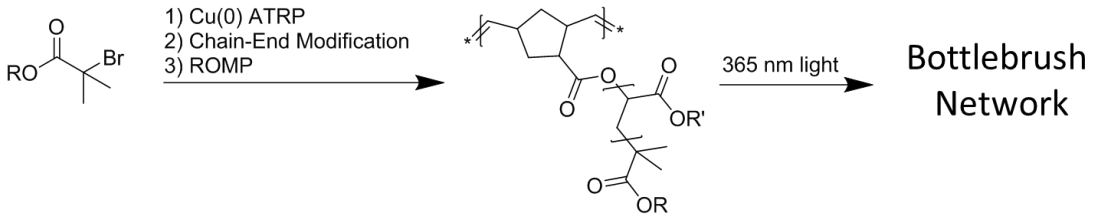


**Figure 140: Proposed modular synthetic route to photo-crosslinkable bottlebrushes.**

This more concise approach also makes use of the more user friendly Cu(0) ATRP chemistry as well as the more robust ring opening metathesis polymerization (ROMP) technique to synthesis the bottlebrush materials[87,88,89]. The first attempt at this synthesis made use of a norbornene ATRP initiator (Figure 141).

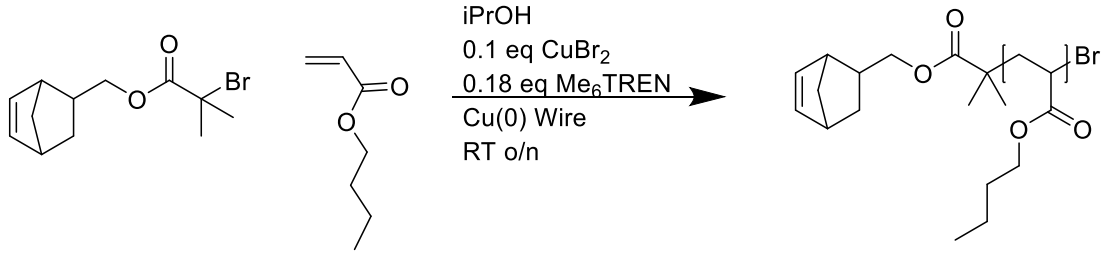


**Figure 141: Synthesis of poly(nButyl Acrylate) using a norbornene initiator.**

These conditions gave polymer with an undesired high molecular weight shoulder in the GPC trace (Figure 142).

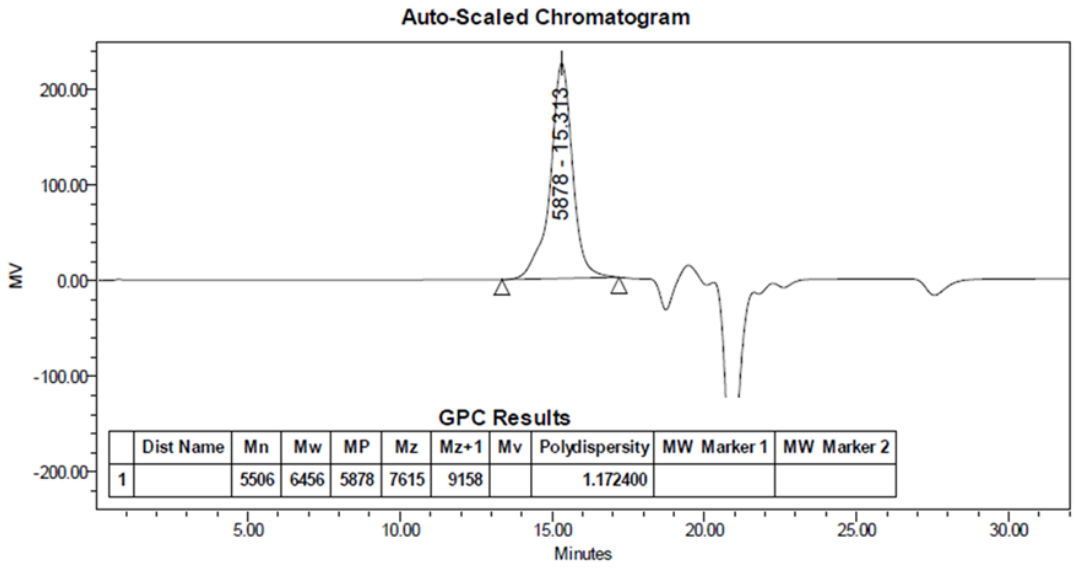


**Figure 142: GPC (chloroform) of ATRP product using norbornene initiator showing asymmetric peak.**

This high molecular weight shoulder was reasoned to derive from participation of the strain activated norbornene initiator in the ATRP reaction. For this reason, a second approach was sought wherein the photocrosslinking unit was used as the ATRP initiator. In this approach anthracene was used as the photocrosslinker owing to the fact that anthracene is known to undergo photodimerization when exposed to 365 nm light, and these dimers are thermally reversible (Figure 143)[90].

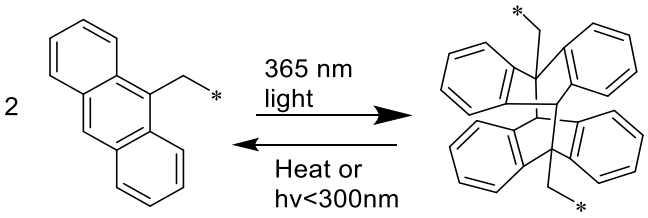


**Figure 143: Reversible anthracene dimer formation.**

An anthracene ATRP initiator was synthesized and the Cu(0) ATRP reaction was performed.

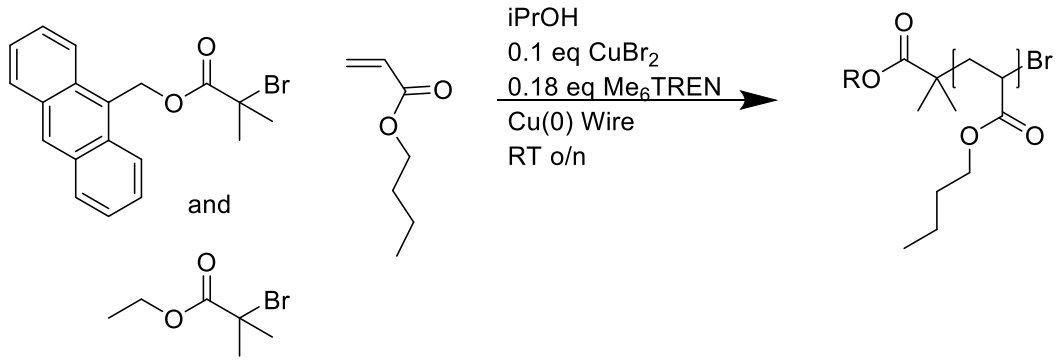


**Figure 144: ATRP reaction using anthracene based initiator as well as ethyl isobutyryl bromide.**

When the anthracene initiator was used as 1 to 10% of the total initiator in the reaction with the remaining percentage consisting of the ethyl isobutyryl bromide, the reactions produced polymer with more symmetric GPC traces, and the presence of the anthracene chain end was confirmed with the UV detector on the GPC (Figure 145,Figure 146).

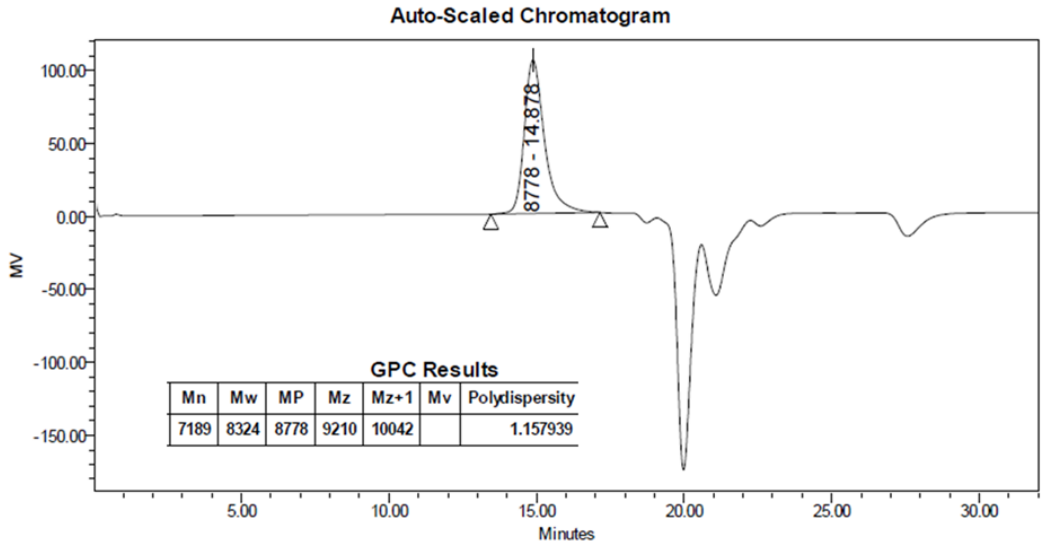


**Figure 145: Representative GPC trace (chloroform) for ATRP product using <10% anthracene based initiator.**

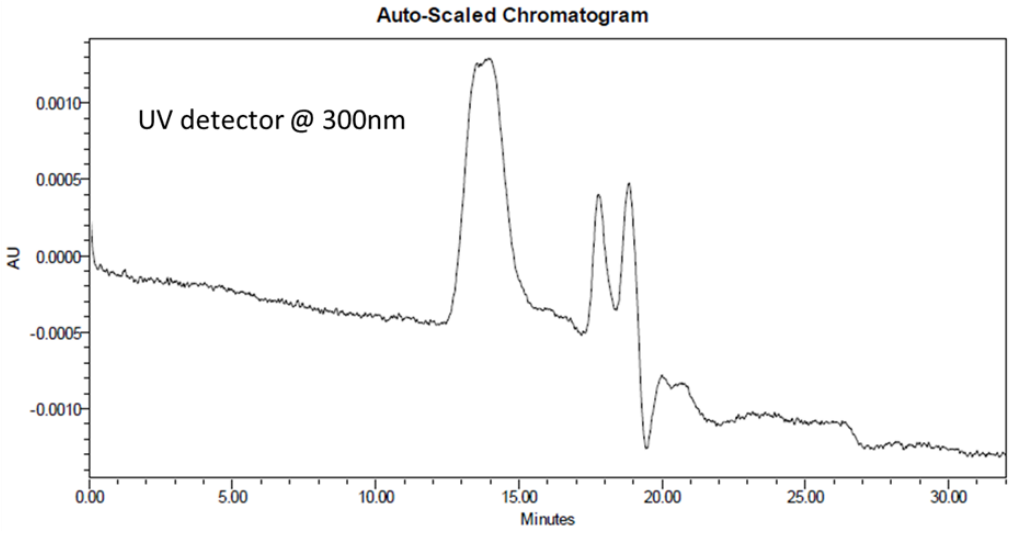


**Figure 146: Representative UV signal from GPC trace (chloroform) for ATRP product using <10% anthracene based initiator showing presence of anthracene at the chain end.**

These polymers were then functionalized with a norbornene carboxylic acid ROMP initiator (Figure 147).

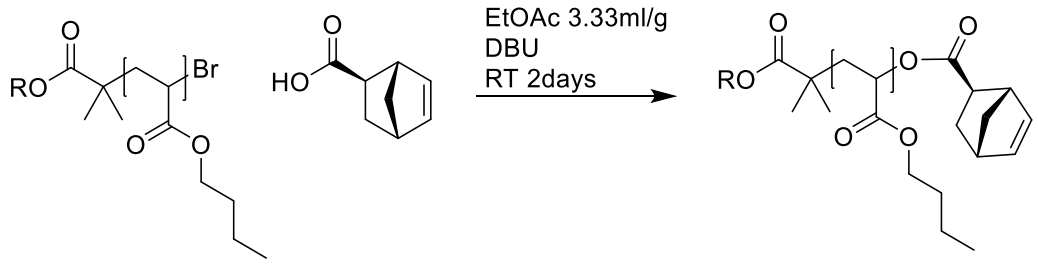


**Figure 147: Chain end functionalization reaction with exo-5-Norbornenecarboxylic acid.**

$^{1}$H NMR confirmed successful functionalization of the polymer chain end (Figure 148).

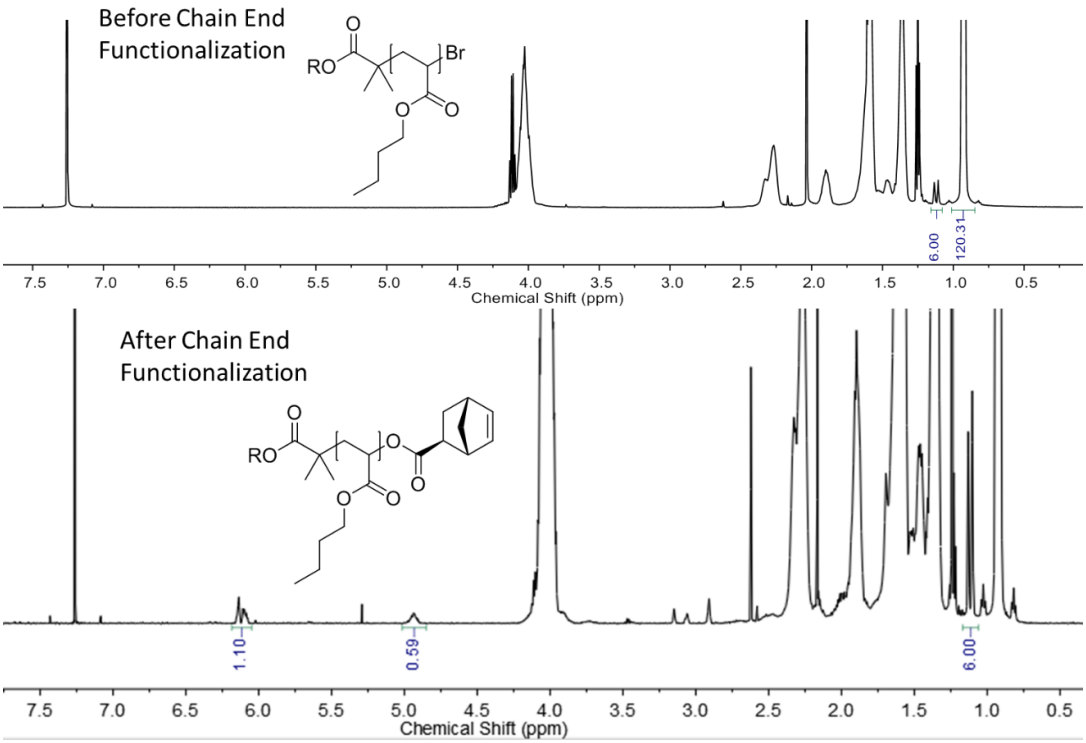


**Figure 148: $^{1}$H NMR spectra before and after chain end functionalization reaction showing successful incorporation of exo-5-Norbornenecarboxylic acid.**

The chain end functionalization reaction did not affect the molecular weight or dispersity of the polymer material as determined via comparing the GPC trace before and after functionalization (Figure 149).

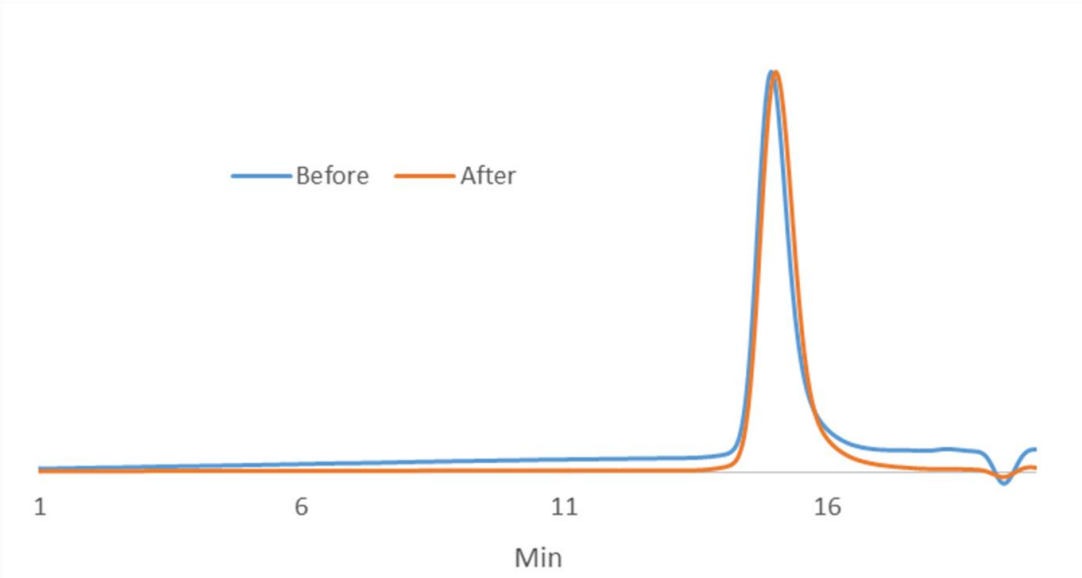


**Figure 149: Normalized GPC traces (chloroform) for before and after the chain end functionalization reaction.**

These materials were then subjected to ROMP conditions using a pyridine modified Grubbs 2 catalyst which will be referred to herein as Grubbs 3 henceforth (Figure 150).

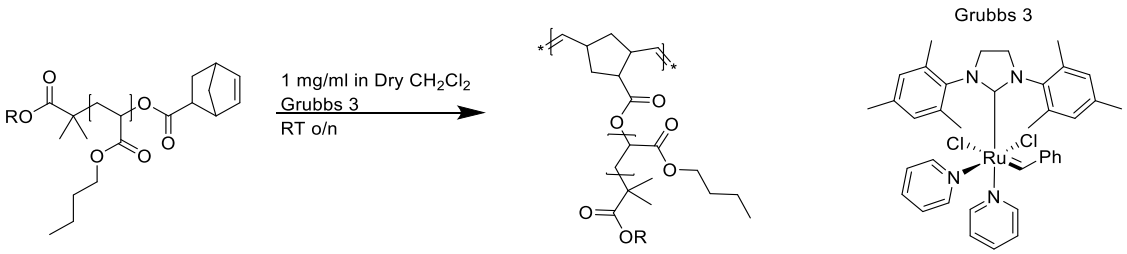


**Figure 150: Ring opening metathesis reaction (ROMP) of exo-5-Norbornenecarboxylic acid functionalized macromonomer.**

These ROMP conditions were successful in preparing bottlebrush materials as determined via GPC (Figure 151).

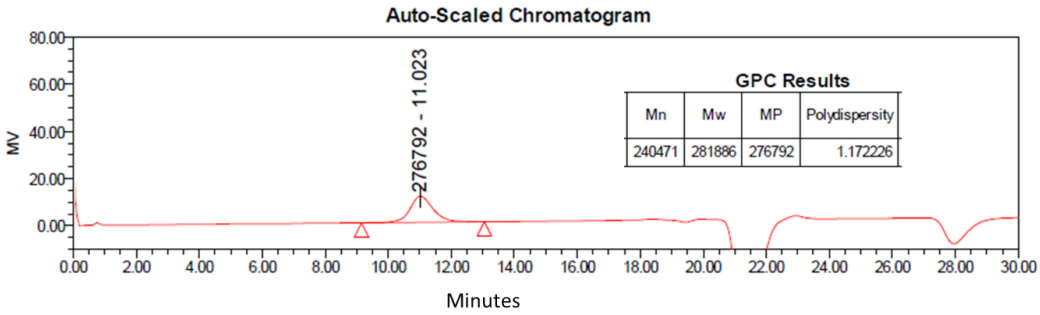


**Figure 151: GPC trace (chloroform) of purified ROMP bottlebrush product.**

Crosslinking of these materials via exposure to 365 nm light proved unsuccessful with the material remaining as a viscous liquid regardless of the length of exposure. In order to understand whether this lack of crosslinking was due to inefficient dimerization or some other cause, the synthetic procedure was restarted using 100% anthracene initiator. Interestingly, the room temperature Cu(0) ATRP conditions used previously did not make any polymer when only the anthracene initiator was used. When these conditions were modified based on a literature procedure, polymer with a high molecular weight shoulder in the GPC trace resulted (Figure 152, Figure 153)[91].

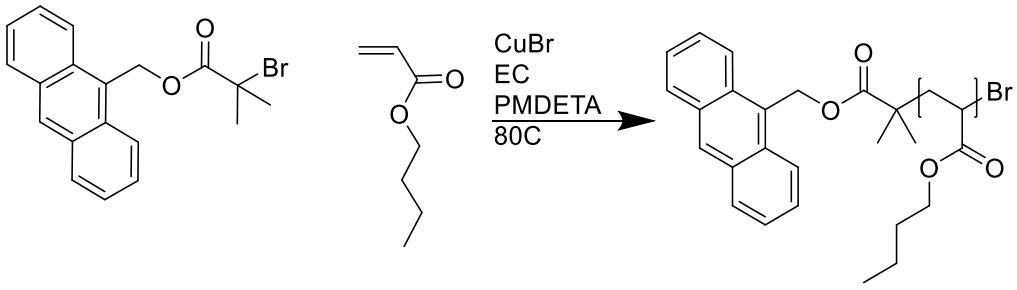


**Figure 152: ATRP reaction using only anthracene based initiator.**

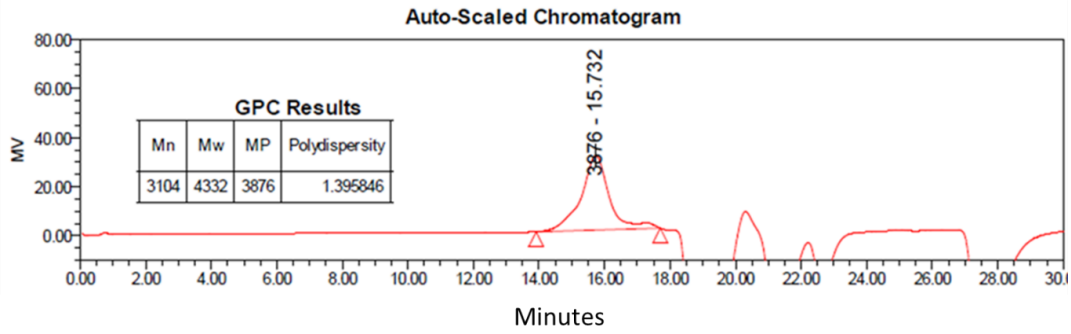


**Figure 153: Asymmetric GPC trace (chloroform) of ATRP product for reaction using only the anthracene based initiator.**

The anthracene chain end was confirmed via the UV channel of the GPC as well as from $^{1}$H NMR (Figure 154, Figure 155).

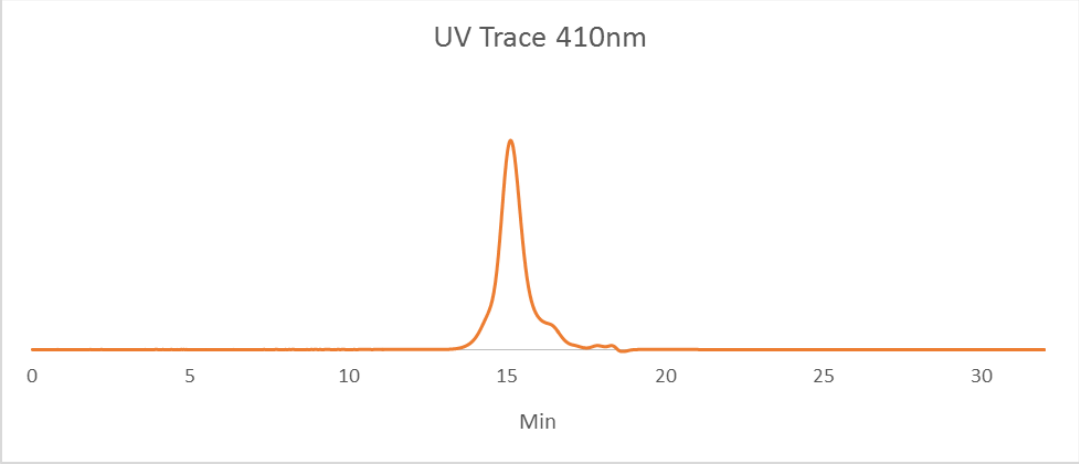


**Figure 154: UV single from the ATRP reaction using only the anthracene based initiator showing incorporation of the anthracene unit.**

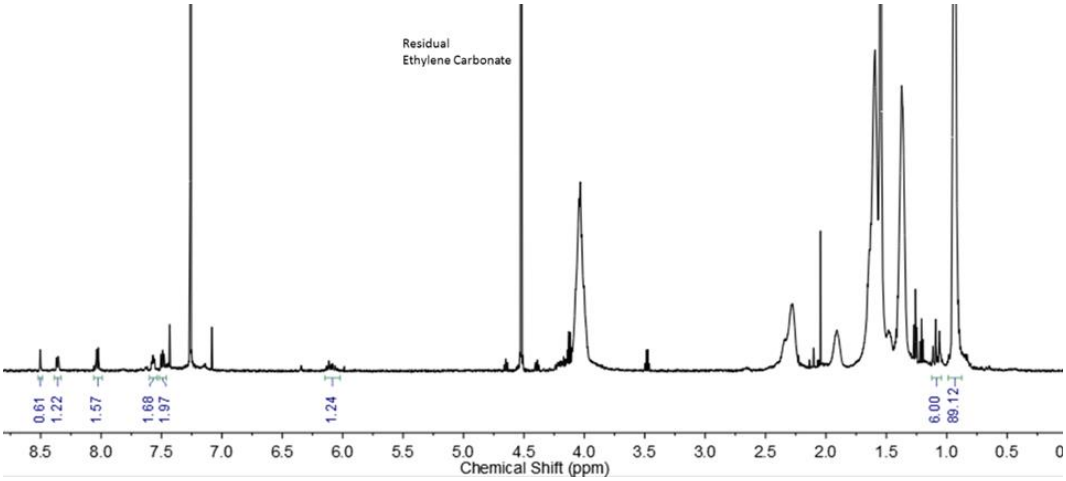


**Figure 155: $^{1}$H NMR spectrum of the product of the ATRP reaction using only the anthracene based initiator showing incorporation of the anthracene unit.**

The chain end functionalization of this material with the norbornene carboxylic acid was successful; however, subsequent subjection of the chain end functionalized material to the ROMP conditions resulted in the material crosslinking during the reaction to form a gel. Heating the resulting gel with the hopes of thermally reversing any anthracene dimers crosslinks proved unsuccessful. These observations of a high molecular weight shoulder in the GPC of the ATRP grown material as well as the resulting crosslinked gel with the ROMP reaction can be explained via radical side reactions of the anthracene initiator during the ATRP reaction resulting in the formation of bifunctional polymers which end up crosslinking the material during the ROMP reaction. This hypothesis is supported by the literature wherein anthracene is known to undergo various side reactions with radicals (Figure 156)[92]:

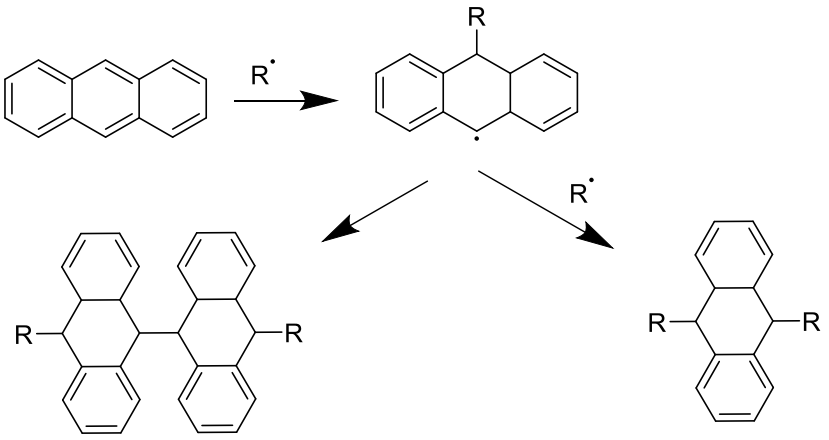


**Figure 156: Known radical side reactions of anthracene[92].**

This is despite the fact that this same anthracene initiator is reported to work in ATRP reactions with styrene in the literature[91,93,94,95,96].

A different photo-crosslinkable initiator was desired. Benzophenone is another well-known photocrosslinking agent. When exposed to 365 nm light, benzophenone generates a radical which can react with nearby C-H bonds to form cross-links (Figure 157)[97].

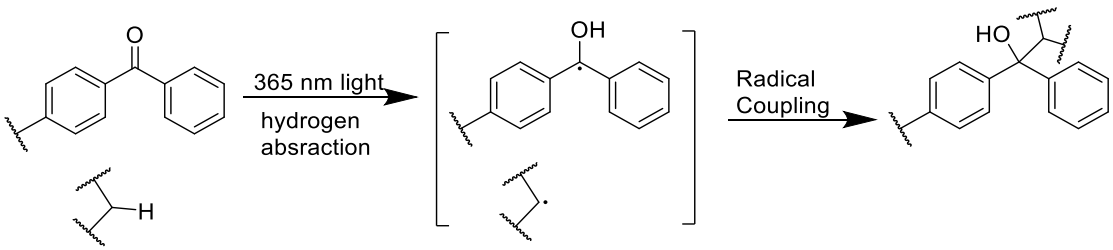


**Figure 157: Benzophenone photo-crosslinking reaction[97].**

A benzophenone based ATRP initiator was synthesized, and this benzophenone based approach proved successful in the synthesis of photocrosslinkable bottlebrushes according to the 3 step synthetic scheme in Figure 158.

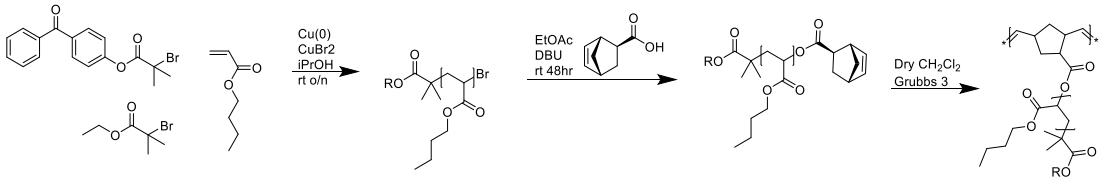


**Figure 158: Three step synthesis of benzophenone functionalized bottlebrushes.**

First, this procedure was carried out using 100% benzophenone initiator. Figure 159 shows an overlay of the GPC traces for the ATRP reaction (solid green line), the chain end functionalization reaction (dashed green line).

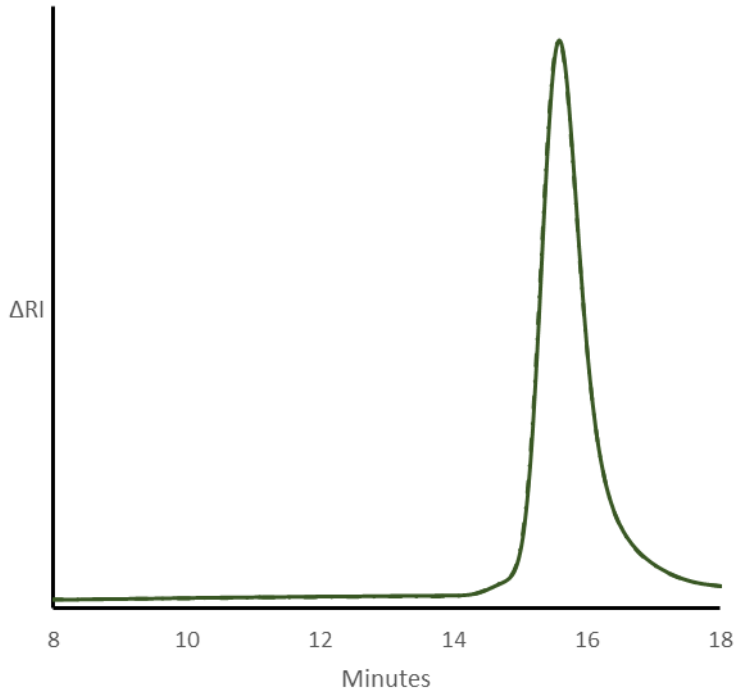


**Figure 159: Normalized GPC traces (chloroform) for the ATRP product and chain end functionalized polymer with 100% benzophenone chain end.**

The GPC polystyrene equivalents Mn for the ATRP product was 9.6 kDa with a dispersity of 1.2. The Mn for this material as determined by NMR was 9.2 kDa. Additionally, the

$^{1}$H NMR of the purified ATRP product shows successful incorporation of the benzophenone unit (Figure 160).

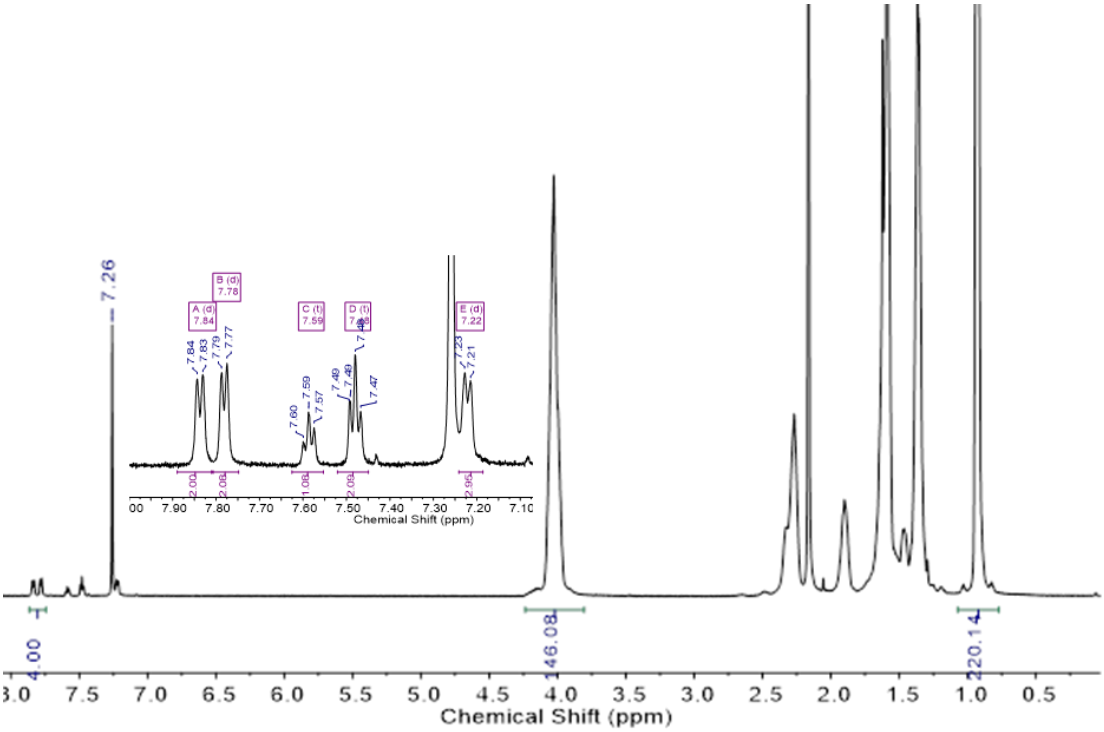


**Figure 160: $^{1}$H NMR for ATRP product with 100% benzophenone chain end confirming presence of benzophenone.**

Note that the isobutyryl protons for the benzophenone functionalized chain-end are partial obscured by the large polymer peak at δ1.34. The GPC trace for the chain-end functionalized material matches that of the ATRP product material, and $^{1}$H NMR analysis shows successful incorporation of the norbornene unit with the olefin peaks at δ6.1 and the proton of the chain end on the last butyl acrylate group appearing at δ4.9 (Figure 161).

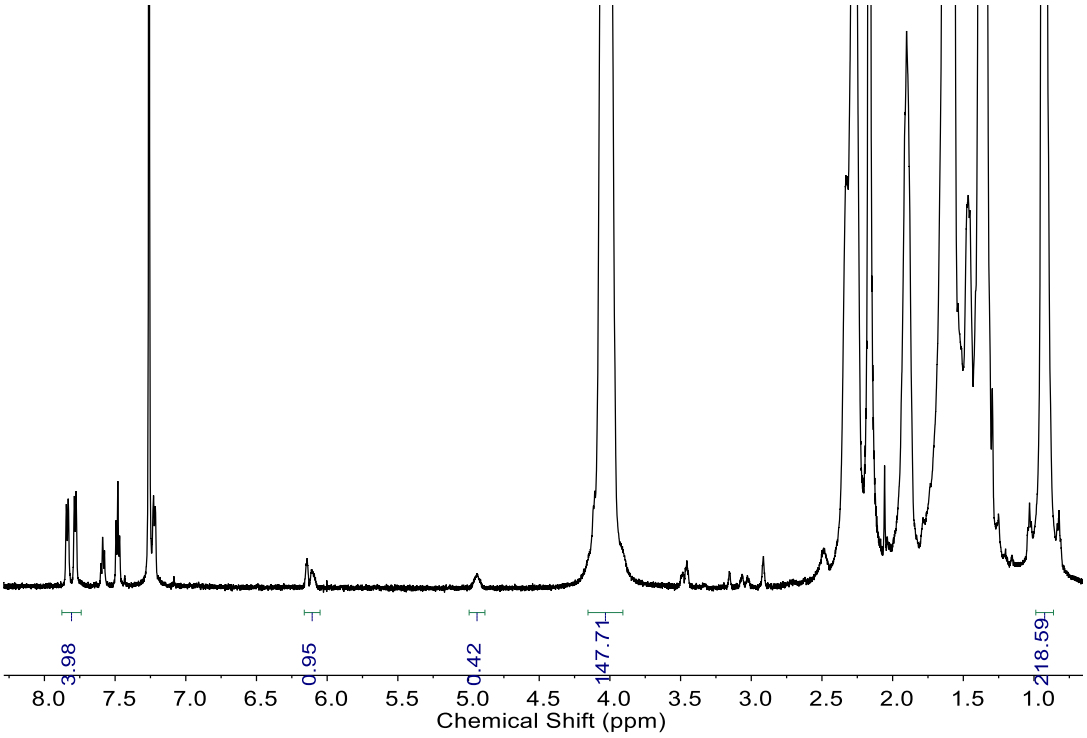


**Figure 161: 1H NMR spectrum of the chain end functionalized macromonomer confirming the exo-5-Norbornenecarboxylic acid functionalized chain end.**

When the ROMP reaction was conducted over night at room temperature, GPC analysis of the crude reaction mixture showed that only 30% of the macromonomer had been consumed (Figure 162).

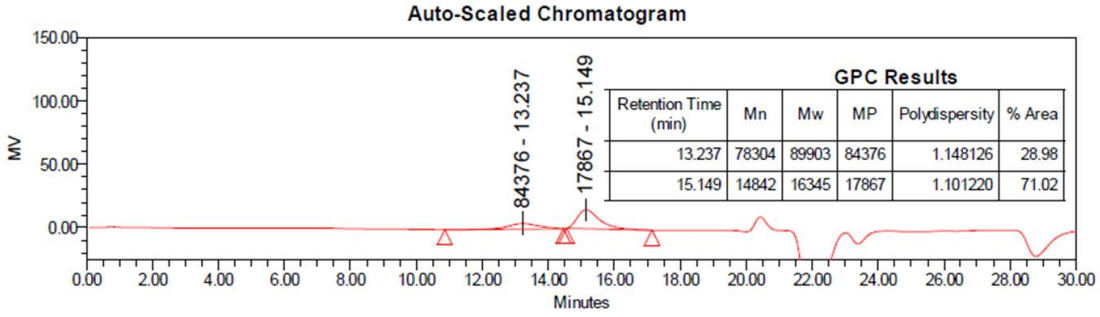


**Figure 162: Crude ROMP GPC trace (chloroform) for macromonomer with 100% benzophenone chain end.**

To determine whether the conversion was limited by the degree of chain end functionalization or the ROMP catalyst, an additional aliquot of Grubbs 3 dissolved in dry $CH_2Cl_2$ was injected into the reaction and the reaction was allowed to proceed further for several hours at which point it was opened to air and quenched with ethylvinyl ether. The product was purified via column chromatography over silica gel eluting with a gradient of dichloromethane in hexanes from 0% to 40%. The bottlebrush material elutes first before the residual macromonomer suggesting that the selectivity of the purification is via size exclusion rather than affinity. The GPC trace of the resulting purified material is bimodal owing to the second catalyst injection and suggests that the conversion of the reaction is limited by the catalyst turn-over rather than the macromonomer (Figure 163).

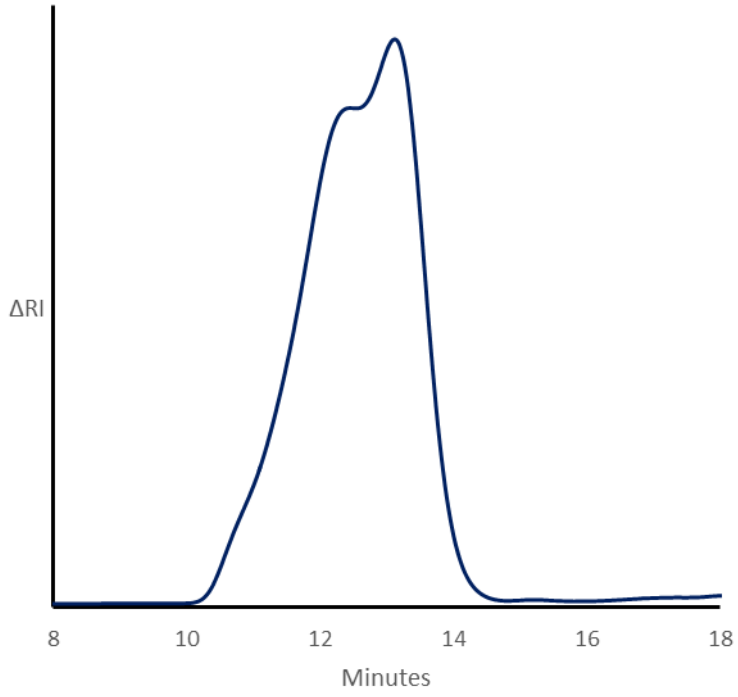


**Figure 163: Final purified ROMP product after second in situ addition of Grubbs 3 catalyst.**

Multi-angle light scattering (MALS) GPC analysis of the purified bottlebrush material showed a Mn of 95 kDa with a dispersity of 2.8. Rheology of the bottlebrush material shows it to be a viscous liquid with the loss modulus G" less than the elastic modulus G'. The bottlebrush was then scooped into a mold formed by a PDMS cutout placed on top of Teflon and heated in a vacuum oven at 60°C overnight to remove solvent before being crosslinked with 365 nm light for 3 hours. The resulting crosslinked material was much stiffer with a G' greater than G". Tensile testing of the material showed into to extend to a strain of about 0.45 before failure and the elastic modulus was found to be 333 kPa (Figure 164).

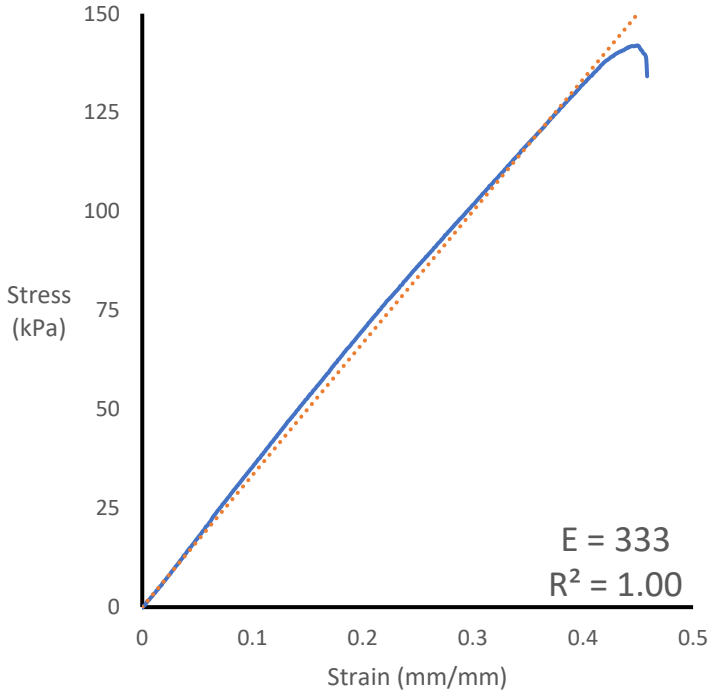


**Figure 164: Tensile measurement for crosslinked bottlebrush network with 100% benzophenone chain end.**

Seeing that the chemistry for this approach works with the benzophenone initiator, softer more compliant materials were then targeted. To achieve this, the benzophenone, and hence the resulting maximum degree of crosslinking, was reduced from 100% to 5% and the molecular weights of the macromonomers were varied from 4 kDa, to 6 kDa, and 9 kDa.

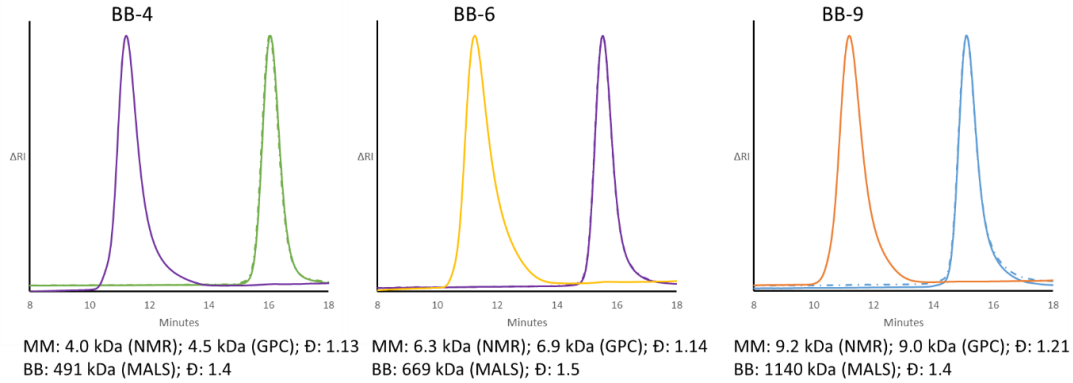


**Figure 165: Normalized GPC traces (chloroform) for the ATRP products, chain end functionalized products, and ROMP products for three separate poly(n-butyl acrylate) based materials with 5% benzophenone chain ends and 95% ethyl isobutyryl chain ends and corresponding molecular weights.**

For each of these materials, the GPC traces for the ATRP polymers and chain end functionalized polymers overlay nicely and show a single monomodal peak with narrow dispersity ranging from 1.13 to 1.21 (Figure 165). The resulting bottlebrush materials, synthesized without including a second catalyst injection as was done for the 100% benzophenone initiated sample discussed previously, were also well-defined with monomodal peaks and dispersities of 1.5 and less. Crude GPC analysis of a representative reaction showed a higher conversion of about 70% (Figure 166).

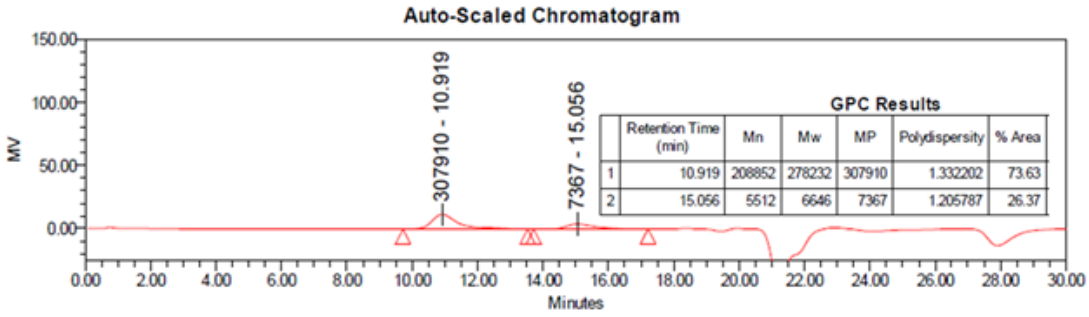


**Figure 166: Representative crude GPC trace (chloroform) for the ROMP reaction of the butyl acrylate based materials with 5% benzophenone chain end and 95% ethyl isobutyryl chain end.**

MALS GPC showed that these bottlebrush materials ranged in molecular weight from 491 kDa to 1140 kDa with degrees of polymerization ranging from 106 macromonomer units for BB-6 to 124 macromonomer units for BB-9. Molding a crosslinking these materials resulting in free standing crosslinked bottle brush networks with excellent clarity. Rheology of these materials before and after exposure to 365 nm light for 3 hours demonstrated successful crosslinking. It was found that the low frequency elastic modulus for both the crosslinked and uncrosslinked materials increased with decreasing molecular weight of the macromonomer side-chain as expected (Figure 167, Figure 168)[9,98,99,100]. Tensile measurements of these materials showed that BB-4 and BB-6 had similar elastic moduli and max strains of 12.45 kDa about 2 respectively whereas BB-9 had a much lower elastic modulus of 8.07 with a max strain of about 2.5 (Figure 169).

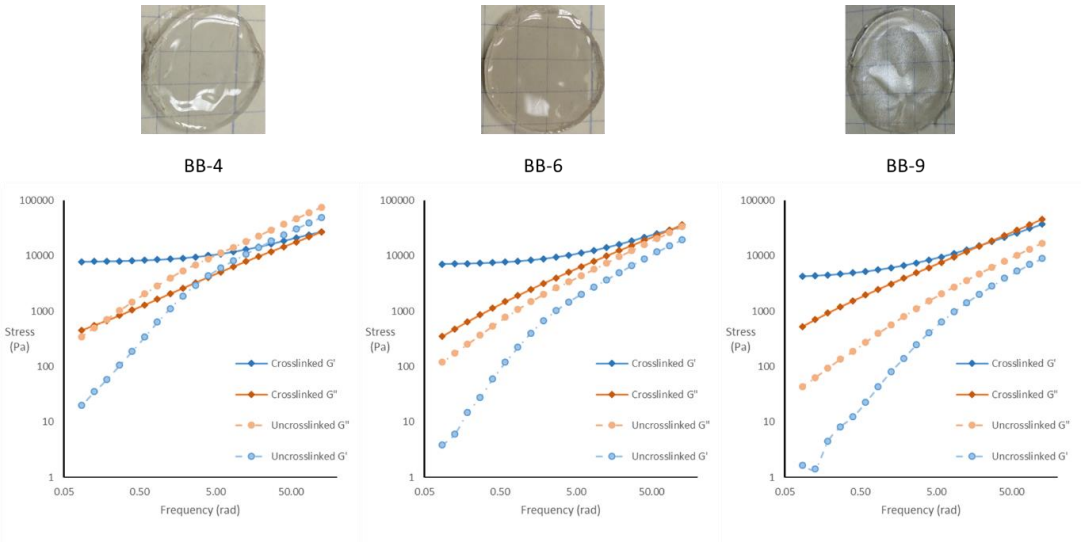


**Figure 167: Free standing crosslinked materials pictured on top with corresponding rheological measurements below showing a pronounced difference upon crosslinking consistent with the formation of a more elastic like solid.**

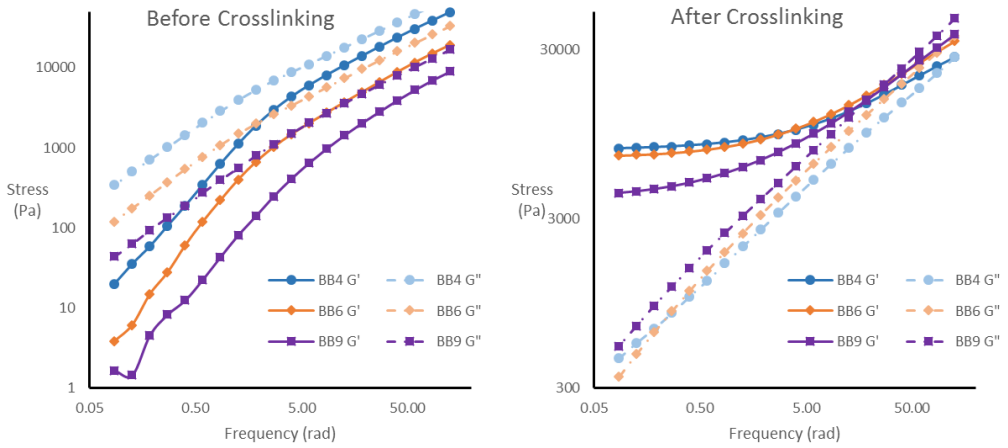


**Figure 168: Comparison of molecular weight effects on rheological properties of the uncrosslinked (left) and crosslinked (right) materials showing softer more compliant materials with increased macromonomer molecular weight.**

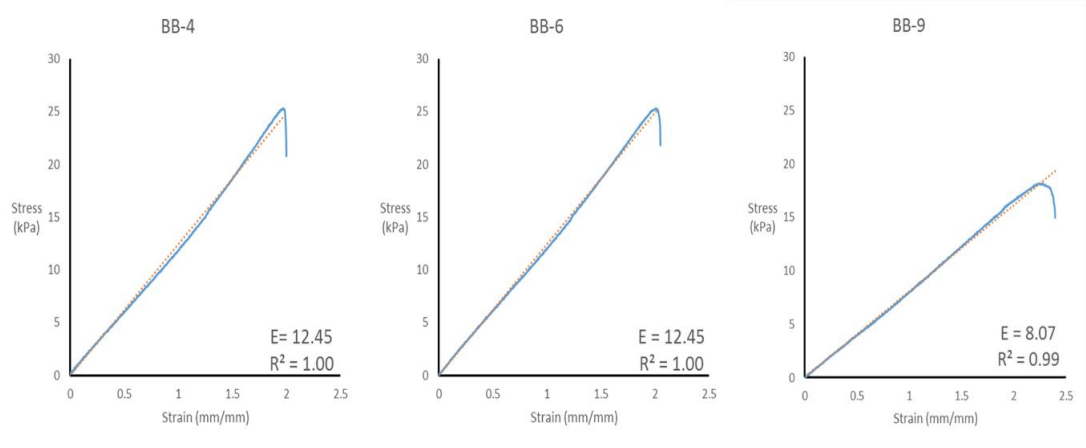


**Figure 169: tensile measurements for crosslinked bottlebrush materials.**

In order to demonstrate synthetic versatility beyond just butyl acrylate polymers, a diethylene glycol diethyl ether (DEGE) acrylate bottlebrush material was prepared (Figure 170). It was found to be necessary to first purify the commercial DEGE monomer via column chromatography over silica gel eluting with a gradient of ethyl acrylate in hexanes from 0% to 15% so as to remove any diacrylate impurities which would later cause crosslinking during the ROMP reaction. After this purification, the three step synthetic procedure proceeded without incident to afford well defined materials (Figure 171).

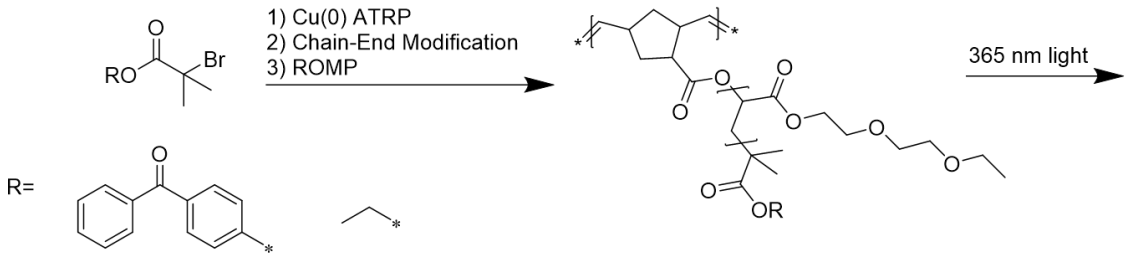


**Figure 170: Synthesis of DEGE based bottlebrush materials.**

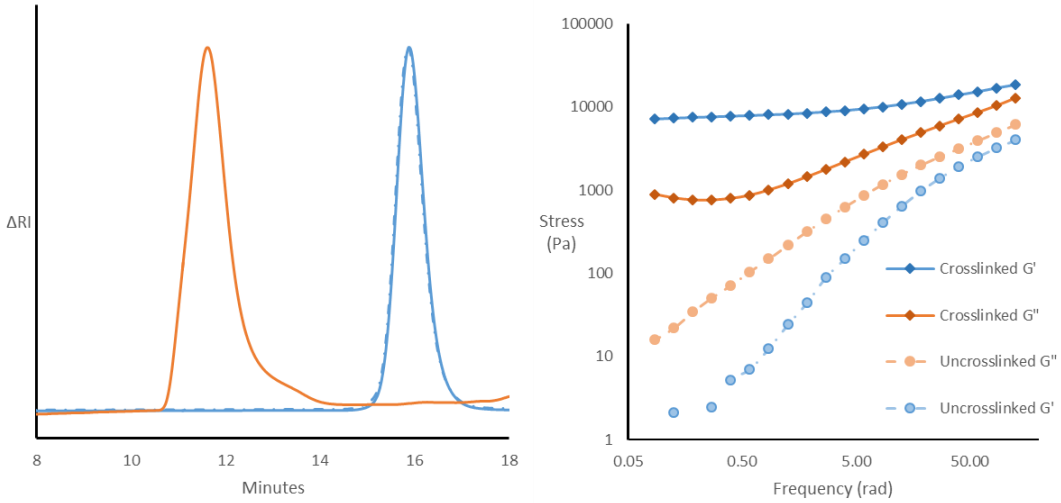


**Figure 171: GPC traces (chloroform) and molecular weights (left) and rheological properties (right) for DEGE based materials.**

Diethylene glycol diethyl ether acrylate is a more hydrophilic polymer than butyl acrylate and is known to be blood compatible[101]. One could imagine using such a DEGE bottlebrush in biomedical applications such as to make dialysis tubing more biocompatible or as a coating for stents as such biological interfaces require both the appropriate surface chemistry and mechanical properties for optimal functionality[102,103,104]. Water contact angle measurements were used to demonstrate the impact of this synthetic versatility on the resulting material properties (Figure 172). In this experiment, the BB-4, BB-6, and BB-DEGE materials were spread separately onto a plastic transparency slide and heated at 60°C in a vacuum oven overnight before being photo-cured under 365 nm light for 3 hours. The water contact angle for these thick crosslinked polymer films were then measured using 2 µl deionized water droplets three times for each material.

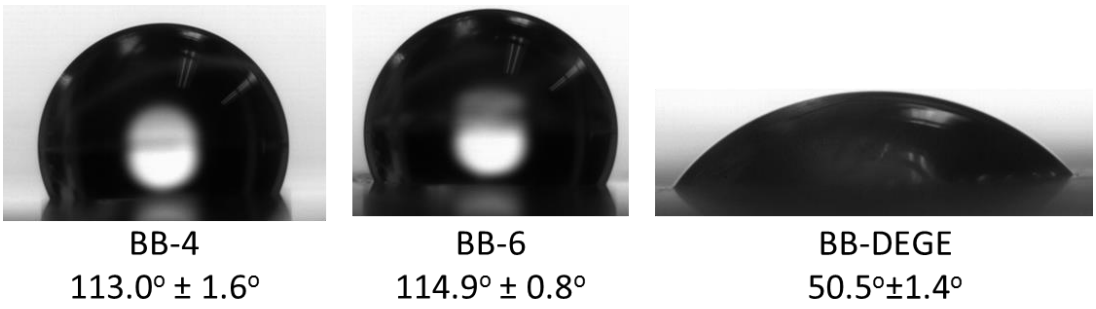


**Figure 172: Comparison of water contact angle showing more hydrophilic nature of the DEGE based bottlebrush network.**

Next, it was desired to expand this approach to more functional materials which would include available chemical moieties attached to the bottlebrush network for further functionalization. The first attempt to achieve this relied on incorporating a pentafluorophenol activated ester via ATRP initiator (Figure 173)[105]. It was discovered that this activated ester underwent undesired side reactions during the ATRP reaction as evidenced by $^{19}F$ NMR (Figure 174).

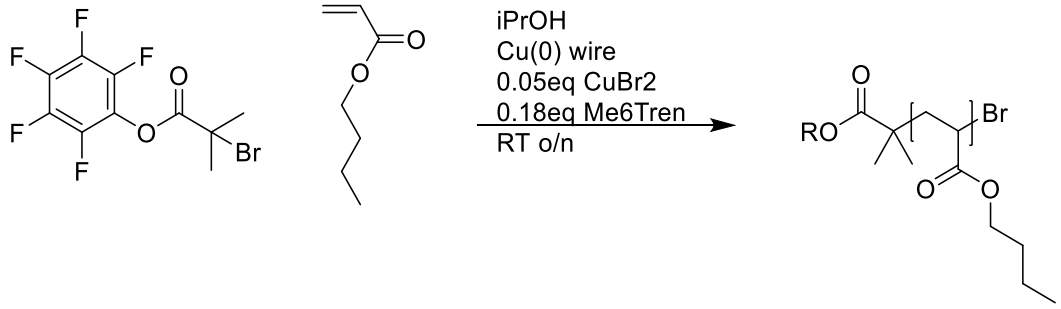


**Figure 173: Synthesis of functional polymer using pentafluorophenol ester based ATRP initiator.**

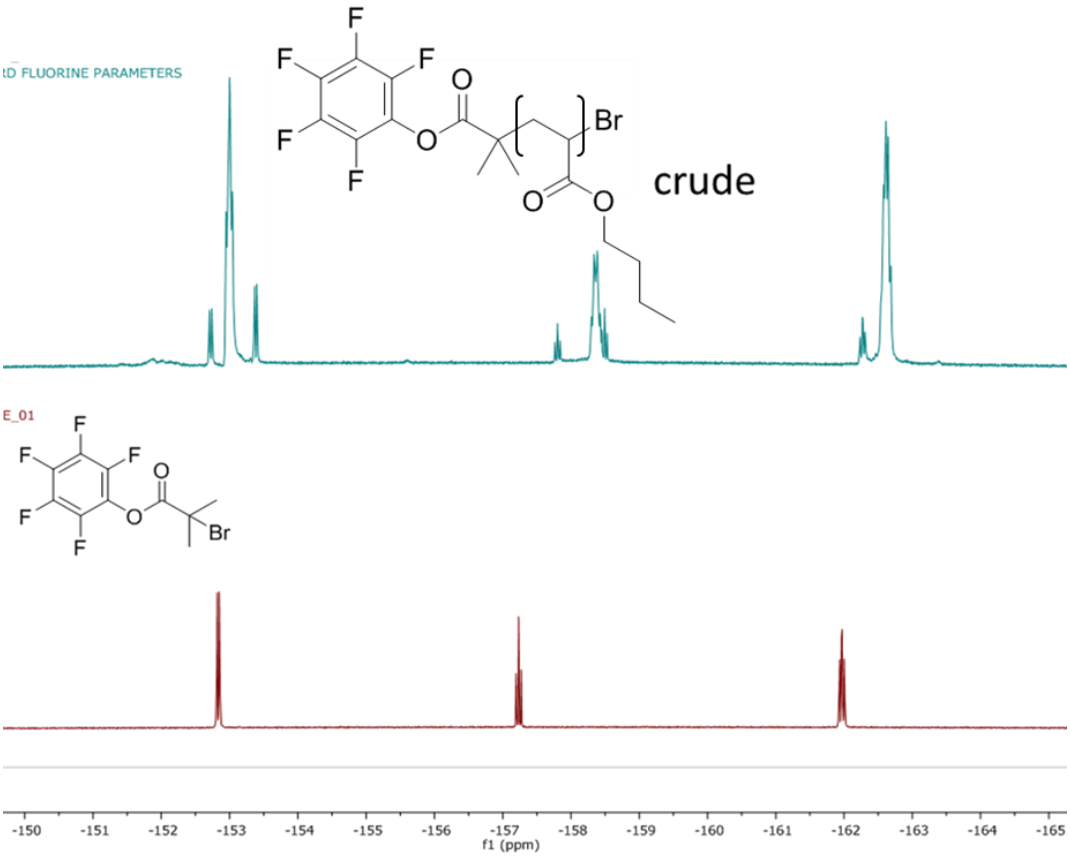


**Figure 174: $^{19}$F NMR spectra for the crude ATRP product (top) and pentafluorophenol ester initiator (bottom) showing evidence of side products during the ATRP reaction.**

A variety of conditions were then screen via $^{19}$F NMR by preparing mixtures of $CuBr_2$, ligand, solvent, and the pentafluorophenol initiator in NMR tubes and observing the $^{19}$F NMR signal after 20 hours at room temperature for various combinations of ligand and solvent (Figure 175). It was discovered that the pentafluorophenol initiator was most stable in the protic solvent isopropanol (iPrOH) with the pyridine type aromatic ligand bipyridine (bpy).

Bpy is not a sufficient catalyst for the ATRP of acrylates; however, tris(2-pyridylmethyl)amine (TPMA) is a ligand known to effect the ATRP of acrylates and

consists predominately of aromatic pyridine type amines rather than trialkyl amines so this ligand was

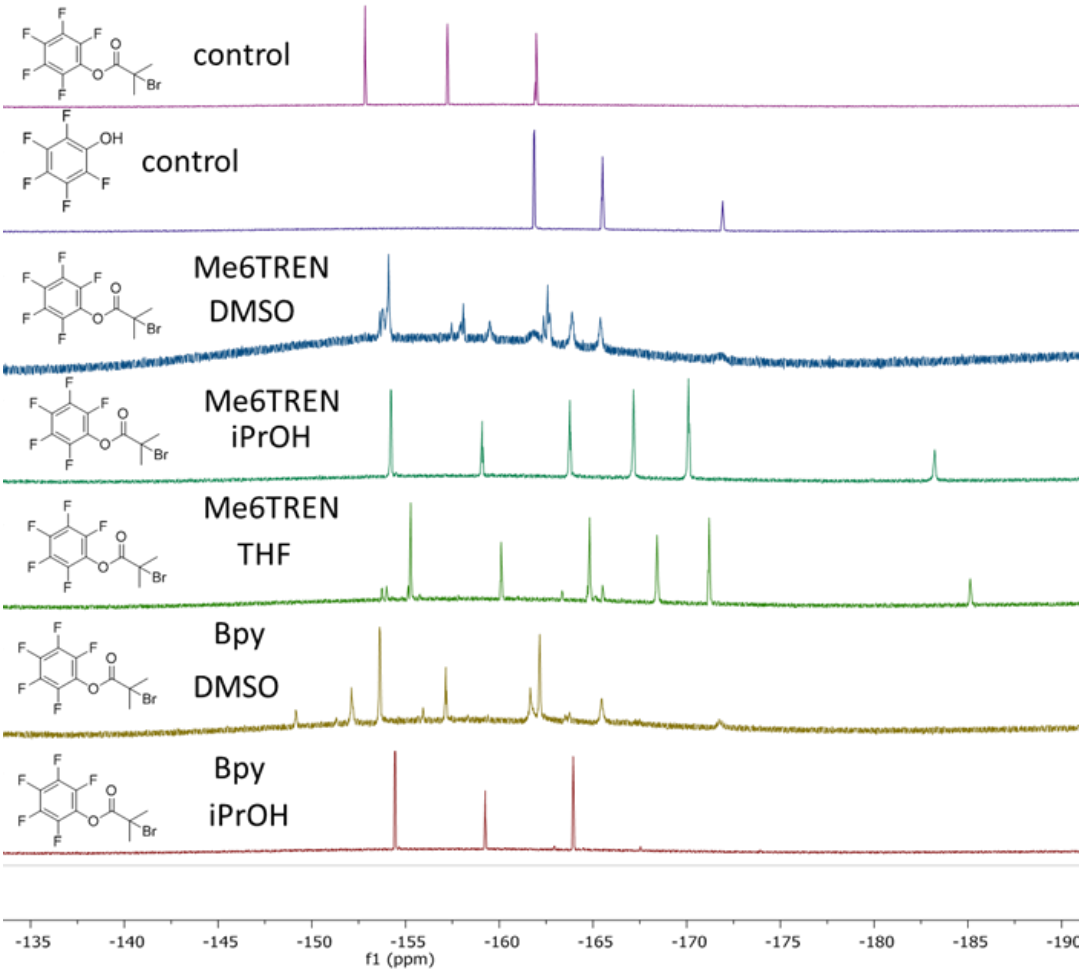


**Figure 175: 19F NMR screening of solvent and ligand combinations showing iPrOH/Bpy to be the most stable.**

tested next[105,106]. While the TPMA ligand did prove to enhance the stability of the pentafluorophenol ester under these reaction conditions relative to $Me_6$TREN and TPMA did effect polymerization of butyl acrylate under these conditions, there was still about 5% to 10% of undesired side product in the $^{19}$F NMR under these conditions (Figure 176-Figure 178).

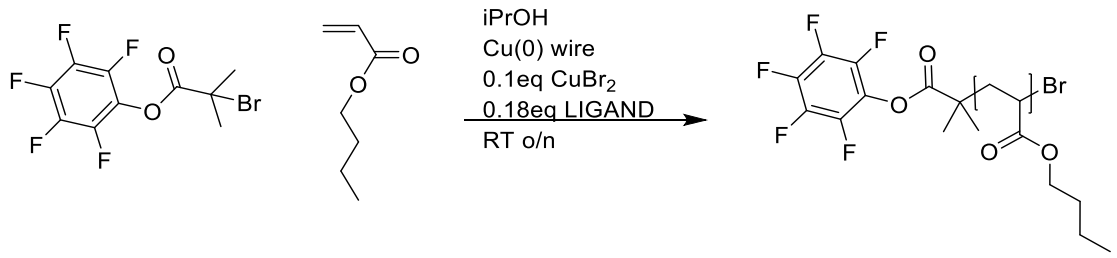


**Figure 176: ATRP reaction of pentafluorophenol ester based initiator using either TPMA or Me6TREN as the ligand.**

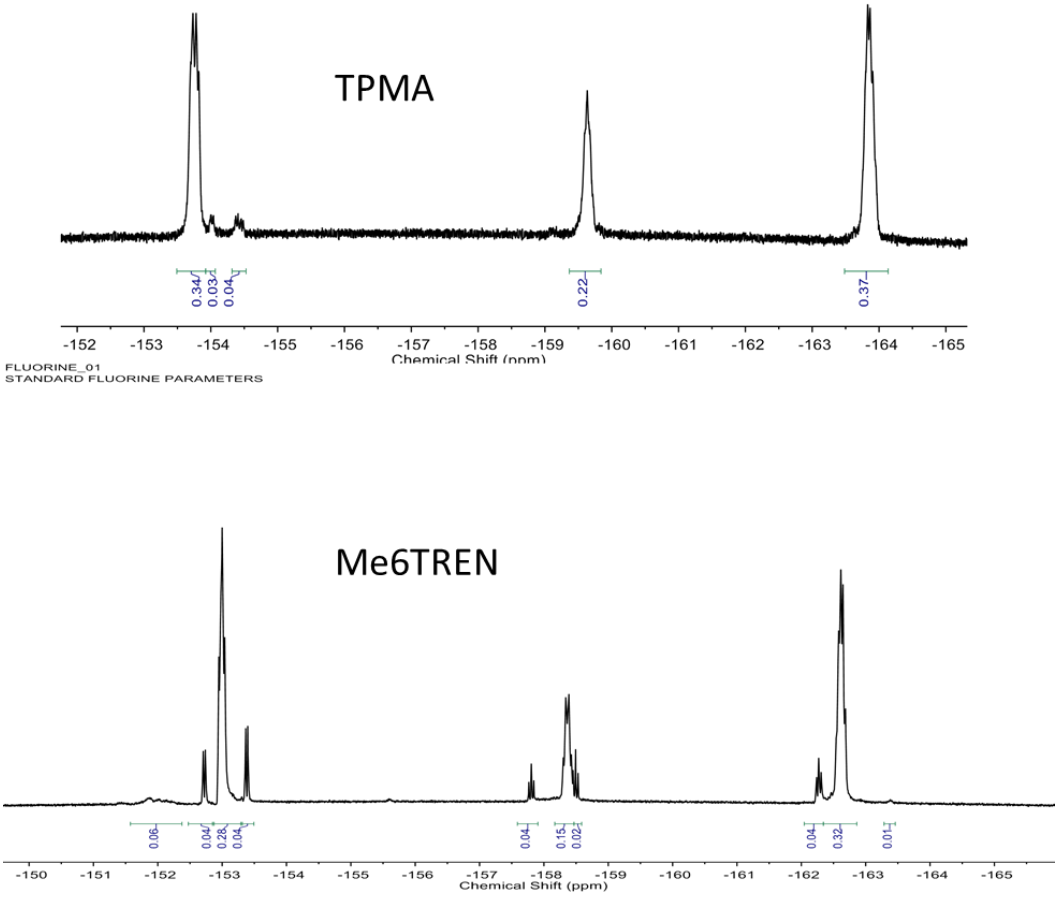


**Figure 177: 19F NMR spectra showing the pentafluorophenol ester to be more stable under the TPMA conditions than the Me6TREN conditions.**

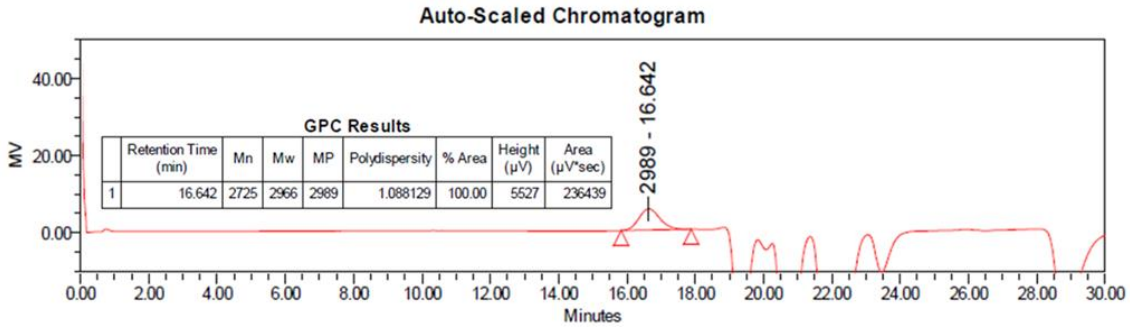


**Figure 178: GPC trace of ATRP product from using TPMA as ligand and pentafluorophenol as the initiator.**

For this reason, a new approach was sought. A boc protected amine based initiator was synthesized (Figure 179).

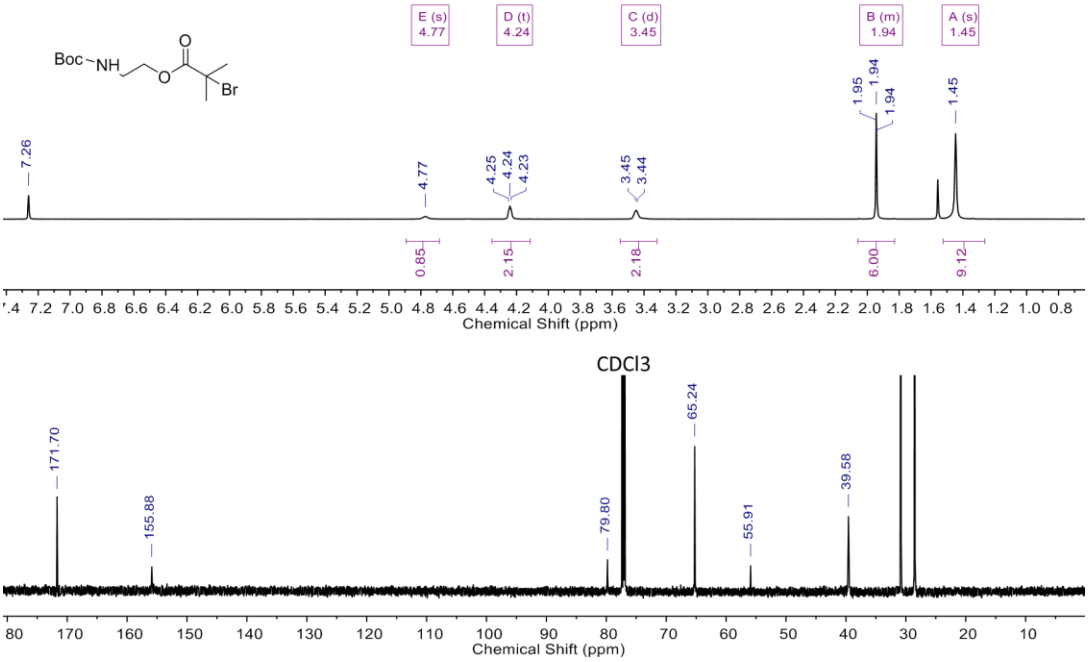


**Figure 179: 1H and 13C NMR spectra for boc protected amine based initiator.**

This boc-amine initiator proved successful in the 3 step synthetic procedure allowing the synthesis of well-defined bottlebrush materials with functional end groups (Figure 180).

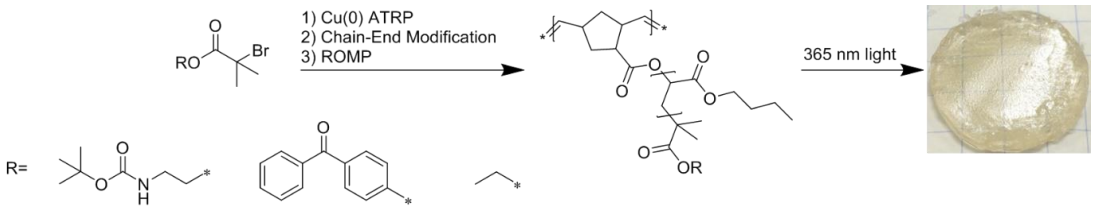


**Figure 180: Synthesis of boc protected amine functionalized bottlebrush materials.**

A sample using 10% boc-amine, 5% benzophenone, and 85% ethyl ATRP initiators was prepared as well as another sample using only the boc-amine initiator. The 10% boc-amine material had a macromonomer with a Mn of 3.5 kDa by NMR and 4.2 kDa by GPC (polystyrene equivalents) and a dipersity of 1.10 and a final bottlebrush Mn of 647 kDa by MALS GPC with a dispersity of 1.4. The 100% boc-amine initiator based material had used a macromonomer with a NMR Mn of 3.2 kDa, a GPC Mn of 4.3 kDa, and a dispersity of 1.1 to generate the bottlebrush material with a MALS GPC Mn of 110 kDa and dispersity of 1.4. For both polymer series, the GPC trace of the first ATRP step (solid line) overlaid well with the GPC trace of the second chain-end functionalization step (dashed line) (Figure 181).

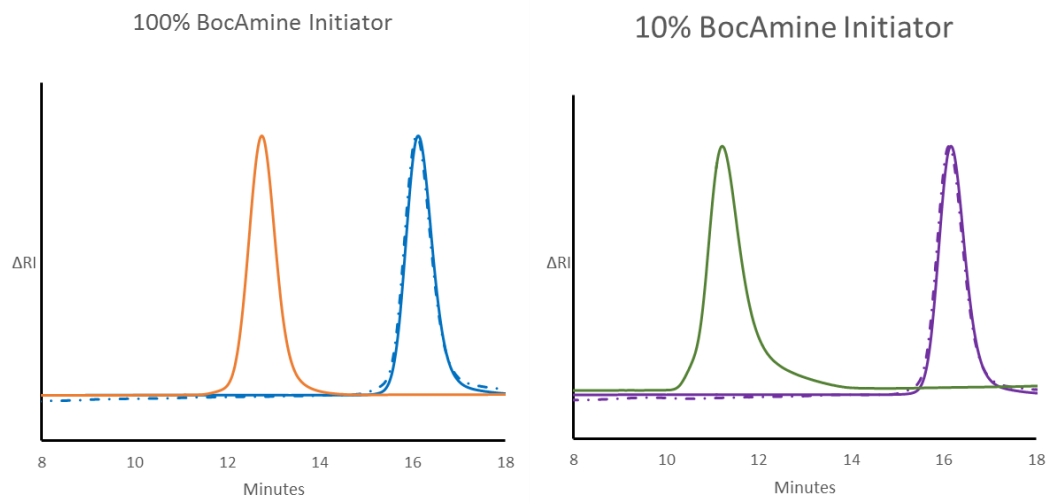


MM: 3.2 kDa (NMR); 4.3 kDa (GPC); Đ: 1.11
BB: 110 kDa (MALS); Đ: 1.4

MM: 3.5 kDa (NMR); 4.2 kDa (GPC); Đ: 1.10
BB: 647 kDa (MALS); Đ: 1.4

**Figure 181: Normalized GPC traces and measured molecular weights for materials made with either 100% boc-amine initiator (left) or 10% boc-amine initiator plus 5% benzophenone initiator plus 90% ethyl isobutyryl bromide (right).**

The deprotection of the boc group was first attempted via thermal deprotection which is known to occur starting at 150°C[107]. When the 100% boc-amine based material was heated to 150°C under nitrogen overnight, the material was observed to crosslink. While this suggests that thermal removal of the boc group was successful, it also suggests that the primary amine generated after loss of the boc group was reactive enough at this temperature to effect reaction with the butyl ester group to generate the amide with loss of butyl alcohol. Attempts to thermally deprotect the boc group at lower temperatures were unsuccessful. For this reason, a chemical deprotection strategy was employed. Boc groups are known to be easily removed under acidic conditions[107]. When the 100% boc-amine based material was treated with trifluoroacetic acid in chloroform, the boc group

was removed as evidenced by the loss of the tert-butyl ester resonances as well as the amide resonances from the $^{1}$H NMR spectra (Figure 182).

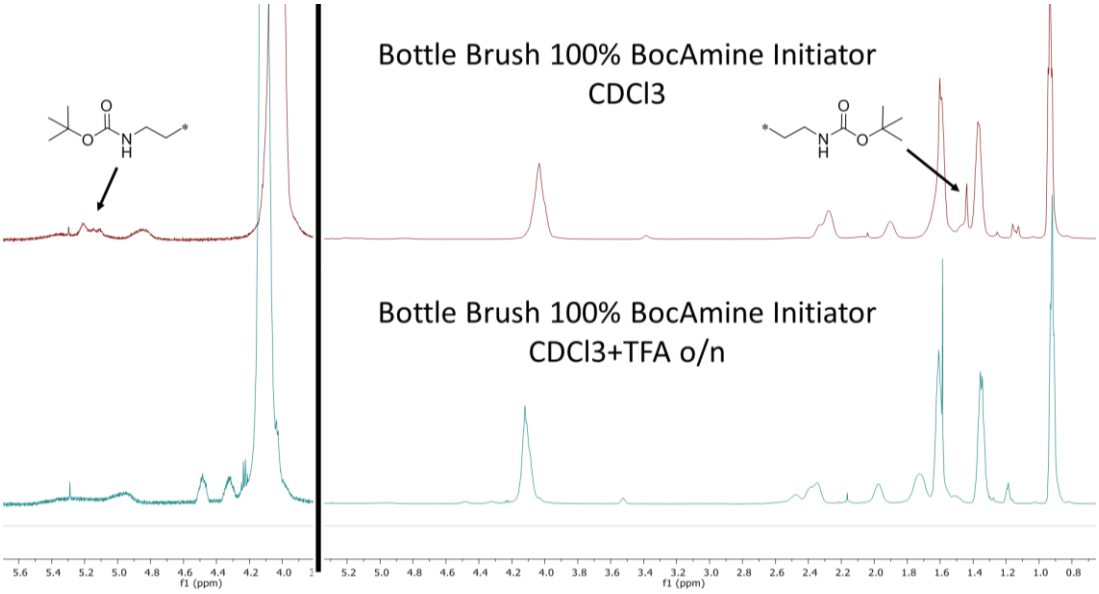


**Figure 182: $^{1}$H NMR spectra for boc-amine functionalized bottlebrush before (top) and after Boc deprotection with TFA/$CHCl_3$ (bottom).**

This strategy was then used to make bottlebrush networks with incorporated functional amines. First, crosslinked material were made from the 10% BocAmine based bottlebrush materials by applying the bottlebrush material to a PDMS mold on top of a Teflon substrate, heating in a vacuum oven at 60$^{o}$C, and then crosslinking for 3 hours with 365 nm light. A portion of this crosslinked material was then deprotected by submerging the material in TFA/$CHCl_3$ 1:2 at room temperature overnight. The solution was pipetted away and the material was soaked in chloroform for an hour. The solution was pipetted away and the material was soaked in a saturated solution of $KHCO_3$ in DMSO for an hour. The solution was replaced with a fresh solution of saturated $KHCO_3$ in DMSO and soaked for 6 hours before being replaced again with a fresh solution of saturated $KHCO_3$

in DMSO and soaked for an additional 5 hours. This solution was then replaced with pure DMSO and soaked for 1 hour before being replaced with ethanol and soaked for 1 hour. The ethanol then pipetted away and the crosslinked material was dried by heating in vacuum oven at 60°C for 30 min. A 10 mg/ml solution of dye (either fluorescein isothiocyanate or Rhodamine B isothiocyanate) in ethanol was then applied to the crosslinked material by touching a dye solution loaded pipette to the material's surface and letting the solution slowly wick into the material overnight. The dye functionalized crosslinked bottlebrush material was then wash with ethanol in a Soxhlet for two days. The exact same dye functionalization and washing procedure was applied to a separate non-deprotect portion of the crosslinked bottlebrush material. The deprotected material showed incorporation of the dyes after washing whereas the non-deprotect control material did not (Figure 183).

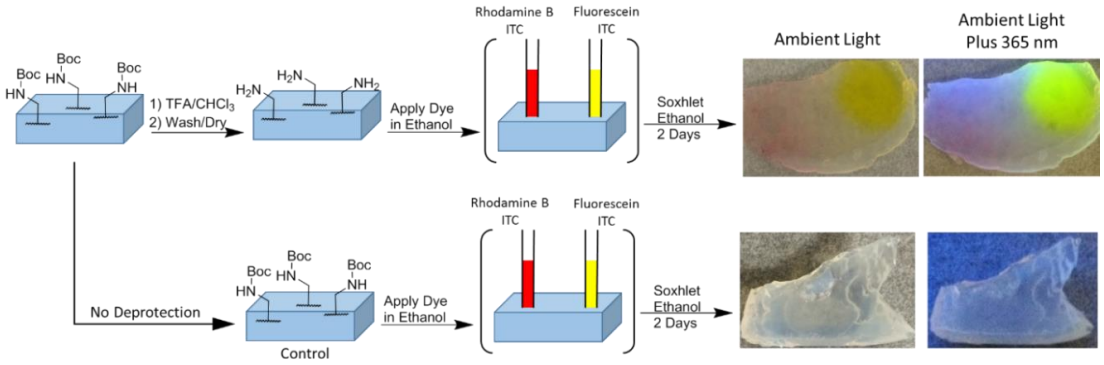


**Figure 183: Dye functionalization experiments showing dye incorporation in the deprotect bottlebrush network and no dye incorporation in the non-deprotected bottlebrush network control.**

Further characterization of these dye incorporation experiments were carried out using the Boc protected amine initiator and octylamine to represent the Boc protected control

bottlebrush network and the deprotect bottlebrush network respectively. These experiments were conducted by adding fluorescein isothiocyanate (FITC) to either the Boc protect amine initiator or octylamine followed by methanol-d4. The solution was kept at room temperature overnight before being analyzed by $^{1}$H NMR (Figure 184, Figure 185, Figure 186).

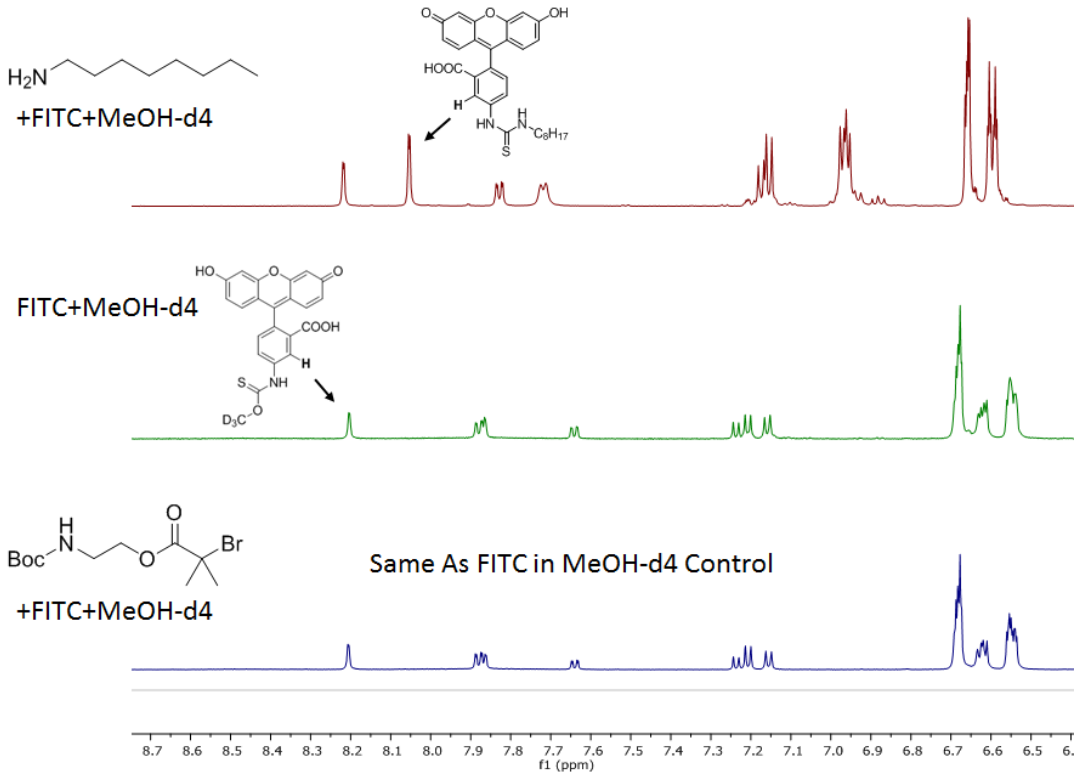


**Figure 184: $^{1}$H NMR (aryl region) of small molecule control reactions. The top shows successful reaction of the primary amine with FITC in MeOH-d4, the middle shows the FITC in MeOH-d4 control, and the bottom shows no reaction between the Boc protected amine and FITC in MeOH-d4.**

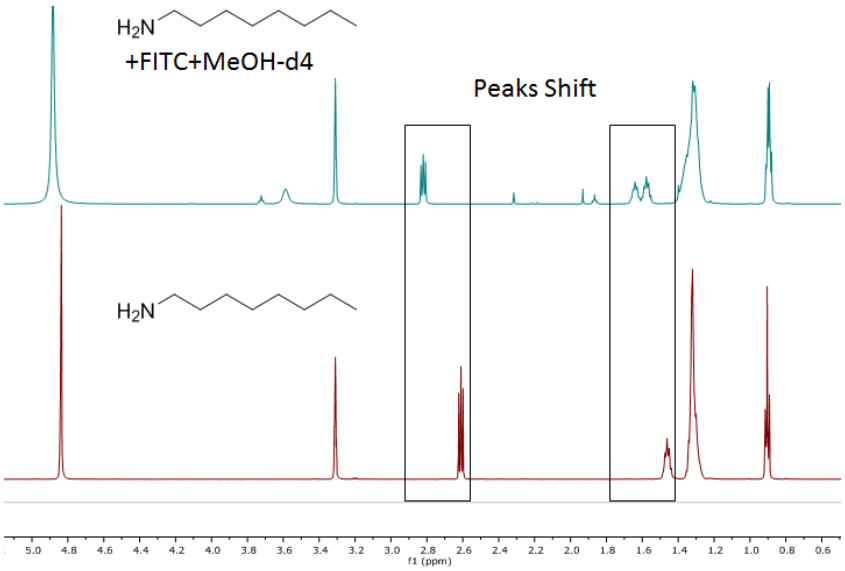


**Figure 185: $^{1}$H NMR (alkyl region) showing reaction of the primary amine with FITC in MeOH-d4.**

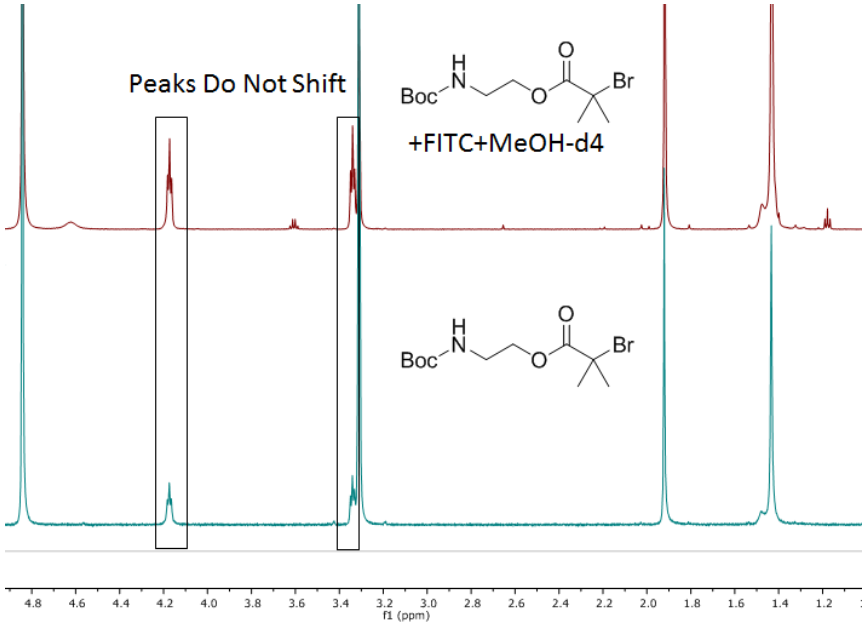


**Figure 186: $^{1}$H NMR (alkyl region) showing no reaction of the Boc protected amine control with FITC in MeOH-d4.**

These small molecule NMR experiments show the reaction of FITC with the primary amine and no reaction between FITC and the Boc protect amine control as expected. The reaction between the primary amine and FITC in methanol-d4 was then further confirmed via LC-MS which showed two separate peaks with one corresponding to the decomposition product of FITC with methanol-d4 and the other corresponding to the reaction product of FITC with the primary amine (Figure 187).

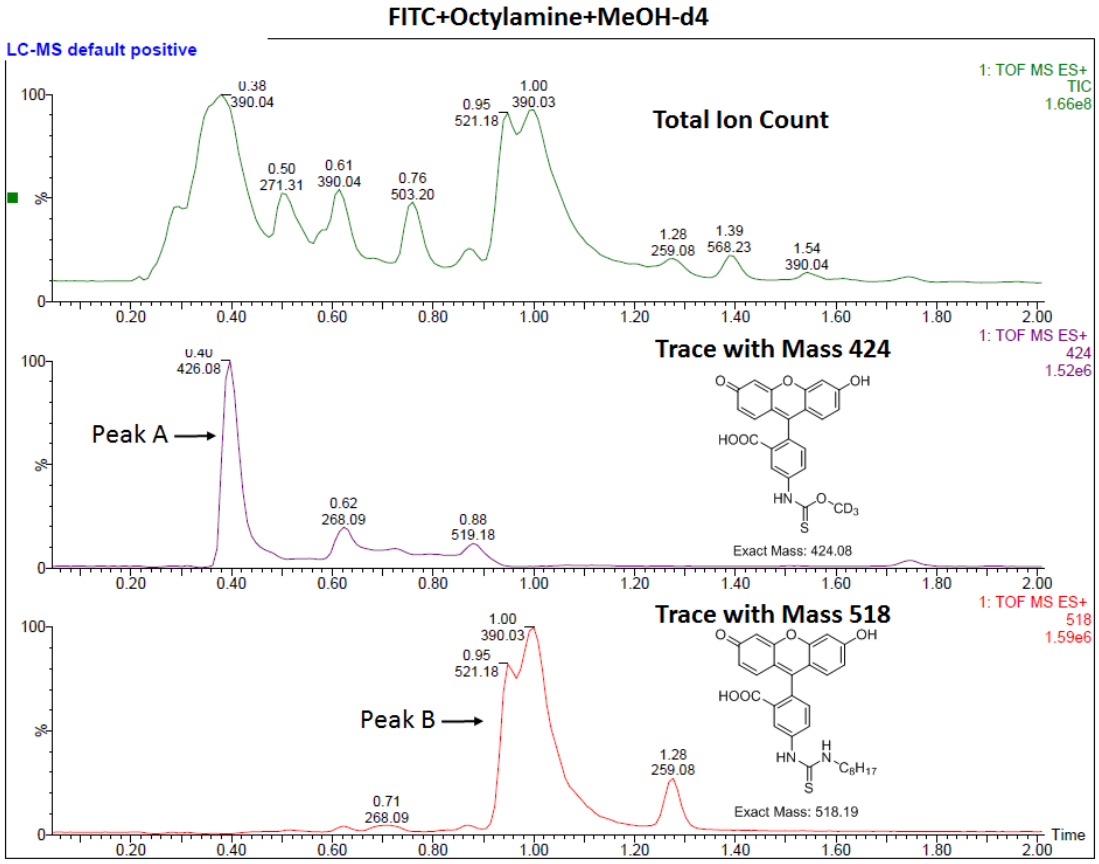


**Figure 187: LC-MS trace of total ion count with time in minutes (top), trace of observed mass 424 (middle), and trace of observed mass 518 (bottom) further confirming the reaction of the primary amine with FITC in methanol-d4.**

In conclusion, a simple, concise, and modular synthetic strategy for making functional photocrosslinkable bottlebrush networks has been developed. These well-defined materials can be modulated by tuning the molecular weight of the macromonomer, the chemical identity of the repeat unit, and the functionality of the initiator. This gives access to materials with tunable mechanical properties, surface properties, and chemical functionality. Such materials are of interest in the field of biomaterial science wherein the mechanical properties, surface properties, and chemical functionality of a biomaterial scaffold are known to impact cell biology, biocompatibility, and biomedical utility[108,109,110,111,112,113,114].

## VI. Conclusions

A novel pentacyclic building block has been developed utilizing a concise and modular synthetic strategy. This pentacyclic unit was demonstrated to have versatile properties enabling the synthesis of low band gap donor-acceptor polymers capable of operating in field effect transistors and solar cell devices as well as redox active quinone based materials which could potentially have applications in energy storage type applications. This simple approach both broadens the scope of available building blocks for organic electronic materials as well as making such materials more easily accessible.

A study on the effects of side-chain topology on conjugated polymer aggregation and resulting properties was conducted by comparing a novel macrocyclic benzodithiophene compound to its more traditional linear acyclic analogue. The macrocycle was observed to strongly effect the thermodynamics and kinetics of aggregation and self-assembly. In

small molecule model compounds, the melting entropy and enthalpy were both decreased as a result of the macrocyclic loop. Additionally, the macrocycle was observed to affect the geometric constrains of self-assembly and aggregation owing to the steric requirements of the more constrain macrocycle. In conjugated polymers, this was seen to decrease aggregation in solution and increase fluorescence relative to the acyclic analogues. In the solid state, π-π stacking was disrupted influencing texturing as well as the resulting morphology.

A simple synthetic approach to well-defined and functional bottlebrush networks was developed. This versatile approach was demonstrated to give access to materials with: 1) variable mechanical properties via tuning either the crosslinking density or the macromonomer molecular weight; 2) variable interfacial properties via changing the macromonomer repeat unit; and 3) variable functional chemical properties via incorporating latent functional groups in the material design. This simple and versatile platform enables easier access to a diverse array of interesting bottlebrush materials.

Together, these projects highlight the underlying structure-property relationship inherent to functional organic materials and both expands the scope of interesting structures and building blocks as well as making such structures and materials more easily accessible for future study and development. These projects span the range from novel molecular building blocks controlling the electronic structure of conjugated polymer backbones and their self-assembly to macromolecular architecture controlling the bulk mechanical properties of bottlebrush networks. Through these many length scales, molecules can be designed and materials engineered to possess the desired properties and functionalities necessary to meet future needs.

## References


1. Griffiths, David J. Introduction to Quantum Mechanics. 2nd Edition. Pearson Prentice Hall, 2005.
2. Coropceanu, Veaceslav, Jérôme Cornil, Demetrio A. da Silva Filho, Yoann Olivier, Robert Silbey, and Jean-Luc Brédas. "Charge transport in organic semiconductors." Chemical reviews 107, no. 4 (2007): 926-952.
3. Brédas, Jean-Luc, David Beljonne, Veaceslav Coropceanu, and Jérôme Cornil. "Charge-transfer and energy-transfer processes in π-conjugated oligomers and polymers: a molecular picture." Chemical reviews 104, no. 11 (2004): 4971-5004.
4. Hertel, D., H. Bässler, Ullrich Scherf, and H. H. Hörhold. "Charge carrier transport in conjugated polymers." The Journal of chemical physics 110, no. 18 (1999): 9214-9222.
5. Kline, R. J., and M. D. McGehee. "Morphology and charge transport in conjugated polymers." Journal of Macromolecular Science Part C: Polymer Reviews 46, no. 1 (2006): 27-45.
6. Noriega, Rodrigo, Jonathan Rivnay, Koen Vandewal, Felix PV Koch, Natalie Stingelin, Paul Smith, Michael F. Toney, and Alberto Salleo. "A general relationship between disorder, aggregation and charge transport in conjugated polymers." Nature materials 12, no. 11 (2013): 1038-1044.

7. Sheiko, Sergei S., Brent S. Sumerlin, and Krzysztof Matyjaszewski. "Cylindrical molecular brushes: Synthesis, characterization, and properties." Progress in Polymer Science 33, no. 7 (2008): 759-785.
8. Pakula, Tadeusz, Ying Zhang, Krzysztof Matyjaszewski, Hyung-il Lee, Hans Boerner, Shuhui Qin, and Guy C. Berry. "Molecular brushes as super-soft elastomers." Polymer 47, no. 20 (2006): 7198-7206.
9. Daniel, William FM, Joanna Burdyńska, Mohammad Vatankhah-Varnoosfaderani, Krzysztof Matyjaszewski, Jarosław Paturej, Michael Rubinstein, Andrey V. Dobrynin, and Sergei S. Sheiko. "Solvent-free, supersoft and superelastic bottlebrush melts and networks." Nature materials 15, no. 2 (2016): 183-189.
10. Zou, Yingping, Ahmed Najari, Philippe Berrouard, Serge Beaupré, Badrou Réda Aïch, Ye Tao, and Mario Leclerc. "A thieno [3, 4-c] pyrrole-4, 6-dione-based copolymer for efficient solar cells." Journal of the American Chemical Society 132, no. 15 (2010): 5330-5331.
11. Zhang, Yong, Steven K. Hau, Hin-Lap Yip, Ying Sun, Orb Acton, and Alex K-Y. Jen. "Efficient polymer solar cells based on the copolymers of benzodithiophene and thienopyrroledione." Chemistry of Materials 22, no. 9 (2010): 2696-2698.
12. Piliego, Claudia, Thomas W. Holcombe, Jessica D. Douglas, Claire H. Woo, Pierre M. Beaujuge, and Jean MJ Fréchet. "Synthetic control of structural order in N-alkylthieno [3, 4-c] pyrrole-4, 6-dione-based polymers for efficient solar cells." Journal of the American Chemical Society 132, no. 22 (2010): 7595-7597.

13. Hou, Jianhui, Mi-Hyae Park, Shaoqing Zhang, Yan Yao, Li-Min Chen, Juo-Hao Li, and Yang Yang. "Bandgap and molecular energy level control of conjugated polymer photovoltaic materials based on benzo [1, 2-b: 4, 5-b′] dithiophene." Macromolecules 41, no. 16 (2008): 6012-6018.
14. Wolfe, Rylan MW, and John R. Reynolds. "Direct Imide Formation from Thiophene Dicarboxylic Acids Gives Expanded Side-Chain Selection in Thienopyrrolediones." Organic Letters 19, no. 5 (2017): 996-999.
15. Cabanetos, Clément, Abdulrahman El Labban, Jonathan A. Bartelt, Jessica D. Douglas, William R. Mateker, Jean MJ Fréchet, Michael D. McGehee, and Pierre M. Beaujuge. "Linear side chains in benzo [1, 2-b: 4, 5-b′] dithiophene–thieno [3, 4-c] pyrrole-4, 6-dione polymers direct self-assembly and solar cell performance." Journal of the American Chemical Society 135, no. 12 (2013): 4656-4659.
16. El Labban, Abdulrahman, Julien Warnan, Clement Cabanetos, Olivier Ratel, Christopher Tassone, Michael F. Toney, and Pierre M. Beaujuge. "Dependence of crystallite formation and preferential backbone orientations on the side chain pattern in PBDTTPD polymers." ACS applied materials & interfaces 6, no. 22 (2014): 19477-19481.
17. Graham, Kenneth R., Clement Cabanetos, Justin P. Jahnke, Matthew N. Idso, Abdulrahman El Labban, Guy O. Ngongang Ndjawa, Thomas Heumueller et al. "Importance of the donor: fullerene intermolecular arrangement for high-efficiency organic photovoltaics." Journal of the American Chemical Society 136, no. 27 (2014): 9608-9618.

18. Constantinou, Iordania, Tzung-Han Lai, Erik D. Klump, Subhadip Goswami, Kirk S. Schanze, and Franky So. "Effect of polymer side chains on charge generation and disorder in PBDTTPD solar cells." ACS applied materials & interfaces 7, no. 48 (2015): 26999-27005.
19. Bartelt, Jonathan A., Zach M. Beiley, Eric T. Hoke, William R. Mateker, Jessica D. Douglas, Brian A. Collins, John R. Tumbleston et al. "The importance of fullerene percolation in the mixed regions of polymer–fullerene bulk heterojunction solar cells." Advanced Energy Materials 3, no. 3 (2013): 364-374.
20. Aïch, Badrou Réda, Jianping Lu, Serge Beaupré, Mario Leclerc, and Ye Tao. "Control of the active layer nanomorphology by using co-additives towards high-performance bulk heterojunction solar cells." Organic Electronics 13, no. 9 (2012): 1736-1741.
21. Bartelt, Jonathan A., Jessica D. Douglas, William R. Mateker, Abdulrahman El Labban, Christopher J. Tassone, Michael F. Toney, Jean MJ Fréchet, Pierre M. Beaujuge, and Michael D. McGehee. "Controlling Solution-Phase Polymer Aggregation with Molecular Weight and Solvent Additives to Optimize Polymer-Fullerene Bulk Heterojunction Solar Cells." Advanced Energy Materials 4, no. 9 (2014).
22. Mühlbacher, David, Markus Scharber, Mauro Morana, Zhengguo Zhu, David Waller, Russel Gaudiana, and Christoph Brabec. "High photovoltaic performance of a low-bandgap polymer." Advanced Materials 18, no. 21 (2006): 2884-2889.
23. Zhu, Zhengguo, David Waller, Russell Gaudiana, Mauro Morana, David Mühlbacher, Markus Scharber, and Christoph Brabec. "Panchromatic conjugated

polymers containing alternating donor/acceptor units for photovoltaic applications." Macromolecules 40, no. 6 (2007): 1981-1986.

24. Hou, Jianhui, Hsiang-Yu Chen, Shaoqing Zhang, Gang Li, and Yang Yang. "Synthesis, characterization, and photovoltaic properties of a low band gap polymer based on silole-containing polythiophenes and 2, 1, 3-benzothiadiazole." Journal of the American Chemical Society 130, no. 48 (2008): 16144-16145.
25. Tamao, Kohei, Manabu Uchida, Takenori Izumizawa, Kenji Furukawa, and Shigehiro Yamaguchi. "Silole derivatives as efficient electron transporting materials." Journal of the American Chemical Society 118, no. 47 (1996): 11974-11975.
26. Peet, Jeffery, Jin Young Kim, Nelson E. Coates, Wang Li Ma, Daniel Moses, Alan J. Heeger, and Guillermo C. Bazan. "Efficiency enhancement in low-bandgap polymer solar cells by processing with alkane dithiols." Nature materials 6, no. 7 (2007): 497-500.
27. Peet, Jeffrey, Nam Sung Cho, Sang Kyu Lee, and Guillermo C. Bazan. "Transition from solution to the solid state in polymer solar cells cast from mixed solvents." Macromolecules 41, no. 22 (2008): 8655-8659.
28. Gu, Yu, Cheng Wang, and Thomas P. Russell. "Multi-Length-Scale Morphologies in PCPDTBT/PCBM Bulk-Heterojunction Solar Cells." Advanced Energy Materials 2, no. 6 (2012): 683-690.
29. Rogers, James T., Kristin Schmidt, Michael F. Toney, Edward J. Kramer, and Guillermo C. Bazan. "Structural order in bulk heterojunction films prepared with solvent additives." Advanced materials 23, no. 20 (2011): 2284-2288.

30. Agostinelli, Tiziano, Toby AM Ferenczi, E. Pires, Samuel Foster, Andrea Maurano, Christian Müller, Amy Ballantyne et al. "The role of alkane dithiols in controlling polymer crystallization in small band gap polymer: fullerene solar cells." Journal of Polymer Science Part B: Polymer Physics 49, no. 10 (2011): 717-724.
31. Fischer, F. S. U., K. Tremel, A-K. Saur, S. Link, N. Kayunkid, M. Brinkmann, D. Herrero-Carvajal, JT López Navarrete, MC Ruiz Delgado, and S. Ludwigs. "Influence of processing solvents on optical properties and morphology of a semicrystalline low bandgap polymer in the neutral and charged states." Macromolecules 46, no. 12 (2013): 4924-4931.
32. Schulz, G. L., F. S. U. Fischer, D. Trefz, Anton Melnyk, A. Hamidi-Sakr, M. Brinkmann, Denis Andrienko, and S. Ludwigs. "The PCPDTBT Family: Correlations between Chemical Structure, Polymorphism, and Device Performance." Macromolecules 50, no. 4 (2017): 1402-1414.
33. Fischer, Florian SU, Daniel Trefz, Justus Back, Navaphun Kayunkid, Benjamin Tornow, Steve Albrecht, Kevin G. Yager et al. "Highly Crystalline Films of PCPDTBT with Branched Side Chains by Solvent Vapor Crystallization: Influence on Opto-Electronic Properties." Advanced Materials 27, no. 7 (2015): 1223-1228.
34. Fischer, Florian SU, Navaphun Kayunkid, Daniel Trefz, Sabine Ludwigs, and Martin Brinkmann. "Structural Models of Poly (cyclopentadithiophene-alt-benzothiadiazole) with Branched Side Chains: Impact of a Single Fluorine Atom

on the Crystal Structure and Polymorphism of a Conjugated Polymer." Macromolecules 48, no. 12 (2015): 3974-3982.

35. Scharsich, Christina, Florian SU Fischer, Kevin Wilma, Richard Hildner, Sabine Ludwigs, and Anna Köhler. "Revealing structure formation in PCPDTBT by optical spectroscopy." Journal of Polymer Science Part B: Polymer Physics 53, no. 20 (2015): 1416-1430.
36. Takacs, Christopher J., Michael A. Brady, Neil D. Treat, Edward J. Kramer, and Michael L. Chabinyc. "Quadrites and crossed-chain crystal structures in polymer semiconductors." Nano letters 14, no. 6 (2014): 3096-3101.
37. Scharber, Markus C., Markus Koppe, Jia Gao, Fabrizio Cordella, Maria Loi, Patrick Denk, Mauro Morana et al. "Influence of the Bridging Atom on the Performance of a Low-Bandgap Bulk Heterojunction Solar Cell." Advanced materials 22, no. 3 (2010): 367-370.
38. Chen, Hsiang-Yu, Jianhui Hou, Amy E. Hayden, Hoichang Yang, K. N. Houk, and Yang Yang. "Silicon Atom Substitution Enhances Interchain Packing in a Thiophene-Based Polymer System." Advanced materials 22, no. 3 (2010): 371-375.
39. Morana, Mauro, Hamed Azimi, Gilles Dennler, Hans-Joachim Egelhaaf, Markus Scharber, Karen Forberich, Jens Hauch et al. "Nanomorphology and Charge Generation in Bulk Heterojunctions Based on Low-Bandgap Dithiophene Polymers with Different Bridging Atoms." Advanced Functional Materials 20, no. 7 (2010): 1180-1188.

40. Schaffer, Christoph J., Johannes Schlipf, Efi Dwi Indari, Bo Su, Sigrid Bernstorff, and Peter Müller-Buschbaum. "Effect of Blend Composition and Additives on the Morphology of PCPDTBT: PC71BM Thin Films for Organic Photovoltaics." ACS applied materials & interfaces 7, no. 38 (2015): 21347-21355.
41. Guilbert, Anne AY, Jarvist M. Frost, Tiziano Agostinelli, Ellis Pires, Samuele Lilliu, J. Emyr Macdonald, and Jenny Nelson. "Influence of bridging atom and side chains on the structure and crystallinity of cyclopentadithiophene–benzothiadiazole polymers." Chemistry of Materials 26, no. 2 (2014): 1226-1233.
42. Huo, Lijun, Shaoqing Zhang, Xia Guo, Feng Xu, Yongfang Li, and Jianhui Hou. "Replacing alkoxy groups with alkylthienyl groups: a feasible approach to improve the properties of photovoltaic polymers." Angewandte Chemie 123, no. 41 (2011): 9871-9876.
43. Liao, Sih-Hao, Hong-Jyun Jhuo, Po-Nan Yeh, Yu-Shan Cheng, Yi-Lun Li, Yu-Hsuan Lee, Sunil Sharma, and Show-An Chen. "Single junction inverted polymer solar cell reaching power conversion efficiency 10.31% by employing dual-doped zinc oxide nano-film as cathode interlayer." Scientific reports 4 (2014): srep06813.
44. Liao, Sih-Hao, Hong-Jyun Jhuo, Yu-Shan Cheng, and Show-An Chen. "Fullerene Derivative-Doped Zinc Oxide Nanofilm as the Cathode of Inverted Polymer Solar Cells with Low-Bandgap Polymer (PTB7-Th) for High Performance." Advanced materials 25, no. 34 (2013): 4766-4771.
45. Liu, Chang, Chao Yi, Kai Wang, Yali Yang, Ram S. Bhatta, Mesfin Tsige, Shuyong Xiao, and Xiong Gong. "Single-junction polymer solar cells with over

10% efficiency by a novel two-dimensional donor–acceptor conjugated copolymer." ACS applied materials & interfaces 7, no. 8 (2015): 4928-4935.

46. Wan, Qun, Xia Guo, Zaiyu Wang, Wanbin Li, Bing Guo, Wei Ma, Maojie Zhang, and Yongfang Li. "10.8% Efficiency Polymer Solar Cells Based on PTB7-Th and PC71BM via Binary Solvent Additives Treatment." Advanced Functional Materials 26, no. 36 (2016): 6635-6640.
47. Liu Peng, Kai Zhang, Feng Liu, Yaocheng Jin, Shengjian Liu, Thomas P. Russell, Hin-Lap Yip, Fei Huang, and Yong Cao. "Effect of fluorine content in thienothiophene-benzodithiophene copolymers on the morphology and performance of polymer solar cells." Chemistry of Materials 26, no. 9 (2014): 3009-3017.
48. Huang, Wenchao, Eliot Gann, Naresh Chandrasekaran, Lars Thomsen, Shyamal KK Prasad, Justin Hodgkiss, Dinesh Kabra, Yi-Bing Cheng, and Christopher R. McNeill. "Isolating and Quantifying the Impact of Domain Purity on the Performance of Bulk Heterojunction Solar Cells." Energy & Environmental Science (2017). DOI: 10.1039/c7ee01387f
49. Collins, Brian A., Zhe Li, John R. Tumbleston, Eliot Gann, Christopher R. McNeill, and Harald Ade. "Absolute measurement of domain composition and nanoscale size distribution explains performance in PTB7: PC71BM solar cells." Advanced Energy Materials 3, no. 1 (2013): 65-74.
50. Saxon, A.M.; Liepins, F.; Aldissi, M. (1985). "Polyacetylene: Its Synthesis, Doping, and Structure". Prog. Polym. Sci. 11: 57.

51. MacDiarmid, Alan G. (2001). ""Synthetic Metals": A Novel Role for Organic Polymers (Nobel Lecture)". Angewandte Chemie International Edition. 40 (14): 2581

52. Venkateshvaran, Deepak, Mark Nikolka, Aditya Sadhanala, Vincent Lemaur, Mateusz Zelazny, Michal Kepa, Michael Hurhangee et al. "Approaching disorder-free transport in high-mobility conjugated polymers." Nature 515, no. 7527 (2014): 384-388.

53. Zhang, Shaoqing, Long Ye, Wenchao Zhao, Delong Liu, Huifeng Yao, and Jianhui Hou. "Side chain selection for designing highly efficient photovoltaic polymers with 2D-conjugated structure." Macromolecules 47, no. 14 (2014): 4653-4659.

54. Vezie, M. S.; Few, S.; Meager, I.; Pieridou, G.; Dörling, B.; Ashraf, R. S.; Goñi, A. R.; Bronstein, H.; McCulloch, I.; Hayes, S. C.; Campoy-Quiles, M.; Nelson, J. Nature Materials 2016, 15, 746–753.

55. Yuan, M., Durban, M.M., Kazarinoff, P.D., Zeigler, D.F., Rice, A.H., Segawa, Y. and Luscombe, C.K., Journal of Polymer Science Part A: Polymer Chemistry, 2013, 51(19), 4061-4069.

56. Yuan, M., Yang, P., Durban, M.M. and Luscombe, C.K., Macromolecules, 2012, 45(15), pp.5934-5940.

57. Acharya, R. V.; Tilak, B. D.; Venkiteswaran, M. R. J. Sci. Ind. Res. 1957, 16B, 400.

58. Gripenberg, J.; Lounasmaa, M. Acta Chemica Scandinavica 1965, 19 1063-1070.

59. Phillip M. Hudnall "Hydroquinone" in Ullmann's Encyclopedia of Industrial Chemistry 2002, Wiley-VCH, Weinheim. 2005 Wiley-VCH, Weinheim.
60. Wang, Xiaochen, Song Chen, Yeping Sun, Maojie Zhang, Yongfang Li, Xiaoyu Li, and Haiqiao Wang. "A furan-bridged D-π-A copolymer with deep HOMO level: synthesis and application in polymer solar cells." Polymer Chemistry 2, no. 12 (2011): 2872-2877.
61. Yuning, L.; Sonar, P.; Murphy, L.; Hong, W. Energy & Environmental Science 2013, 6, 1684-1710.
62. Chen, Z., Lee, M.J., Shahid Ashraf, R., Gu, Y., Albert-Seifried, S., Meedom Nielsen, M., Schroeder, B., Anthopoulos, T.D., Heeney, M., McCulloch, I. and Sirringhaus, H. Advanced materials, 2012, 24(5), pp.647-652.
63. Schulz, G. L., F. S. U. Fischer, D. Trefz, Anton Melnyk, A. Hamidi-Sakr, M. Brinkmann, Denis Andrienko, and S. Ludwigs. "The PCPDTBT Family: Correlations between Chemical Structure, Polymorphism, and Device Performance." Macromolecules 50, no. 4 (2017): 1402-1414.
64. Sirringhaus, Henning, P. J. Brown, R. H. Friend, Martin Meedom Nielsen, Klaas Bechgaard, B. M. W. Langeveld-Voss, A. J. H. Spiering et al. "Two-dimensional charge transport in self-organized, high-mobility conjugated polymers." Nature 401, no. 6754 (1999): 685-688.
65. Li W, Roelofs WS, Wienk MM, Janssen RA. Enhancing the photocurrent in diketopyrrolopyrrole-based polymer solar cells via energy level control. Journal of the American Chemical Society. 134: 13787-95

66. Chen, Xiao, Jiao-Jie Li, Xue-Shi Hao, Charles E. Goodhue, and Jin-Quan Yu. "Palladium-Catalyzed Alkylation of Aryl C− H Bonds with sp3 Organotin Reagents Using Benzoquinone as a Crucial Promoter." Journal of the American Chemical Society 128, no. 1 (2006): 78-79.
67. Jung, Michael E., and Pierre Koch. "Mild, selective deprotection of PMB ethers with triflic acid/1, 3-dimethoxybenzene." Tetrahedron letters 52, no. 46 (2011): 6051-6054.
68. Chabinyc, Michael L. "X-ray Scattering from Films of Semiconducting Polymers." Polymer Reviews 48, no. 3 (2008): 463-492.
69. Huskinson, B.; Marshak, M. P.; Suh, C.; Er, S.; Gerhardt, M. R.; Galvin, C. J.; Chen, X.; Aspuru-Guzik, A.; Gordon, R. G.; Aziz, M. J. Nature 2014, 505, 195–198.
70. Vonlanthen, D.; Lazarev, P.; See, K. A.; Wudl, F.; Heeger, A. J. Advanced Materials 2014, 26, 5095-5100.
71. Mamada, M.; Kumaki, D.; Nishida, J.; Tokito, S.; Yamashita, Y. ACS Applied Materials & Interfaces 2010, 2, 1303-1307.
72. Akagi, Kazuo, Andrew B. Holmes, Richard McCullough, Alaa S. Abd-El-Aziz, Pierre Audebert, Stephen Craig, Lynn Loo et al. Conjugated polymers: a practical guide to synthesis. Royal Society of Chemistry, 2013.
73. Yao, Huifeng, Long Ye, Hao Zhang, Sunsun Li, Shaoqing Zhang, and Jianhui Hou. "Molecular design of benzodithiophene-based organic photovoltaic materials." Chem. Rev 116, no. 12 (2016): 7397-7457.

74. Lüttringhaus, A. "Über vielgliedrige Ringsysteme: X. Neuartige Dioxybenzol- und Dioxynaphtalinäther." European Journal of Organic Chemistry 528, no. 1 (1937): 181-210.
75. Kanda, Kazumasa, Kohei Endo, and Takanori Shibata. "Enantioselective Synthesis of Planar-Chiral 1, n-Dioxa [n] paracyclophanes via Catalytic Asymmetric ortho-Lithiation." Organic letters 12, no. 9 (2010): 1980-1983.
76. Bolduc, Philippe, Alexandre Jacques, and Shawn K. Collins. "Efficient Macrocyclization Achieved via Conformational Control Using Intermolecular Noncovalent π-Cation/Arene Interactions." Journal of the American Chemical Society 132, no. 37 (2010): 12790-12791.
77. Raymond, Michaël, Michael Holtz-Mulholland, and Shawn K. Collins. "Macrocyclic Olefin Metathesis at High Concentrations by Using a Phase-Separation Strategy." Chemistry-A European Journal 20, no. 40 (2014): 12763-12767.
78. Mack, Daniel J., and Jon T. Njardarson. "Recent advances in the metal-catalyzed ring expansions of three-and four-membered rings." ACS Catalysis 3, no. 2 (2013): 272-286.
79. Shimada, Tomohiro, and Yoshinori Yamamoto. "Carbon− Carbon Bond Cleavage of Diynes through the Hydroamination with Transition Metal Catalysts." Journal of the American Chemical Society 125, no. 22 (2003): 6646-6647.
80. Bédard, Anne-Catherine, and Shawn K. Collins. "Phase separation as a strategy toward controlling dilution effects in macrocyclic Glaser-Hay couplings." Journal of the American Chemical Society 133, no. 49 (2011): 19976-19981.

81. Rossiter, Walter J., McClure Godette, Paul W. Brown, and Kevin G. Galuk. "An investigation of the degradation of aqueous ethylene glycol and propylene glycol solutions using ion chromatography." Solar Energy Materials 11, no. 5-6 (1985): 455-467.
82. Hutchings, Ian M., and Graham D. Martin, eds. Inkjet technology for digital fabrication. John Wiley & Sons, 2012.
83. Spano, Frank C., and Carlos Silva. "H-and J-aggregate behavior in polymeric semiconductors." Annual review of physical chemistry 65 (2014): 477-500.
84. Li, Mengmeng, Cunbin An, Tomasz Marszalek, Martin Baumgarten, He Yan, Klaus Müllen, and Wojciech Pisula. "Controlling the Surface Organization of Conjugated Donor–Acceptor Polymers by their Aggregation in Solution." Advanced Materials 28, no. 42 (2016): 9430-9438.
85. Huang, Ye, Edward J. Kramer, Alan J. Heeger, and Guillermo C. Bazan. "Bulk heterojunction solar cells: morphology and performance relationships." Chemical reviews 114, no. 14 (2014): 7006-7043.
86. Mukumoto, Kosuke, Saadyah E. Averick, Sangwoo Park, Alper Nese, Anastasia Mpoukouvalas, Yukai Zeng, Kaloian Koynov, Philip R. Leduc, and Krzysztof Matyjaszewski. "Phototunable Supersoft Elastomers using Coumarin Functionalized Molecular Bottlebrushes for Cell-Surface Interactions Study." Macromolecules 47, no. 22 (2014): 7852-7857.
87. Whitfield, Richard, Athina Anastasaki, Vasiliki Nikolaou, Glen R. Jones, Nikolaos G. Engelis, Emre H. Discekici, Carolin Fleischmann, Johannes Willenbacher, Craig J. Hawker, and David M. Haddleton. "Universal conditions

for the controlled polymerization of acrylates, methacrylates, and styrene via Cu (0)-RDRP." Journal of the American Chemical Society 139, no. 2 (2017): 1003-1010.

88. Bielawski, Christopher W., and Robert H. Grubbs. "Highly efficient ring-opening metathesis polymerization (ROMP) using new ruthenium catalysts containing N-heterocyclic carbene ligands." Angewandte Chemie International Edition 39, no. 16 (2000): 2903-2906.
89. Xia, Yan, Julia A. Kornfield, and Robert H. Grubbs. "Efficient synthesis of narrowly dispersed brush polymers via living ring-opening metathesis polymerization of macromonomers." Macromolecules 42, no. 11 (2009): 3761-3766.
90. Bouas-Laurent, Henri, Alain Castellan, Jean-Pierre Desvergne, and Rene Lapouyade. "Photodimerization of anthracenes in fluid solution: structural aspects." Chemical Society Reviews 29, no. 1 (2000): 43-55.
91. Durmaz, Hakan, Gurkan Hizal, and Umit Tunca. "Linear tetrablock quaterpolymers via triple click reactions, azide-alkyne, diels–alder, and nitroxide radical coupling in a one-pot fashion." Journal of Polymer Science Part A: Polymer Chemistry 49, no. 9 (2011): 1962-1968.
92. Beckwith, A. L. J. "432. Reaction of anthracene with free radicals derived from 2, 2, 4-trimethylpentane (iso-octane)." Journal of the Chemical Society (Resumed) (1962): 2248-2257.

93. Dag, Aydan, Hakan Durmaz, Volkan Kirmizi, Gurkan Hizal, and Umit Tunca. "An easy way to the preparation of multi-miktoarm star block copolymers via sequential double click reactions." Polymer Chemistry 1, no. 5 (2010): 621-623.
94. Durmaz, Hakan, Aydan Dag, Gurkan Hizal, and Umit Tunca. "Cyclic homo and block copolymers through sequential double click reactions." Journal of Polymer Science Part A: Polymer Chemistry 48, no. 22 (2010): 5083-5091.
95. Erdogan, Tuba, Cigdem Bilir, Elif Erdal Unveren, A. Levent Demirel, and Umit Tunca. "Novel multiarm star block copolymer ionomers as proton conductive membranes." Polymer Chemistry 6, no. 4 (2015): 561-572.
96. Sun, Hao, Christopher P. Kabb, Yuqiong Dai, Megan R. Hill, Ion Ghiviriga, Abhijeet P. Bapat, and Brent S. Sumerlin. "Macromolecular metamorphosis via stimulus-induced transformations of polymer architecture." Nature Chemistry (2017).
97. Christensen, Scott Kenneth. Photo-reaction of copolymers with pendent benzophenone. University of Massachusetts Amherst, 2013.
98. López-Barrón, Carlos R., Patrick Brant, Aaron PR Eberle, and Donna J. Crowther. "Linear rheology and structure of molecular bottlebrushes with short side chains." Journal of Rheology 59, no. 3 (2015): 865-883.
99. Hu, Miao, Yan Xia, Gregory B. McKenna, Julia A. Kornfield, and Robert H. Grubbs. "Linear rheological response of a series of densely branched brush polymers." Macromolecules 44, no. 17 (2011): 6935-6943.

100. Dalsin, Samuel J., Thomas G. Rions-Maehren, Marissa D. Beam, Frank S. Bates, Marc A. Hillmyer, and Mark W. Matsen. "Bottlebrush block polymers: Quantitative theory and experiments." ACS nano 9, no. 12 (2015): 12233-12245.

101. Sato, Kazuhiro, Shingo Kobayashi, Miho Kusakari, Shogo Watahiki, Masahiko Oikawa, Takashi Hoshiba, and Masaru Tanaka. "The Relationship Between Water Structure and Blood Compatibility in Poly (2-methoxyethyl Acrylate)(PMEA) Analogues." Macromolecular bioscience 15, no. 9 (2015): 1296-1303.

102. Bär, Frits W., Frederik H. van der Veen, Abder Benzina, Jo Habets, and Leo H. Koole. "New biocompatible polymer surface coating for stents results in a low neointimal response." Journal of Biomedical Materials Research Part A 52, no. 1 (2000): 193-198.

103. Wang, You-Xiong, John L. Robertson, William B. Spillman, and Richard O. Claus. "Effects of the chemical structure and the surface properties of polymeric biomaterials on their biocompatibility." Pharmaceutical research 21, no. 8 (2004): 1362-1373.

104. Banerjee, Akhilesh, Manish Arha, Soumitra Choudhary, Randolph S. Ashton, Surita R. Bhatia, David V. Schaffer, and Ravi S. Kane. "The influence of hydrogel modulus on the proliferation and differentiation of encapsulated neural stem cells." Biomaterials 30, no. 27 (2009): 4695-4699.

105. McRae, Samantha, Xiangji Chen, Katrina Kratz, Debasis Samanta, Elizabeth Henchey, Sallie Schneider, and Todd Emrick. "Pentafluorophenyl ester-functionalized phosphorylcholine polymers: preparation of linear, two-arm, and

grafted polymer–protein conjugates." Biomacromolecules 13, no. 7 (2012): 2099-2109.

106. Xia, Jianhui, and Krzysztof Matyjaszewski. "Controlled/“living” radical polymerization. Atom transfer radical polymerization catalyzed by copper (I) and picolylamine complexes." Macromolecules 32, no. 8 (1999): 2434-2437.

107. Wuts, Peter GM, and Theodora W. Greene. Greene's protective groups in organic synthesis. John Wiley & Sons, 2006.

108. Engler, Adam J., Shamik Sen, H. Lee Sweeney, and Dennis E. Discher. "Matrix elasticity directs stem cell lineage specification." Cell 126, no. 4 (2006): 677-689.

109. Watt, Fiona M., and Wilhelm TS Huck. "Role of the extracellular matrix in regulating stem cell fate." Nature reviews. Molecular cell biology 14, no. 8 (2013): 467.

110. Lutolf, Matthias P., Penney M. Gilbert, and Helen M. Blau. "Designing materials to direct stem-cell fate." Nature 462, no. 7272 (2009): 433.

111. Trappmann, Britta, Julien E. Gautrot, John T. Connelly, Daniel GT Strange, Yuan Li, Michelle L. Oyen, Martien A. Cohen Stuart et al. "Extracellular-matrix tethering regulates stem-cell fate." Nature materials 11, no. 7 (2012): 642.

112. Valamehr, Bahram, Steven J. Jonas, Julien Polleux, Rong Qiao, Shuling Guo, Eric H. Gschweng, Bangyan Stiles et al. "Hydrophobic surfaces for enhanced differentiation of embryonic stem cell-derived embryoid bodies."

Proceedings of the National Academy of Sciences 105, no. 38 (2008): 14459-14464.

113. Rabinow, B. E., Y. S. Ding, C. Qin, M. L. McHalsky, J. H. Schneider, K. A. Ashline, T. L. Shelbourn, and R. M. Albrecht. "Biomaterials with permanent hydrophilic surfaces and low protein adsorption properties." Journal of Biomaterials Science, Polymer Edition 6, no. 1 (1995): 91-109.

114. Burdick, Jason A., and Gordana Vunjak-Novakovic. "Engineered microenvironments for controlled stem cell differentiation." Tissue Engineering Part A 15, no. 2 (2008): 205-219.